UV Stellar Populations in Globular Clusters: Horizontal Branch morphology and Blue Straggler Stars

A thesis

submitted for the degree of

Doctor of Philosophy

in

The Department of Physics,

Pondicherry University,

Puducherry - 605 014, India

by

Snehalata Sahu

Indian Institute of Astrophysics,

Bangalore - 560 034, India

September 2019

UV Stellar Populations in Globular Clusters: Horizontal Branch morphology and Blue Straggler Stars

Snehalata Sahu

Indian Institute of Astrophysics

Indian Institute of Astrophysics

Bangalore - 560 034, India

Title of the thesis	:	**UV Stellar Populations in Globular Clusters: Horizontal Branch morphology and Blue Straggler Stars**
Name of the author	:	**Snehalata Sahu**
Address	:	Indian Institute of Astrophysics II Block, Koramangala Bangalore - 560 034, India
Email	:	snehalata@iiap.res.in
Name of the supervisor	:	**Prof. Annapurni Subramaniam**
Address	:	Indian Institute of Astrophysics II Block, Koramangala Bangalore - 560 034, India
Email	:	purni@iiap.res.in

Declaration of Authorship

I hereby declare that the matter contained in this thesis is the result of the investigations carried out by me at the Indian Institute of Astrophysics, Bangalore, under the supervision of Annapurni Subramaniam. This work has not been submitted for the award of any other degree, diploma, associateship, fellowship, etc. of any other university or institute.

Signed: _____

Date: _____

Certificate

This is to certify that the thesis titled **'UV Stellar Populations in Globular Clusters: Horizontal Branch morphology and Blue Straggler Stars'** submitted to the Pondicherry University by Ms. Snehalata Sahu for the award of the degree of Doctor of Philosophy, is based on the results of the investigations carried out by her under my supervision and guidance, at the Indian Institute of Astrophysics. This thesis has not been submitted for the award of any other degree, diploma, associateship, fellowship, etc. of any other university or institute.

Signed: _____

Date: _____

List of Publications

1. Subramaniam, Annapurni; Tandon, Shyam N.; Hutchings, John; Ghosh, Swarna K.; George, Koshy; Girish, V.; Kamath, P. U.; Kathiravan, S.; Kumar, Amit; Lancelot, J. Paul; Mahesh, P. K.; Mohan, Rekhesh; Murthy, Jayant; Nagabhushana, S.; Pati, Ashok K.; Postma, Joe; Rao, N. Kameswara; Sankarasubramanian, Kasiviswanathan; Sreekumar, P.; Sriram, S. Stalin, Chelliah S.; Sutaria, Firoza; Sreedhar, Yuvraj Harsha; Barve, Indrajit V.; Mondal, Chayan; **Sahu, Snehalata.,** 2016, "In-orbit Performance of UVIT on ASTROSAT", *SPIE*, 9905, 99051F. [arXiv:1608.01073], (Impact Factor:3.5, citations:13)

2. Subramaniam, Annapurni; Sindhu, N.; Tandon, S. N.; Kameswara Rao, N.; Postma, J.; Côté, Patrick; Hutchings, J. B.; Ghosh, S. K.; George, K.; Girish, V.; Mohan, R.; Murthy, J.; Sankarasubramanian, K.; Stalin, C. S.; Sutaria, F.; Mondal, C.; **Sahu, S.,** 2016, "A Hot Companion to a Blue Straggler in NGC 188 as Revealed by the Ultra-Violet Imaging Telescope (UVIT) on ASTROSAT", *ApJ Letters*, 833, L27. (Impact Factor:8.374, citations:9)

3. Tandon, S. N.; Hutchings, J. B.; Ghosh, S. K.; Subramaniam, A.; Koshy, G.; Girish, V.; Kamath, P. U.; Kathiravan, S.; Kumar, A.; Lancelot, J. P.; Mahesh, P. K.; Mohan, R.; Murthy, J.; Nagabhushana, S.; Pati, A. K.; Postma, J.; Rao, N. Kameswara; Sankarasubramanian, K.; Sreekumar, P.; Sriram, S. Stalin, C. S.; Sutaria, F.; Sreedhar, Y. H.; Barve, I. V.; Mondal, C.; **Sahu, S.,** 2017, "In-orbit Performance of UVIT and First Results", *Journal of Astrophysics and Astronomy*, 38, 28. [arXiv:1612.00612], (Impact Factor:1.217, citations:16)

4. S.N. Tandon, Annapurni Subramaniam, V. Girish, J. Postma, K. Sankarasubramanian, S. Sriram, C.S. Stalin, C. Mondal, **S. Sahu**, P. Joseph, J. Hutchings, S.K. Ghosh, I.V. Barve, K. George, P.U. Kamath, S. Kathiravan, A. Kumar, J.P. Lancelot, D. Leahy, P.K. Mahesh, R. Mohan, S. Nagabhushana, A.K. Pati, N. Kameswara Rao, Y.H. Sreedhar, P. Sreekumar, 2017, "In-orbit Calibrations of the Ultra-Violet Imaging Telescope", *Astronomical Journal*, 154, 128. [arXiv:1705.03715], (Impact Factor:5.497, citations:22)

5. Subramaniam, Annapurni; **Sahu, Snehalata;** Postma, Joseph E.; Côté, Patrick; Hutchings, J. B.; Darukhanawalla, N.; Chung, Chul; Tandon, S. N.; Kameswara Rao, N.; George, K.; Ghosh, S. K.; Girish, V.; Mohan, R.; Murthy, J.; Pati, A. K.; Sankarasubramanian, K.; Stalin, C. S.; Choudhury, S., 2017, "The Horizontal Branch Population of NGC 1851 as Revealed by the Ultraviolet Imaging Telescope (UVIT)", *Astronomical Journal*, 154, 233. [arXiv:1710.03730], (Impact Factor:5.497, citations:2)

6. Singh, Avinash; Bhalerao, Varun; Anupama, G. C.; Mondal, Chayan; **Sahu, Snehalata.,** 2018, "AstroSat UVIT Observations of AT2018cow", *The Astronomer's Telegram*, 11822, 1.

7. **Sahu, Snehalata;** Subramaniam, Annapurni; Côté, Patrick; Rao, N. Kameswara; Stetson, Peter B., 2019, "UVIT-HST-GAIA view of NGC 288: a census of the hot stellar population and its properties from UV", *MNRAS*, 482, 1080-1095. [arXiv:1810.01846], (Impact Factor:5.231, citations:1)

8. **Sahu, Snehalata;** Subramaniam, Annapurni; Simunovic, Mirko; Postma, J.; Côté, Patrick; Kameswera Rao, N.; Geller, Aaron M.; Leigh, Nathan; Shara, Michael; Puzia, Thomas H.; Stetson, Peter B., 2019, "Detection of a White Dwarf Companion to a Blue Straggler Star in the Outskirts of Globular Cluster NGC 5466 with the Ultraviolet Imaging Telescope (UVIT)", *Astrophysical Journal*, 876, 34. [arxiv:1903.08212], (Impact Factor:5.58, citations:1)

9. **Sahu, Snehalata;** Subramaniam, Annapurni, 2019, "Radial Distribution of Blue Stragglers in NGC 5466 using AstroSat", Proceedings of IAU Symposium No. 351 Star Clusters: From the Milky Way to the Early Universe, in press.

10. Nayak P. K.; Subramaniam, Annapurni; Subramaniam, Smitha; Sahu, Snehalata; Mondal, Chayan; Cioni, Maria Rosa; Bell, Cameron, 2019, "Detecion of extended Red Clump in the SMC cluster Kron 3", Proceedings of IAU Symposium No. 351 Star Clusters: From the Milky Way to the Early Universe, in press.

Presentations

1. Poster presentation in the *Astronomical Society of India meeting 2016 (ASI:2016)* held at the University of Kashmir, Srinagar, Kashmir, India, during 10-13 May 2016.

2. Oral presentation in the *Astronomical Society of India meeting 2017 (ASI:2017)* held at B. M. Birla Auditorium, Jaipur, Rajasthan, India, during 6-10 March 2017.

3. Oral presentation in the international conference *Modelling and observing dense stellar systems, being MODEST*[17] *Under Prague's Starry Skies* held at Charles University, Prague, Czech Republic during 18-22 September 2017.

4. Poster presentation in the *Astronomical Society of India meeting 2018 (ASI:2018)* held at Osmania University, Hyderabad, India, during 5-9 February 2018.

5. Poster presentation in the *Star Clusters: from the Milky Way to the Early Universe, IAU Symposium 351 & MODEST-19* held at Bologna, Italy, during 27-31 May 2019.

Acknowledgements

I would like to express my gratitude to my Supervisor Annapurni Subramaniam for her guidance and motivation throughout my PhD work. I am very fortunate to come across with such a wonderful personality in my life. Her infinite energy, passion and dedication towards her work always inspired me to handle any type of situations very practically. The science discussions made with her always encouraged me to think and explore new things. Her immense support during my illness helped me to continue my research work without any hindrance. I enjoyed every moment of working with her and I owe my progress in PhD and the knowledge that I have gained to her mentorship.

I am very much thankful to be a part of a good research group and acknowledge all the discussions held in the weekly meetings. I am thankful to Ram Sagar, Smitha Subramaniam, and Koshy George for their valuable suggestions. I thank my seniors Samyaday, and Prasanta for their guidance during my initial years of PhD which helped me to pick up the work. I also thank Chayan, Sindhu and Avinash for useful discussions in learning new tools and techniques.

I wish to thank my collaborators S.N. Tandon, N. Kameswara Rao, Patrick Côté, J. Hutchings, Peter Stetson, Chul Chung, Thomas Puzia, Mirko Simunovic, Nathan Leigh, Aaron Geller, and Micahel Shara for their valuable suggestions and inputs which helped me to improve my work. I thank Joesph Postma for helping me to learn UVIT data reduction. I thank Francesco R. Ferraro, Barbara Lanzoni, Emanuele Dalessandro, for giving me the opportunity to present my work at the INAF, Bologna and appreciate their hospitality during my stay. I also thank A. P. Milone, A. F. Marino and Marco Tailo for their hospitality and discussions during my visit to University of Padua, Italy.

I would also take this opportunity to thank my doctoral committee members Gajendra Pandey and D. Bharathi Mohan for their help and suggestions.

I thank Avrajit, Priyanka, Rubinur, Amit, Anirban, Dipanweeta, Megha, Tanya, Aritra, Bhoomika, Sandeep and Samrat for their support during my work. Apart from that, I am grateful to my friends, my seniors and juniors for making my stay at Bhaskara memorable.

I thank my school and college teachers for motivating me to choose research field. I wish to thank my parents, my sister Sunita and my brothers Manoj and Prasan for their constant support, love and encouragement to pursue my dream.

Last but not the least, I thank the Universe for creating a beautiful night sky that always makes me wonder.

Data usage

We acknowledge the data usage from several space and ground based telescopes that is used in our thesis work.

Major part of the thesis work is done using UVIT data from the AstroSat mission of the Indian Space Research Organisation (ISRO), archived at the Indian Space Science Data Centre (ISSDC). UVIT project is a result of collaboration between IIA, Bengaluru, IUCAA, Pune, TIFR, Mumbai, several centres of ISRO, and Canadian Space Agency (CSA). Several groups from ISAC (ISRO), Bengaluru, and IISU (ISRO), Trivandrum have contributed to the design, fabrication, and testing of the payload. The Mission Group (ISAC) and ISTRAC (ISAC) continue to provide support in making observations with, receiving, and initially processing the data. We gratefully thank all the individuals involved in the various teams for providing their support of the project, from the early stages of the design to launch and in-orbit observations.

Apart from the UVIT, we have also used other space data for our work such as GALEX, HST and Gaia. We have used the GALEX archival data available from various programs/surveys that have been made available by Multi-Mission archive at the Space Telescope Science Institute (MAST) (http://galex.stsci.edu/GR6/). GALEX is operated for NASA by the California Institute of Technology under NASA contract NAS5-98034. The data from HST ACS survey of GCs by Sarajedini et al. (2007) has been used for combining with the UVIT data of the clusters.

We have used the *Gaia* DR2 catalogue of the cluster members provided by Gaia Collaboration et al. (2018b), that is obtained from the European Space Agency (ESA) mission *Gaia* (`https://www.cosmos.esa.int/gaia`)and processed by the *Gaia* Data Processing and Analysis Consortium (DPAC, `https://www.cosmos.esa.int/web/gaia/dpac/consortium`). Funding for the DPAC has been provided

by national institutions, in particular the institutions participating in the *Gaia* Multilateral Agreement.

We have used the data obtained from our observations at the Gemini Observatory, which is operated by the Association of Universities for Research in Astronomy, Inc., under a cooperative agreement with the NSF on behalf of the Gemini partnership: the National Science Foundation (United States), the National Research Council (Canada), CONICYT (Chile), Ministerio de Ciencia, Tecnología e Innovación Productiva (Argentina), and Ministério da Ciência, Tecnologia e Inovação (Brazil).

We have used archival data from several ground based observations such as SDSS and Pan-STARRS. Funding for the SDSS, SDSS-II and SDSS-III has been provided by the Alfred P. Sloan Foundation, the Participating Institutions, the National Science Foundation, the U.S. Department of Energy, the National Aeronautics and Space Administration, the Japanese Monbukagakusho, the Max Planck Society, and the Higher Education Funding Council for England. The SDSS Web Site is http://www.sdss.org/.

We have used IRAF for the data reductions. IRAF is distributed by the National Optical Astronomy Observatory (NOAO), which is operated by the Association of Universities for Research in Astronomy (AURA) under cooperative agreement with the National Science Foundation. For the data analysis and science, we have used VOSA, developed under the Spanish Virtual Observatory project supported by the Spanish MINECO through grant AyA2017-84089. This work also made use of TOPCAT, Matplotlib, IPython, and Astropy, a community-developed core Python package for Astronomy.

Dedicated to

my

family and friends

Abstract

Globular Clusters (GCs) are the systems that contains million of stars bound together by gravity forming a spherical distribution. As the timescales of dynamical encounters occurring in these dense systems are shorter than the age of the universe, they serve as ideal laboratories to study the formation and properties of exotic interacting stellar systems such as Blue Straggler Stars (BSSs), X-ray binaries etc. The Ultra-Violet (UV) observations of Galactic GCs (GGCs) in the past decade with HST and GALEX has uncovered interesting results such as detection of BSSs and very hot horizontal branch (HB) stars like Extreme horizontal branch (EHB) and blue hook (BHk) stars, multiple stellar populations (MSPs) in the color-magnitude diagrams (CMDs) etc. These results have shed new light in our understanding of the stellar evolution and dynamics in GCs.

In this thesis work, we adopted UV approach to study the hot stellar populations in three GCs: NGC 1851, NGC 288 and NGC 5466. We used Ultra-Violet Imaging Telescope (UVIT) data onboard Indian space observatory, AstroSat to obtain the Far-UV and Near-UV observations of the clusters. To identify the clusters members, we used the proper motion data of Gaia DR2. By combining UVIT with HST for the central regions and with ground observations for the outer regions, we generated the UV and UV-optical CMDs for the entire cluster region. These combinations along with the model isochrones made it possible to identify the locations of the hot stellar populations and classify them in UV CMDs.

The UV study on the HB morphology of the cluster NGC 288 unravels important results such as two peaks in the temperature distribution, the presence of several gaps in the HB, identification of three EHB candidates, etc. An important result is the deviation of the observed HB in the FUV CMDs from the isochrone at temperature 11,500 K

suggesting an onset of atomic diffusion. Similarly, our study on the HB population in a massive GC NGC 1851 using UV-optical CMDs reveals that the cluster hosts at least two stellar populations with either an age difference of 2 Gyr or an initial helium difference of 0.04 dex with a similar metallicity. We also studied the UV variability of the RR Lyrae stars and detected three new such candidates in this cluster.

Our study on the cumulative radial distribution of BSSs with respect to the HB stars in two low density GCs NGC 288 and NGC 5466, suggests that the BSSs are more centrally concentrated than HB stars. A study of the specific frequency of BSSs as a function of radius suggest that the clusters are of intermediate dynamical age, which in turn indicates that the dynamical friction has affected only up to a certain radius (1.5 times the half-light radius of the clusters) causing the segregation of massive BSSs. These clusters were found to have the highest specific frequency of BSSs known among the GGCs. Since stellar collisions are not that effective to create a BSS in these low-density clusters, the mass transfer in binaries might have led to such high rate of formation. This is supported by the detection of a hot white dwarf (WD) companion to a BSS located in the outskirts of cluster NGC 5466 which is described in this work.

Thus, our study demonstrates the capability of UVIT in resolving the stars in the centre of the clusters for example NGC 288 and NGC 5466. With its superior resolution and large field of view, UVIT provides the best platform for the sample selection of BSSs and HB stars to study their radial distribution in the entire cluster region. In addition, its multiple filters are useful for constructing the SEDs and estimating the parameters of the hot stellar populations.

Contents

List of Figures

List of Tables

Abbreviations

1G	First **G**eneration
2G	Second **G**eneration
ACS	**A**dvanced **C**amera for **S**urveys
AGB	**A**symptotic **G**iant **B**ranch
AGBM	**A**symptotic **G**iant **B**ranch **M**anqué
AIS	**A**ll sky **I**maging **S**urvey
BaSTI	**B**ags of **S**tellar **T**racks and **I**sochrones
BBSS	**B**right **B**lue **S**traggler **S**tar
BHB	**B**lue **H**orizontal **B**ranch
BHk	**B**lue **H**oo**k**
BP	**B**lue **P**hotometer
BSS	**B**lue **S**traggler **S**tar
CCD	**C**harge **C**oupled **D**evices
CDF	**C**umulative **D**istribution **F**unction
CFHT	**C**anada **F**rance **Ha**waii **T**elescope
CMD	**C**olor-**M**agnitude **D**iagram
CMOS	**C**omplementary **M**etal **O**xide **S**emiconductor
cog	**c**urve **o**f **g**rowth
CPS	**C**ounts **P**er **S**econd
CV	**C**ataclysmic **V**ariables
CZTI	**C**admium **Z**inc **T**elluride **I**mager
Dec	**Dec**lination

DIS	**D**eep **I**maging **S**urvey
DR	**D**ata **R**elease
EBSS	**E**volved **B**lue **S**traggler **S**tar
EHB	**E**xtreme **H**orizontal **B**ranch
ESA	**E**uropean **S**pace **A**gency
ESO	**E**uropean **S**outhern **O**bservatory
FBSS	**F**aint **B**lue **S**traggler **S**tar
FOV	**F**ield **O**f **V**iew
FRMS	**F**ast **R**otating **M**assive **S**tars
FSPS	**F**lexible **S**tellar **P**opulation **S**ynthesis
FUV	**F**ar **U**ltra-**V**iolet
FWHM	**F**ull **W**idth **H**alf **M**aximum
GALEX	**G**alaxy **E**volution **E**xplorer
GC	**G**lobular **C**luster
GGC	**G**alactic **G**lobular **C**luster
GI	**G**uest **I**nvestigator
GlobULeS	**U**VIT **Le**gacy **S**urvey of **Glob**ular clusters
GMOS-N	**G**emini **M**ulti-**O**bject **S**pectrograph-**N**orth
H-R	**H**ertzsprung-**R**ussell
HB	**H**orizontal **B**ranch
HRC	**H**igh **R**esolution **C**hannel
HST	**H**ubble **S**pace **T**elescope
HUT	**H**opkins **U**ltraviolet **T**elescope
IMF	**I**nitial **M**ass **F**unction
IR	**I**nfra**r**ed
IRAF	**I**mage **R**eduction and **A**nalysis **F**acility
ISRO	**I**ndian **S**pace **R**esearch **O**rganisation
IUE	**I**nternational **U**ltraviolet **E**xplorer
K-S	**K**olmogorov-**S**mirnov
KDE	**K**ernel **D**ensity **E**stimate

KPNO	**K**itt **P**eak **N**ational **O**bservatory
L1	**L**evel **1**
LAXPC	**L**arge **A**rea **X**-ray **P**roportional **C**ounter
LBC	**L**arge **B**inocular **C**ameras
LMXB	**L**ow **M**ass **X**-ray **B**inaries
LTE	**L**ocal **T**hermodynamic **E**quilibrium
MAST	**M**ikulski **A**rchive for **S**pace **T**elescopes
MCP	**M**icro **C**hannel **P**late
MIS	**M**edium **I**maging **S**urvey
MS	**M**ain **S**equence
MSP	**M**ultiple **S**tellar **P**opulations
MSTO	**M**ain **S**equence **T**urn **O**ff
MT	**M**ass **T**ransfer
MW	**M**ilky **W**ay
NASA	**N**ational **A**eronautics and **S**pace **A**dministration
NGC	**N**ew **G**eneral **C**atalogue
NICMOS	**N**ear **I**nfrared **C**amera and **M**ulti-**O**bject **S**pectrometer
NIR	**N**ear **I**nfra**r**ed
NOAO	**N**ational **O**ptical **A**stronomy **O**bservatory
NUV	**N**ar **U**ltra-**V**iolet
OAO-2	**O**rbiting **A**stronomical **O**bservatory **2**
OC	**O**pen **C**luster
PAGB	**P**ost **A**symptotic **G**iant **B**ranch
Pan-STARRS	**Pan**oramic **S**urvey **T**elescope **A**nd **R**apid **R**esponse **S**ystem
PC	**P**hoton **C**ounting
PM	**P**roper **M**otion
PSF	**P**oint **S**pread **F**unction
RA	**R**ight **A**scension
RGB	**R**ed **G**iant **B**ranch
RHB	**R**ed **H**orizontal **B**ranch

RP	**R**ed **P**hotometer
RRL	**RR L**yrae
SBC	**S**olar **B**lind **C**hannel
SDSS	**S**loan **D**igital **S**ky **S**urvey
SED	**S**pectral **E**nergy **D**istribution
SGB	**S**ub **g**iant **B**ranch
SSM	**S**canning **S**ky **M**onitor
SSP	**S**imple **S**tellar **P**opulations
SX Phe	**SX P**hoenicis
SXT	**S**oft **X**-ray **T**elescope
TOPCAT	**T**ool for **OP**erations on **C**atalogues **A**nd **T**ables
UV	**U**ltra-**V**iolet
UVIS	**U**ltra-**V**iolet **I**maging **S**pectrograph
UVIT	**U**ltra-**V**iolet **I**maging **T**elescope
VOSA	**V**irtual **O**bservatory **S**ED **A**nalyzer
WD	**W**hite **D**warf
WFC3	**W**ide **F**ield **C**amera **3**
WFPC2	**W**ide **F**ield and **P**lanetary **C**amera **2**
YSS	**Y**ellow **S**traggler **S**tar
ZAHB	**Z**ero **A**ge **H**orizontal **B**ranch
ZP	**Z**ero **P**oint

Chapter 1

Introduction

Star clusters are groups of stars that are located at the same distance and move together in space. They were traditionally regarded as Simple Stellar Populations (SSPs) i.e all the stars in a cluster are born at same time from a single molecular cloud, having same initial chemical composition. Two main types of star clusters known in the Milky Way (MW) are Open Clusters (OCs) and Globular Clusters (GCs) (Figure 1.1). OCs contain hundred to thousand stars spread in a volume of roughly 5 parsec with ages ranging from a few Myr to a few Gyr, whereas GCs contain millions of stars packed in a volume of $\sim$10 parsec with ages in the range 10-13 Gyr.

Star clusters are regarded as the fundamental building blocks of galaxies (Assmann et al. 2011), playing an important role in their formation and chemical evolution (Brodie & Strader 2006). Among the star clusters, GCs serve as excellent laboratories to study the effects and interplay between stellar evolution and stellar dynamics. Study of stellar populations in GCs can help in inferring the initial mass function (IMF) which are in turn related to the integrated stellar IMF of galaxies (Weidner & Kroupa 2005). When considered as a system, GCs provide a

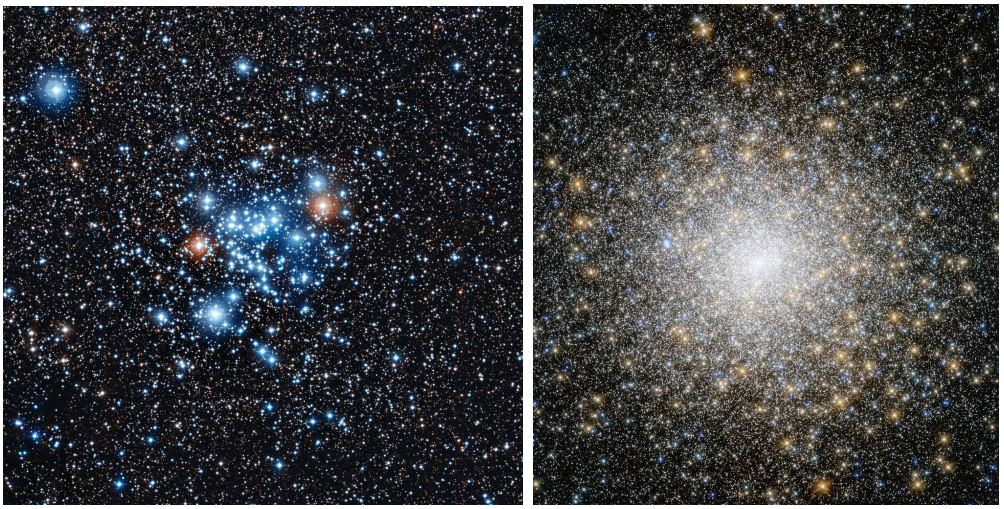

FIGURE 1.1: *Left*: Open cluster NGC 3766 (Credits: ESO) and *Right*: Globular Cluster M15 (Credits: HST).

fossil record of the various dynamical and chemical conditions in the galaxy during its early epoch of formation. Their estimation of ages can help us in constraining several cosmological theories regarding the formation and early evolution of the universe (Krauss & Chaboyer 2003).

There are about 200 GCs known in the MW that form a halo of roughly spherical shape around the galaxy with the highest concentration towards the galactic centre. Below we introduce the different phases of a star and its evolution in the GCs with their significance.

1.1 Stellar Evolution in GCs

The Color-Magnitude Diagram (CMD) of a GC is a basic and powerful tool to determine the fundamental parameters such as metallicity and age of the cluster from the observable parameters such as color and magnitude of stars. The observational CMD (color versus magnitude) of a GC M55 is shown in Figure 1.2

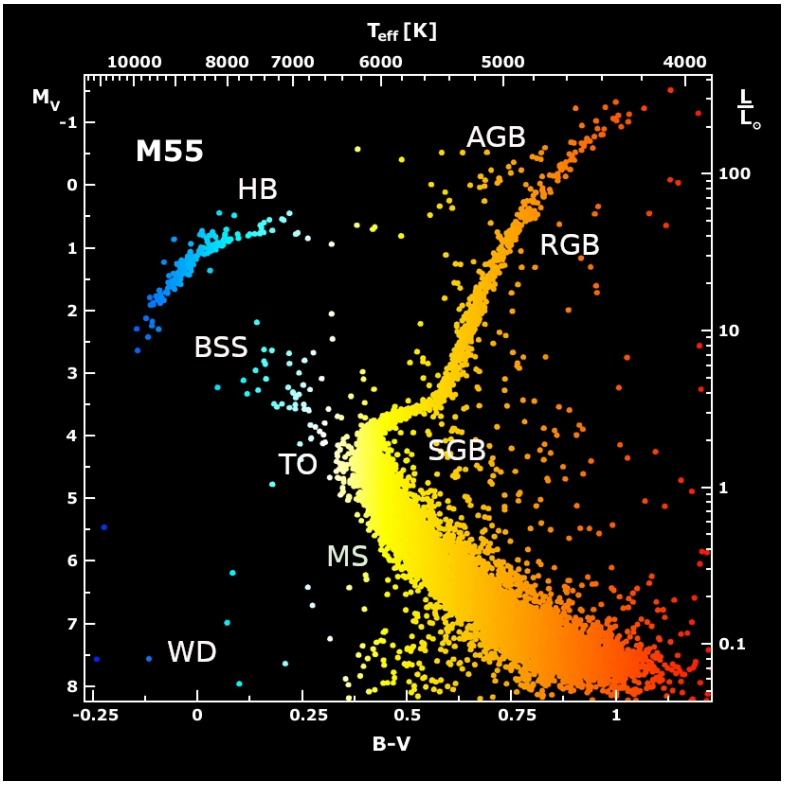

FIGURE 1.2: CMD of GC M55 with different evolutionary stages marked in the figure. Here, the color indicates the relative temperature of stars with red and blue corresponding to cool and hot stars. Credits: APOD/B.J. Mochejska, J. Kaluzny (CAMK), 1m Swope Telescope

along with the luminosity and surface temperature where the labels indicate the main evolutionary phases. The evolution of a star strongly depends on the initial mass which in turn determines the end fate of the star. Stars with an initial mass $< 8M_{\odot}$, eventually end up as a white dwarf (WD), whereas the more massive stars end their lives as a Supernova with a neutron star or a black hole as the remnant. We describe in brief the important evolutionary stages of low mass stars ($< 2M_{\odot}$) relevant to the GCs. The Hertzsprung-Russell (H-R) diagram in Figure 1.3 shows the evolutionary track of 1 $M_{\odot}$ star along with its structure during different phases of its post main sequence (MS) evolution.

Since the GCs are of very old age, the massive MS stars are already evolved off resulting in a MS which is populated by only low-mass ($< 1M_{\odot}$) stars. The star

spends most of its time (∼70%) in the MS phase, undergoing nuclear burning of the hydrogen (H) in the cores. As the core of the star gradually runs out of the H fuel, the star leaves the MS and starts evolving off to the redder side in the H-R diagram. The bluest and hottest point of the MS at which it happens is termed as the main sequence turn-off (MSTO) point. The MSTO serves as a stellar clock which indicates the age of a star and hence that of the GC. The mass of the MSTO stars in the Galactic GCs (GGCs) is typically around 0.78-0.8 $M_{\odot}$.

After H exhaustion in the core of the MS stars, a helium (He) core remains which is surrounded by a H-rich envelope (Figure 1.3). Since, the temperature is too low ($< 10^8$ K) to ignite the He burning in the core, only the shell burning of the H takes place at the base, resulting in the core contraction and envelope expansion. This expansion causes the outer layers to cool and the opacity of the envelope increases. During this phase, the star starts to move to the redder side in the H-R diagram at constant surface luminosity, which is called as sub-giant branch (SGB) phase. In this phase, one important change in the structure is that envelope becomes convective providing energy which in turn slows down the expansion of star. The further expansion causes the star to move up in the H-R diagram at a constant effective temperature (T_{eff}) with an increase in luminosity leading to the red giant branch (RGB) phase. The convection causes the He produced during the MS phase to get mixed up with the H burning shell and the other chemical species involved in it resulting in their mixing. A study of surface abundances of the elements can throw light on the convection and the degree of mixing in RGB stars.

Due to the large central density after the end of the MS phase, the low mass stars ($< 2M_{\odot}$) have a He electron degenerate core as compared to the massive stars. During the RGB phase, the H burning shell keeps dumping the He into the core which leads to a increase in the mass and hence, the density of the He core. As the mass of the He core becomes 0.47-0.5 $M_{\odot}$, the star reaches a temperature

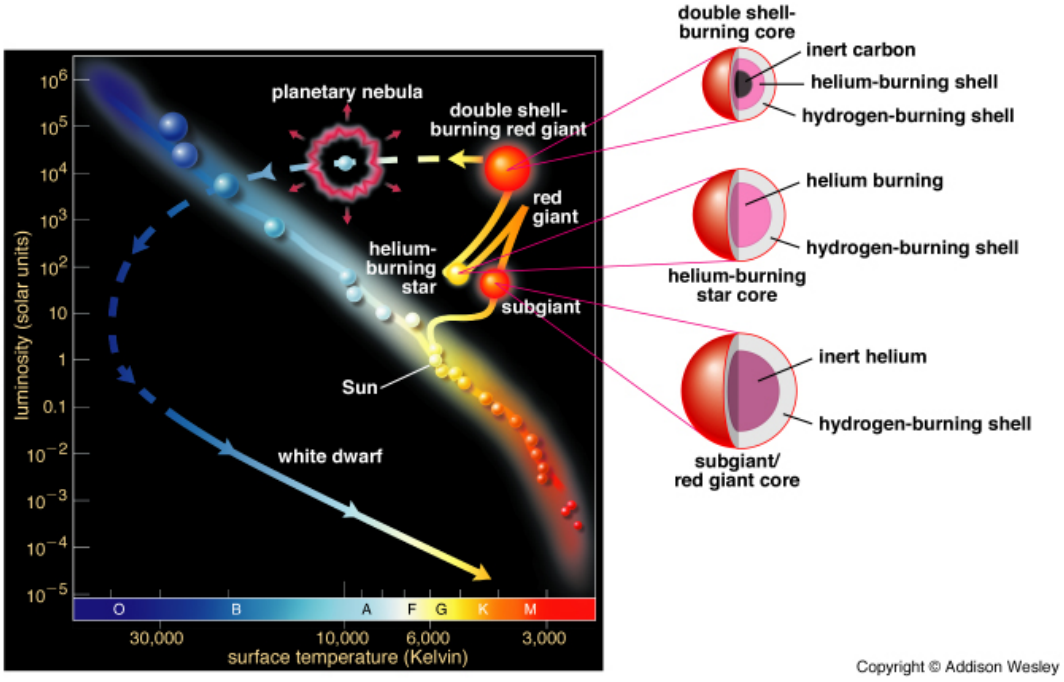

FIGURE 1.3: Stellar evolution of 1 $M_{\odot}$ in the H-R diagram (left) with the right side showing the structure of the star in different evolutionary phases. Image Credits: Pearson Addison-Wesley.

($\sim 10^8$ K) sufficient to lift the electron degeneracy and ignite He in the core. This stops the core contraction and the nuclear burning of the He starts (Figure 1.3). Since the core was highly degenerate, the nuclear burning of the He is unstable at the tip of the RGB which leads to He flash, thus ending the RGB phase. As the nuclear He burning in the centre starts, the H burning shell cools down decreasing the surface luminosity, which causes the star to move down to the bluer side in H-R diagram called as the horizontal branch (HB) stars. This phase lasts for $\sim 10^8$ yrs converting He into Carbon (C) and Oxygen (O) in the core. Now, as the He vanishes in the core, the star starts burning He in a shell which causes it to move asymptotically towards a larger luminosity and lower T_{eff} in the H-R diagram, merging with the RGB. This phase is known as asymptotic giant branch (AGB) phase, which is similar to the RGB phase with a double shell burning (H and He) and a C-O core. The thermal pulses in the AGB phase causes the stars to lose most of its envelope. Thus, the C-O degenerate core no longer reaches

the sufficient temperature to ignite the nuclear burning and the star leaves the AGB phase moving towards higher T_{eff}. The rapid mass loss in the AGB phase leaves behind a hot white dwarf in the centre of planetary nebula. After that, the WD cools down and becomes faint evolving at a constant radius towards a lower luminosity in the H-R diagram (Figure 1.3). The mean mass of the WDs observed in GCs is $\sim$ 0.5-0.6 $M_{\odot}$. Thus, GCs are the systems where we can study the advanced stages of stellar evolution very well.

One of the important and prominent evolutionary phase found in the GCs is the HB which is populated by the core-He burning stars. This is an important feature as it is used to measure distance of the cluster as well as its age. In this thesis we study the HB stars, particularly the hot Ultra-Violet (UV) bright stellar populations.

1.2 HB morphology

The distribution of the color (temperature) of stars in the HB is referred as HB morphology. The HB stars are given different names according to their color distribution as shown in the CMD of GC NGC 2808 in Figure 1.4 which is well populated by all types where BHB, RHB and EHB refers to Blue, Red and Extreme HB stars respectively. RR Lyrae (RRL) stars are pulsating HB stars located between BHB and RHB stars with periods varying from 0.3-1.5 days. BHB stars are those hotter than RRL stars with $T_{eff} > 8000$ K.

The structure of the zero-age HB (ZAHB) is determined by three parameters: the size of the He core mass, the chemical composition and mass of the envelope. The "first parameter" which determines the morphology of HB stars is metallicity where a metal-rich cluster is generally found to have a redder HB while a

metal-poor cluster, a bluer HB. For a fixed metallicity, the colour of the HB stars is determined by the thickness of the envelope. The star looks red (cool) if the envelope is thicker or the star had less mass loss in the RGB phase whereas it looks blue (hot) if the envelope is thinner or the star had large mass loss in the RGB phase. From the study of CMDs of different GCs, e.g. NGC 288 and NGC 362 (Catelan et al. 2001), it has been found that same metallicity clusters have different HB morphology. Thus, apart from metallicity, there are other parameters which can affect their distribution known as "second parameter" problem (Dotter et al. 2010). Some of these second parameters are age, mass loss, initial He abundance (Y_{ini}), stellar rotation etc. Since, they have similar effect on the HB, there is no established explanation for which of these second parameters are mainly responsible for the distribution of stars along HB in GGCs.

One important feature noticed in the HB morphology is the presence of regions devoid of stars which result in several gaps in the HB distribution as marked in Figure 1.4. Grundahl et al. (1999) with accurate strömgren photometry (u vs $u-y$) found a gap/discontinuity at $T_{eff} \sim$ 11,500 K known as G-jump within the BHB stars in the CMDs of GCs. This gap was attributed to the atmospheric effects such as atomic diffusion and radiative levitation in HB stars (Moehler et al. 1999). Radiative levitation is the effect in which the radiation pressure pushes certain elements outward leading to an increase in metal content in the outermost layers. Sweigart (2002) found that the onset of radiative levitation matches with the disappearance of surface convective layers present at He I ionization region corresponding to $T_{eff} \sim$ 11,500 K which results in a gap (G-jump) at that temperature. Similarly, gaps were found between BHB and EHB stars at $T_{eff} \sim$ 20,000 K known as M-jump (Momany et al. 2002, 2004) and EHB and blue hook (BHk) stars at $T_{eff} \sim$ 32000-35000 K (Sweigart 1987; Brown et al. 2001) known as B gap. EHB stars are core-He burning stars with $T_{eff} >$ 20,000 K whereas BHk stars are those with $T_{eff} >$ 32,000 K with a fainter luminosity than EHB stars. They have insufficient envelope mass to support a H burning shell and thus, have

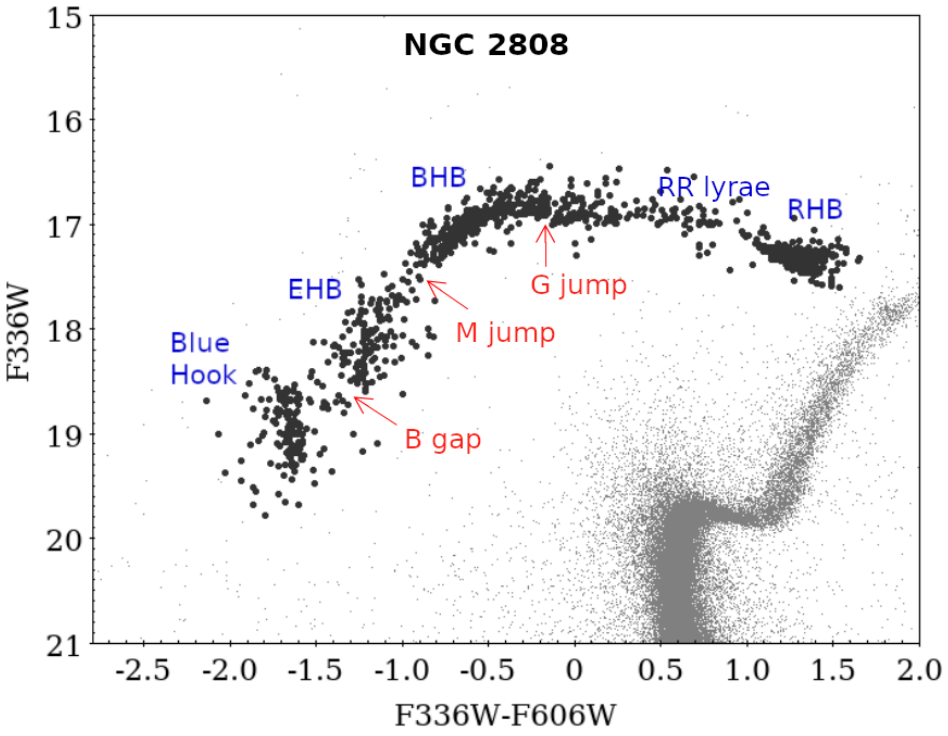

FIGURE 1.4: F336W−F606W vs F336W HST CMD of GC NGC 2808 (Piotto et al. 2015) with different HB stars marked in the Figure. The HB gaps are shown in red arrow where G jump, M jump and B gap corresponds to the Grundahl jump, Momany jump and the gap between EHB and blue hook stars respectively.

fainter luminosities than BHB stars. EHB stars are also known as sub-dwarfs because they lie below the MS in the optical CMDs. After exhausting the He in their core, EHB stars do not have enough mass ($< 0.52 M_{\odot}$) to evolve to AGB phase and thus end up as AGB manqué (AGBM) stars. Brown et al. (2001) suggested that these stars might have formed as a result of late He flash while descending the WD cooling curve, due to the rapid mass loss in the RGB phase known as 'late hot flash scenario' which is not well understood.

The EHB and BHk stars are hotter than the rest of the BHB stars and hence appear bright in the UV. These stars are easily detectable in the Far-UV wavelength whereas the RHB and RGB stars are too faint to be detected. Therefore, UV images are ideal to detect and characterize the hot population of this HB stars.

1.3 Stellar dynamics in GCs

There are three important timescales that govern the dynamical behaviour of star clusters. They are as follows:

- Evolution time (t_{evol}) : the time required for the typical stellar evolution of the member stars in a cluster which is typically around 10^{10} years.
- Crossing time (t_{cr}) : the time required for a star to travel across the cluster i.e. from one side to the other. For a typical GC of size few parsec, it varies from 10^5-10^6 years.
- Relaxation timescale (t_{relax}) : the time required to change the orbit of a star to such an extent (by cumulative stellar encounters) that it can no longer be described by its regular orbit. It typically varies from $10^8 - 10^{10}$ years in GCs (Harris 2010).

There is a well known relation between crossing time and relaxation time which is given by:

$$t_{relax} = \frac{0.1N}{ln(N/2)} t_{cr} \tag{1.1}$$

where N is the total number of stars in a system. Thus, the number of orbits a star takes before it is significantly perturbed by other stars in the system depends on N. Given, the large number of stars in a GC (N $\sim 10^6$), $t_{relax} \sim 10^4 t_{cr}$ which suggests that $t_{cr} << t_{relax} << t_{evol}$. Since, the timescale for the stellar encounters in GCs is much shorter than the age of the universe, they produce a lot of exotic interacting stellar systems such as Blue Straggler Stars (BSSs), Cataclysmic Variables (CVs), low mass X-ray binaries (LMXBs), etc. We introduce here one such exotic object, BSSs that is studied in this thesis.

1.4 Blue Straggler Stars

Sandage (1953) first discovered BSSs in the CMD of GC M3 as a part of his PhD work. He identified 34 such objects in the cluster outskirts and suggested that they cannot be field stars due to their bluer color and lack of any random distribution. The situation was very different by 1992, where with the help of high-resolution Hubble Space Telescope (HST) and wide-field CCD surveys with ground telescopes, it was found that the BSSs do not just exist in the outer regions but also populate the dense central cores of the GCs. The first catalog of BSSs was published by Fusi Pecci et al. (1992) with the most recent one by Piotto et al. (2004) using HST/Advanced Cameras for Surveys (ACS) of GCs, which consists of 3000 BSSs in 56 GCs.

The most general definition of BSSs is, they are core-hydrogen burning stars lying above the MSTO in the CMD (Figure 1.2) that appear bluer and brighter than the MS stars. BSSs are called so (Burbidge & Sandage 1958), because they were bluer in color than the MS stars and "straggle" or lag in age behind their ancient neighbours. Since their existence cannot be explained by the standard theory of stellar evolution for single stars, the question was how these stars formed, appearing young in such old and metal-poor environments devoid of gas. Several formation mechanisms were put forth by scientists with the two leading scenarios being: stellar collisions leading to mergers in high density environments (Hills & Day 1976) and mass transfer (MT) from an evolved donor to a lower-mass star in a binary system in low density environments (McCrea 1964; Chen & Han 2008). Three different cases of MT were proposed for the BSS formation (Kippenhahn & Weigert 1967; Paczyński 1971) through Roche lobe overflow, depending on the evolutionary type of donor star are: Case A where donor is a MS star; Case B where donor is in RGB; and Case C where donor is in AGB phase. Case A MT can produce either single BSSs or short-period BSS binaries whereas Case B and

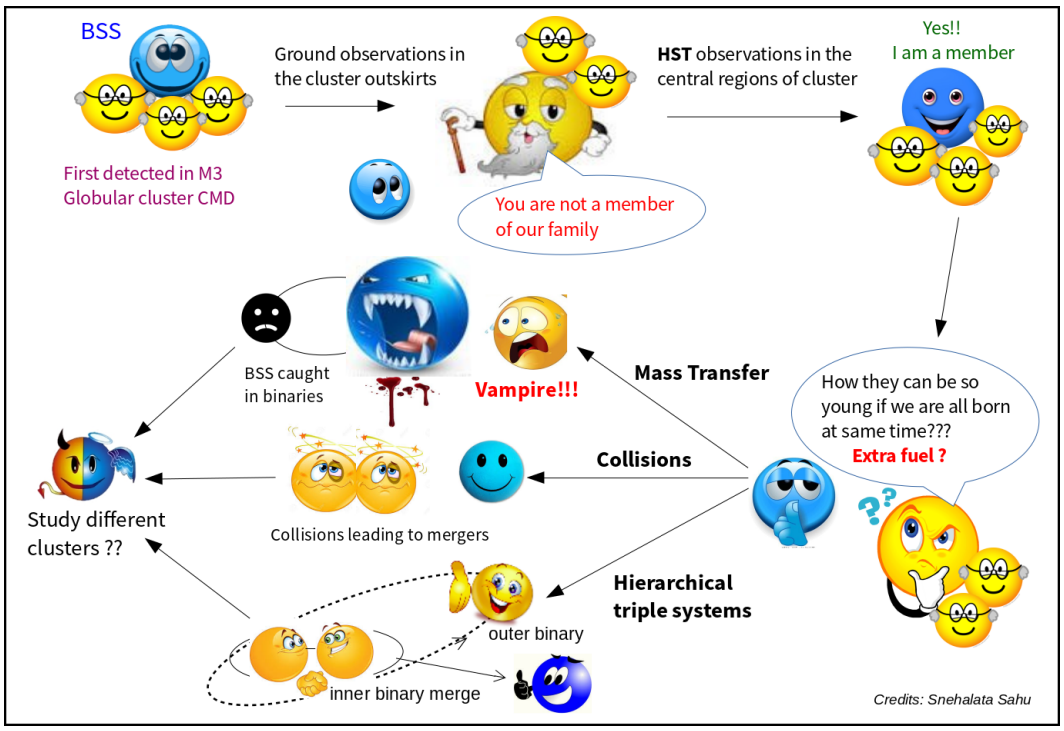

FIGURE 1.5: A cartoon of BSSs giving an overview of their detection and formation.

Case C can produce BSSs with a He or CO WD companion of masses 0.5-0.6 and 0.2-0.4 $M_{\odot}$ respectively (Perets & Fabrycky 2009).

The observational signatures of the binary origin of BSSs came from the identification of Algol-type eclipsing binaries and contact binaries at the location of BSSs, in GC CMDs (Mateo et al. 1990). It was also found that the radial distribution of binaries in clusters are similar to the distribution of BSSs confirming their binary origin (Beccari et al. 2013). To explain the existence of BSS binaries with a long period companion, a third mechanism is proposed for their formation which is the evolution of hierarchical triple systems (Eggleton & Kisseleva-Eggleton 2006; Fabrycky & Tremaine 2007). In such systems, a third star is being orbited by a tight inner binary through their common centre of mass, like a wider outer binary. The outer companion can cause Kozai-Lidov oscillations (Kozai 1962; Lidov 1962) perturbing the orbit of the inner binary and causing it to merge to form a BSS.

Stellar collisions involving multiple systems are needed to explain the location of brightest BSSs in the GC CMDs with luminosities twice that of the MSTO stars. A cartoon depicting an overview of BSSs with the formation mechanisms as explained above is shown in Figure 1.5.

After the BSSs form, they evolve like a normal massive MS star (1.2-1.4 $M_{\odot}$) through other phases. Like HB stars, they pulsate when they pass through the instability strip. These pulsating BSSs with short periods ranging from 0.03-0.08 days are known as SX Phoenicis (SX Phe) variables. Since, SX Phes follow period-luminosity relation (Cohen & Sarajedini 2011), they provide a direct way to estimate the masses of BSSs (Fiorentino et al. 2015) and distances to GCs (Nemec & Mateo 1990). During their evolution, if BSSs are detected lying above the SGB they are known as yellow straggler stars (YSSs) whereas those lying above the RHB are referred as evolved BSSs (EBSSs). Studying their evolution can help in understanding what processes might have led to their formation.

BSSs are important to study as they can throw light on the dynamical status of the GCs. As the BSS population are more massive (1.2-1.4 $M_{\odot}$) than the majority of the stars (0.4 $M_{\odot}$) in the cluster, they are affected by the dynamical friction (Chandrasekhar 1943) which makes them sink towards the cluster center as shown in Figure 1.6. This sinking leads to mass segregation in GCs with the more massive BSSs being centrally concentrated than the less massive ones. To study this effect, Ferraro et al. (1993) introduced a parameter called "double normalised ratio" defined as:

$$R_{BSS} = \frac{N_{BSS}/N_{BSS}^{tot}}{L^{sampled}/L_{tot}^{sampled}} \tag{1.2}$$

where N_{BSS} is the number of BSSs in a selected cluster region, N_{BSS}^{tot} is the total number of observed BSSs, $L^{sampled}$ is the fraction of light sampled in the same cluster region selected for N_{BSS} and $L_{tot}^{sampled}$ is the total sampled luminosity. Ferraro et al. (2012) demonstrated that the morphology of this parameter is strongly

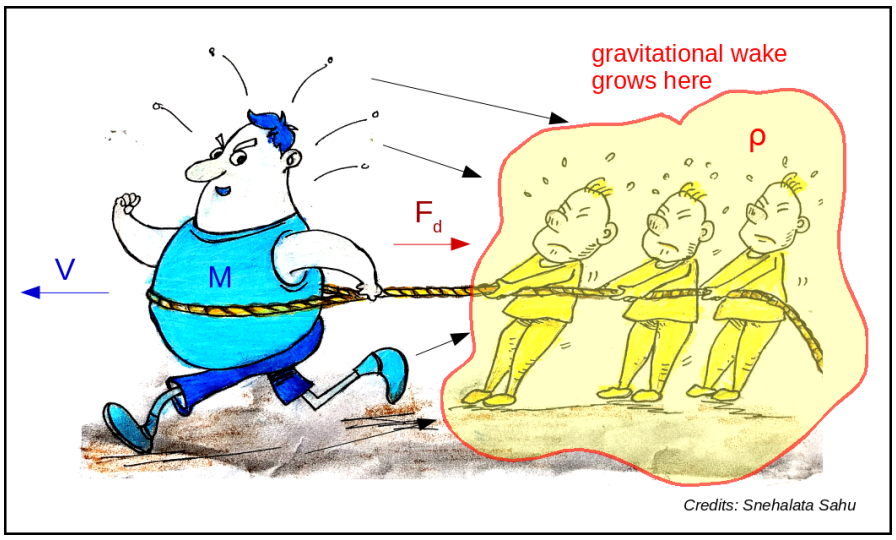

FIGURE 1.6: Cartoon depicting the dynamical friction experienced by the BSS of mass M moving with a velocity V though a medium of uniform density ρ, consisting of low mass stars (m<<M). The BSS perturbs the medium as it passes through it creating a gravitational wake behind, which in turn causes a drag force (F_d) on the BSS making it to slow down.

shaped by the action of dynamical friction. Based on the distribution of this parameter, they classified the GCs in three different families: Family I where the R_{BSS} has a flat distribution and is dynamically young age, Family II where the R_{BSS} has a bimodal distribution and is of dynamically intermediate age and Family III where R_{BSS} has a unimodal distribution and is dynamically old age. This parameter can thus be used as a "dynamical clock", which reflects the dynamical evolutionary stage of the cluster, in comparison to its stellar evolutionary age. Another definition of the parameter adopted in the literature is specific frequency of BSSs, $S_{BSS} = N_{BSS}/N_{pop}$ (Ferraro et al. 2003), where N_{BSS} is the number of BSSs and N_{pop} is the number of the normal population of stars (MS, RGB or HB) considered as a reference for study.

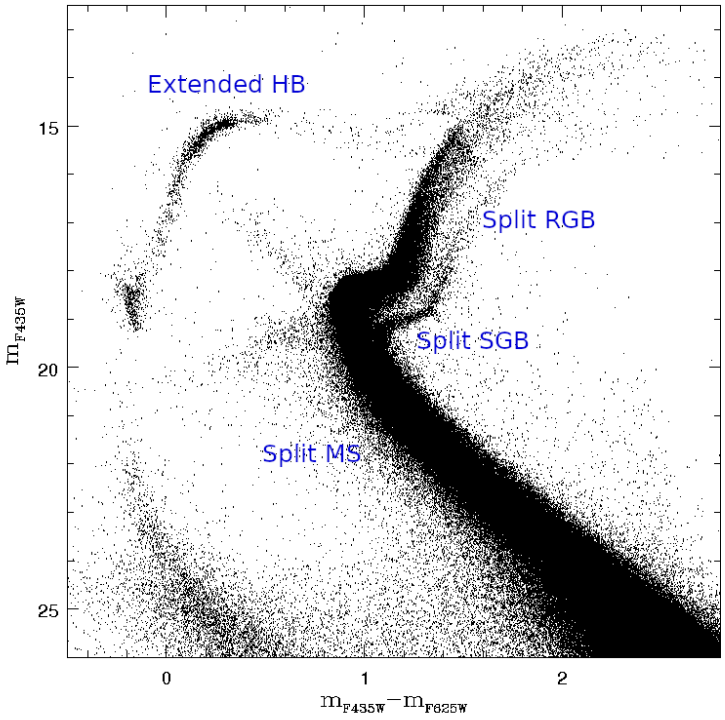

FIGURE 1.7: F435W−F625W vs F435W CMD of GC ω Centauri obtained from HST/WFC3 observations showing the presence of multiple sequences in MS, RGB and SGB (Bellini et al. 2010).

1.5 Multiple Stellar Populations in GCs

The definition of GCs being SSPs has changed with the discovery of multiple sequences in the optical CMDs of almost all GCs (see recent review by Bastian & Lardo (2018). GCs are now considered as Multiple Stellar Populations (MSPs) i.e. systems harboring more than one stellar populations. The first direct observational evidence of MSPs came from the discovery of two MS below the MSTO in the CMD of ω Centauri by Bedin et al. (2004). With further studies (Sollima et al. 2005), it was found that the CMD of GC ω Centauri shows split in all the sequences (MS, SGB, RGB) as shown in Figure 1.7. Later, Piotto et al. (2012) conducted an HST survey of eight GCs to check the presence of MSPs and found multiple SGBs in all of them.

The photometric signatures of the MSPs in GCs and their possible explanations are the following:

- split MS: difference (ΔY_{ini}) in initial He abundances (Y_{ini}) between the stellar populations with the bluer ones being more He rich than the redder population. e.g. $\Delta Y_{ini} \sim 0.14$ between the bluest and reddest MS of GC NGC 2808 (Piotto et al. 2007).

- split SGB: difference in age, metallicity or CNO abundances. e.g. the faint SGB population is 1 Gyr older than the bright SGB in NGC 1851 (Milone et al. 2008).

- split RGB: variations in light element abundances such as Sodium (Na) and Oxygen (O). e.g. the redder RGB population in M4 are Na rich and O poor than the bluer RGB ones (Marino et al. 2008).

- Extended HB: presence of EHB stars that are populated by the He rich MS, for example, varying Y_{ini} from 0.25 to 0.4 can reproduce the HB morphology in NGC 2808 (Dalessandro et al. 2011).

Similarly, the spectroscopic signatures validating the MSPs in GCs are- abundance pattern of light elements such as C-N anti-correlation, Na-O and Magnesium (mg) -Aluminium (Al) anti-correlation observed in the RGB, MS and SGB stars in GCs (Carretta et al. 2009; Villanova et al. 2010; Marino et al. 2013). These evidences suggest that the GCs are composed of at least two stellar populations which are referred as first generation (1G) and second generation (2G) stars. 1G stars are defined as those showing same chemical abundances as that of the field stars whereas 2G stars are those showing enhanced chemical abundances (N, Na, Al) and depleted O and C with respect to the field stars for the same metallicity ([Fe/H]). From observations, it was found that the fraction of 2G stars in GCs is generally higher than that of the 1G stars.

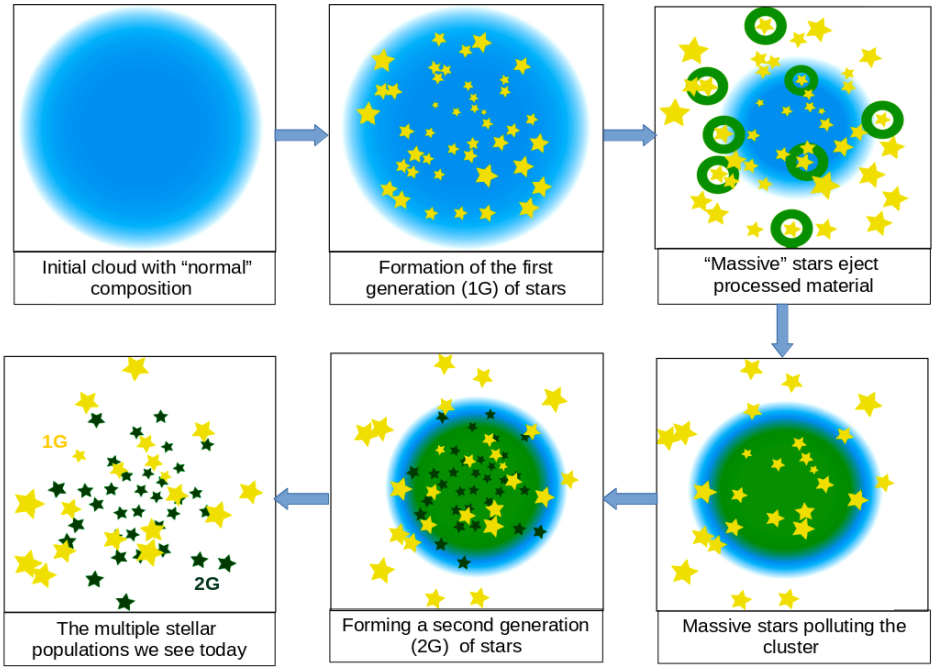

FIGURE 1.8: Simplified scenario of formation of MSPs in GCs. Image Credits: S.E. de Mink/STScI

A simplified formation scenario such as "self enrichment sceanrio" (Prantzos & Charbonnel 2006) proposed for the origin of MSPs in GCs is shown in Figure 1.8. In this scenario, a fraction of 2G stars in GCs form from the ejecta of the 1G massive stars. 1G stars lose huge amounts of mass through stellar winds polluting the intracluster medium, which can be retained by the gravitational potential well of the cluster forming circumstellar discs from which 2G stars are born. Two such possible polluters are the fast-rotating massive stars (FRMS) (20-120 $M_{\odot}$, Decressin et al. (2007)) and massive AGB stars (4 to 10 $M_{\odot}$, D'Ercole et al. (2008); Ventura et al. (2011)). However, these models are unable to reproduce all the chemical peculiarities of MSPs observed in GCs and thus need further attention.

1.6 Importance of Ultra-Violet study

The identification of BSSs in optical wavelengths, especially in the central regions of GCs is not easy even with HST because the optical emission in GCs is mainly dominated by the cool and bright RGB and AGB stars. Also, the SGB and RGB stars cause photometric blends mimicking the location of BSSs in optical CMDs and hence creating a problem in their proper selection. On the other hand, the EHB and BHk stars are very faint in optical CMDs making their selection difficult. Since, the BSSs and HB stars are hot, their peak emission lies in UV wavelengths. Switching to UV wavelengths, the RGB/AGB stars become fainter reducing the blends arising due to the crowding, whereas the BSS and HB population become bright making their identification easier. Figure 1.9 shows the image of a GC NGC 288 in different wavelengths. We can clearly notice that the crowding in the central regions is severe in the visible and infrared (IR) bands whereas it is the least in FUV band that is dominated by the emission from only hot stars. The MS and RGB stars are relatively faint in Near-UV (NUV) as compared to visible. Thus, UV observations serve as the best choice for the study of hot stellar populations in GCs.

The schematic diagrams of the optical and UV CMDs are shown in Figure 1.10. We notice that the HB stars are no longer horizontal, instead, they from a diagonal sequence spanning more than 3 magnitudes (mag) in UV CMDs. The BSSs are also brighter and form a narrow vertical sequence that span more than 3 mag, similar to HB stars. Thus, UV plane serves as best plane for the identification and study of BSSs and HB stars as compared to optical CMDs. Since, the UV plane is very favorable for the selection of HB stars, the HB population is used as reference for deriving the specific frequency and studying the radial distribution of BSSs in GCs as described in Section 1.4.

UV observations are also helpful in detecting the MSPs in GCs. Piotto et al.

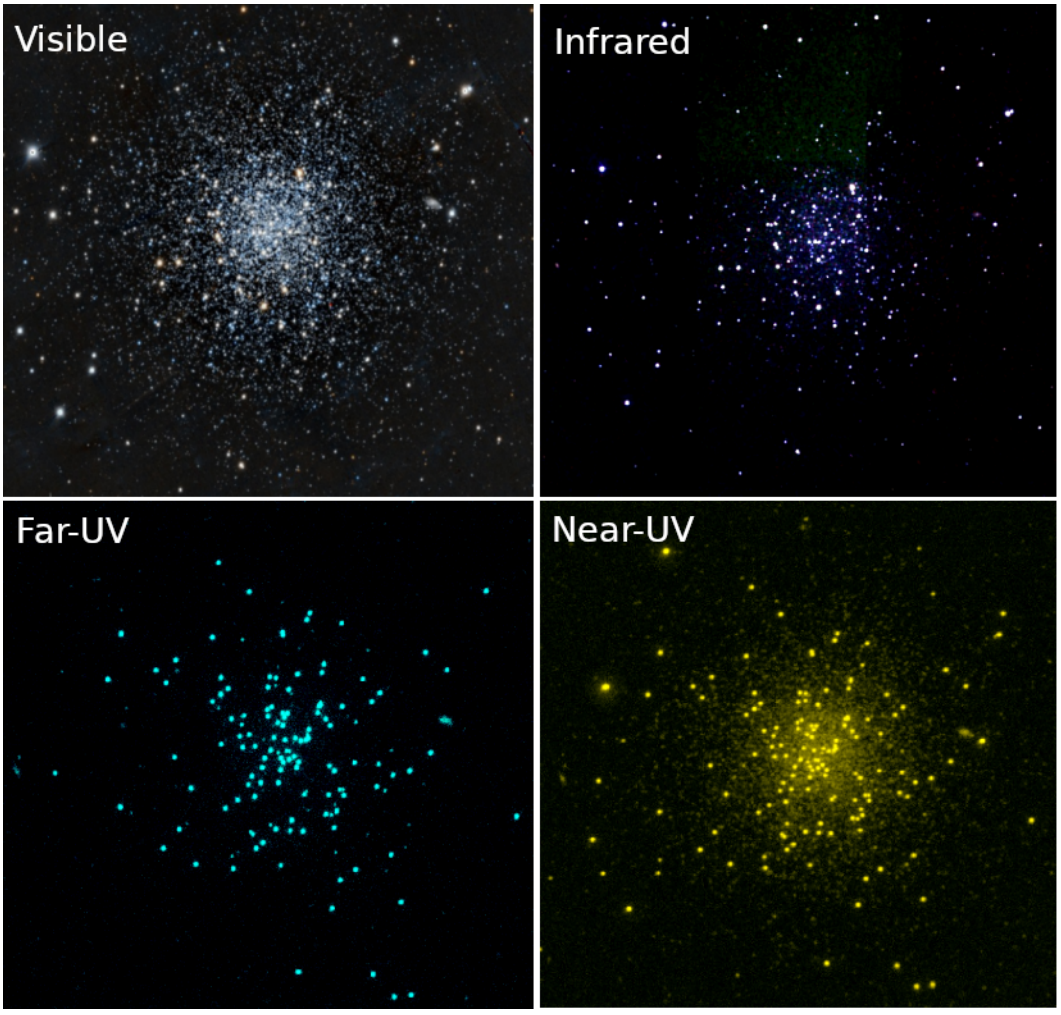

FIGURE 1.9: Images of GC NGC 288 in different wavelengths: Visible is from Pan-STARRS (top left), IR is from 2MASS (top right), and FUV (bottom left), NUV (bottom right) is from GALEX.

(2015) conducted HST UV legacy survey of 54 GGCs and found the presence of MSPs in all the GCs. The three filters- F275W, F336W and F435W of HST/Wide Field Camera 3 (WFC3) UVIS channel called as "magic trio" were found to be the best combination to identify and characterize the MSPs in GCs. The main advantage of these filters is that they fall in the wavelength range (3000-4000 $\mathring{A}$) where CN and NH absorption bands are located. For example, using these three filter combinations along with F814W, Milone et al. (2015) clearly detected the presence of splits in almost all sequences in the NUV CMD of GC NGC 2808. This also showed that the MSPs in GCs are filter dependent with the UV filters being

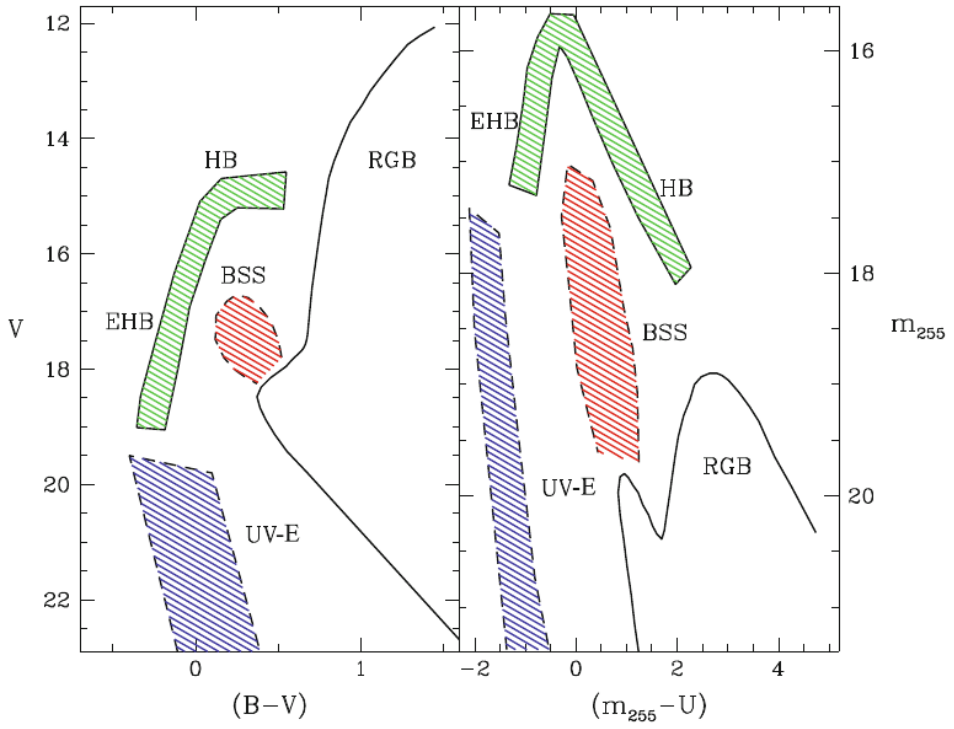

FIGURE 1.10: Schematic diagram showing the location of stellar evolutionary sequences in optical (left) and UV (Right) CMDs. Credits: Ferraro et al. (2012)

sensitive to the variations in C, N, O and He abundances. The filters enhance the split in the sequences making it easier to distinguish the features of MSPs in the CMDs.

The importance of UV observations was recognised with the discovery of UV upturn phenomenon in elliptical galaxies by Code & Welch (1979) using OAO-2 space telescope. They found that the spectra of the bright elliptical galaxies show a rise in flux below 2500$\mathring{A}$ that falls in FUV region. This was unexpected in a system consisting of only old stellar populations where the metal-rich cool stars dominate the optical light. Later, the UV upturn was confirmed by several space missions such as Hopkins Ultra-Violet Telescope (HUT) (Bertola et al. 1982), International Ultra-Violet Explorer (IUE) (Brown et al. 1997), Galaxy Evolution Explorer (Yi et al. 2011) etc. Brown et al. (1997) found that the slopes of the UV spectra (1000-2000 Å) are identical for the six bright elliptical galaxies, suggesting

that the UV sources lie in a narrow temperature range varying from 20000-23000 K. With the detection of EHB and BHk stars in the GGCs using HST (Piotto et al. 1999), it was noticed that their properties are very similar to the UV sources found in elliptical galaxies and it was suggested that they might be responsible for the UV upturn. It is therefore important to locate, characterise and infer the evolutionary pathways for the formation of these stars.

1.7 Motivation and Aim

Using NUV observations with HST, Ferraro et al. (2003) studied the BSS distribution of six clusters that revealed peculiar cases not known before such as the BSS population was found to be very different in twin clusters, M3 and M13 with M13 having the lowest specific frequency in a GC. Similarly, the largest specific frequency was found in the clusters NGC288 and M80 which are at extremes in their central densities.

Schiavon et al. (2012) did a seminal study of 44 GGCs using GALEX data and generated their FUV vs FUV−NUV CMDs which covered the full cluster region. They showed that HBs form a diagonal sequence stretching more than 4 mag in color in UV CMDs thus lifting the degeneracy in B−V color in optical CMDs. The BSSs lie in a region 1 mag fainter than HB forming a narrow vertical sequence which stretches more than 3 mag in UV color. They also noticed that the AGBM and PAGB stars populate a region brighter than the HB stars and thus are easy to identify in UV CMDs as compared to the optical CMDs. However, due to the poor resolution (4.5-5.5″), GALEX was unable to resolve the core of the cluster in both FUV and NUV. Their study also lack the comparison of the UV CMDs with the stellar evolutionary models.

On the other hand, HST UV legacy survey of GCs (Piotto et al. 2015) made it possible to detect the MSPs in GCs due to the high resolution of HST ($0.05''$), but this survey was limited to only the core regions of the clusters owing to its small field of view (FOV $\sim 3.4'$ square). In addition, this survey was restricted to only NUV wavelengths because the FUV filters of the HST suffer from red leaks which leads to overestimation of the FUV fluxes of MS and RGB stars, making them appear brighter in UV.

Brown et al. (2016) studied the HB morphology of 53 GCs using three HST filters (F275W, F336W, F475) and showed that the UV CMDs are best suited to study the HB morphology in GCs and identify any discontinuity associated with it. But, their analysis was limited to only central regions of GCs in NUV. Thus, our main motivation is to study the hot stellar populations of GCs in both FUV and NUV wavelengths and extend it to larger radial distances from the cluster center.

The aim of this thesis is as follows:

- to present the FUV and NUV CMDs of the GCs covering the full cluster region and explain them with the stellar evolutionary models.
- to classify and study the behaviour of UV bright stars in GCs as we switch from optical to UV CMDs.
- to study the HB morphology and their spatial distribution in GCs and characterize the MSPs present in them.
- to identify and derive the parameters of EHB stars in order to understand their UV properties.
- to study the radial distribution of BSSs with respect to HB stars in a variety of GCs and understand the dynamical status.

- to identify the BSS candidates showing UV excess and derive their physical parameters to decipher their formation pathways.

In order to achieve the above aims, we have used Ultra-Violet Imaging Telescope (UVIT) onboard Astrosat, India's first multi-wavelength space observatory and combined it with several archival data that are described in Chapter 2. The advantage of UVIT is that it has a large FOV (28′ in diameter), good spatial resolution (<1.5″) and multiple filters within FUV (130-180 nm) and NUV (200-300 nm) wavelengths. The large FOV of UVIT will help us in detecting the UV stellar populations over full cluster region (beyond half-light radius of the GCs) with good resolution. Combining the UV data with the optical data available from various archives (HST, Gaia) will help us in identifying the cluster members and classifying them in UV. The multiple filters within FUV and NUV filters of UVIT will help us in sampling the UV wavelength region more precisely and detect the BSSs and other UV bight candidates showing UV excess.

1.8 Overview of the Thesis

- **Chapter 1:** We introduce the GCs, the UV stellar populations, their properties and characteristics relevant to the thesis. We present the motivation and aim of the thesis. The UV stellar populations that we refer in our study are mainly the HB, BSSs and other objects which are bright in UV.

- **Chapter 2:** The observations and multi-wavelength data used in this study are presented.

- **Chapter 3:** We have described the methods and tools used to study and estimate the parameters of the UV stellar populations in the GCs.

- **Chapter 4:** We study the MSPs in GC NGC 1851 with a special focus on the HB stars using UV observations and present the important results of its comparison with the stellar models.

- **Chapter 5:** We present the results obtained by the UVIT-HST-Gaia study of HB morphology and EHB stars of GC NGC 288.

- **Chapter 6:** We present the results obtained by the UV study of radial distribution of BSSs of NGC 288 and derive their parameters using UV photometry.

- **Chapter 7:** We present the UV results obtained for the BSSs of low-density cluster NGC 5466 with a detailed spectroscopic and photometric study of one BSS located in the cluster outskirts.

- **Chapter 8:** We summarize the results of this study and present our conclusions along with future prospects.

Chapter 2

Observations and Data

For addressing the science goals as mentioned in Chapter 1, we used the data from different telescopes covering a wavelength range from FUV to near infrared (NIR). Since BSSs and HB stars are bright in UV as explained in chapter 1, our main objective is to obtain the UV observations of the GCs. As UV light is blocked by the earth's atmosphere, it cannot be collected through ground facilities. Thus, we have to rely on space telescopes to acquire the data. The space telescopes used for obtaining the UV data for our study are UVIT, GALEX and HST.

We combined the UV observations with all the previously available data which are obtained in visible bands. The motivation behind this was to i) construct the UV-optical CMDs ii) to identify and compare the features of a GC UV CMD as we switch from optical to UV. For achieving this, we used several archival data available from ground telescopes such as Canada-France-Hawaii Telescope (CFHT), Kitt Peak National Observatory (KPNO), Sloan Digital Sky Survey (SDSS) and Panoramic Survey telescope and Rapid Response System (Pan-STARRS).

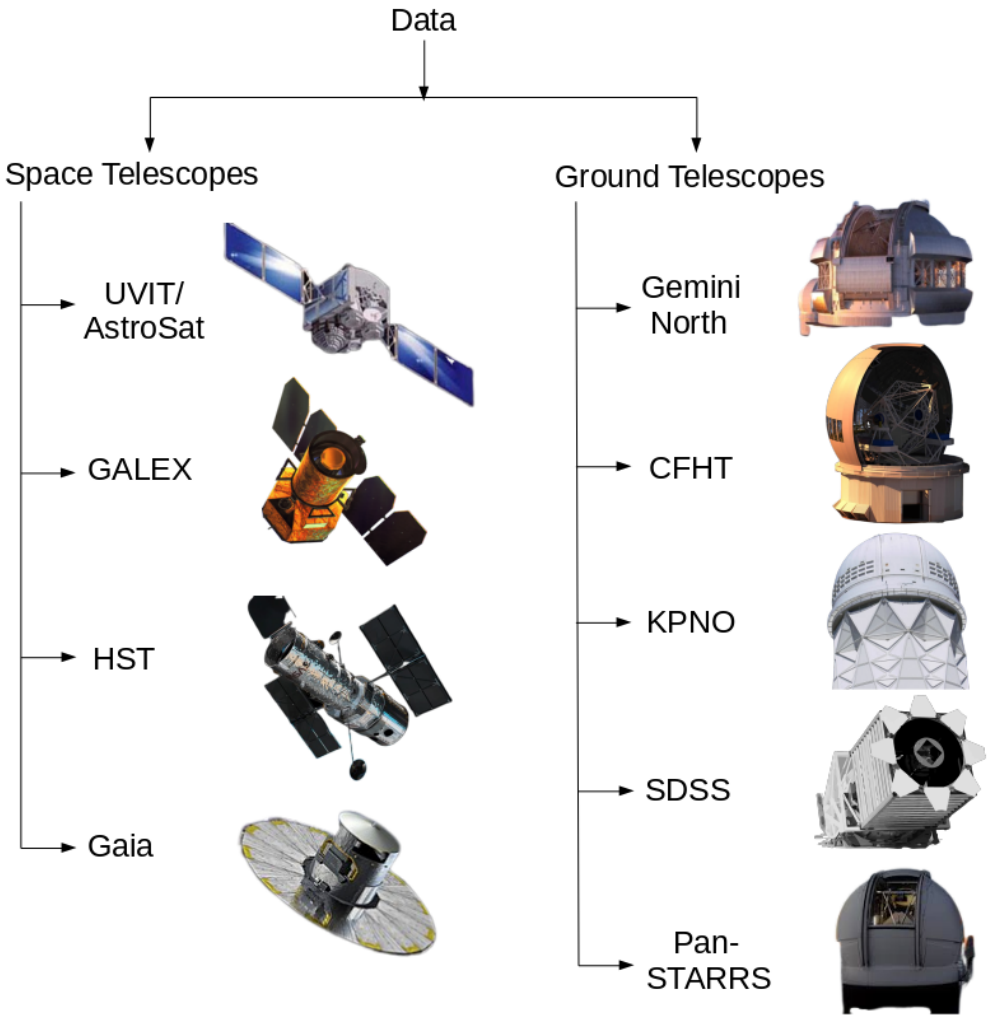

FIGURE 2.1: Data from different telescopes that are used in our study.

The data used from different telescopes for our study are shown in Figure 2.1 which are described briefly in the following sub-sections:

2.1 Space Telescopes

2.1.1 UVIT

UVIT is an imaging instrument designed to observe in UV and visible bands. It is one of the payloads of AstroSat, India's first multi-wavelength space observatory. AstroSat was launched on September 28, 2015 in a 600 km low Earth orbit by Indian Space research Organization (ISRO) carrying four X-ray instruments namely, three Large Area X-ray Proportional Counters (LAXPCs), Soft X-ray focussing Telescope (SXT), Cadmium Zinc Telluride Imager (CZTI) and Scanning Sky Monitor (SSM), in addition to UVIT as shown in Figure 2.2. SSM continuously scans the sky for X-ray transients. All telescopes are co-aligned to simultaneously observe the celestial sources, covering a large wavelength range from hard X-rays to visible.

UVIT consists of two 38 cm aperture Ritchey-Chrétien telescopes (Left panel of Figure 2.3). One telescope observes in FUV (130-180 nm) and another in NUV (200-300 nm) and visible wavelengths (320-550 nm) simultaneously. With a circular FOV of $\sim 28'$ in diameter it creates images with a Full Width Half Maximum (FWHM) $\sim 1.5''$. Multiple filters are available within FUV, NUV and visible bands. UV detectors work in photon counting (PC) mode whereas the visible in integration mode. The visible channel is primarily used for correcting the satellite drift during an observation. The effective area curves of UVIT in the FUV and NUV filters as a function of wavelength are shown in Figure 2.4 (Subramaniam et al. 2016; Tandon et al. 2017b). A detailed description of the UVIT is available in Kumar et al. (2012).

The detector system shown in Figure 2.3 (Right panel) consists of a CMOS image sensor of aperture 39mm, fiber optic coupling and an image intensifier tube, which

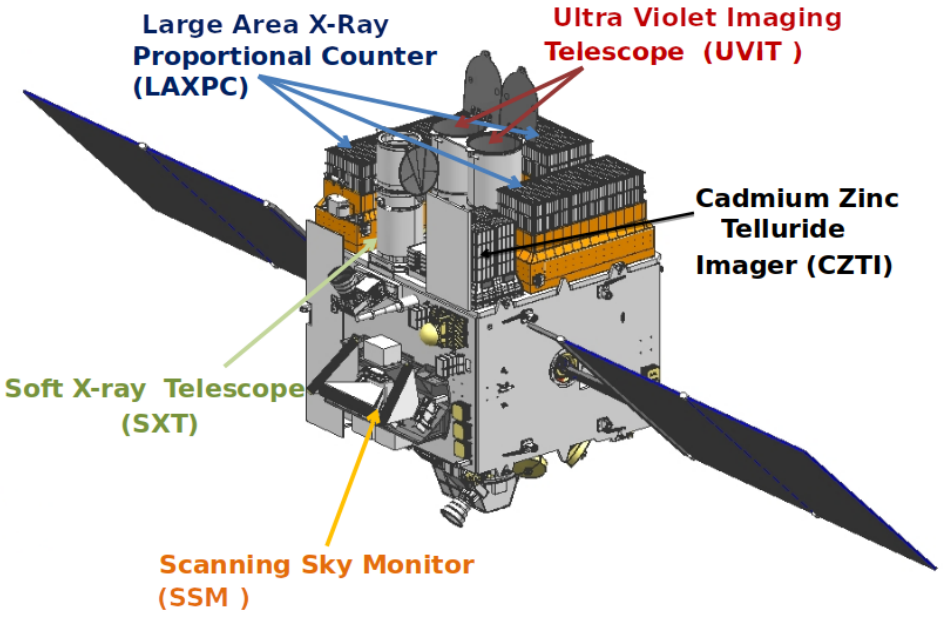

FIGURE 2.2: Configuration of AstroSat with each instrument identified and marked in the Figure. Image Credits: ISRO

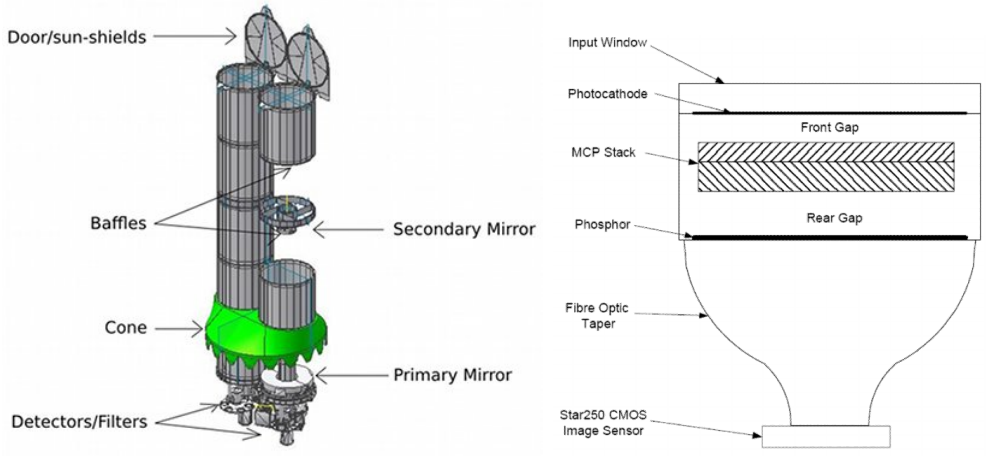

FIGURE 2.3: Configuration of UVIT (Tandon et al. 2017a) and its detector system (Hutchings et al. 2007) in the left and right panels respectively.

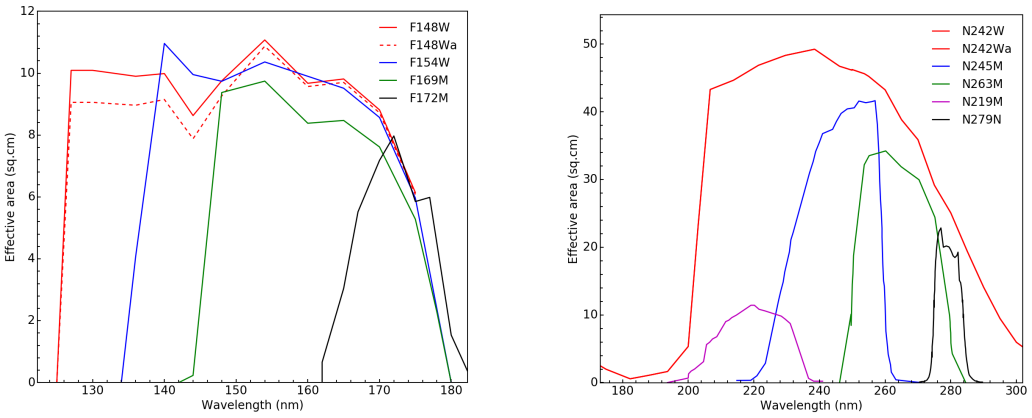

FIGURE 2.4: The effective area curves of all the FUV and NUV filters of UVIT (Tandon et al. 2017b)

is identical for all the channels of UVIT. When an incident photon hits the photo-cathode in the image intensifier tube, it ejects a primary electron which is then accelerated towards the Micro-Channel Plate (MCP) creating an electron shower. This shower illuminates the phosphor anode which is then fed to the CMOS image sensor through fiber-optic taper. The photon pulse which covers several pixels of the CMOS is then used to estimate the centroid of the incident photon, using a centroiding algorithm described in detail by Hutchings et al. (2007) and Postma et al. (2011). The CMOS (512 X 512 pixel array) is read out at a maximum frame-rate of 29 frames/sec for the full field. The frames are recorded at the above frame rate, stacked in the ground using shift and add algorithm. While a CMOS pixel (25 micron in size) spans $\sim$ 3.34" in the sky, centroiding the photon helps in reaching the sub-pixel (1/8 pixel) resolution. Typically, The point sources are resolved to a Point-Spread Function (PSF) of $\sim 1.5''$ FWHM, and less than that at times. Full details of the detector and their properties can be found in Postma et al. (2011).

The first light in-orbit image of the UVIT was obtained on 30 November 2015, when it opened its shutters in the direction of the open cluster NGC 188. In orbit calibrations of the instrument were done by observing primary photometric standard star, HZ4 (a bright WD with flux calibrated spectrum in the UV) to

TABLE 2.1: Properties of individual filters for two channels, where λ_{mean} is the Mean Wavelength and $\Delta\lambda$ is the Band Width, ZP is the zero point magnitude and erros UC is the unit conversion. The ZP_Err and UC_Err are the errors associated with ZP and UC respectively (Tandon et al. 2017b).

Filter Name	λ_{mean} (Å)	$\Delta\lambda$ (Å)	ZP	ZP_Err	UC	UC_Err
FUV:						
F148W	1481	500	18.016	0.01	3.09E-15	2.9E-17
F148Wa	1485	500	17.994	0.01	3.28E-15	2.5E-17
F154W	1541	380	17.778	0.01	3.55E-15	4.0E-17
F172M	1717	125	16.342	0.02	1.07E-14	1.6E-16
F169M	1608	290	17.455	0.01	4.39E-15	3.7E-17
NUV:						
N242W	2418	785	19.81	0.002	2.22E-16	6.5E-19
N245M	2447	280	18.5	0.07	7.25E-16	3.6E-18
N263M	2632	275	18.18	0.01	8.44E-16	9.6E-18
N219M	2196	270	16.59	0.02	5.25E-15	8.2E-17
N279N	2792	90	16.5	0.01	3.50E-15	3.5E-17

estimate the zero point (ZP) magnitudes, unit conversion etc. Table 2.1 gives the parameters of the individual filters obtained from the calibrations (Tandon et al. 2017b).

Image generation

The UVIT data comes in the Level 1 (L1) format that are a set of fits tables packed with the centroid data along with other spacecraft and observational metadata. This data can be processed using CCDLAB software provided by Postma & Leahy (2017). The steps to be performed in CCDLAB for generating the final science images from the raw L1 data are following:

a) Digestion of L1 data: to digest the L1 data files and extract the centroid list

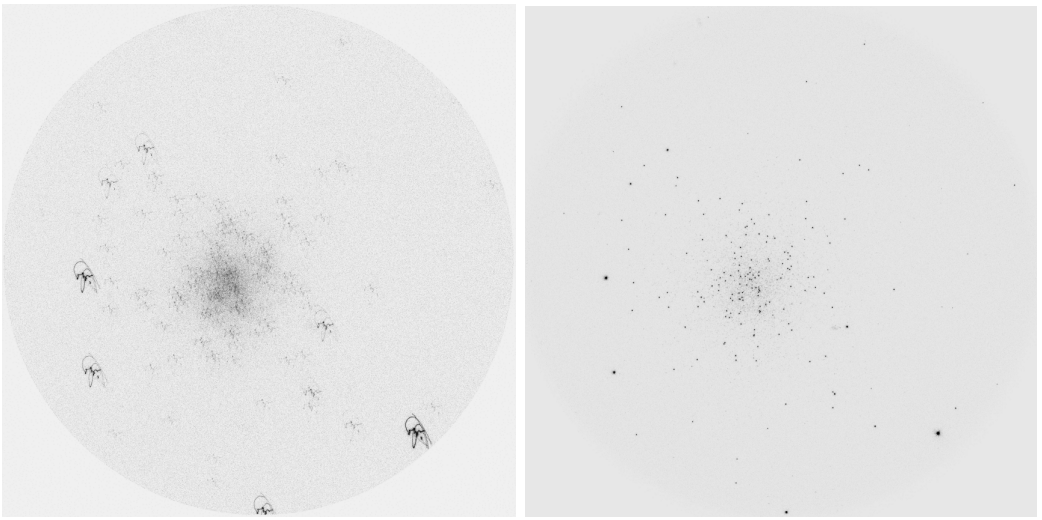

FIGURE 2.5: UVIT image of the cluster NGC 288 in N279N filter before (Left) and after drift (Right) correction.

and headers containing the useful information such as target name, detector and filter used, etc.

b) Distortion Correction: to correct for the geometric distortion of the field which is due to the fiber-optic taper. This is required for astrometric accuracy.

c) Centroiding Bias Correction: to correct for the bias in the coordinates due to the centroiding algorithm.

d) Flat Field Correction: to correct the sensitivity variations from pixel to pixel, for the UV detectors in PC mode.

e) Drift Correction: to correct for the satellite drift. An image of the cluster before and after drift correction is shown in left and right panels of Figure 2.5.

f) Alignment: to co-align the centroid lists and add them to create the final images.

g) Exposure Array Correction: to correct the imaging field with unequal exposures (mainly in the periphery) due to the drift of the satellite.

TABLE 2.2: UVIT observation details of the studied GCs

Cluster Name	Date of observation	Proposal ID	Filters	Exposure Time (sec)
NGC 1851	19-21 March 2016	T01_071	F148W, F169M, N279N	6982, 5274, 12234
NGC 288	21-22 August 2016	G05_009	F148W, F169M, N279N	7057, 4573, 14778
NGC 5466	3-4 June 2016	G05_009	F148W, F169M, N245M, N263M	2609, 6036, 6091, 4258

Observations

The observations of the three GCs - NGC 1851, NGC 288 and NGC 5466 were carried out during March-August 2016 in different filters of UVIT. NGC 1851 was observed during the performance verification phase of UVIT whereas the other two clusters were observed as a part of guaranteed time (P.I. Annapurni Subramaniam). Table 2.2 gives the observation log of the GCs with the details of the filters used and exposure time in each filter. The 1/8 pixel resolution images of the GCs with dimensions 4096 X 4096 were generated using CCDLAB.

2.1.2 GALEX

GALEX is a UV space telescope launched on April 28, 2003 by National Aeronautics and Space Administration (NASA). It consists of a Ritchey-Chrétien Telescope with a primary mirror of diameter 50 cm which images the sky in two different bands; FUV ($\lambda_{eff} \sim 1528\mathring{A}$) and NUV ($\lambda_{eff} \sim 2310\mathring{A}$). It has a circular FOV which is $\sim 1.2^{\circ}$ in diameter and its spatial resolution is 4.5-5.5″ (Morrissey et al. 2007). The detection limit in NUV magnitude is 25 mag. The primary goal of the mission was to investigate and study the star formation in galaxies.

The GALEX conducted several sky surveys in imaging mode, among which the principal studies are Deep (DIS), Medium (MIS) and All Sky Imaging Surveys (AIS). The GALEX database contains the images of $\sim$ 500 million sources taken

TABLE 2.3: GALEX observation details of the studied GCs

Cluster Name	Tile name	Filters	Exposure Time (sec)
NGC 1851	GI1_056007_NGC1851	FUV, NUV	2777, 4473
NGC 288	MIS2DFSGP_30531_0144	FUV, NUV	1594, 1594
NGC 5466	GI1_056017_NGC5466	FUV, NUV	1838, 3529

in FUV and NUV bands. The data are publicly available through the Mikulski Archive for Space Telescopes (MAST).

We used the GALEX data of the clusters NGC 1851, NGC 288 and NGC 5466 for our study. We chose those survey data which had the deepest exposure of the clusters. For clusters NGC 1851 and NGC 5466, we used the data that are obtained under the Guest Investigator (GI) program and made available in the name GII survey in MAST website. In case of NGC 288, we used the data from MIS survey. We downloaded the FUV and NUV intensity maps of the clusters for analysis. The observation details of the clusters are given in Table 2.3.

2.1.3 HST

HST is a 2.4 meter optical space telescope launched on April 24, 1990 by NASA. The four HST instruments which are widely used by science community are Wide Field and Planetary Camera 2 (WFPC2), Near Infrared Camera and Multi-Object Spectrometer (NICMOS), Fine Guidance Sensor 1R, and ACS. The ACS camera is a third-generation instrument onbaord HST which consists of three independent channels: Wide Field Channel (WFC), High Resolution Channel (HRC) and Solar blind Channel (SBC). WFC is the most used channel with a plate scale of around $0.05''$/ pixel and a FOV $\sim 202''$ X $202\ ''$. It has several filters covering a spectral range of 350-1100 nm. The detection limit in V magnitude for ACS/WFC channel is 28 mag.

TABLE 2.4: Comparison of UVIT with GALEX and HST/ACS-WFC which are used for the photometric study of the clusters

Parameters	UVIT	GALEX	HST/ACS-WFC
Passbands	FUV, NUV, VIS	FUV, NUV	VIS
Filters within passbands	Yes	No	Yes
Field of View	$28'$	1.2°	$3.4'$
Spatial resolution (FWHM)	1.2 - $1.5''$	$5''$	$0.05''$

Sarajedini et al. (2007) conducted an imaging survey of 66 GCs within 20 Kpc from the Sun, using ACS/WFC on HST (HST program-10775). The observations were obtained in F606W and F814W filters of ACS/WFC. This treasury program mainly targeted the cores of the GCs reaching the lower main sequence stars of mass $\sim 0.2\ M_{\odot}$. Their primary aim was to derive the basic parameters of GCs such as ages, distances, mass function etc.

We used the catalog (https://archive.stsci.edu/prepds/acsggct/) provided under the ACS GC treasury program to cross-match with the UVIT and generate the CMDs of the GCs. The catalog contains the star positions (RA and Dec), photometric magnitudes (Vega mag system) and errors corresponding to F606W and F814W filter observations. We used Vg and Ig magnitudes in the catalog which are calibrated to the ground based VI system.

Table 2.4 gives the comparison between the UVIT with GALEX and HST, which are mainly used for this thesis study.

2.1.4 Gaia

Gaia is the space-astrometry mission launched on 19 December, 2013 by European Space Agency (ESA). Its main objective was to obtain a three-dimensional structural map of our Galaxy by measuring the positions and radial velocities of

nearly 1% of the galaxy's total stellar population. It consists of two common telescopes that are separated by an angle 106.5°, sharing a common focal plane. The focal plane houses 106 CCDs which are of three different types: the broad band CCD, blue CCD and red CCD which are mainly used in astrometric field, blue photometer (BP) and red photometer (RP) respectively. The three main function of the detectors are astrometry, photometry and spectrometry. For more details can be found in Gaia Collaboration et al. (2016).

Gaia contains three passbands: G(330-1050 nm), G_{BP} (330-680 nm) and G_{RP} (640-1050 nm). The angular resolution of Gaia is $\sim 0.4''$. We used the Gaia Data Release 2 (DR2) for our study which was released on 25 April, 2018. The data can be accessed through Gaia Archive. Gaia DR2 contains the positions (RA and Dec), parallaxes and proper motions (PMs) of 1.3 billion sources. The limiting magnitude is G=21 mag. The uncertainties in parallaxes and PM components are around 0.7 mas and 1.2 mas yr^{-1} for G = 20 mag. More details about Gaia DR2 can be found in van Leeuwen et al. (2018).

Gaia Collaboration et al. (2018b) determined the PMs of 75 GGCs using Gaia DR2 data. They provided a catalog containing the PM members for each of the 75 GGCs. The procedure used for selecting the cluster members is described in detail in the Appendix A1 of their paper. We used the catalog of the two GCs (NGC 288 and NGC 5466) to select the PM members for our analysis.

2.2 Ground Telescopes

2.2.1 Gemini-North Telescope

The Gemini North Telescope is one of the twin 8.1 meter diameter optical/IR telescopes of Gemini observatory, located in Mauna Kea, Hawaii. It has an adaptive optics system that corrects for the distortion caused by the Earth's atmosphere.

Gemini Multi-Object Spectrograph North (GMOS-N) is an optical/NIR spectrograph mounted on Gemini North Telescope. It can obtain spectra of 100 objects simultaneously. It provides both spectroscopy and imaging over a $5.5'$ square FOV. It consists of two long slits covering a spectral range 360-940 nm. The spectral resolution (R) is 1260-8800 and 210-1460 for $0.25''$ and $1.5''$ long slits respectively. We used GMOS-N for obtaining the spectra of BSSs in the cluster NGC 5466 which is described in Chapter 7.

2.2.2 CFHT

CFHT is a 3.6 meter optical/IR telescope located at Mauna Kea, Hawaii. The telescope contains two imaging instruments- MegaCam and WIRCam. MegaCam is a wide field optical imaging camera that consists of 36 CCDs (2048 X 4612 array), covering a 1° square FOV. Its spatial resolution is $\sim 0.187''$ per pixel. It contains five filters (u,g,r,i,z) covering a wavelength range 380-1000 nm.

The photometric catalog of the clusters obtained from CFHT and other telescopes are provided by P.B.Stetson. The catalog contains the positions and U,B,V,R,I magnitudes of the sources in the cluster. NGC288 catalog is based on 1,081 images (in UBVRI), while that for NGC5466 is based on 389 V and I images.

2.2.3 SDSS

SDSS is the largest sky survey done to map one quarter of the whole sky in detail using a 2.5 meter Sloan foundation telescope located at Apache Point Observatory, in New Mexico. Its main aim is to provide positions and absolute brightness of more than a million objects and determine the distances of fainter galaxies and quasars. The imaging camera of the telescope consists of an imaging array of 30 CCDs (2048 $\times$ 2048 size) that obtains images in five broadband color filters (u,g,r,i,z) covering a wavelength range 3000-10,000 $\mathring{A}$, over a FOV of 2.5 square degrees. In addition to the imaging camera, it also contains a fiber-fed multiple-object spectrograph with a spectral resolution R$\sim$ 1500-2500. More details of the telescope and instruments can be found in York et al. (2000).

We used the imaging catalog available from SDSS DR9 (Ahn et al. 2012) for our study which contains the data of more than 1.2 billion objects spread over an area 31,637 deg^2. The catalog provides the positions, the magnitudes (AB system) and errors in the five filters along with the type/class of object (3:star, 6:galaxy).

2.2.4 Pan-STARRS

Panoramic Survey Telescope and Rapid Response System (Pan-STARRS) located at Haleakala Observatory in Hawaii, is a system designed for wide-field astronomical imaging. It consists of two 1.8 meter Ritchey-Crétien telescopes.

We used data release 1 (Flewelling et al. 2016) available from the Pan-STARRS1 (PS1) Surveys (Chambers & Pan-STARRS Team 2018). The survey imaged the sky in five broadband filters (g,r,i,z,y) using a 1.8 meter telescope with a FOV$\sim 3^\circ$ in diameter. The filters cover a wavelength range 400 -1000 nm. Details about the

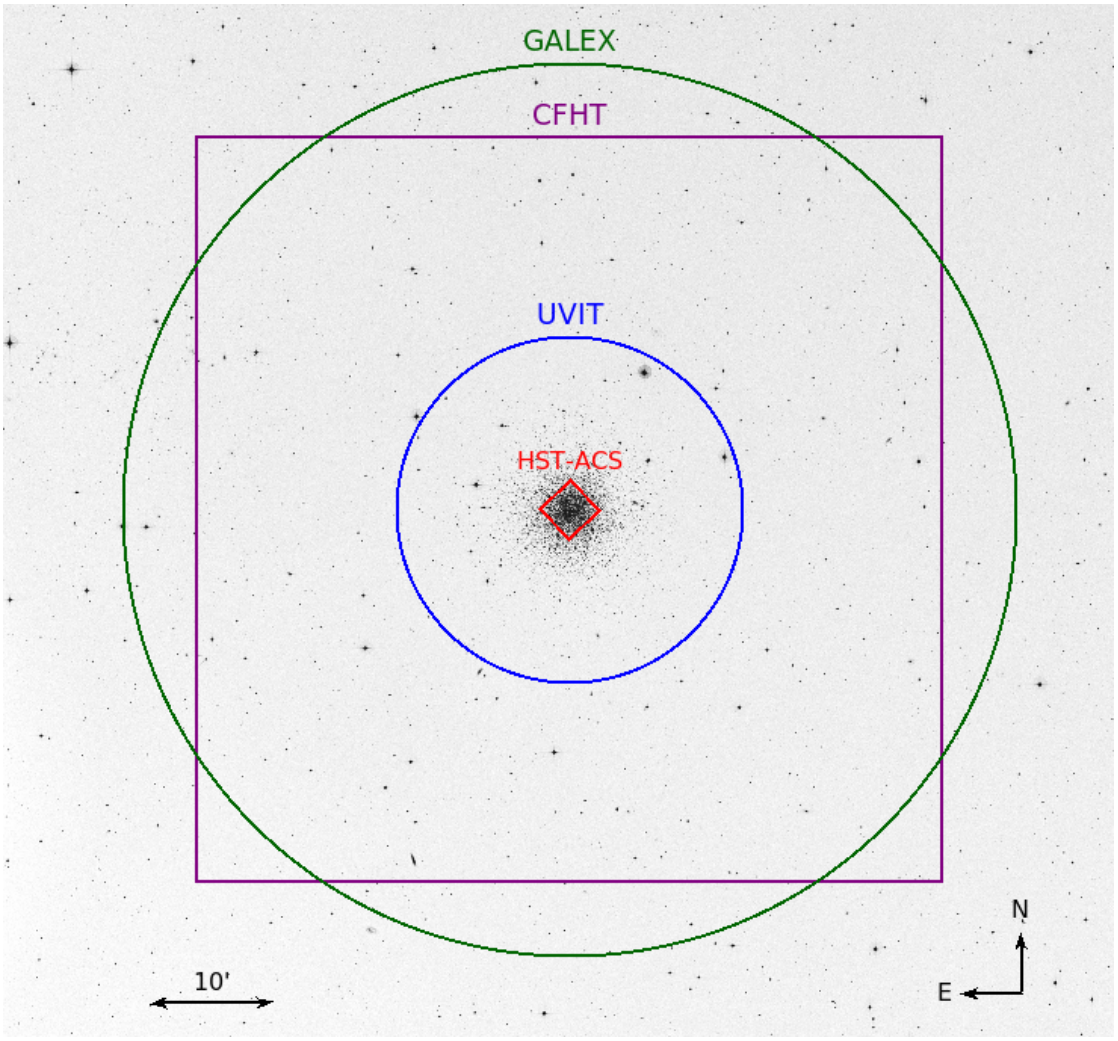

FIGURE 2.6: FOV of the telescopes (HST/ACS, GALEX, UVIT and CFHT) that are used for the photometry study of the clusters overplotted on DSS image of NGC 288.

filter properties and photometric system can be found in Tonry et al. (2012). The PS1 DR1 catalog contains the positions and magnitudes (AB system) of around 2 billion sources is used for the analysis in Chapter 7.

In Figure 2.6, we show a comparison of the FOV covered by different telescopes (UVIT, GALEX, HST, CFHT) which are mainly used for our analysis. The figure shows that the UVIT coverage is just enough to sample the stellar populations of the entire cluster.

2.3 Summary

The data and observations used in this study are summarised below:

- We discuss the main properties of different space and ground based telescopes which are used in the study of three clusters NGC 1851, NGC 288 and NGC 5466.
- We present and discuss the UV observation details of the three clusters acquired from UVIT telescopes.
- We describe the details of GALEX, HST and GAIA telescopes.
- We describe the details of the Gemini spectrograph used for spectroscopic observations.
- We also briefly discuss a few ground based telescopes such as Pan-STARRS, SDSS etc.

Chapter 3

Methods and Tools

After obtaining the observations of the clusters from telescopes, we adopted different methods to analyze the data. The different methods used in this thesis are:

- Photometry: measurement of flux to obtain magnitudes of sources
- Isochrones: Generating model isochrones in the required pass bands to study the CMDs of the clusters and their properties.
- Spectral Energy Distributions (SEDs): to fit multi-wavelength photometric data with synthetic flux from models to derive the physical parameters of BSSs, HB and other UV bright objects.
- Kolmogorov-Smirnov test: to compare cumulative radial distribution functions of two populations.

The methods and tools used to perform them are described in detail in the following sections:

3.1 Photometry

Photometry is the technique of measuring the brightness of an astronomical object. Generally, the brightness of a star is expressed by magnitude which is defined as:

$$m = -2.5log\frac{f}{f_0} \tag{3.1}$$

where f_0 is the zero point of the magnitude scale, which is chosen such that the magnitude of star Vega is zero.

We used DAOPHOT package (Stetson 1987) available in Image Reduction and Analysis Facility (IRAF) software produced by National Optical Astronomy Observatory to perform the photometry on the science images.

3.1.1 Aperture photometry

Aperture photometry works by adding the number of counts enclosed in a circular aperture of radius r around a star and then, subtracting off the sky background, estimated from a surrounding annulii.

Suppose, F_0 is the total flux enclosed in a circular aperture as shown in Figure 3.1 including the sky background in that aperture. Then, the real flux of the object F is given by

$$F = F_0 - N_{pix} \times S \tag{3.2}$$

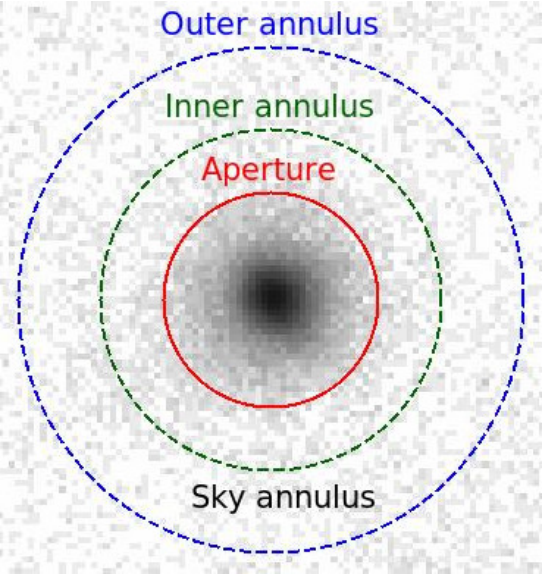

FIGURE 3.1: Basic principle of aperture photometry. A circular aperture surrounding the point source and the sky annulus used for calculating the local sky background is shown here.

where N_{pix} is the number of pixels in that aperture and S is sky per pixel chosen in a source free region by considering a sky annulus outside the aperture radius (Figure 3.1). Thus, aperture photometry is the absolute measurement of flux emitted by object which can be directly converted to a true magnitude (standard system) using equation 3.1.

The first step to perform aperture photometry is to identify the objects in the image. The object detection is done by defining a detection threshold in *daofind* task in *digiphot*. For running *daofind* task, we need to provide certain parameters of the image such as Full Width at Half Maximum (FWHM) of a stellar source and standard deviation (σ) of the sky. Once the objects are detected and the centroids are known, we need to run *phot* task to obtain the magnitudes of all the objects in the image. In phot, the *photpars* task requires a list of aperture radii surrounding the star and photometric ZP magnitude which is used to transform the instrumental magnitudes to a standard system. The aperture should be chosen in such a way that it includes most of the star light but excludes the background

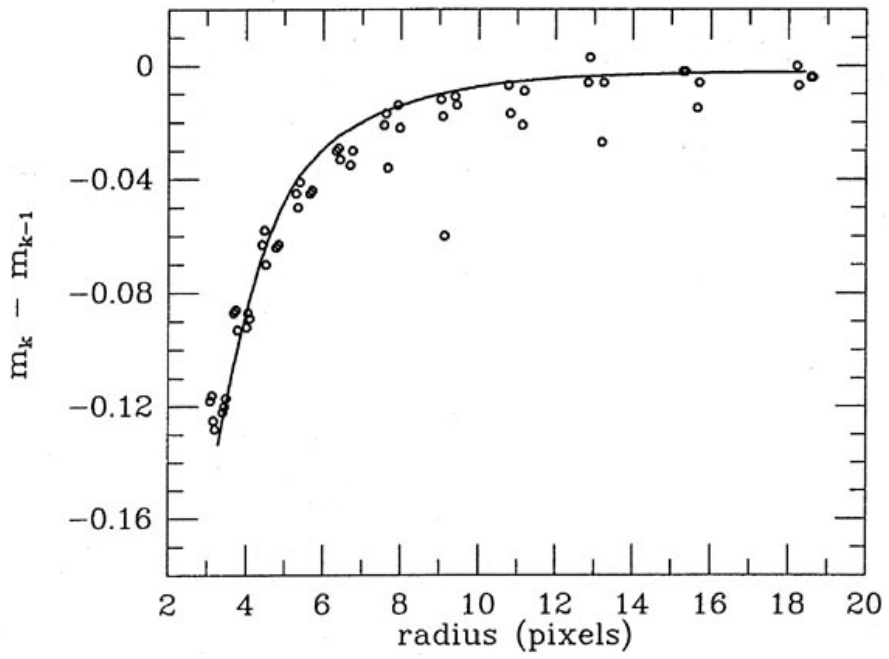

FIGURE 3.2: Curve of growth. The observed magnitude differences with respect to the radius in pixels (Stetson 1990).

light. Then, *fitskypars* is used to determine the local sky brightness by defining an annular region around each star. The observed magnitudes or their differences obtained at different radii is used to plot the curve of growth (cog) (Stetson 1990) which is shown in Figure 3.2. In the cog, we notice that the magnitudes get brighter at increasing radius and levels off at larger r, asymptotically approaching the total brightness of the star at infinite radius. The cog is well defined for bright stars whereas, for faint stars, it is subjected to random fluctuations due to the sky noise. The presence of a neighbouring star near the target star can also affect the cog. The cog technique is used to determine the exact fiducial aperture where the star light is completely captured. The aperture correction, given by the difference between magnitudes estimated at the fiducial aperture and the usually adopted smaller aperture, is calculated by choosing isolated bright stars in the field and plotting their cog.

The aperture photometry works well for isolated point sources but it fails in

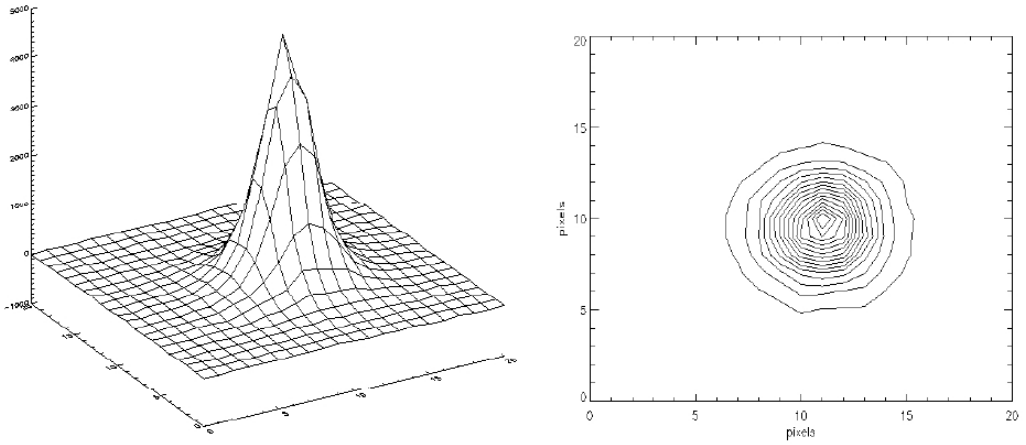

FIGURE 3.3: Surface plot of a bright star which resembles a 2D Gaussian profile along with its contour plot.

crowded regions where the sources are not well resolved. In case of crowded regions, the aperture photometry includes the flux contribution from nearby neighbouring stars, thus overestimating the flux of the target star. In such cases, PSF photometry is used.

3.1.2 PSF photometry

Stars are unresolved point-like sources owing to their large distances ($> 10^{15}$ km) when compared to their sizes ($\sim 10^6$ km). In addition, the seeing, diffraction pattern of optics and CCD sampling spread them to sizes of the order of $1''$. The shape of this distribution of light is determined by the "point spread function" (PSF). Stars on the image appear like a roundish disk of light with an axi-symmetric centrally peaked profile as shown in Figure 3.3. The core of the PSF resembles a 2D Gaussian with the counts falling off at increasing distance from the star's centre. The shape of PSF is characterised by its FWHM.

Typically, the PSFs are parametrised by Gaussian or Moffat functions given by:

$$Gaussian : I(r) = e^{\frac{-r^2}{2\sigma^2}}, F(r) = 1 - e^{\frac{-r^2}{2\sigma^2}}, FWHM = 2\sigma\sqrt{2ln2} \tag{3.3}$$

$$Moffat : I(r) = \left(1+\left(\frac{r}{\alpha}\right)^2\right)^{-\beta}, F(r) = 1-\left(1+\left(\frac{r}{\alpha}\right)^2\right)^{1-\beta}, FWHM = 2\sigma\sqrt{2^{\frac{1}{\beta}}-1} \tag{3.4}$$

where I(r) is the intensity profile and F(r) is the enclosed flux profile of the star which is fitted to determine the best parameters. Typically, three times of the FWHM encompasses over 90 % emission from a star.

The basic principle of PSF photometry is that all the stars have same intrinsic profile, with source to source variation in brightness or amplitude. Thus, PSF photometry works by building a model PSF and scaling the profile up or down in amplitude to fit the individual stars in the image. The model PSF is created by choosing isolated stars in the field using IRAF task *pstselect*. One example of a model PSF generated using task *psf* for a UVIT image is shown in Figure 3.4. Once the model PSF is generated, *allstar* task is run to fit the profiles of all the stars in the image. This task generates a star subtracted image (shown in Figure 3.5) where stars, which are successfully fitted with the PSF profile, are removed from the image. In the image, traces of residuals can be seen for some of the stars, which are not fitted properly by the model PSF. As the bright stars are removed, many faint sources also appear in the subtracted image. These faint sources can be identified again and the PSF fitting can be performed once again to retrieve the PSF photometry of fainter stars. Multiple iterations may be needed to complete the photometry of fainter sources present near the central regions of the GCs.

The advantage of PSF photometry is in the crowded fields where the PSF fitting considers only the pixels in the core of the star's profile ignoring the wings. Since the PSF photometry gives the relative magnitudes, we need to convert them to instrumental magnitudes and then to a standard system. As a first step, we have

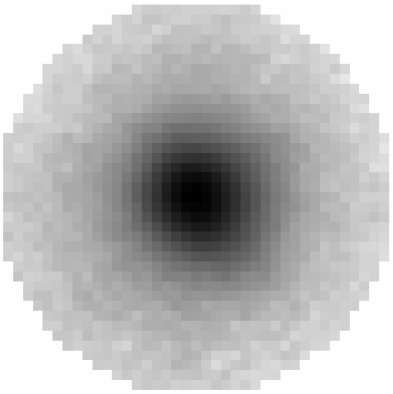

FIGURE 3.4: Model PSF generated for the NUV image of UVIT.

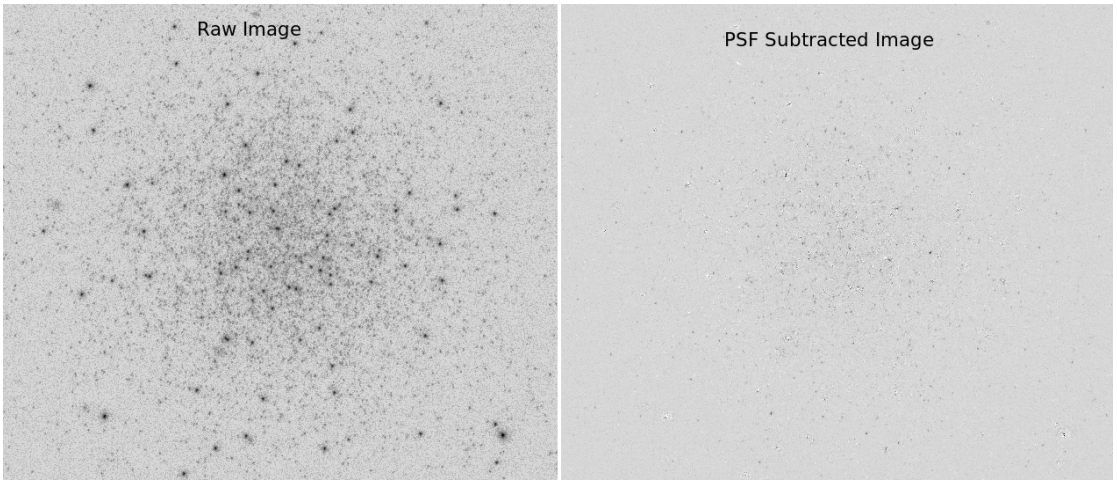

FIGURE 3.5: N245M UVIT image of NGC5466 before and after PSF subtraction.

to convert the PSF magnitudes to the aperture photometry scale. This is done by plotting the difference between the magnitudes obtained from *phot* and *allstar* with respect to the magnitudes obtained from phot, and calculating the mean value, preferably for bright stars. This value is added to the PSF magnitudes and then aperture correction is done to obtain the final magnitudes. For the UVIT science images, the instrumental magnitudes are converted to the standard magnitudes (AB system) using the formula given in equation 3.1 where the ZPs are taken from Table 2.1 of Chapter 2.

The magnitudes obtained in UVIT filters need to be corrected for saturation (Tandon et al. 2017b). The steps for saturation correction are as follows. The saturation is applied to Counts per frame (CPF), which is given by:

$$CPF = \frac{CPS}{28.7}, \tag{3.5}$$

where CPS is counts per sec.

$$CPF5 = 0.97 \times CPF \tag{3.6}$$

The saturation is found to be affected within inner 5 pixels, which in general corresponds to 97% of the total CPF. The correction for 97% of CPF as per Poisson statistics is:

$$CPF5 = 1 - exp(-ICPF5) \tag{3.7}$$

Ideal Correction for saturation is given by:

$$ICORR = ICPF5 - CPF5 \tag{3.8}$$

Real correction is obtained using the following relation:

$$RCORR = ICORR \times (0.89 - 0.30 \times (ICORR)^2) \tag{3.9}$$

The corrected CPF (CCPF) and corrected CPS (CCPS) are given by:

$$CCPF = CPF + RCORR \tag{3.10}$$

$$CCPS = CCPF \times 28.7 \tag{3.11}$$

The corrected CPS is then converted back to the magnitude by using the following equation:

$$m = -2.5log(CCPS) + ZP \tag{3.12}$$

After obtaining the saturation corrected final UVIT magnitudes, we used TOPCAT tool (Taylor 2011) to cross-match the positions (RA and DEC) of sources detected in different UVIT filters, to generate the CMDs of the clusters. The sky algorithm was used for cross-match sources with a maximum separation of $< 2''$ which is the typical FWHM of the PSF for UVIT filters.

3.2 Isochrones

An isochrone specifies the location of stars in the H-R diagram, having same age and metallicity but different masses. Thus, isochrones are theoretical representation of the CMDs of SSPs such as star clusters. The isochrones are used for determining the age and metallicity of a star cluster by comparing them with its observational CMD, by assuming a distance modulus and reddening. There are various isochrone models available among which the popular ones are Padova (Marigo & Girardi 2007; Marigo et al. 2008) and Bags of Stellar Tracks and Isochrones (BaSTI) (Pietrinferni et al. 2004) models. The model isochrones for a fixed metallicity and different ages are shown in Figure 3.6. The differences between the two models at younger ages (10^8 and 10^9 yrs) are due to the different treatments of convection in their models.

In this study, we generated isochrones using Flexible Stellar Population Synthesis (FSPS) models (Conroy et al. 2009; Conroy & Gunn 2010). FSPS computes SSPs for a variety of metallicities and IMFs by calling a set of FORTRAN routines contained in the package. The advantages of FSPS are i) it has the flexibility of choosing from a given set of isochrones, stellar spectral libraries, metallicities etc., ii) new filters can be added in the code and synthetic magnitudes can be generated for the filters, iii) it can compute SSPs for various stellar evolution phases that are optional, such as HB, BSS, PAGB and thermally pulsing-AGB. The code includes

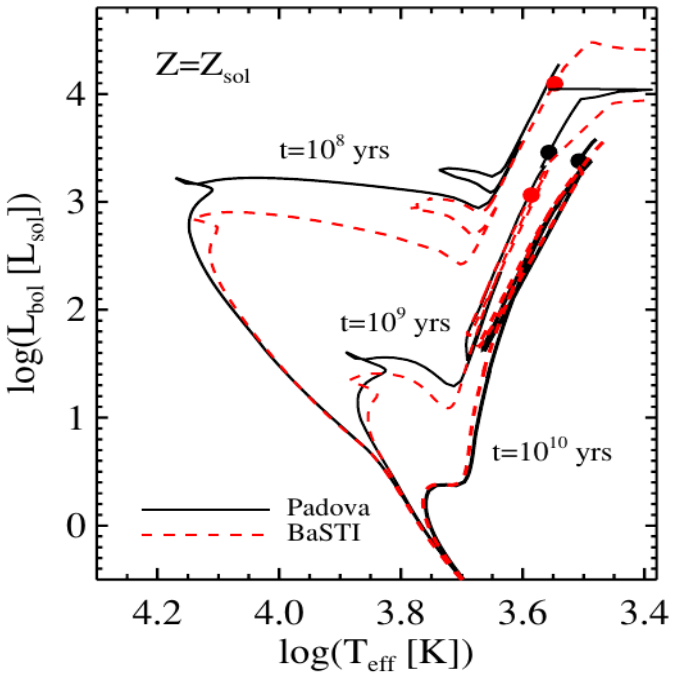

FIGURE 3.6: H-R diagram of different isochrones corresponding to Padova (black solid line) and BaSTI (red dash line) models with solar metallicity and three different ages (10^8, 10^9 and 10^{10} yrs) (Conroy & Gunn 2010).

the Padova, BaSTI and Geneva models. The range of metallicities existing in the Padova model isochrones are $-1.98 < [Fe/H] < +0.2$ whereas the range is $-1.8 < [Fe/H] < +0.32$ for BaSTI model isochrones. The ages range from $10^{6.6} < t < 10^{10.2}$ yrs and $10^{7.5} < t < 10^{10.2}$ yrs in Padova and BaSTI model isochrones respectively.

The HB model sequence is populated by specifying the parameter f_{BHB} which is defined as the fraction of HB stars that are blue. The BHB stars are added for older populations with age more than 5 Gyr which spread uniformly in temperature from the red end of the HB to 10^4 K. The f_{BHB} parameter varies from 0 to 0.5 in the FSPS models. The BSS sequence is populated using the parameter specific frequency, S_{BSS} which is defined as the number of BSSs (N_{BSS}) divided by the number of HB (N_{HB}) stars. The BSSs uniformly populate a region 0.5 magnitudes to 2.5 magnitudes above the MSTO, lying along the zero-age MS. Just like BHB stars,

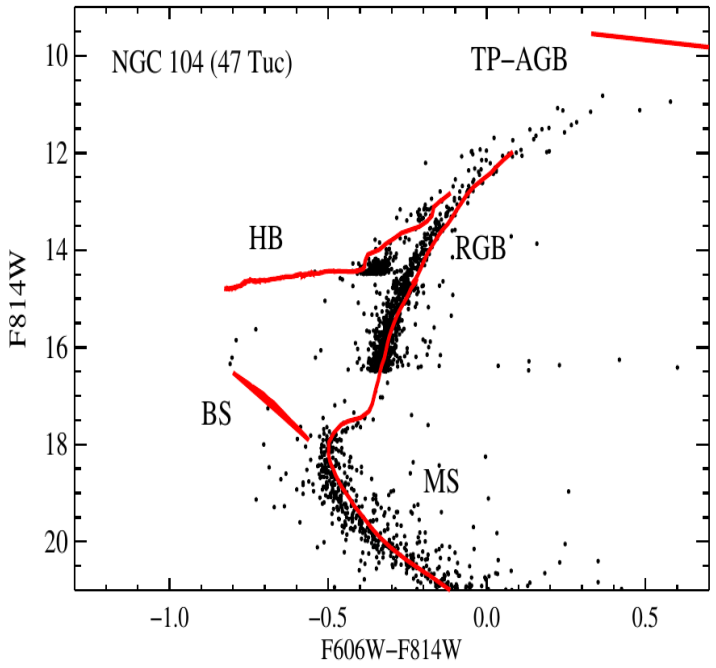

FIGURE 3.7: HST CMD of GC NGC 104 (Brown et al. 2005) along with the FSPS model where the model isochrone plotted in red, is of age 12.6 Gyr and [Fe/H]= −0.68. The BSS and HB model sequence are also plotted in the CMD (Conroy et al. 2009).

the BSS sequence is added for ages older than 5 Gyr. The parameter S_{BSS} varies from 0.1 to 1 in the models. The CMD of a GC (Brown et al. 2005) along with the FSPS model with different evolutionary phases labeled are shown in Figure 3.7. The FSPS can be downloaded from github (https://github.com/cconroy20/fsps). For more details about the FSPS code, refer to their manual (Conroy et al. 2009).

We convolved the models with the UVIT filter response curves by adding the UVIT filters in the FSPS code, for generating the isochrones in UVIT filters. These isochrones are used for studying the UV CMDs of the three clusters.

3.3 SEDs

Stars emit electromagnetic radiation over the full possible range of frequency or wavelength. The distribution of this radiation over frequency/wavelength is known as the Spectral Energy Distribution (SED). Analysing the SEDs of the stars helps us in estimating their fundamental parameters and thereby understanding their formation and evolution.

Since, a stellar flux is very similar to a black body emission, the amount of energy radiated by a star depends only on its temperature, for a given radius. According to the Wien's displacement law, the emission from a hotter star peaks at shorter wavelengths whereas that of a cooler star peaks at longer wavelengths. In astronomy, it is very challenging to obtain the spectra of an object in a broad range of wavelengths. Instead, it is relatively easy to obtain the observations at different filters covering certain wavelength range and perform photometry to obtain the fluxes. A plot of photometric fluxes as a function of effective wavelength corresponding to the observed filter is comparable to a low-resolution spectrum, and there is a powerful tool to study stellar properties.

We used python SEDfitter program (Robitaille et al. 2007) and Virtual Observatory SED Analyser (VOSA) (Bayo et al. 2008) tool to generate and fit the SEDs of stars with theoretical models. VOSA is developed by Spanish Virtual Observatory (SVO) to perform the following useful functions: i) build the SEDs of the objects by combining the data uploaded by user with the VO photometry services, ii) calculate the synthetic photometry for a selected theoretical model using filter transmission curves, iii) estimate the physical properties of the objects by comparing synthetic photometry with the observed data using different techniques such as χ^2 fit, Bayesian analysis etc. We used χ^2 fit technique for our study.

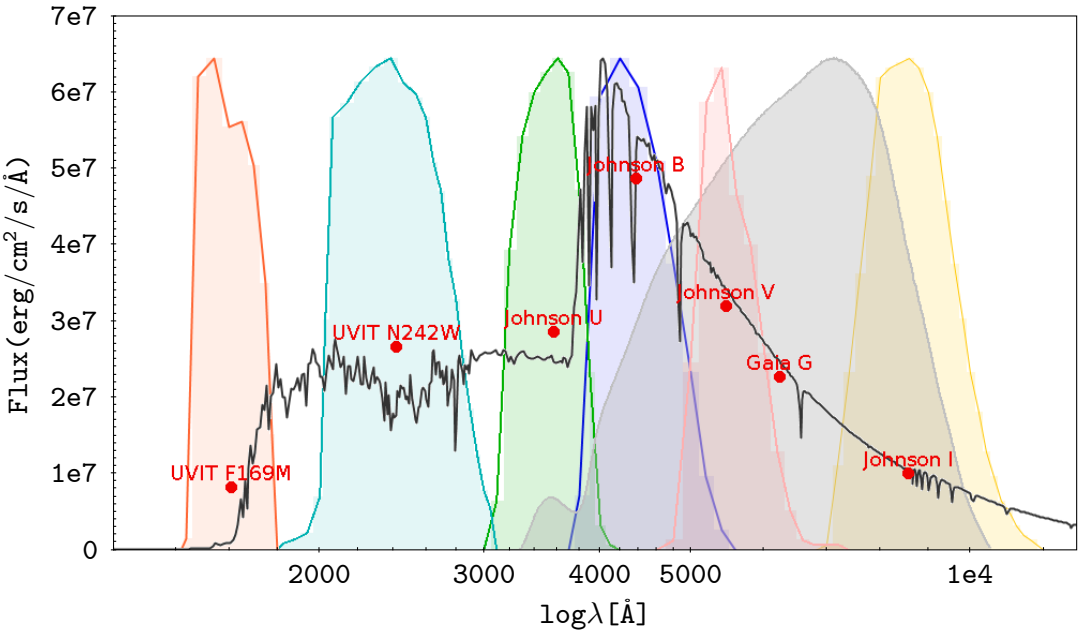

FIGURE 3.8: Kurucz model Spectra of a sample star of T_{eff} = 8000 K, [Fe/H]= −0.5 dex and log g 4 shown as black line. The response curves of various filters are also marked and plotted as a function of wavelength. The red dots are the synthetic flux in the respective filters for the plotted spectra.

The expression for reduced χ^2 (χ^2_{red}) is given by

$$\chi^2_{red} = \frac{1}{N - N_f} \sum_{i=1}^{N} \left\{ \frac{(F_{o,i} - M_d F_{m,i})^2}{\sigma^2_{o,i}} \right\} \tag{3.13}$$

where N is the number of photometric data points, N_f is the number of free parameters in the model, $F_{o,i}$ is the observed flux, $F_{m,i}$ is the model flux of the object, $M_d = \left(\frac{R}{D}\right)^2$ is the scaling factor corresponding to the object (where R is the radius and D is the distance to the object) and $\sigma_{o,i}$ is the error in the observed flux. Thus, if the distance to the object is known, we can derive the radius by scaling the model flux with the observed data where the best fit corresponds to the one with minimum χ^2_{red}. The luminosity of the object is given by

$$\frac{L}{L_\odot} = \left(\frac{R}{R_\odot}\right)^2 \left(\frac{T_{\rm eff}}{T_\odot}\right)^4 \tag{3.14}$$

where T_{eff} is the effective temperature obtained from the best fit model to the SED.

Figure 3.8 shows the spectra of a sample star along with the effective area curves of the filters as a function of wavelength. If we have the observed flux of a object in various filters, we can compare it with the synthetic flux computed from the models and derive the parameters from the best fit.

3.3.1 Theoretical Models

As our observed data cover the FUV-IR region, we used models which cover this wavelength range. We considered Kurucz stellar atmospheric models and Koester WD models for the SED fitting, and are described below:

Kurucz Models:
The Kurucz models (Castelli et al. 1997; Castelli & Kurucz 2003) are local thermodynamic equilibrium (LTE) and hydrostatic equilibrium models for the stellar atmospheres which incorporate appropriate stellar convection, rotation, opacities etc. The real flux distribution of stars are predicted directly by the flux distribution of the synthetic spectra from these models. The models consist of grids of ATLAS9 model atmospheres (Kurucz 1993). The grid covers a wide range of parameters with [Fe/H] ranging from -2.5-0.5 in steps of 0.5 dex, T_{eff} from 3500-50000 K (in steps of 250 K for $T_{eff} < 13000$ K and 1000 K for $T_{eff} > 13000$ K) and log g from 0-5 in steps of 0.5, covering the wavelength range from UV to IR.

Koester WD Models:
(Koester 2010) published models for WDs of spectral type DA with hydrogen rich atmospheres. These model atmospheres for the WDs are calculated by assuming homogeneous plane parallel layers, LTE, hydrostatic, radiative and convective

equilibrium. The model free parameters are T_{eff} and log g. The grid of the Koester models consist of T_{eff} ranging from 5000-80000 K (in steps of 250 K for T_{eff} from 5000-20000 K, 1000 K for 20000-30000 K, 2000 K for 30000-40000 K, and 5000 K for 40000-80000 K) and log g ranging from 6.5-9.5 in steps of 0.25.

3.4 Kolmogorov-Smirnov test

In astrophysics, there are many situations where an observational data needs to be compared with some theoretical and empirical models and vice versa, in order to verify between the theoretical and observational results. For example, in the case of a parametric test, the population under investigation is often assumed to be a normal distribution, $N(\mu, \sigma)$, where μ and σ are the mean and the standard deviation of the normal distribution respectively. Kolmogorov-Smirnov (K-S) test is a statistical test which gives a quantitative study for verifying that a sample data comes from a known population, and whether two populations follow the same distribution. This is an alternative method to the χ^2 goodness of fit test, which can also be applied for a small sample.

Let us assume that, $x_1, x_2, ..., x_n$ are the independent and identically distributed observations of the random variables $X_1, X_2, ..., X_n$ which follows the cumulative distribution function (CDF), $F_O(x)$. Our motivation is to test the null hypothesis

$$H_0 : F_O(x) = F_M(x), \quad \forall x, \tag{3.15}$$

where, $F_M(x)$ is the CDF of a known (model) function. The K-S test statistic, D_n is defined as

$$D_n = \max |F_O(x) - \hat{F}_M(x)|, \tag{3.16}$$

where $\hat{F}_M$ is the CDF of the known function, defined as

$$\hat{F}_M = \frac{\#(i : x_i \leq x)}{n}. \tag{3.17}$$

To check if the sample data has come from the known population, we compare the value between D_{crit} with D_n, where D_{crit} is the critical value for the KS statistics, which depends on the sample size and level of confidence given by p-value. p-value gives the probability whether the sample is drawn from a known population under the null-hypothesis assumption. A p-value close to 0 indicates that the null-hypothesis is false whereas a large p-value (close to 1) indicates that the hypothesis is true. A p-value of 0.05 is a typical threshold for the null hypothesis. For example, at p-value = 0.05 i.e. at the 95 % confidence level and for a sample size n, the critical value is given by,

$$D_{\text{crit},0.05} \approx \frac{1.36}{\sqrt{n}}, \tag{3.18}$$

where the factor in the numerator in equation 3.18 is obtained from the standard numerical table. If $D_n < D_{\text{crit}}$, we will accept the null hypothesis, H_0, i.e. the sample data has come from the model distribution with a specific level of confidence (p-value).

In the Figure 3.9, we have analyzed the K-S test for a normal distribution with $\mu = 0$ and $\sigma = 1$, i.e. $N(0, 1)$. Here, we have randomly generated 51 sample points in the domain of $x \in [-2.5, 2.5]$ and compare with the empirical form of the $N(0, 1)$. We obtained the absolute difference between the CDFs of the sample data, $F_{\text{obs}}(x)$, and the empirical distribution $F_{\text{exp}}(x)$, which is $D_n = 0.15944$. From equation 3.17, we obtained $D_{\text{crit, 0.05}} \approx 0.1904$. We notice that, $D_n < D_{\text{crit, 0.05}}$, and hence we can retain the null hypothesis.

We can also extend it for the two-sample data which checks whether both the samples are drawn from same distribution or not. Here, we compare one empirical

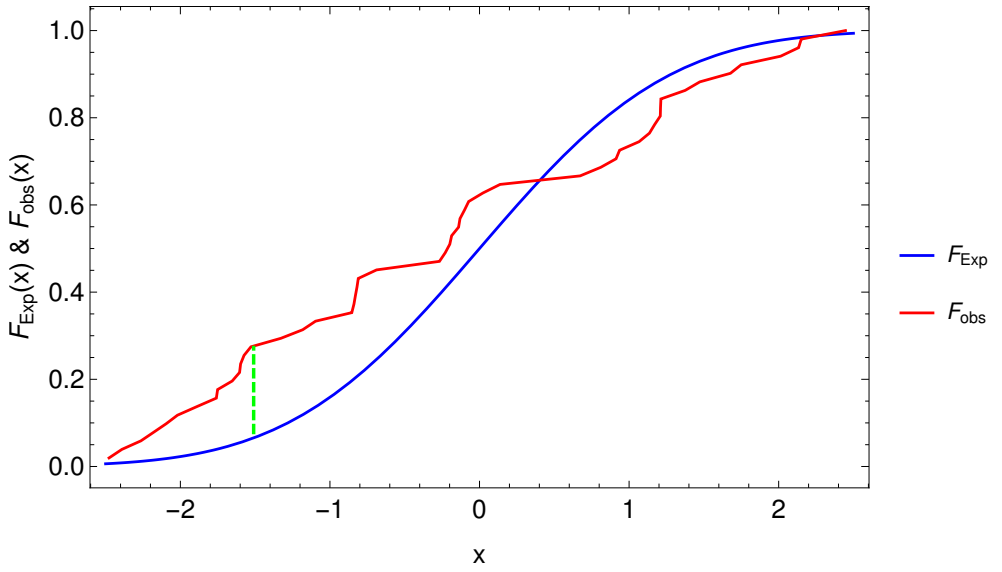

FIGURE 3.9: Comparison between the randomly generated sample points [with CDF $F_{\text{obs}}(x)$] and empirical function [with CDF $F_{\text{exp}}(x)$], for $N(0,1)$ distribution as an example for K-S test. The maximum absolute difference between $F_{\text{obs}}(x)$ and $F_{\text{exp}}(x)$ is 0.15944 as shown in green dashed line.

distribution function with another instead of a theoretical distribution function. Suppose, we have two sets of sample data of sizes n_1 and n_2, then the maximum absolute difference between the CDFs should be smaller than

$$D_{\text{crit, }0.05} \approx 1.36\left(\frac{1}{\sqrt{n_1}} + \frac{1}{\sqrt{n_2}}\right) \tag{3.19}$$

for the validation of the null hypothesis. The critical values for different sample sizes (n_1 and n_2) are available in Biometrika table which can be used for the significance testing.

3.5 Summary

The methods and tools used in this study are summarised below:

- We discuss the aperture and PSF photometry techniques along with the IRAF/DAOPHOT package used for performing it.

- We describe the FSPS code and stellar models used to generate the theoretical isochrones for studying the CMDs of the clusters.

- We describe the generation of SEDs and the tools (VOSA and python SED-fitter) used for generating and fitting them with the theoretical models. We also discuss the various theoretical models used for fitting the SEDs using χ^2 test.

- We discuss the K-S test and the significance levels useful for the comparison of distributions of two data sets.

Chapter 4

The Horizontal Branch of NGC 1851 as revealed by the UVIT †

4.1 Introduction

NGC 1851 is a massive GC of intermediate metallicity ([Fe/H]= -1.2 dex, Kunder et al. (2013)). It is located in the Southern constellation Columba, spanning around 11′ of sky. Several photometric and spectroscopic studies have concluded that this cluster contains MSPs (e.g., Milone et al. (2008); Carretta et al. (2011); Gratton et al. (2012)). The observational evidences for multiple populations include, double RGB (Han et al. 2009), bi-modal HB and RRL stars intermediate of the OoI and OoII class(Kunder et al. 2013). All of the above noted population differences should be fitted by a difference in age, helium or chemical composition, apart from the other details such as mass loss and mixing. The cluster is also remarkable in that it appears to be surrounded by a diffuse stellar halo extending to radii of ∼250 pc (Olszewski et al. 2009).

†Results of this chapter are published in Subramaniam et al. (2017)

An early study of the cluster by Walker (1992) found its core, although unresolved, to have an unusually blue color. At the same time, the HB was found to be clearly bimodal, with both a red clump and an extended blue tail. Subsequent HST/ACS photometry of the cluster from (Milone et al. 2008) revealed the existence of two distinct sub-giant branches (SGBs) as well. These authors found that the bright SGB component to outnumber the fainter component by ∼10%, and that the percentages of red and blue HB stars are 63% (RHB) and 37% (BHB), respectively. These multiple SGB populations were interpreted as evidence either for two populations having either an age difference of about 1-2 Gyr or a significant difference in their C+N+O content (Piotto et al. 2012; Cassisi et al. 2008). Salaris et al. (2008), on the basis of detailed synthetic modeling of HB stars, concluded that these two populations are distributed in different regions of the HB. The evolved stars, belonging to the bright SGB component, are confined to the red portion of HB whereas the the faint SGB population have HB stars distributed from the blue to the red, even populating the RRL instability strip. Salaris et al. (2008) also argued that large variations in the initial He abundance between the two sub-populations could be ruled out.

Gratton et al. (2012) studied the chemical composition and Na-O anti-correlation of HB stars from moderately high resolution spectra for 91 stars on the bimodal HB and 13 stars on the RGB. This spectroscopic study found that the RHB stars divide into two groups, with the vast majority of stars being Na-poor and O-rich. About 10-15% of the stars are Na-rich and moderately O-poor, with most, but not all, being Ba-rich. The two groups were found to occupy distinct regions of the CMD, where the Na-rich stars being redder and slightly brighter than the Na-poor ones. They found the BHB stars to be enriched in N, but not exceptionally so, and the total CNO abundance unlikely to be anomalous. The He abundance of the BHB was found to be consistent with both the cosmological value and a small He enhancement. This confirmed the lack of evidence for very large He enhancements within NGC 1851. Their study identified an age spread of $\sim$ 1.5 Gyr as the only

viable explanation for the split of the SGB and suggested that most of the BHB stars are older than their RHB counterparts based on their computed synthetic HB and adopting the bright and faint SGB fractions of Milone et al. (2008).

This conclusion is in agreement with the findings of Carretta et al. (2011), who first suggested that the cluster might be the product of a merger between two GCs having an age difference of ∼1 Gyr. Han et al. (2009) modelled the HB stars and suggested that the presence of bimodal HB distribution in NGC 1851 can be naturally reproduced if the metal-rich second generation stars are also enhanced in helium. Joo & Lee (2013) later argued that the two populations were similar in age and metallicity, but differed in Helium content, after comparing their (Yonsei-Yale) models with the observed CMD. Kunder et al. (2013) modelled the HB stars using He enhanced models, and noted synthetic BHB stars, along with the RRL stars, having an increasing He content and ages ∼ 1.5 Gyr older than their RHB counterparts. They too argued that the cluster may be a merger remnant. Using deep HST imaging, Piotto et al. (2015) presented NUV-optical CMDs for a number of GGCs. The CMD of NGC 1851, which is shown in their Figure 5, reveals a broad and complex HB. Yong & Grundahl (2008) also suggested that two stellar populations might exist in NGC 1851 and noted that this cluster has experienced a complicated formation history bearing some similarities to Omega Centauri. In summary, there is a general agreement that the HB population in this cluster shows an age difference, and small differences in [Fe/H], CNO and He enhancement. Among the above parameters, particularly, the differences in age and He content are expected to produce similar effects in the HB morphology. Hence, it has not been possible to have a unique interpretation of HB morphology and population difference. Though there are a lot of modelling studies of the HB stars, but the detection and separation of distinct populations in the HB has not happened so far. It is expected that the UV studies help in lifting this degeneracy.

Schiavon et al. (2012) presented FUV vs (FUV−NUV) CMD for NGC 1851 in

TABLE 4.1: Parameters of NGC 1851 used for analysis.

Parameter	Value	Reference
R.A. (J2000)	$05^h14^m06.76^s$,	Goldsbury et al. (2010)
Dec (J2000)	$-40°02'47.6''$	Goldsbury et al. (2010)
$[Fe/H]$	-1.2 dex	Kunder et al. (2013)
E(B−V)	0.01	Harris (2010)
Distance modulus	15.52	Cassisi et al. (2008)
Core radius, r_c	$0.09'$	Watkins et al. (2015)
Half-light radius, r_h	$0.51'$	Watkins et al. (2015)

Figure 11 of their paper that contained a few dozen HB stars and a handful of candidate hot stars. However, due to crowding issues, this study was restricted to the region beyond the central $50''$ and did not include a detailed comparison to stellar evolutionary models. In this study, we present the results of a pilot study to showcase the capability of UVIT to study GGCs, by presenting the UV images, photometry which can probe the inner regions of the cluster and the UV CMDs of NGC 1851.The cluster parameters use in this study are given in Table 4.1.

The chapter addresses the following aspects of the cluster: 1. to characterise the HB populations in the cluster by comparing our UV/optical CMDs to those generated with two widely used stellar evolutionary models, 2. to investigate the possibility of He enrichment among the BHB stars using He enhanced models and FUV CMD, 3. to explore the spatial distribution of the distinct HB populations in the cluster and, 4. to present the first UV light curves for RRL stars in this cluster.

4.2 Data and Analysis

We obtained the observations of the cluster in three filters (2 FUV and 1 NUV) of UVIT. The observation details of the cluster are given in Chapter 2. We used CCDLAB to generate the images of the cluster in the different filters. The UVIT image of the cluster is shown in Figure 4.1 where blue and yellow corresponds to detections in F169M and N245M filters of UVIT respectively. In the FUV, we are able to resolve stars well into the core of the cluster (although the NUV image still suffers from crowding in the central regions). In Figure 4.2, we show the GALEX image of the cluster for comparison. Isolated stellar sources in the UVIT images have FWHM $\sim 1.5''$ and $\sim 1.2''$ in the FUV and NUV channels, respectively. In terms of angular resolution, the UVIT images are thus far superior to those from GALEX ($4.5'' - 5.5''$).

We performed PSF photometry on the images to obtain the magnitudes of the sources as described in chapter 3. Figure 4.3 show the photometric errors as a function of PSF magnitude. Although, we detect stars as faint as 23 magnitude in all filters, we have limited the comparison to the models to 22 mag in FUV and 20.5 in NUV filters. This effectively puts an upper limit of 0.2 mag on our photometric errors. Of course, as Figure 4 shows, brighter stars will have photometric errors that are considerably smaller than this.

4.3 The UV and Optical Color-Magnitude Diagrams

To identify and classify the stars detected with UVIT into various evolutionary phases, we used the HST/ACS survey data for GGCs (Sarajedini et al. 2007) to

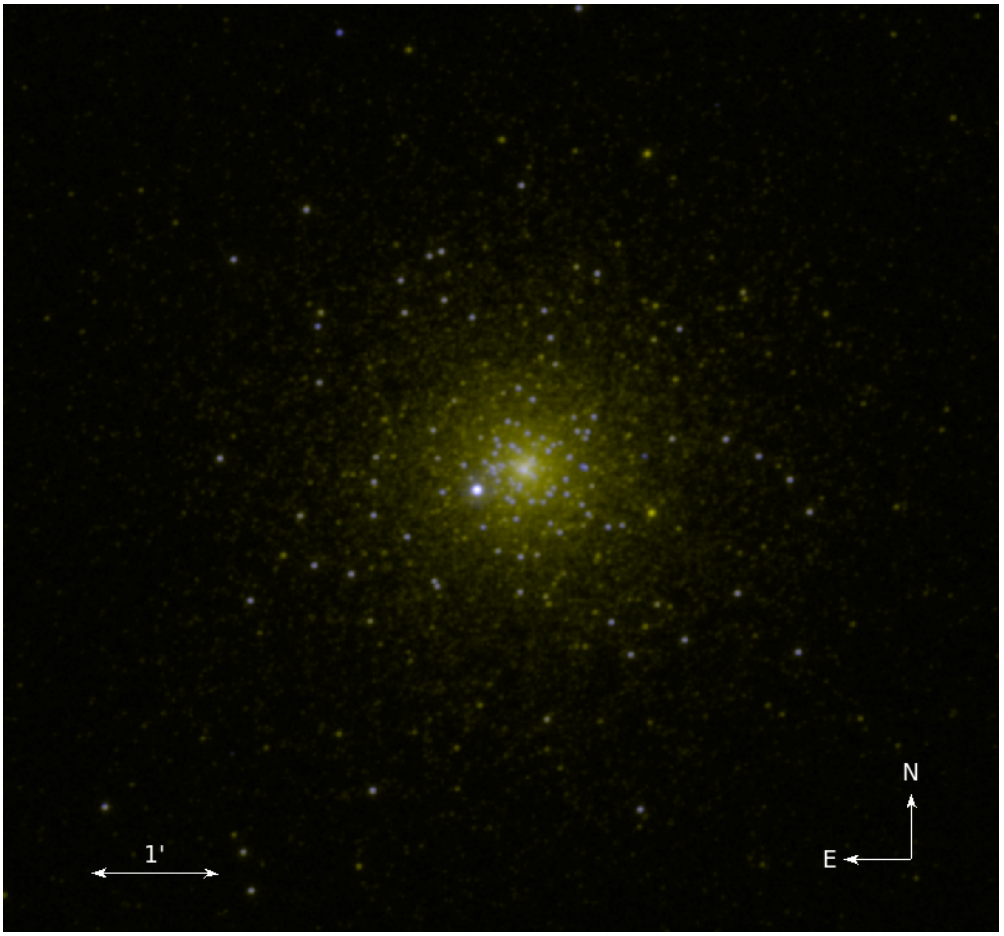

FIGURE 4.1: UVIT image of the GC NGC 1851 where blue corresponds to the FUV detections and yellow corresponds to the NUV detections acquired with F148W and N279N filters of UVIT respectively.

cross match our stars inside a region of diameter $\sim 4.0'$. The HST image of the cluster is shown in right panel of Figure 4.2. We converted the V magnitude to the AB magnitude system, to make it similar to the UVIT magnitude system. The cross matched stars shown in the CMD (Figures 4.4 and 4.5) were found to primarily belong to the HB of the cluster. The identified stars are separated into the horizontal part of the BHB (H-BHB), vertical part of the BHB (V-BHB), red part of the HB (RHB) and the post-AGB stars, according to their location in the optical HST-ACS CMD. On the AB magnitude scale, V-BHB stars are those with $(V - I) < -0.38$, which is the starting point of this nearly vertical sequence. For comparison, BHB stars are those having $-0.38 \leq (V - I) < -0.17$ while RHB

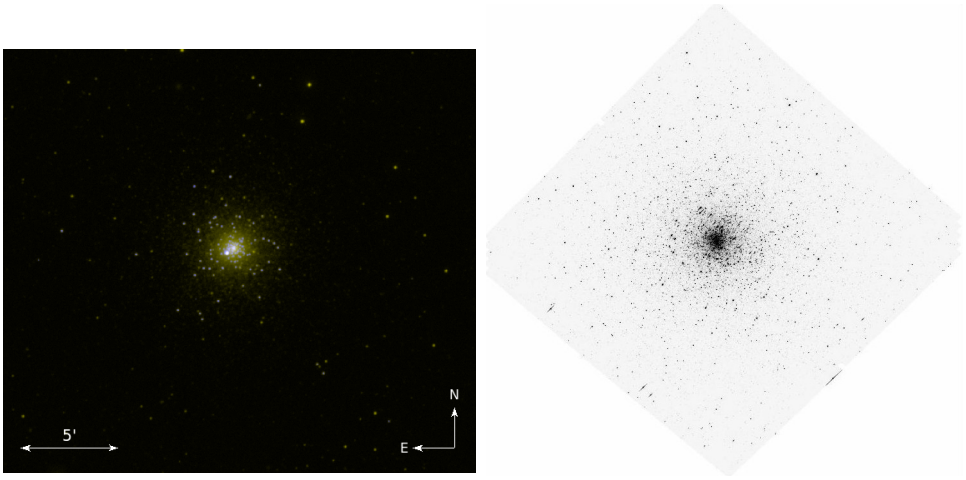

FIGURE 4.2: *Left:* GALEX image of the NGC 1851 where blue and yellow corresponds to the detections in FUV and NUV filters of GALEX respectively. *Right:* HST image of NGC 1851 obtained with F606W filter of ACS/WFC camera under HST/ACS GC Treasury Program (Sarajedini et al. 2007).

stars have $0.02 < (V - I) < 0.22$. The RRL stars detected in this study are also shown in these figures.

The isochrones shown in Figures 4.4 and 4.4 are generated using the FSPS models. These isochrones refer to the Padova models, for a metallicity of [Fe/H] = −1.2 dex (Kunder et al. 2013), a distance modulus of 15.52 mag and an assumed age of 10 Gyr (Cassisi et al. 2008). We point out that the HB stars no longer define a horizontal sequence in the UV CMD; note that even the H-BHB gets stretched in magnitude when compared to the V-BHB.

In the right panel of Figure 4.4, we show all stars detected in the FUV (188 stars), in the F148W vs (F148W−N279N) CMD. In the left panel we show the same stars in the optical CMD based on HST photometry. We are able to detect V-BHB and H-BHB stars, and five RRL stars, in the central region of the cluster but are unable to detect RHB stars in the FUV. Hence, these stars are not present in the observed CMD. The H-BHB stars are found to closely match the isochrone, with the V-BHB stars located at the brighter end of the sequence. The V-BHB stars tend to

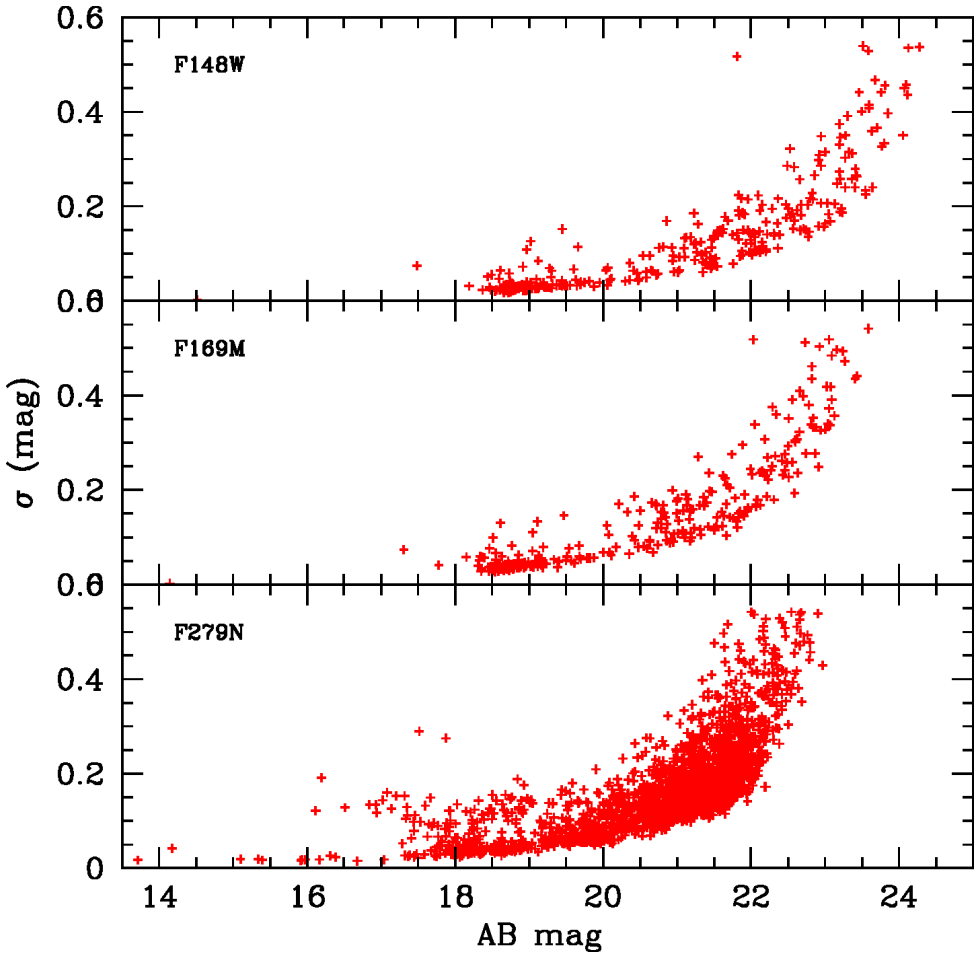

FIGURE 4.3: Photometric errors as a function of magnitude for our UVIT observations of NGC 1851. From top to bottom, the panels show results for the F148W, F169M and N279N bandpasses, respectively.

show relatively more scatter, when compared to the H-BHB stars. We also note the presence of a few H-BHB stars, as bright as the V-BHB stars. In summary, we do not see significant differences between the V-BHB and H-BHB populations, except for a large scatter in the distribution of the V-BHB stars. The RRL stars are suggestive of belonging to this population. We detected two BSSs which are also shown in the figure. In Figure 4.5, we show the F169M vs. (F169M−N279N) CMD. The corresponding optical CMD based on HST photometry, is similar to that shown in the left panel of Figure 4.4. The principle features of the CMD are similar to those in the Figure 4.4, suggesting that the V-BHB and H-BHB populations appear to be similar. We also detected five BSSs that are shown as

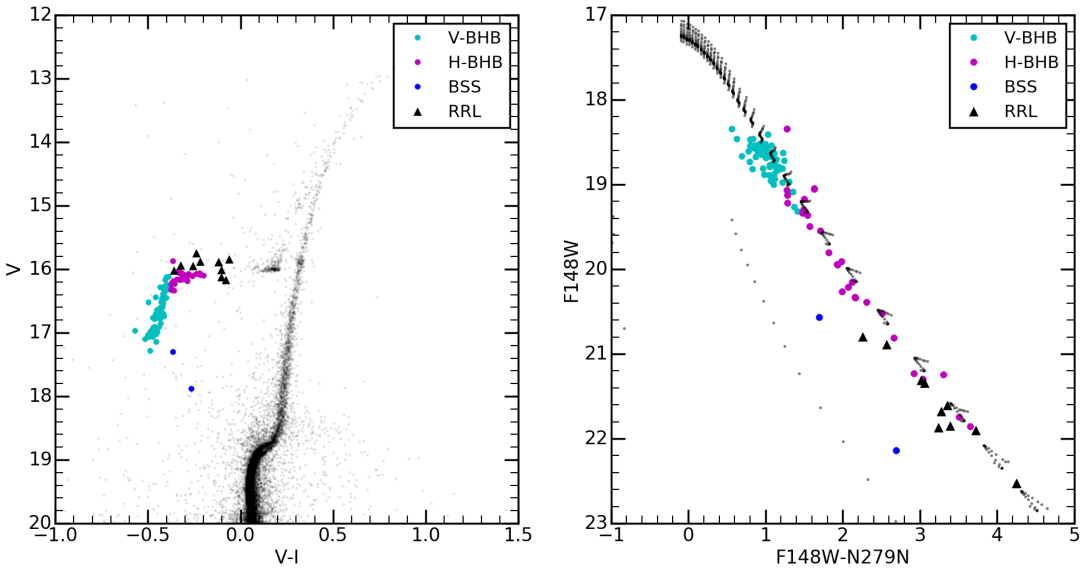

FIGURE 4.4: CMD for NGC 1851 based on F148W and N279N photometry from UVIT (right panel). For comparison, we overlay a Padova model isochrone with 10 Gyr and [Fe/H] = −1.2 dex generated using the FSPS models in the UV CMD which are shown as black dots. The panel on the left shows the optical CMD based on HST/ACS photometry. Stars detected by UVIT have been separated into five components: vertical-blue horizontal branch (V-BHB), horizontal-blue horizontal branch (H-BHB), RHB (not shown in this CMD), BSSs, and RRL stars.

blue dots. In both the CMDs, the B-BHB is stretched to a large magnitude range, while the V-BHB stars scatter over a smaller range in magnitude.

In Figure 4.6, we combine the UVIT and HST photometry to plot UV-optical CMDs. We have shown the F148W vs (F148W−V) (top left panel), F169M vs (F169M−V) (top right panel) and N279N vs (N279N−V) (bottom right panel), along with the cross matched stars in the optical CMD using the HST data (bottom left panel). In the UV-optical CMDs in the top panels, we detect the V-BHB, H-BHB and some RRL stars. In the case of bottom panel, we detect the full HB along with the RRL stars. The HST CMD shows all the detected stars in the NUV, whereas only a subset is detected in the FUV. The isochrones with the same age and metallicity (as in Figures 4.4 and 4.5) are shown here, for the corresponding filters. We also detect some BSSs. It can be seen that, in all the three UV-optical

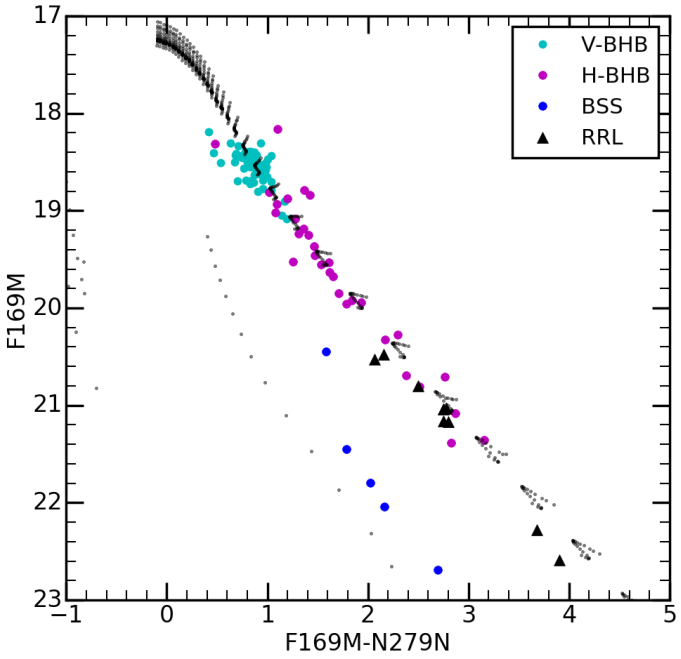

FIGURE 4.5: CMD for NGC 1851 based on F169M and N279N photometry from UVIT. For comparison, we overlay a Padova model isochrone with 10 Gyr and [Fe/H] = −1.2 dex generated using the FSPS models in the UV CMD which are shown as black dots. The various symbols show stars belonging to different evolutionary sequences in the CMD, as described in Figure 4.4.

CMDs, the V-BHB stars deviate from the H-BHB stars. A few of the H-BHB stars are found to continue the H-BHB slope and end up brighter than the V-BHB stars. The blue hook feature can be clearly identified at the bright end of the HB in the FUV CMDs (upper panels), suggesting the presence of the blue hook stars at the end of the V-BHB sequence. The H-BHB stars are found to be in a sequence, which could be an extension of the RHB stars, but we do detect some variation (bottom panel), suggesting that the H-BHB branches off with a shallower slope. As expected, the RRL stars are located between the H-BHB and RHB stars. A careful inspection reveals that the V-BHB stars can be seen to branch off from the sequence of H-BHB stars, with a bit of mixing of stars near the point of deviation. We also see that some RHB stars and H-BHB stars are mixed together, even though these groups are well separated in the optical CMD.

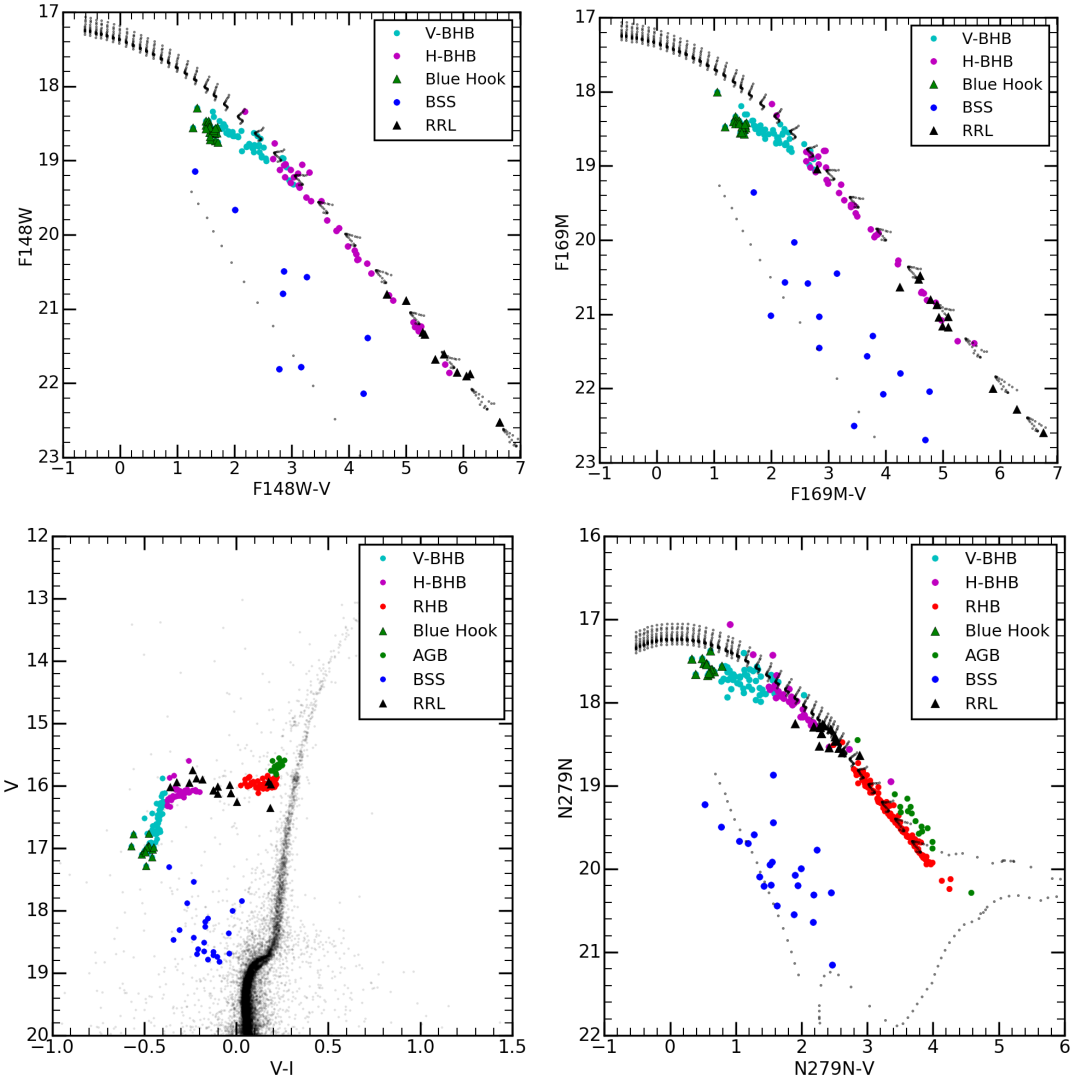

FIGURE 4.6: UV CMDs for NGC 1851 after cross-matching HST/ACS data to UVIT data in the F148W, F169M and N279N filters. FUV CMDs are shown in the upper panels. NUV and the corresponding optical CMDs are shown in the lower panels. For comparison, we over plot a Padova model isochrone with 10 Gyr and [Fe/H] = −1.2 dex generated using the FSPS models in the UV CMDs which are shown as black dots. The various symbols show stars belonging to different evolutionary sequences in the CMD, as described in Figure 4.4.

The RHB stars are found to have a very tight sequence, with very little scatter, when compared to the V-BHB and B-BHB stars. We find the AGB stars to be brighter than the RHB and separated from it (bottom panel).

In all panels, the V-BHB stars are found to be fainter than the isochrone, whereas the B-BHB stars are almost aligned with the isochrone. This may point to some differences between these two types of stars. The RHB stars are found to extend below the magnitude limit of the HB, as delineated by the isochrone (bottom panel). This could suggest that either the RHB is metal-rich or younger than the over plotted isochrone. We find that there could be differences among the V-BHB, H-BHB and the RHB stars, with the V-BHB and RHB stars possibly belonging to two different populations. The differences could be due to a difference in age, metallicity, CNO abundance or mass loss, as mentioned as possible mechanisms by previous studies on this cluster.

Finally, we cross-matched the UVIT detected stars with ground-based V,I photometry provided by Peter Stetson (private communication). In Figure 4.7, we present the CMD obtained by cross matching with the ground data, where the UVIT CMD is on the right panel and the corresponding optical CMD is in the left panel. It can be seen that the number of cross matched stars from the ground data (59 stars) is much less than stars from the HST data (254 stars), which covers the inner $0.5' - 4.0'$ region. Nevertheless, we detect all the three types of HB stars in the ground photometry (28 RHB, 6 HBHB, 13 VBHB), as well as 12 BSSs. By comparing the inner data from the HST and the outer data from the ground, it can be seen that most of the HB stars are located within a region of diameter $0.5' - 4.0'$. Indeed, only a modest fraction of the detected stars ($47/232 \sim 20\%$) are found outside this region.

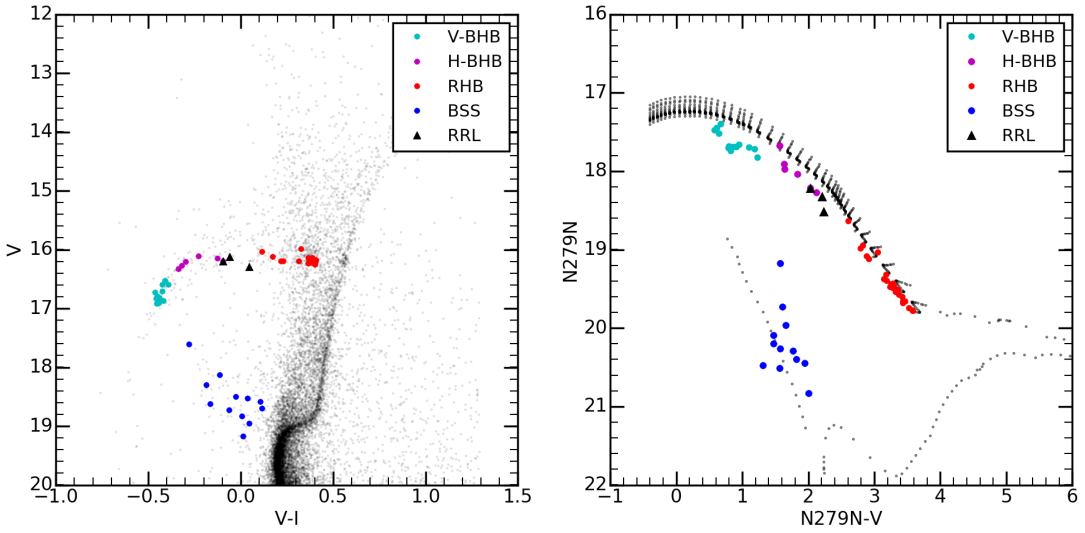

FIGURE 4.7: UV-optical CMDs obtained by cross-matching ground-based data with UVIT data in the N279N filter. For comparison, we over-plot a Padova model isochrone with 10 Gyr and [Fe/H] = −1.2 dex generated using the FSPS models in the UV CMD which are shown as black dots. The various symbols show stars belonging to different evolutionary sequences in the CMD, as described in Figure 4.4.

4.4 Characterizing the HB Population

We have attempted to characterize the HB stars by comparing the UV-optical CMDs with predictions from the stellar evolutionary models. Before proceeding, we note that (Gratton et al. 2012) studied the HB population in NGC 1851 using medium resolution spectroscopy and found that, on average, the RHB stars have [Fe/H] = −1.14±0.01 dex from Fe I lines and [Fe/H] = −1.20±0.01 dex from Fe II lines. They also measured a He abundance of $Y_{ini} = 0.291 \pm 0.055$, and estimated an initial He abundance of about $Y_{ini} = 0.248$ with mild He enhancement thereafter. A large initial He abundance was deemed unlikely.

Figure 4.6 suggests that the isochrone fits the HB in general well, except for the deviation noticed for the V-BHB stars. The isochrone also suggests fainter extension to the RHB. These deviations could suggest that one or more parameters

corresponding to the isochrone plotted, might vary among the detected HB stars. We also used the BaSTI models to generate isochrones with different ages and abundances, instead of the Padova models. As we need to fold in the UVIT filters into the FSPS models, we are able to change only the age and metallicity of the isochrones, keeping the other parameters, such as Y_{ini} constant. In Figure 4.8, we show isochrones for two ages, where in each plot, we have kept the age constant and varied the metallicity as shown in the figure. These isochrones have $Y_{ini} = 0.25$. The figure shows how the isochrones for the HB stars change in the UV with age and metallicity, as per the predictions from BaSTI models. The isochrones shown in both the figures could be used to derive the range of age and metallicity. With the decrease in the value of [Fe/H], the extent of the HB shrinks such that the red end of the HB gets bluer. The presence of an extremely extended HB, as seen in this cluster, can be fitted using isochrones with [Fe/H] ~ -1.0. The fitted value of [Fe/H] is, to within the errors, in good agreement with the values obtained by Gratton et al. (2012).

From the upper panel of Figure 4.8, it is clear that the RHB can be fitted using an isochrone of age 10 Gyr, for the above value of [Fe/H], whereas none of the isochrones in the bottom figure fits the RHB. The bottom figure shows that the fit of the RHB cannot be reproduced by an increase in age. None of the isochrones in the top and bottom panel are able to fit either the V-BHB or the H-BHB. A close examination of the bottom figure suggests that the isochrone shown in green points, corresponding to 12 Gyr, is the closest fit observed for the H-BHB stars. Thus, we find that an age range of up to 2 Gyr might be required to fit the full HB stars, for a constant Y_{ini} and metallicity.

In Figure 4.9, we have shown the CMD with isochrones of two ages (10, 12 Gyr) for Fe/H] ~ -1.0 and $Y_{ini} = 0.25$, for the UV-optical CMDs. These are the parameters we are able to derive for the HB stars using the BASTI isochrones. In summary, we detect the presence of two age groups in the HB of NGC 1851, using

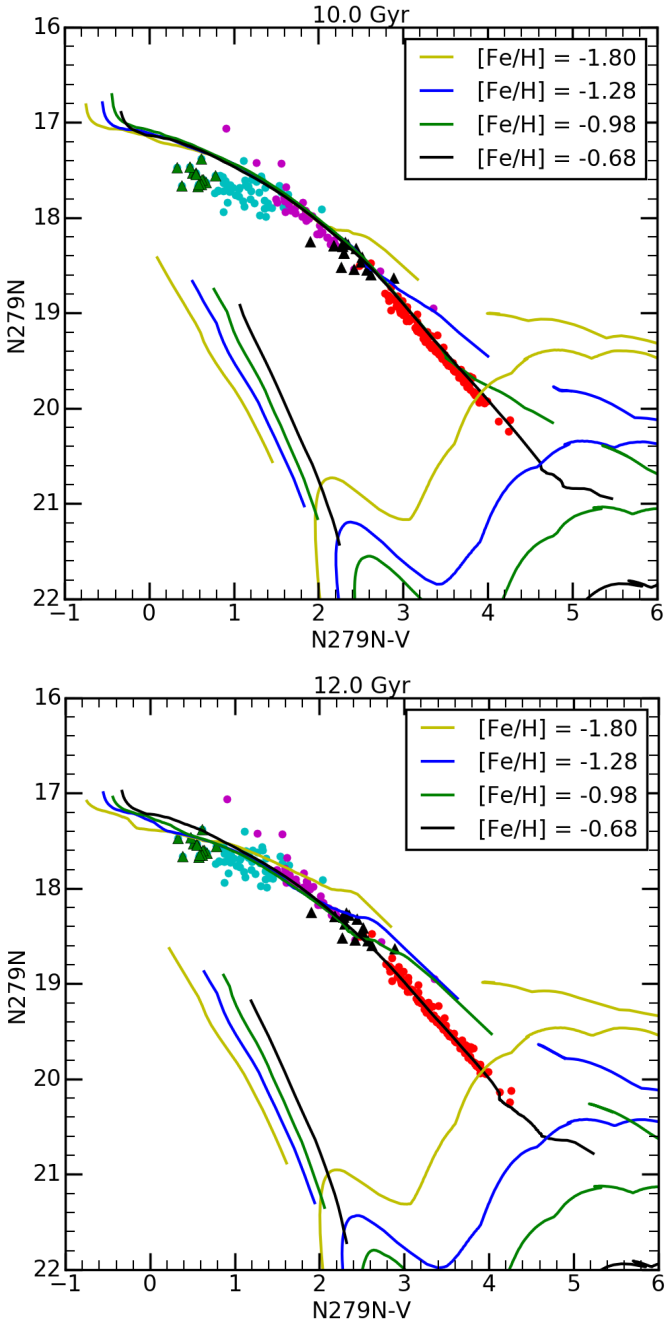

FIGURE 4.8: NUV-optical CMD for NGC 1851 based on UVIT imaging in the N279N filter. BaSTI Isochrones are shown for four different values metallicities, as indicated in the legend, and two assumed ages: 10 and 12.0 Gyr (left and right panels, respectively).

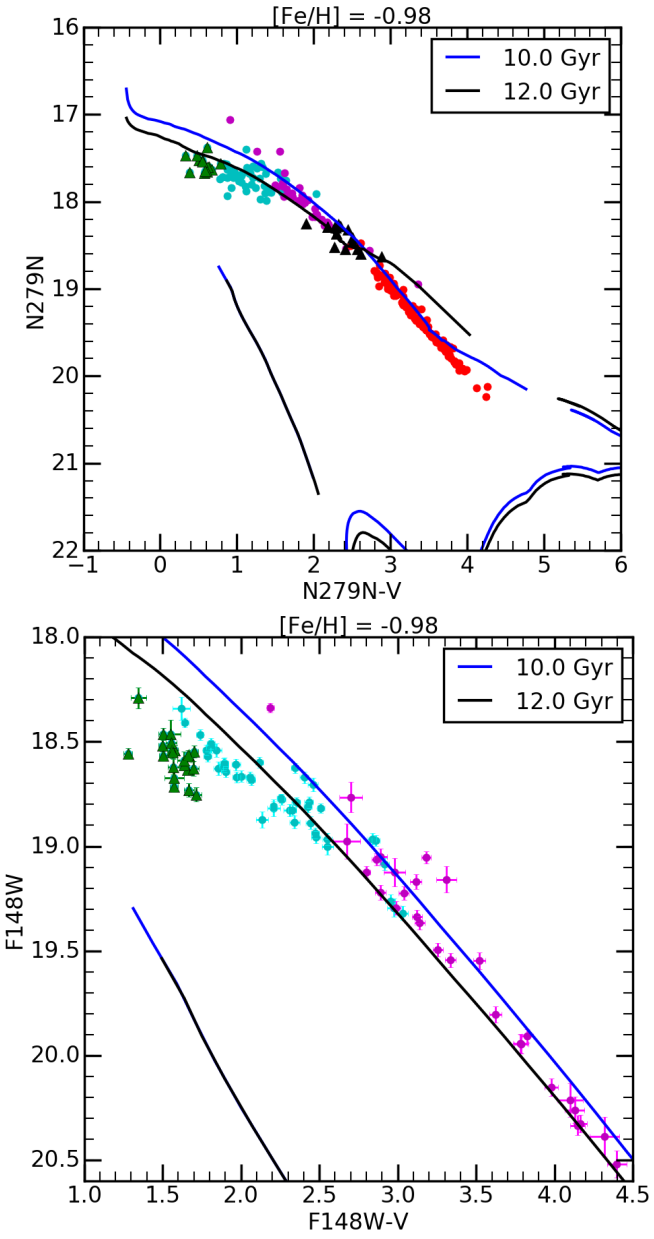

FIGURE 4.9: NUV-optical CMD for NGC 1851 based on UVIT imaging in the N279N filter in the upper panel and FUV-optical CMD for NGC 1851 based on UVIT imaging in the F148W filter in the bottom panel. BaSTI Isochrones are shown for two different ages, as indicated in the legend, and a metallicity of [Fe/H] = −0.98 dex.

the BaSTI isochrones. We find that the RHB stars in the cluster could belong to a relatively younger population (10 Gyr), whereas the BHB stars could be up to 2 Gyr older. We believe that there cannot be large difference in [Fe/H] among the HB stars. Recall that Carretta et al. (2011) and Gratton et al. (2012) suggested that the cluster has two populations, with an age difference of up to 2 Gyr.

As noted above, the N279N filter is centred around the Mg II line and therefore, the flux in this filter depends on the magnesium abundance of the HB stars. Gratton et al. (2012) found a higher abundance of magnesium for their BHB stars, in comparison to the RHB stars. The isochrones in this filter are expected to capture the details of variation in magnesium abundance across the HB. The fact that the FUV CMDs also suggest the deviation of V-BHB stars from the 10 Gyr isochrone suggests that the deviation may not be related to any residual variation in the Mg II strength. This is confirmed from the bottom panel of Figure 4.9, we have overlaid the isochrones on the FUV CMD. The CMD confirms that the V-BHB stars are reasonably well fitted by the 12 Gyr isochrone. The blue hook stars are fainter than the rest of the V-BHB stars and the isochrones do not reproduce this feature. Thus, we note that the blue hook stars appear to be fainter in the FUV, even though they have normal NUV flux. This may provide some specific clues to their structure and evolutionary phase. Dalessandro et al. (2011) presented the FUV-optical CMD of NGC 2808 and used it to confirm the multi-model distribution of stars along the HB. They found that the canonical models are not able to match the hot end of the HB.

4.4.1 He Enrichment

The issue of He enrichment in this cluster has been discussed and contested for some time. The spectroscopic study of Gratton et al. (2012), SGB study of Milone et al. (2008) as well as the HB simulations of Salaris et al. (2008), did not find any

significant enhancement in He. Han et al. (2009), Kunder et al. (2013), suggested that He is enhanced in the BHB stars, apart from them being older. Joo & Lee (2013) also argued that He enhancement can explain the age effect, and therefore an apparent age difference may actually be due to differences in He content.

In order to understand the effect of Y_{ini} on the HB morphology, we considered the He enhanced models. The synthetic HB models presented here are based on Y^2 stellar evolutionary tracks with enhanced initial He abundance (Lee et al. 2015). We adopt Reimers (1977) mass-loss coefficient $\eta = 0.5$ * and the mass dispersion on HB stars $\sigma_M = 0.015 M_{\odot}$. We assume a fixed α-element enhancement of $[\alpha/Fe] = 0.3$. We refer the reader to Chung et al. (2017) for more detailed descriptions of our synthetic HB models. Note that we did not consider the effect of the CNO abundance anomaly in the models. Therefore the variation of HB morphology is solely coming from the combinations of the metallicity, age, and the initial He contents.

In Figure 4.10, we present the synthetic HB plotted over the observed HB. The left panels show the fit to the observed HB in optical colors of V − I. We applied different values of Y_{ini} for the bimodal HB morphology and splits on the sub-giant branch stars of NGC 1851 at the same time. We assume helium enhanced population consists of slightly metal-rich population and fix the age of two population as 12 Gyr. There are still issues on CNO abundance variation between two populations of NGC 1851, but as reported in (Joo & Lee 2013) the variation is less than 0.1 dex which have almost negligible effects on HB morphology and splits of SGB stars. Therefore, both of the HB morphology and the splits on SGB are caused by the difference in initial helium abundances. In the right panels, we present the UV CMDs based on the same stellar parameters of the left panels.

*In order to reproduce the HB morphology of inner halo MWGCs, we assume the age of the inner halo as 13.3 Gyr and the initial helium as Y_{ini}=0.23. Since the increased η value has the same effect as the increased age or the increased initial helium abundance by decreasing the mean mass of HB stars, if we increase the initial helium or include helium spread in the inner halo, the η becomes less than 0.5.

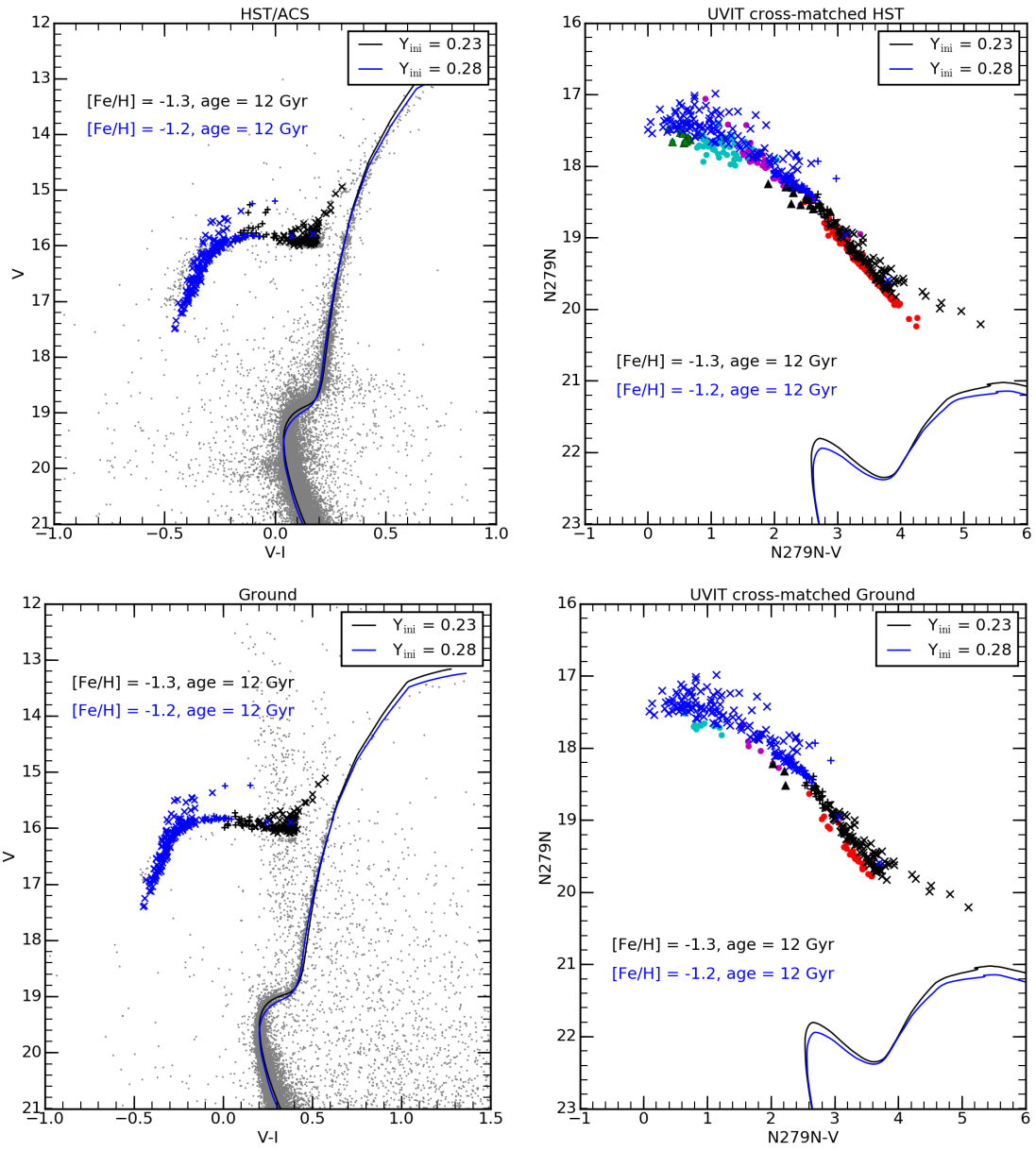

FIGURE 4.10: Synthetic HB models from Y^2 stellar evolutionary tracks with enhanced initial He abundance, Y_{ini} (Lee et al. 2015) are overlaid on the observed data points. The upper left panel and upper right panel shows the HST optical data, and cross matched UVIT data respectively. The lower left panel and lower right panel shows the ground based optical data and cross-matched UVIT data. The crosses denote the generated synthetic HB, the lines indicate the Y^2 for the MSTO and SGB.

The synthetic HB reproduces the RHB and the BHB stars very well, though we see that the model predicts fainter BHB stars in V band and brighter BHB stars in N279N filter. The difference between the model and the observed magnitude in the N279N is more than 3σ. Thus, the synthetic CMD models with He enhancement suggest the following parameter combination for the HB population: an age of 12 Gyr, and a range in Y_{ini} of 0.23 - 0.28 with a metallicity range of [Fe/H] $\sim$ -1.2 to -1.3. In particular, the parameter range for the RHB stars are Y_{ini}=0.23, 12 Gyr, and [Fe/H]=-1.3, whereas those for the BHB are, Y_{ini}=0.28, 12 Gyr, and [Fe/H]=-1.2. These parameters are estimated from the UV CMDs for the first time and are in good agreement with the previous estimated values of Y_{ini}, [Fe/H] and age, in the literature.

In order to explore population difference among the BHB stars, we used the two FUV filters in the UVIT to produce a F148W vs (F148W$-$F169M) CMD. Here the color term corresponds to the ratio of flux within the FUV band. The F148W is a FUV window with 1300-1800Åcoverage, whereas the F169M filter has 1450 - 1750Åcoverage. The CMD is shown in Figure 4.11. We have overlaid the BaSTI isochrones in the upper panel and the synthetic HB from Y^2 models in the lower panel. The photometric errors are also shown for better comparison. The H-BHB stars span a range of 3 magnitudes, whereas the V-BHB stars span a range of one magnitude, with the blue-hook stars co-located with the brightest V-BHB stars. The color difference for the H-BHB stars is $\sim$ 0.3 mag, whereas for the V-BHB stars, it is about $\sim$ 0.1 mag. The brightest of the H-BHB stars have similar colors as the V-BHB stars. The HB stars are tend to be bluer than the predictions, suggesting that they are relatively hotter. On the other hand, we do not see a significant color difference between the H-BHB and the V-BHB stars, more than that is suggested by the isochrone. The temperature of the brightest BHB stars, as per BaSTI as well as Padova models is found to be $\sim$ 12,000K. The Y^2 models reproduce the BHB stars better and the best fit parameters for the H-BHB stars are 12 Gyr, Y_{ini} = 0.28 and [Fe/H] $\sim$ -1.2 dex. They also predict the BHB stars

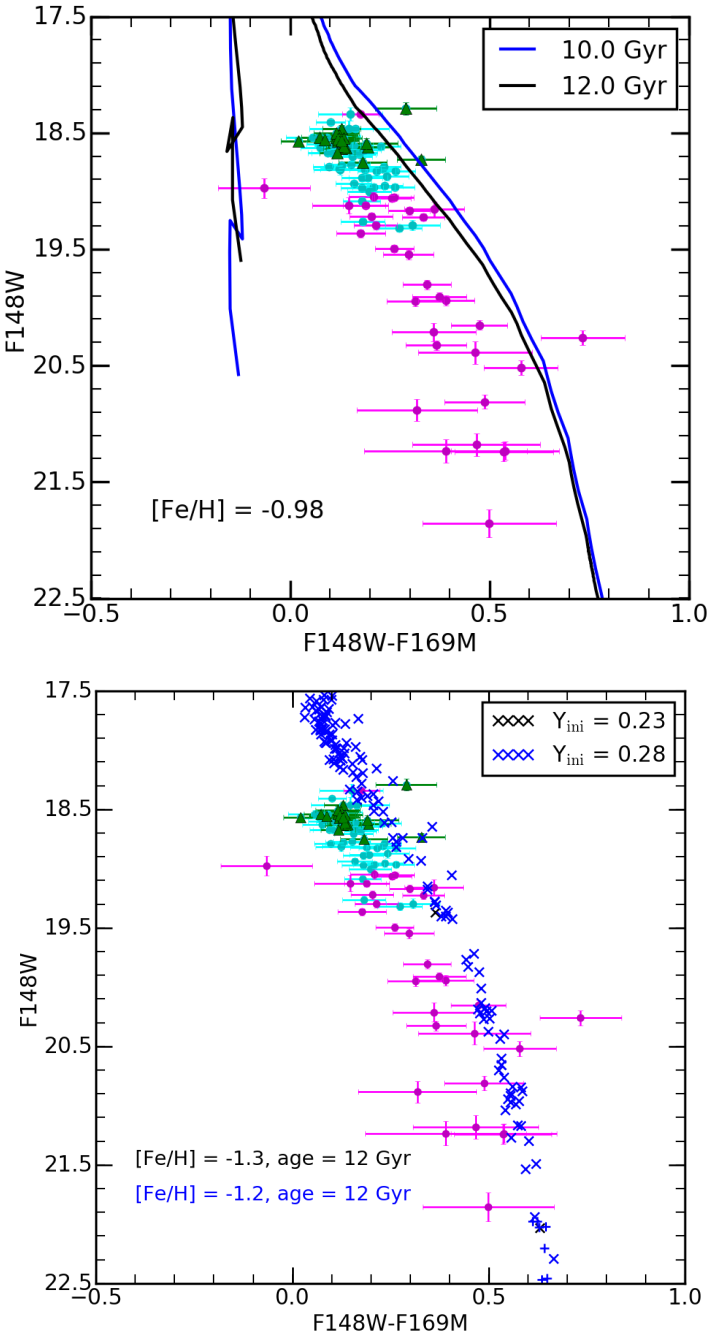

FIGURE 4.11: FUV CMD based on UVIT photometry the F148W and F169M filters. BaSTI isochrones at three different ages are shown in the top panel. The synthetic HB from the Y^2 models are shown in the bottom panel.

to be more then 1 mag brighter than the observed BHB stars in the F148W filter. This needs further attention. The estimated parameters are in overall agreement with Gratton et al. (2012).

4.5 Spatial Distribution of HB Stars

Milone et al. (2008) divided stars on the sub-giant branch into faint (fSGB) and bright (bSGB) populations, with 45% and 55% of the stars belonging to these two components. They found the HB to be bimodal as well, with 63±7% and 37±9% associated with the red and blue branches, respectively. In our data, cross matched the HST data, we detect 232 HB stars in total, with 131 stars (∼56%) on the RHB and and 101 stars (∼44%) on the BHB. These fractions are similar to those found by Milone et al. (2008) for SGB and HB stars. The spatial distribution of the SGB and HB components were found to be same by Milone et al. (2008). The radial distribution of HB stars detected by UVIT and cross matched to HST are shown in Figure 4.12. The upper panel shows the distribution of V-BHB, H-BHB and RHB, with the same color code as in the earlier figures. In the bottom panel, we have combined the V-BHB and the H-BHB stars in to a single group (BHB) and their radial distribution (blue line) is shown along with the distribution of RHB stars (red line). We note that the inner regions ($< 1'$) have more BHB stars. Beyond $> 1.4'$, we see an excess of RHB stars, as suggested by the cross-over of the two distributions. A K-S test for this pair of distributions (bottom panel) returns a probability of 2%, which suggests that the two populations differ in their radial distribution. The data used here for K-S test are those detected by UVIT from the original HST sample. Due to crowding, we were not able to detect stars in the central $\sim 10''$, highlighting that our data suffers from incompleteness in the core. Milone et al. (2008) found that the probability that the BHB and RHB stars are

drawn from the same sample is 19%. Therefore, radially, the BHB and the RHB distributions may only be marginally different.

In Figure 4.13, we show the spatial distribution of the BHB stars in the upper panel and the histogram of the azimuthal distribution in the lower panel. We converted the HB stars to an XY coordinate system with origin at the cluster center. In the upper panel, we have color coded the stars according to their azimuthal angle, ϕ, which increases towards the positive Y axis, starting from the negative X axis. The inner region with data incompleteness ($\sim 10''$ radius) is indicated. We have also indicated the half-light radius of the cluster as the dotted circle, with a radius of $r_h = 30.6''$ (Watkins et al. 2015). The figure suggests that the BHB stars show a non-uniform azimuthal distribution. In the lower panel, the histogram is shown to bring out the details, where we have show a bin width of 30^o, in azimuth angle. We have also shown the average number as the straight line, and the hashed area denotes the 1σ width. We see that two bins are below and one bin is above this width. Therefore, there are less stars in the 60-90^o and 150-180^o bins, whereas there are more stars in the 180-210^o bin.

In Figure 4.14, we present a similar test for the RHB stars. This also points to an azimuthally non-uniform distribution, albeit one that differs from the BHB stars. The spatial plot suggests that the RHB stars outside the half-light radius are preferentially located in three specific value of ϕ. This is indicated by the histogram which shows a wavy pattern with three peaks and two troughs. Inside the half-light radius, the RHB stars are located mostly in the first and fourth quadrants, which is different from the distribution seen outside. The histogram shown suggests that two bins (120-150 and 240-270) have less stars, whereas the 150-180 bin has more stars than 1σ width. Thus, the RHB stars are also found to show a non-uniform azimuthal distribution. Both the BHB and RHB stars are azimuthally asymmetric, suggesting that they perhaps are not well mixed. The spatial distribution presented by Milone et al. (2008) shows similar features (i.e.,

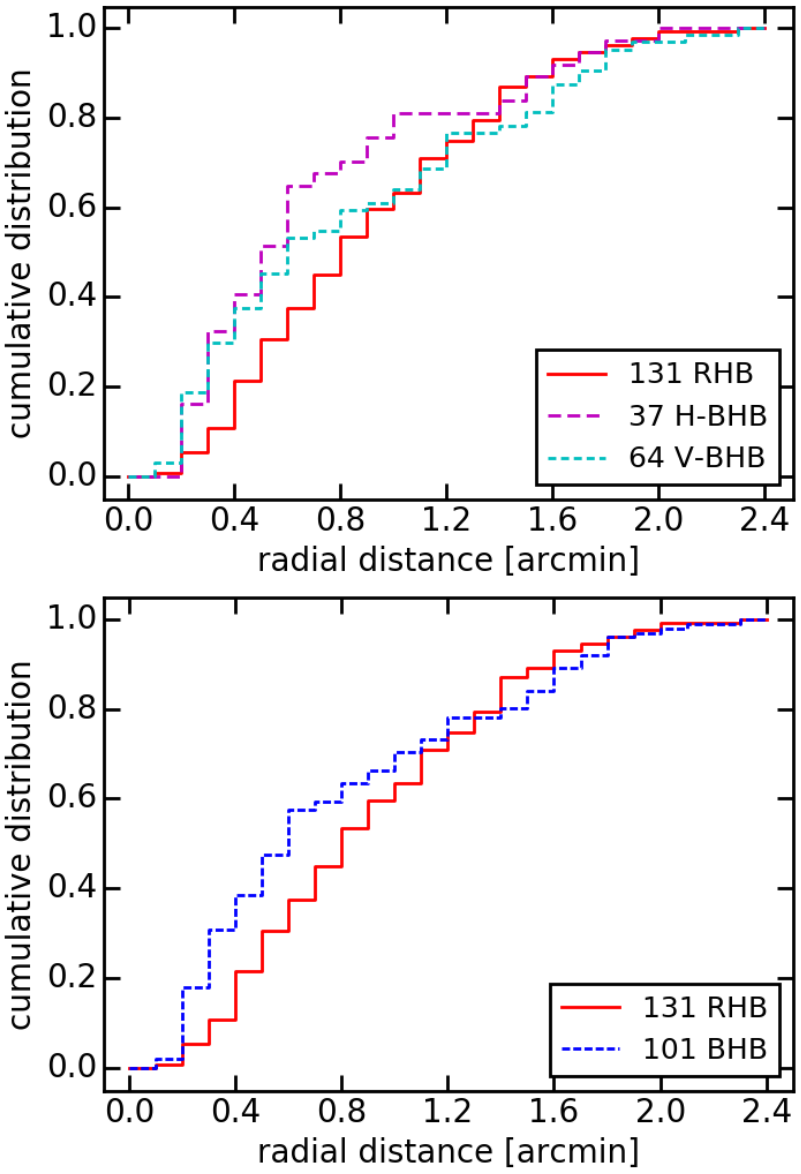

FIGURE 4.12: The radial distribution of HB stars. The upper panel shows the distribution of V-BHB, H-BHB and RHB stars. In the lower panel, the V-BHB and the H-BHB stars are combined into a BHB sample and shown along with their RHB counterparts.

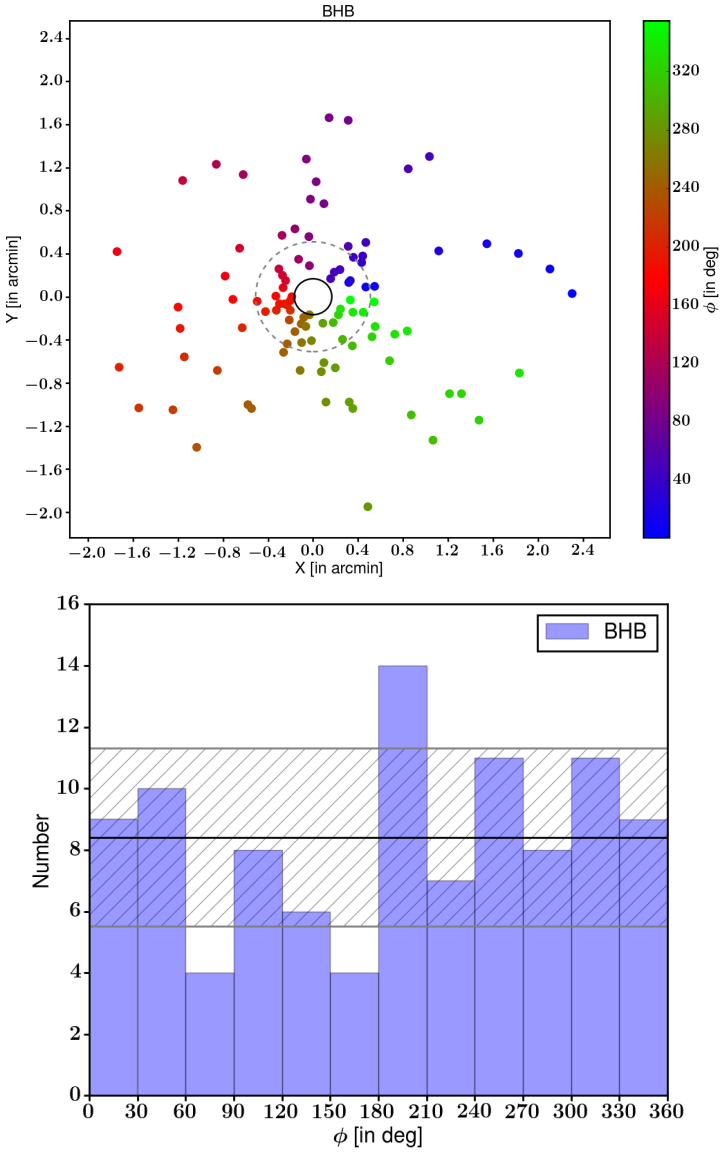

FIGURE 4.13: The spatial distribution of BHB stars in NGC 1851. On the top panel, we plot the distribution of BHB star in the cluster. The origin marks the cluster center, while the inner circle (10″) corresponds to the region with significant sample incompleteness, and the outer circle corresponds to the half-light radius (30.6″, Watkins et al. (2015)). The bottom panel shows the histogram of position angles, using bin width of 30°. The straight line shows the mean value and the hatched region shows the 1σ error width.

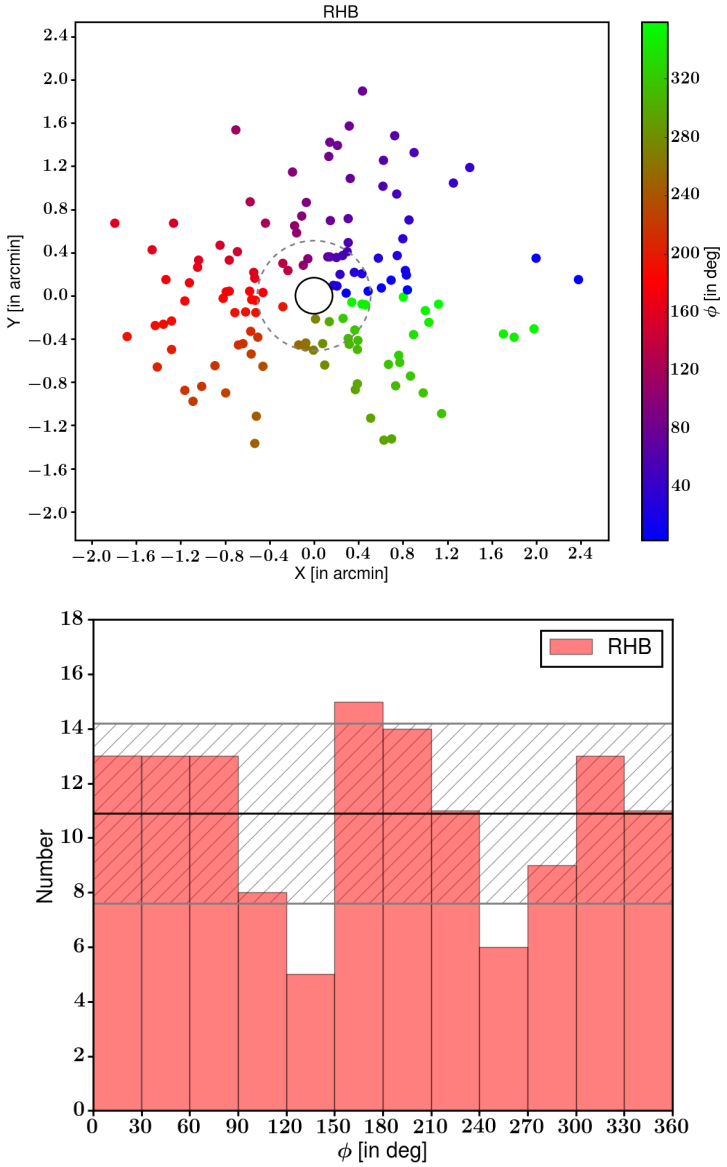

FIGURE 4.14: Same as Figure 4.13, except showing the distribution of RHB stars within the cluster.

see their Figure 7). The analysis provided here uses all stars outside the central 10″. The missing inner stars could alter the radial distribution, but may not affect the azimuthal distribution. As the number involved is not large, we do not attempt to derive statistical significance of the azimuthal variation. Our finding could provide additional support for the possibility that this cluster is a merger remnant (Carretta et al. 2011).

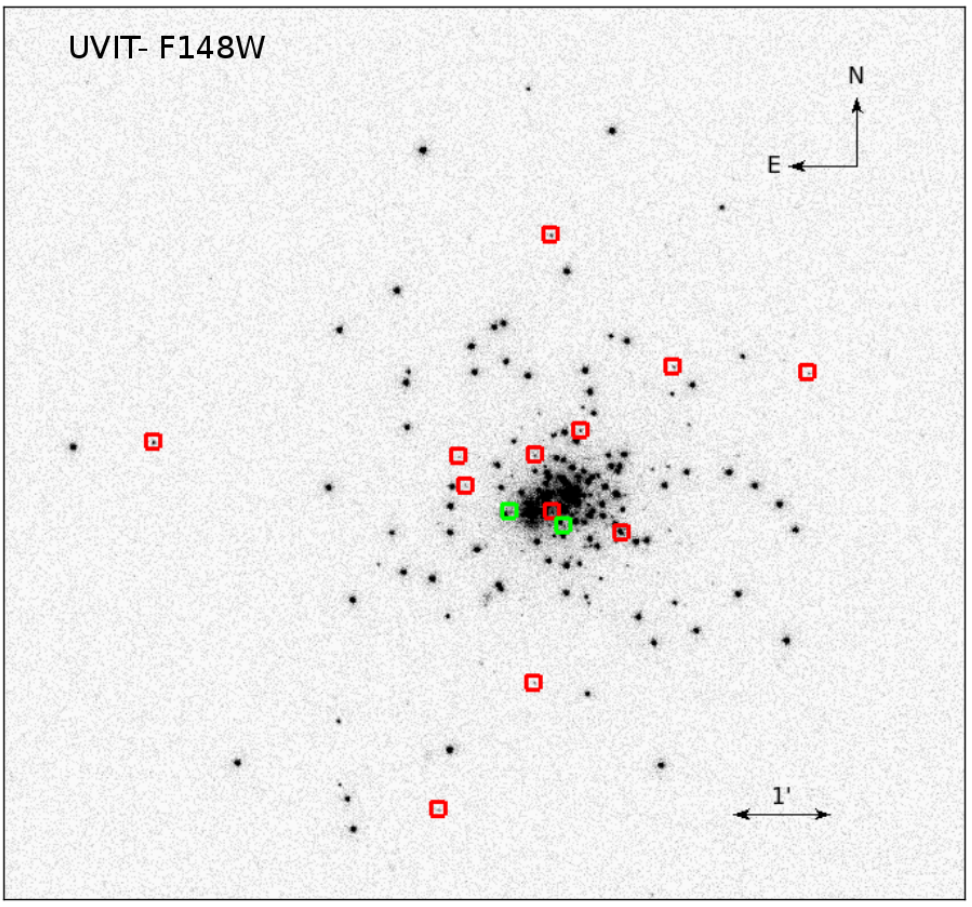

FIGURE 4.15: RRL stars in NGC 1851 identified from our the FUV UVIT images. Two newly detected variables are shown in green. North is up and east is to the left in this image, which measures 1′ on a side.

4.6 UV Variability of RRL stars

Walker (1998) identified 29 RRL variables in the cluster and found the ratio of first-overtone RRL to fundamental mode RRL stars to be consistent with Oo II clusters (although near the end of Oo I distribution). This cluster is known have the most extreme (long) period for RR_{ab} stars, this is considered as one of the unusual OoI object (Downes et al. 2004; Kunder et al. 2013). It has been difficult to conclude whether the differences in the intrinsic magnitudes of RRL variables in Oo I and Oo II clusters are caused by something other than just metallicity, such as age

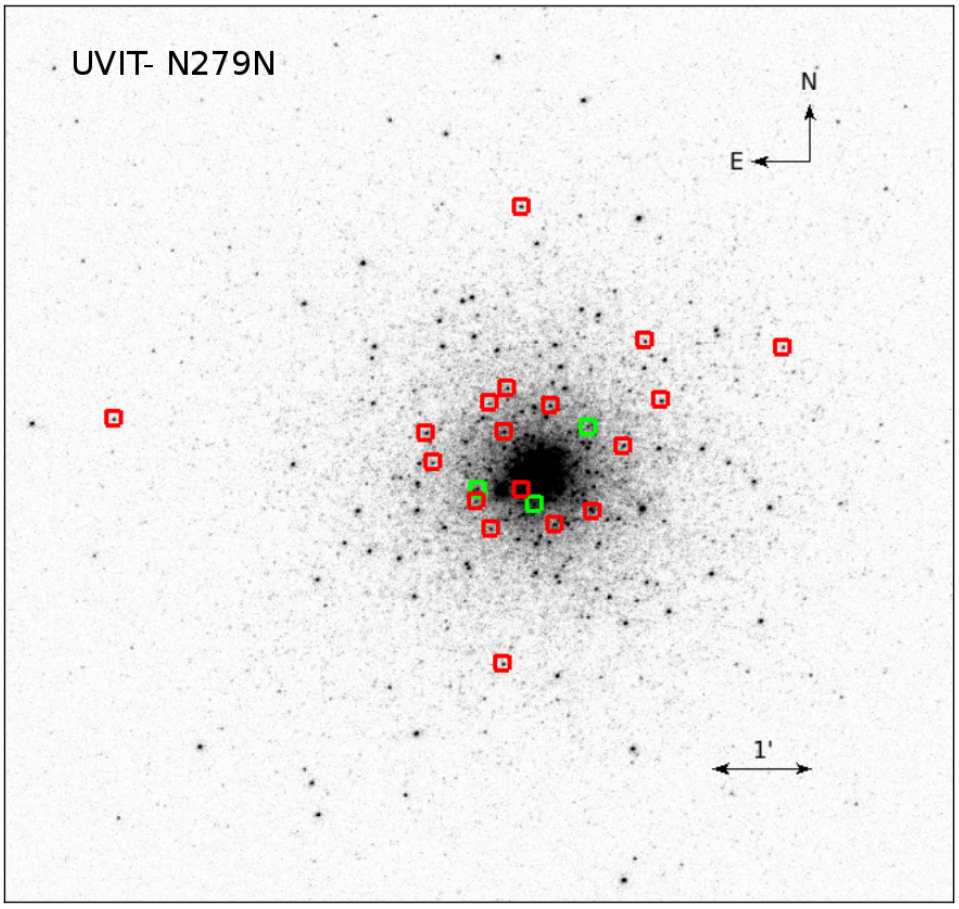

FIGURE 4.16: RRL stars in NGC 1851 identified from our the NUV UVIT images. Three newly detected variables are shown in green. North is up and east is to the left in this image, which measures 1′ on a side.

or helium content. In this cluster, where an internal spread in [Fe/H] is modest, at best, Kunder et al. (2013) suggested that a difference in helium abundance among the RRL variables could explain the observed periods, amplitudes and brightnesses. In the optical, RRL stars have typical amplitudes of 0.5–1.0 mag, whereas our UV data shows much larger variations. For instance, (Downes et al. 2004) identified 11 RRL-like variables in the core of the cluster using the HST FUV data. They found that the amplitudes of these stars to be as large as 4 magnitudes. Their Figure 3 show the light curves of RRL stars in the FUV (although these are not complete light curves).

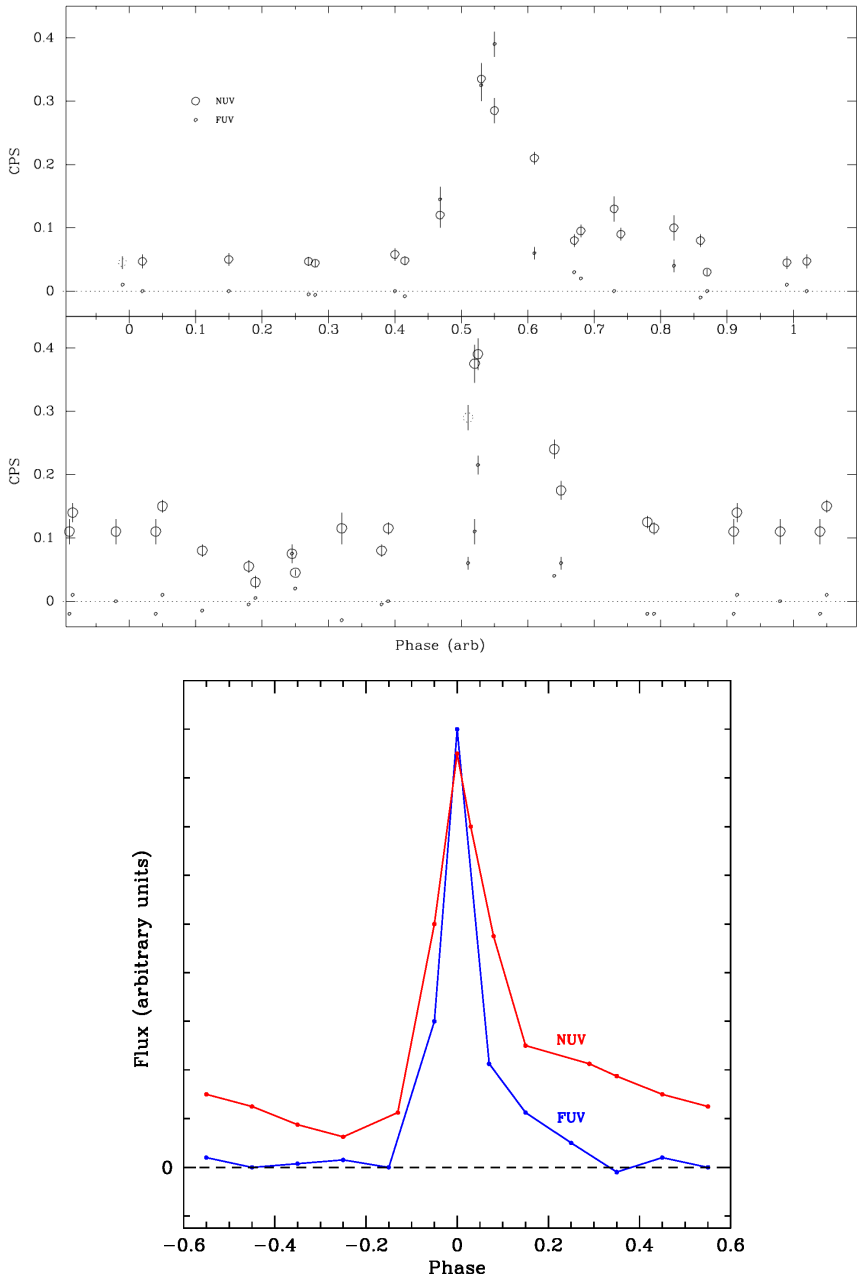

FIGURE 4.17: Upper panel shows the full light curves of two RRL stars in NGC 1851. These full light curves and the rest of the partial light curves were used to create a typical light curve for the FUV and NUV, as shown in the lower panel.

Our UVIT observations of NGC 1851 were taken over multiple orbits as consequence of the early operations of AstroSat. Variable stars were thus sampled over a range of their cycles that would not have been possible in a single pointing. We used the RRL stars from Walker (1998) and Kunder et al. (2013) to cross match our sample. The RRL stars that we have detected are shown in Figures 4.15 and 4.16. In all, we find 12 known and two new variables (red and green squares, respectively) in the FUV. In the NUV, we find 18 previously known and three new variable stars. This brings the total of RRL like variables in this cluster to 43: i.e., 29 RRL stars were known from Walker (1998) and another 11 from Downes et al. (2004). We present full light curves of two RRL stars in the FUV and NUV filters, in the upper panel of Figure 4.17. These light curves demonstrate the structure of the variability in the FUV and the NUV. It can be seen that, in the FUV, the RRL stars are almost non-detectable except during the maximum light, whereas in the NUV, there is a measurable flux through the whole cycle. We can also notice that a larger amplitude in the FUV, than that in the NUV. In order to bring out these features of the light curves, we created a 'typical' light curve profile. The 'typical' light curve is a mean of several individual ones created by a) cross correlating the phased plots to match the maxima, and b) taking the mean of the NUV and FUV phase-shifted values in bins of 0.05 phase. This is presented in the lower panel of figure 4.17. The characteristic of the UV light curves is that the maxima are much sharper and the slow decline seen in visible wavelengths is almost disappeared.

Our analysis of the HB population suggests that there could be RRL stars belonging to the RHB as well as the BHB stars. As noted above, our results suggest that there is an age and/or Helium difference between the BHB and the RHB. Our model HB population shows the presence of two Y_{ini} population in the region of the RRL stars. Therefore, our analysis supports a difference in age or/and Y_{ini} as the possible reason for the RRL properties in the cluster, and perhaps the Oosterhoff dichotomy.

4.7 Discussion

In this study, we have presented the FUV and NUV CMDs which are obtained from the UVIT on ASTROSAT. Our study has added three RRL like stars to the previous catalog of 40 variables.

As it is difficult to identify evolutionary sequences in the UV CMDs, we used the HST-ACS data to cross match and identify them. We detect mostly HB stars and a few BSSs. We divided the detected HB into the RHB, V-BHB and H-BHB stars. We also detect a few blue hook stars in this cluster, appearing at the end of the vertical extension of the HB and the temperature is estimated to be $\sim$ 12,000K.

NGC 1851 is one of the many GCs now known to host multiple stellar populations. Evidence in this particular cluster comes primarily from the detection of two SGB sequences in the HST data (Milone et al. 2008; Piotto et al. 2012). Spectroscopic studies performed on RGB (Carretta et al. 2011) and HB stars (Gratton et al. 2012) support the existence of multiple populations. We used a distance modulus of 15.52 mag (Cassisi et al. 2008). As the reddening is minimal towards this cluster (Harris 1996), we have not incorporated reddening correction. The fit between the observed data and the models do have a slight dependency on these parameters. We identify and locate the full stretch of the HB stars in the UV CMDs, in the inner 4.0$'$ diameter of the cluster. BaSTI models suggest that the HB populations in NGC 1851 may have an age difference of $\sim$ 2 Gyr, for a constant metallicity of [Fe/H] $\sim$ -1.0 dex and Y_{ini} $\sim$ 0.25. We are able to characterise two HB populations using the Y^2 models, and the generated synthetic HB. The best fits were obtained for an age range of $\sim$ 12 Gyr, with a more or less similar [Fe/H] of $\sim$ -1.3 - -1.2 and for two value of Y_{ini}, $\sim$ 0.23 and 0.28. The take away point is that both the models do not support the presence of super Helium rich stars in the HB. There could be a moderate age difference ($\sim$ up to 2 Gyr) or a moderate helium enrichment ($\sim$ up to 0.05 dex) among the HB stars. This is the first time,

the HB parameters are estimated for this cluster from UV observations. These are in agreement with those estimated from optical studies. Our observations are not deep enough to detect the sub-giant branch, which could have added more constraints on the estimated parameters.

The RHB and BHB stars, which were found to have a marginal difference in their radial distribution, were found to have a non-uniform azimuthal distribution outside the cluster's central 10″. The uncorrelated and individually non-uniform distribution of the BHB and RHB stars suggest that these two populations are not very well mixed. This could provide support for the hypothesis that this cluster is a merger remnant. We note that if the merger is recent, the populations could still remain not well mixed. The merging between the two progenitor clusters could have occurred recently, as the relaxation time at the half mass radius is about 0.3 Gyr (Harris 1996), whereas the full cluster relaxation takes about 2-3 relaxation times (Carretta et al. 2011).

Since UVIT is operated in the photon counting mode, we were able to detect variability of known RRL stars in both the FUV and NUV bands. We are able to create typical light curve in FUV and NUV wavelengths. These observations confirm the large amplitude variations of RRL stars previously seen in UV passbands, when compared to the optical. We find that the detected RRL stars may belong to the RHB or the BHB. As mentioned earlier, RRL stars in this cluster are known to belong to Oo I, with properties similar to Oo II. As we find that age and helium abundance to be the main difference among the HB stars in this cluster, then it is likely that the differences among the RRL stars and the Oosterhoff classification may be due to these two parameters.

4.8 Summary

The results obtained from our UV study on GC NGC 1851 is summarised below:

1. We have detected the full HB extent, including the blue hook stars and RRL stars. We have identified 3 new RRL like variable in the cluster, which raises the number of RRL like stars to 43. The simultaneous observation of the FUV and NUV channels in the photon counting mode helped in the identification of RRL stars in the FUV and the NUV bands.

2. We used the Padova and BaSTI isochrones to compare the observed HB. The BaSTI models suggest two populations among the HB stars, which are likely to have similar metallicity ([Fe/H] ~ -1.0) and He abundance, but with two different ages (10 and 12 Gyr).

3. The Y^2 models and the generated synthetic HB suggest one population with an age of 12 Gyr, Y_{ini} =0.23 , and [Fe/H] ~ -1.3 and another population of same age (12 Gyr), a similar Fe/H] ~ -1.2, but with enhanced $Y_{ini} = 0.28$.

4. The distribution of BHB and the RHB stars were found to suggest that the populations are not well mixed, which could lend support to the idea that NGC 1851 is probably a recent merger remnant.

Chapter 5

UVIT-HST-Gaia View of NGC 288: Horizontal branch Morphology[†]

5.1 Introduction

NGC 288 is a low density GC ($\rho_c \sim 60.25\ L_\odot/pc^3$, McLaughlin & van der Marel (2005b)) located in the Constellation Sculptor. It is of intermediate metallicity with [Fe/H] = -1.3 (Carretta et al. 2009). NGC 288 is known to be located close to the South Galactic Pole, with a retrograde orbit (Dinescu et al. 1997) and an evolution strongly driven by the galactic tidal field (Leon et al. 2000). The parameters of NGC 288 used for analysis are given in Table 5.1.

Historically, NGC 288 is considered as a peculiar GC, with the presence of a purely

[†]Results of this chapter are published in Sahu et al. (2019a)

blue Horizontal Branch (HB) stars, coupled with a relatively high metallicity (Cannon 1974; Buonanno et al. 1984). The peculiarities found in the HB morphology are well known, one of which being the second parameter problem (Sandage & Wallerstein 1960; Sandage & Wildey 1967; van den Bergh 1993), which refers to the observation that parameters other than metallicity, such as age and/or He abundance, affects the colour distribution of HB stars. NGC 288 and NGC 362 form one of the best known "second-parameter pair" of GCs (Catelan et al. 2001; Bellazzini et al. 2001), where NGC 362 presenting a very red HB, a complete opposite of the blue HB of NGC 288, given that these clusters have similar chemical compositions. Catelan et al. (2001) found that when the overall HB morphology of the two clusters can be reproduced with an age difference of 2 Gyr, the details are not fitted easily.

The BHB stars hotter than the G-jump exhibit metal abundances enhanced via radiative levitation and He abundances diminished via gravitational settling (Moehler et al. 1999, 2000; Behr 2003; Pace et al. 2006) as described in Chapter 1. Khalack et al. (2010) found observational evidence for vertical stratification of iron, which supports the efficiency of atomic diffusion among the hotter BHB stars, which include three BHB stars in NGC 288. Moehler et al. (2014) also found evidence for the presence of diffusion among the BHB stars hotter than $T_{eff} \sim 11{,}500$ K.

In this chapter, we present the results of a UVIT imaging study of the GC NGC 288 using three filters (F148W, F169M and N279N) of UVIT. This chapter mainly focuses on the following aspect of the cluster: (a) study the HB morphology of the cluster in UV, (b) study the temperature distribution of the BHB and EHB stars, (c) study the gaps/discontinuities found in the BHB distribution in UV CMDs. To achieve the above aims, we combine the UVIT data of the cluster with HST-ACS data (Sarajedini et al. 2007) and ground data. We use the PMs data available from Gaia DR2 (Gaia Collaboration et al. 2018c) to select the cluster members detected by UVIT.

TABLE 5.1: Parameters of NGC 288 used for analysis.

Parameter	Value	Reference
R.A. (J2000)	$00^h52^m45.24^s$,	Goldsbury et al. (2010)
Dec (J2000)	$-26°34'57.4''$	Goldsbury et al. (2010)
$[Fe/H]$	-1.3 dex	Carretta et al. (2009)
E(B−V)	0.03	Harris (2010)
Distance	8.8 Kpc	Paust et al. (2010)
Core radius, r_c	$1.35'$	McLaughlin & van der Marel (2005b)
Half-light radius, r_h	$2.23'$	McLaughlin & van der Marel (2005b)
μ_{RA}	4.2385 ± 0.0035 mas yr^{-1}	Gaia Collaboration et al. (2018b)
μ_{Dec}	-5.6470 ± 0.0026 mas yr^{-1}	Gaia Collaboration et al. (2018b)

5.2 Data and Analysis

We obtained the observations of the cluster in four filters (2 FUV and 1 NUV) of UVIT. The observation details of the cluster are given in Chapter 2. We used CCDLAB to generate the images of the cluster in the different filters. The UVIT image of the cluster is shown in Figure 5.1 where blue and yellow corresponds to detections in F148W and N279N filters of UVIT respectively. We can notice that the cluster centre is completely resolved in both NUV and FUV.

We extracted the magnitudes of the sources detected in different UVIT filters by performing PSF photometry on the images as described in Chapter 3. The FWHM of the PSF is around $1.5''$, $1.6''$ and $1.2''$ in F148W, F169M and N279N filters respectively. The magnitude versus fit errors plot for all the filters are shown in Figure 5.3.

We also performed the PSF photometry on the GALEX FUV and NUV intensity maps of the cluster to obtain the magnitudes of the sources. The GALEX image of the cluster is shown in the left panel of Figure 5.2.

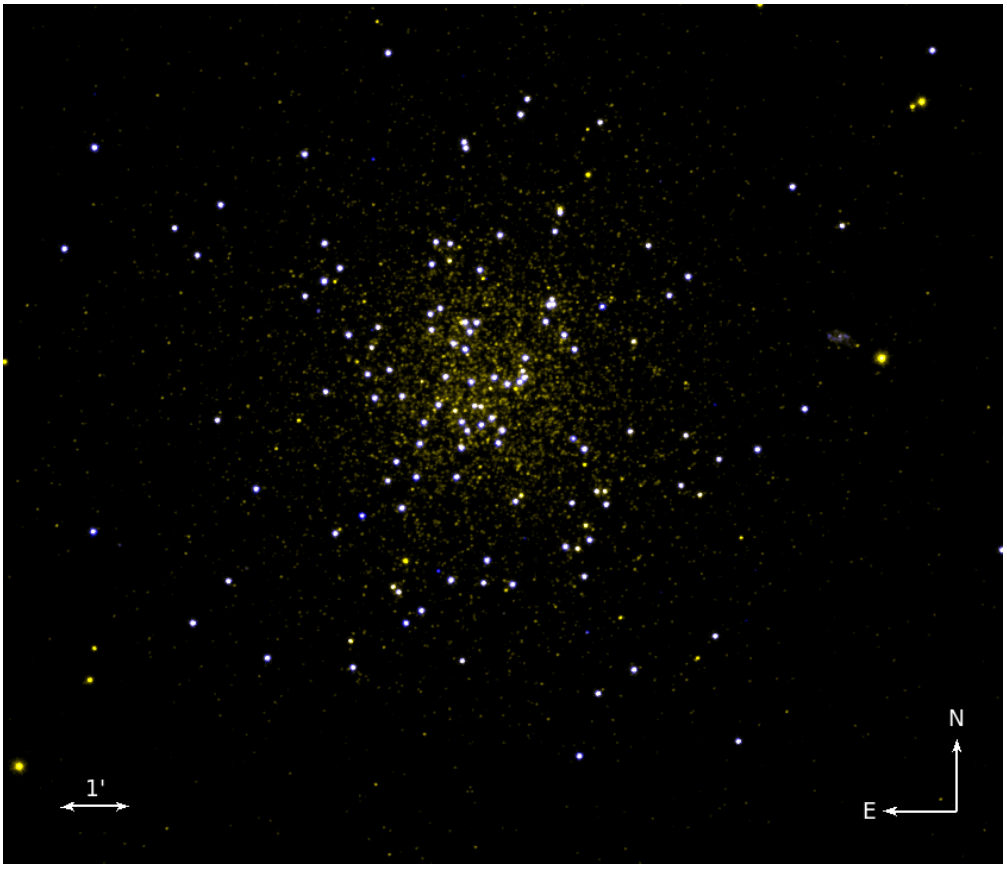

FIGURE 5.1: UVIT image of the GC NGC 288 where blue corresponds to the FUV detections and yellow corresponds to the NUV detections acquired with F148W and N279N filters of UVIT respectively.

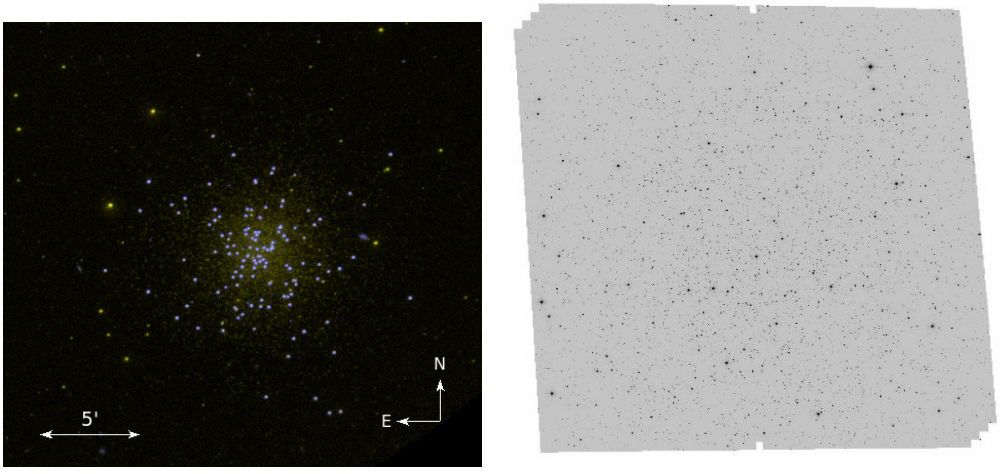

FIGURE 5.2: *Left:* GALEX image of NGC 288 where blue and yellow corresponds to the detections in FUV and NUV filters of GALEX respectively. *Right*: HST image of NGC 288 obtained with F606W filter of ACS/WFC camera under HST/ACS GC Treasury Program (Sarajedini et al. 2007).

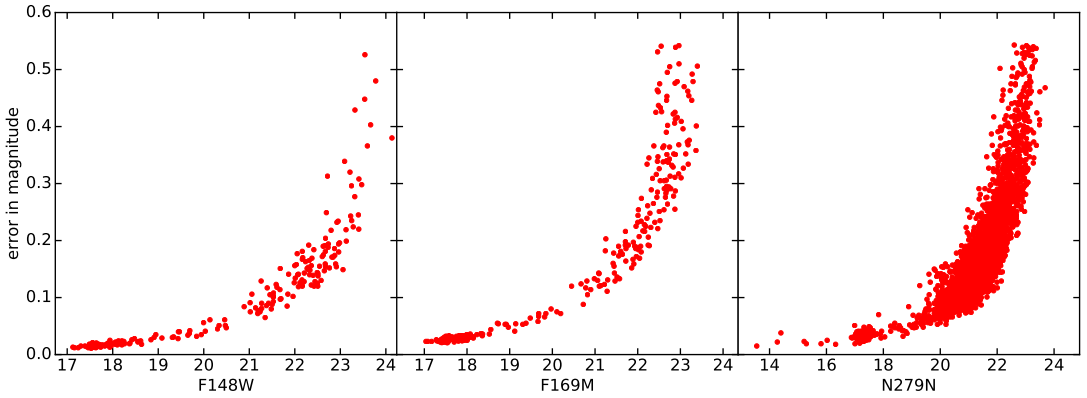

FIGURE 5.3: Errors as a function of magnitude obtained from PSF photometry in F148W, F169M and N279N filters (from left to right) of UVIT respectively.

5.3 UV and Optical Colour-Magnitude Diagrams

In order to identify the stellar populations detected with UVIT in different wavebands, we used the data from the HST-ACS Survey of GCs (Sarajedini et al. 2007) and ground (Peter Stetson in private comm.). The HST-ACS image of the cluster is shown in right panel of Figure 5.2. We used Vg and Ig magnitudes given in the HST-ACS catalogue which are calibrated to ground photometry (Sirianni et al. 2005). The ground data contains U, B, V, R and I magnitudes. We merged both the HST-ACS data and the ground data in such a way that it covers the full cluster region ($\sim 10'$ in radius from the cluster centre). Because the UVIT images have resolved the centre of the cluster, we detected all the HB and EHB stars in the cluster within $10'$ radius, in the FUV and NUV filters. Thus, this chapter presents the identification and analysis of the complete HB sample in this cluster.

The CMDs obtained after cross-matching the data in different filters of UVIT are shown in Figures 5.4-5.8, where the filled symbols are the UVIT cross-matched HST detections and the open symbols are the UVIT cross-matched ground detections. The observed magnitudes and colours are corrected for extinction and

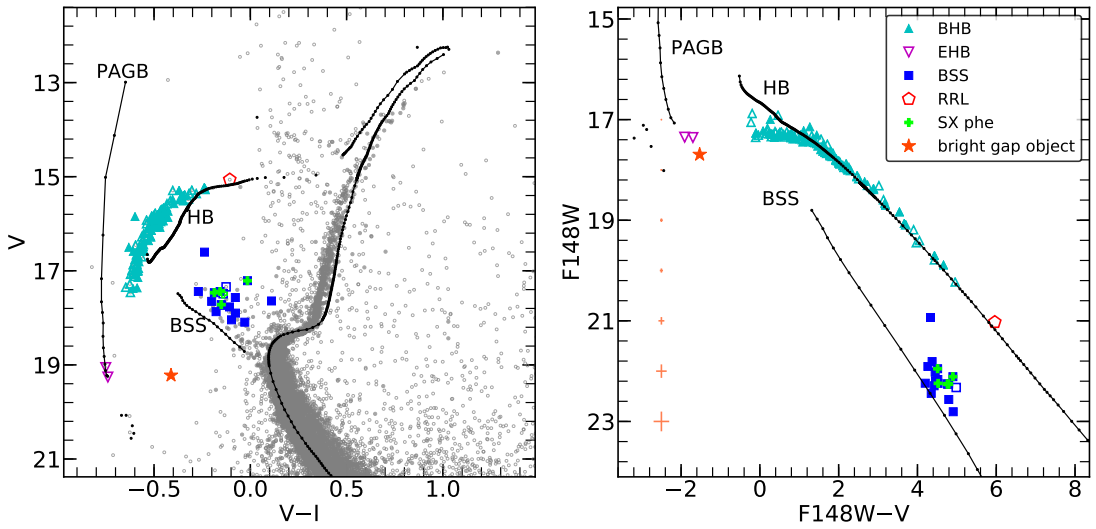

FIGURE 5.4: F148W−V vs F148W CMD (right panel) CMD along with the corresponding optical CMD (left panel). The photometric errors in the colour at different magnitude are shown as light red horizontal lines in the right panel. The filled symbols are UVIT cross-matched HST detections and open symbols are UVIT cross-matched ground detections in both the panels. The Figures are over plotted with a BaSTI isochrone (black line and dots) of age 12.6 Gyr (Wagner-Kaiser et al. 2017), [Fe/H] = −1.28 (Carretta et al. 2009) and distance modulus = 14.84 (Bellazzini et al. 2001). The various stellar populations marked in the legend are BHB - Blue Horizontal Branch (cyan triangle), EHB - Extreme Horizontal Branch (magenta triangle), BSS - Blue Straggler Star (blue squares), RRL - RR Lyrae (red pentagon) and SX Phe - SX Phoenicis (green plus) variables.

reddening considering the value given in Table 5.1. In each figure, we have identified various stellar populations based on their position in the UV CMDs and verified by plotting them in the optical CMDs which are described in the following subsections. The identified populations are shown with same symbols in Figures 5.4-5.8. We have detected BHB, EHB and BSS population in the FUV CMDs which are marked and shown in Figures 5.4-5.7. The N279N−V versus N279N CMD is shown in Figure 5.8, where in addition to the BHB, EHB and BSS population, we have also detected the MS and the RGB stars. These populations are not hot enough to emit in FUV, hence are not detected in the FUV CMDs.

The CMDs are over-plotted with a BaSTI isochrone (Pietrinferni et al. 2004) of

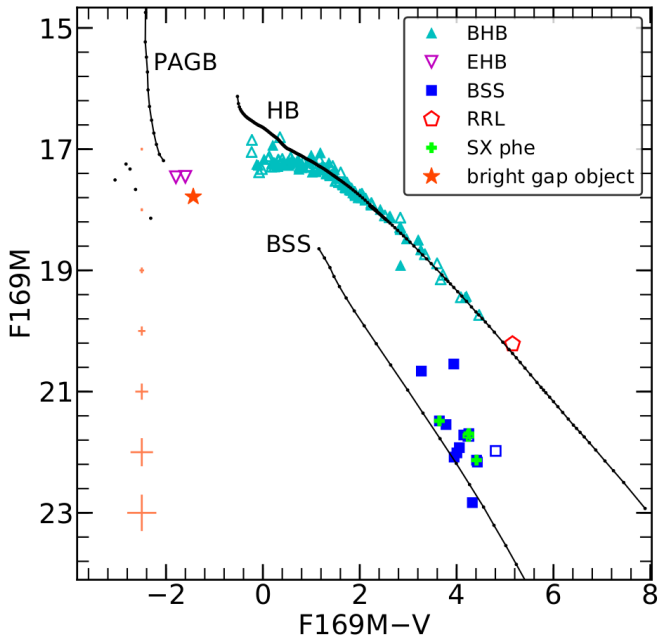

FIGURE 5.5: F169M−V vs F169M CMD. See Figure 5.4 for details.

12.6 Gyr (Wagner-Kaiser et al. 2017) and [Fe/H] = −1.28 (Carretta et al. 2009) adopting a distance modulus of 14.84 (Bellazzini et al. 2001) generated using FSPS.

Blue Horizontal Branch (BHB)

The HB population shown in FUV CMDs in Figures 5.4-5.7 (cyan triangles) mainly consists of BHB stars. In total, we detected 119 BHB sources in the FUV filters of UVIT and 124 BHB sources in the N279N filter of UVIT with 43 of them falling under the FOV of HST-ACS. The BHBs form a diagonal sequence that spans about 3-5 mag in colour in the UV CMDs (Figure 5.4, 5.5 and 5.7) thus, lifting the degeneracy in the V−I colour of the BHB stars in the optical CMD (left panel of Figure 5.4). The BHB distribution in the FUV vs V CMDs (Figure 5.4 and 5.5) fits well with the isochrone till F148W $\sim$ 17.4, F148W−V $\sim$ 1.2 and F169M $\sim$ 17.3, F169M−V $\sim$ 1.2. We note that, stars bluer than FUV−V $\sim$ 1.2 form a horizontal sequence to appear like a plateau in the FUV magnitude. This plateau

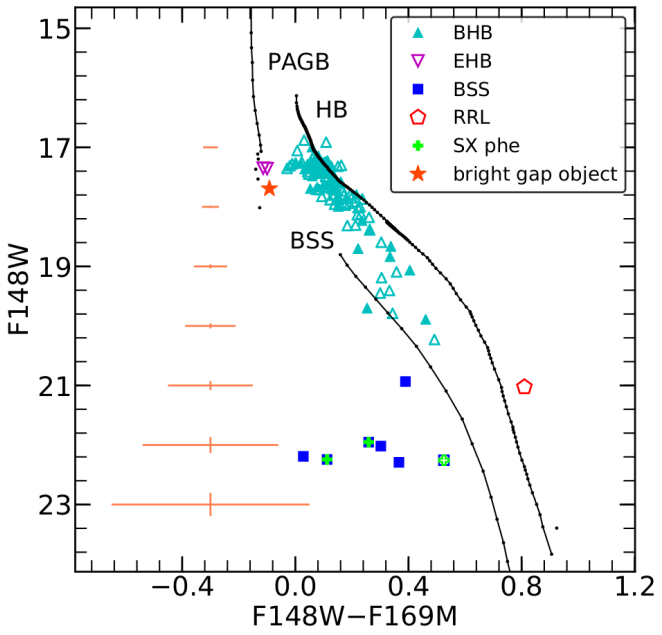

FIGURE 5.6: F148W−F169M vs F148W CMD. See Figure 5.4 for details.

is apparent as the BHB stars are ~ 0.3 mag fainter than the isochrone. This could be attributed to the onset of diffusion which is discussed in Section 5.4.5. We detected 4 BHBs in F148W−V vs F148W CMD with F148W−V < 0.5 which are brighter in F148W magnitude than the rest of the BHB stars. These are classified as AGBM stars by Schiavon et al. (2012).

Moving to the FUV CMD which is shown in Figure 5.6, the BHB stars with F148W > 18.5 show a maximum shift of ~ 0.3 mag in F148W−F169M colour from the model isochrone which are within the 3σ photometric errors. We find a gap in the distribution of BHB stars at F148W ~ 17.5 and F148W−F169M ~ 0.08 where, the stars brighter than this magnitude are all bunched together into a group.

The FUV−NUV vs FUV CMDs are shown in Figure 5.7. Here, we detect a plateau among the BHB stars at F148W > 17.5, F148W−N279N ~ 0.3 (upper panel) and F169M > 17.4, F169M−N279N ~ 0.3 (lower panel), where the stars bluer than this location deviate from the normal BHB diagonal sequence similar to the FUV

vs V CMDs (Figure 5.4 and 5.5). In addition to this, we also notice that the BHBs fainter than the above mentioned FUV magnitude and colour, deviate from the model isochrone as compared to the FUV vs V CMDs, where they were in good agreement with the isochrone. As N279N is a narrow band filter centred around Mg II (2808 Å), it captures the Mg abundance variations within the BHB stars. Moehler et al. (2014) derived the Mg abundances of 51 BHB stars in NGC 288 based on the observations obtained from the medium resolution FLAMES-GIRAFFE spectrograph. A closer look and comparison of the UVIT observations with their spectroscopic observations reveal that the redder BHB stars have a higher Mg abundance as compared to the bluer BHB stars. The N279N mag of the BHB stars are fainter than the isochrone which we notice in the NUV vs V CMD (right panel of Figure 5.8). Thus, the mismatch between the observed BHB distribution and the isochrone could be due to the difference between the assumed Mg abundance of the model with the observed abundance. The temperature distribution and identification of the gaps in the BHB distribution are described in Section 5.4.

RR Lyrae Variables

Kaluzny (1996) and Arellano Ferro et al. (2013) found 2 RRL variables based on the V band light curves obtained from the ground-based observations and derived their properties. We detected these two RRL variables in the N279N filter of UVIT and only one RRL in the FUV filters of UVIT, whose locations in the optical and UV CMDs are shown in Figures 5.4-5.8 as red pentagons. As expected, the RRL variables are located at the red end of the BHB distribution in all the UV CMDs. The FUV bright RRL is of RRc type with a shorter period as compared to the NUV bright RRL of RRab type (Arellano Ferro et al. 2013).

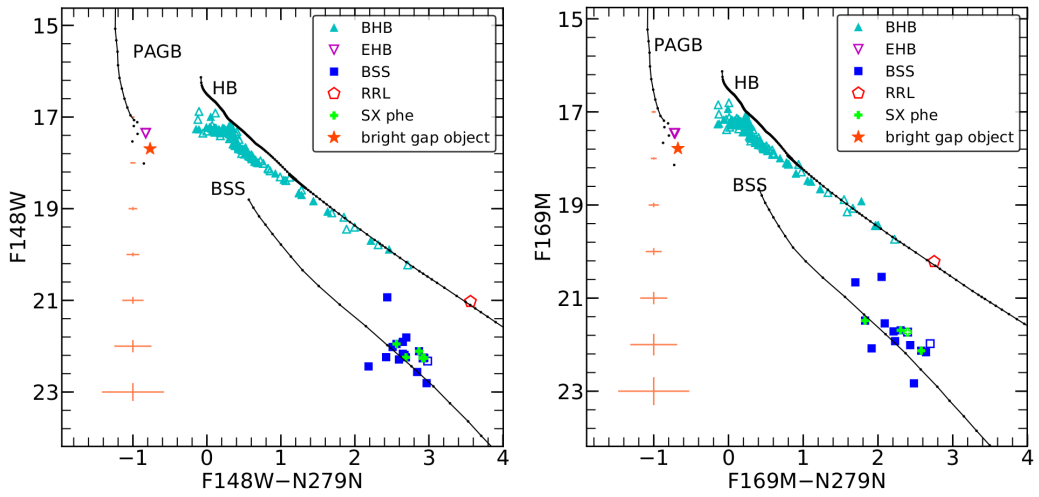

FIGURE 5.7: F148W−N279N vs F148W CMD (left panel) and F169M−N279N CMD vs F169M CMD (right panel). See Figure 5.4 for details.

Extreme Horizontal Branch (EHB)

Kaluzny (1996) reported the presence of three likely hot sub-dwarfs located in the extension of BHB in the optical CMD of NGC 288. In Figure 3 of Dalessandro et al. (2011) where they have shown the location of different HB stars in the FUV CMD of NGC 2808, we can clearly notice a large population of EHB stars bluer than the BHB stars. Considering the definition adopted by Dalessandro et al. (2011), and keeping the HB and PAGB BaSTI model isochrone as the reference for the selection of EHB stars in the UV CMD, we found 2 potential EHB candidates which are shown in Figures 5.4-5.8 (open magenta triangles). These stars are located in the expected EHB region in both the optical and UV CMDs having similar FUV magnitude as the BHB stars. GALEX has also detected these stars which are located in the blue extension of BHB in the FUV−NUV vs FUV CMD of NGC 288 (Schiavon et al. 2012). These EHB candidates are two of the three sub-dwarfs as reported by Kaluzny (1996). The SEDs of the EHB candidates are discussed in Section 5.5.

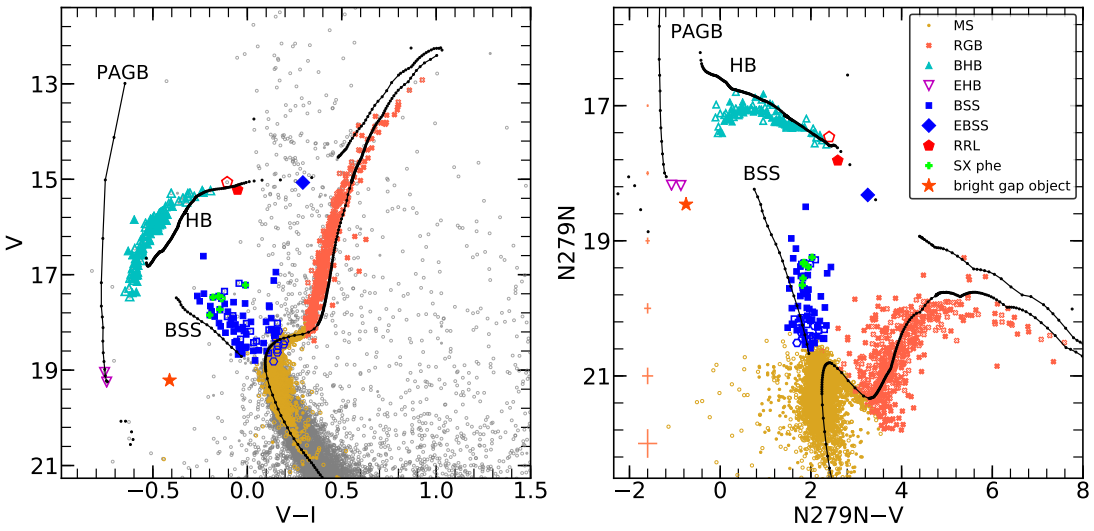

FIGURE 5.8: N279N−V vs N279N CMD (right panel) and corresponding optical CMD (left panel). In addition to the detection of other stellar populations, we also detect main sequence marked as MS (yellow dots) and red giant branch marked as RGB (red cross) in the N279N filter of UVIT. See Figure 5.4 for more details.

Gap Objects

We found one bright gap object which is marked as orange star in Figures 5.4-5.8. This object which is located in the gap region in optical CMD becomes very bright in UV CMDs with its location being close to that of EHB stars. In the UV CMDs, it is fainter by $\sim$ 0.35 mag with a similar colour as compared to the EHB stars. We checked for its variability with the known catalogue of X-ray sources and CVs in this cluster available from the previous study by Kong et al. (2006), but we did not found any match for this object. The SED of this object is described in Section 5.5.

Main Sequence and Red Giant Branch

The MS extends ~ 2.0 mag below the turn-off till ~ 22 mag in N279N (yellow dots in Figure 5.8) with a width of ~ 1 mag. We see a large scatter in the MS in NUV CMD for stars with N279N > 21, partially due to photometric errors. The SGB is narrow as compared to the RGB and MS for the same photometric errors in N279N mag. The BaSTI isochrone shown in Figure 5.8 visually fits well with the observed MS, SGB and RGB distribution. A number of faint sources are detected bluer than the MS, which could be gap objects or MS stars with NUV excess.

Blue Straggler Stars (BSSs)

We present the UV CMDs of the BSSs covering the entire cluster region in this study. We detected 17 BSS candidates in F148W filter and 14 BSS candidates in F169M filter of UVIT whose location in the FUV CMDs are shown in Figures 5.4-5.7. The BSSs stretch ~ 2 mag in the FUV CMDs. In Figure 5.6, we see a spread of ~ 0.5 mag in F148W$-$F169M colour with F148W magnitude being similar for all 6 BSSs. This spread is within the photometric errors.

We detected 78 BSS candidates in N279N$-$V vs N279N CMD marked as blue squares in Figure 5.8 (right panel) among which 7 of them are new candidates (marked as blue hexagons). These 7 new BSS candidates are located in the BSS region in the NUV CMD (marked as blue stars) whereas, they are near the MSTO in the optical CMD. Based on the HST-UV observations, Raso et al. (2017) showed that the NUV CMDs are more suitable for the identification of BSS candidates as compared to the optical CMDs where the faint BSSs remain hidden near the MSTO. We notice that BSSs have similar magnitude and colour range in optical and NUV CMDs. We also detected a star located in the region of RHB stars which

is shown as blue diamond in Figure 5.8. Bellazzini et al. (2002) also found this object to be located in the RHB region and classified it as an EBSS. The EBSS is not detected in the FUV filters of UVIT. The parameters of the BSS derived from the photometry and SEDs are described in next chapter.

SX Phoenicis Variables (SX Phes)

Kaluzny (1996) first detected 4 SX Phe variables in NGC 288 and calculated their periods. Later in 1997, Kaluzny et al. (1997) found two more SX Phe variables leading to 6 SX Phe Variables known in this cluster. Arellano Ferro et al. (2013) generated the light curves of these 6 SX Phe variables and confirmed their variability. Later in 2015, Martinazzi et al. (2015) found 2 new SX Phe variables (V11 and V12) thus, leading to a total of 8 known SX Phe variables in the cluster. We cross-matched UVIT data with the coordinates of the known SX Phe variables to obtain their UV magnitudes in three different filters of UVIT. We detected 5 of them in F148W, 4 in F169M and 6 in N279N filters of UVIT which are shown as green plus symbols in Figures 5.4-5.8. The three SX Phe variables, V8, V11, and V12 also show a spread in F148W−F169M colour like BSSs (Figure 5.6) but are within the photometric errors. In N279N−V vs N279N CMD (right panel of Figure 5.8) we see that the variables stand out clearly from the MSTO stars as compared to the optical CMD. The variables are located in the region of BSSs with N279N < 20 that spans ~ 0.4 mag in N279N and ~ 0.2 mag in N279N−V colour.

5.3.1 Cluster membership from Gaia DR2

The UVIT data was cross-matched with Gaia DR2 to select the UV bright cluster members. The final sample of members comprises of 110 BHB stars detected

TABLE 5.2: A sample catalogue (3 BHBs) of the UV detected possible member stars (Gaia Collaboration et al. 2018c) is presented here. The full catalogue is available in electronic format. Column 1 corresponds to our Star ID, columns 2 & 3 list the RA and Dec of the stars, columns 4 to 9 give the UVIT magnitudes and errors in F148W, F169M and N279N filters respectively, columns 10 and 11 give the optical magnitude and colour corresponding to V and (V−I) from the HST-ACS (Sarajedini et al. 2007) and ground data (Peter Stetson, private comm.) as mentioned in column 12, column 13 gives the radial distance from the cluster centre (r) and columns 14 to 17 give the PMs in RA ($\mu_\alpha cos\delta$) and Dec (μ_δ) with corresponding errors available from Gaia DR2 (Gaia Collaboration et al. 2018c). Note that the magnitudes and colours (AB system) are not corrected for extinction and reddening respectively.

Star ID	RA (J2000)	Dec (J2000)	F148W	err1	F169M	err2	N279N	err3	V
	[h m s]	[^{o} $'$ $''$]	[mag]	[mag]	[mag]	[mag]	[mag]	[mag]	[mag]
V−I	Optical data	r	pmra	pmra_err	pmdec	pmdec_err			
[mag]		[$'$]	[mas/yr]	[mas/yr]	[mas/yr]	[mas/yr]			
BHB1	00 52 48.31	-26 32 58.21	17.880	0.019	17.768	0.026	17.414	0.028	15.935
-0.552	HST	2.43	4.391	0.106	-5.440	0.078			
BHB2	00 52 48.59	-26 33 17.74	17.532	0.017	17.472	0.025	17.380	0.038	17.149
-0.552	HST	2.11	4.366	0.272	-5.572	0.149			
BHB3	00 52 45.47	-26 33 22.72	17.558	0.015	17.418	0.023	17.285	0.028	16.677
-0.561	HST	2.06	4.850	0.184	-6.328	0.156			

in FUV filters and 115 in NUV filter. We have excluded 9 BHB stars that are non-members that are located within the radius $r \sim 2.5'$ from the cluster centre. Similarly, we are left with 15 FUV detected BSSs and 68 NUV detected BSSs which are cluster members. We excluded 10 BSSs that are located at a radius beyond $2'$ from the cluster centre as they were found to be non-members. Out of 68 BSSs, there are 12 BSSs which do not have PM data available in the catalogue though these are observed by Gaia. We assumed them to be cluster members as most of them ($\sim$ 75%) lie inside the half-light radius of the cluster i.e. in the crowded regions. The typical uncertainties in the PMs for BHBs and BSSs are $\sim$ 0.16 and 0.21 mas/yr respectively. The 2 EHBs and the bright gap object are also possible cluster members but have larger PM errors ($\sim$ 0.7-1 mas/yr) as compared to the BHBs and BSSs. The vector-point diagram of BHBs (cyan upper triangles), EHBs (magenta lower triangles) and BSSs (blue squares) relative to other cluster members (grey dots) in the PM catalog is shown in Figure 5.9 where

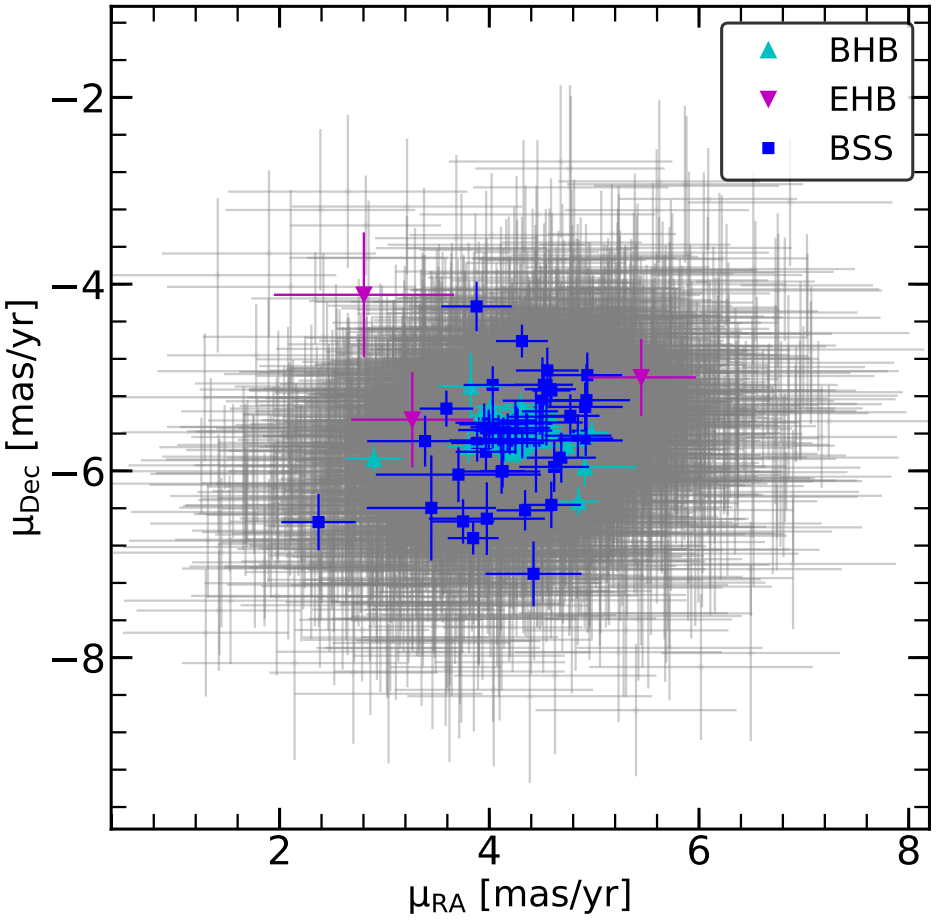

FIGURE 5.9: Vector-point diagram of the BHBs, EHBs and BSSs detected by UVIT relative to other cluster members in the catalog given by Gaia Collaboration et al. (2018b).

we clearly notice that the BHBs are grouped around the mean PM derived by Gaia Collaboration et al. (2018b) whereas the EHBs have large PM errors. A sample catalogue of UVIT detected members along with the PMs from Gaia DR2 is given in Table 5.2. The rest of the analysis is based on this sample.

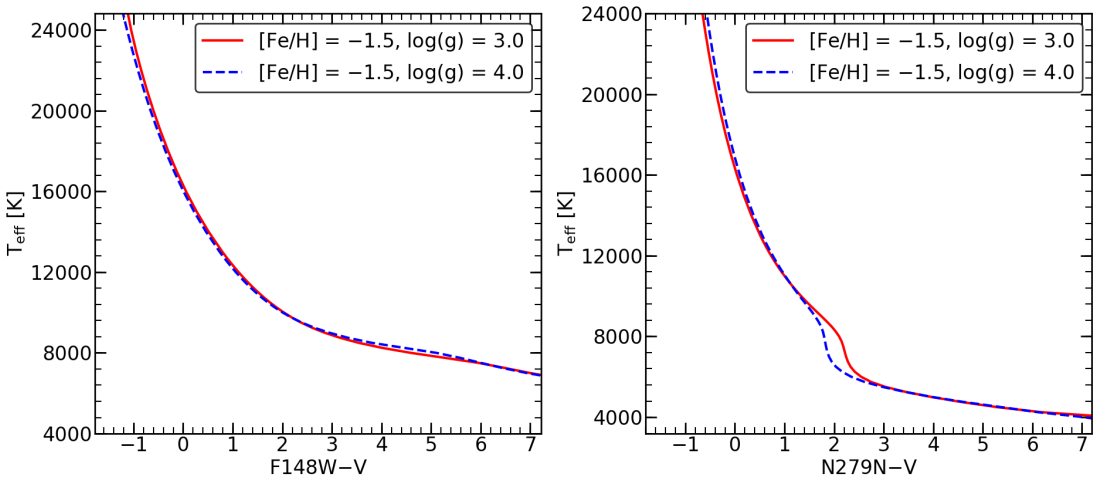

FIGURE 5.10: Variation of temperature (T_{eff}) with theoretical colours F148W−V (left) and N279N−V (right) generated by convolving UVIT filter effective area curves with Kurucz stellar atmospheric models (Castelli et al. 1997) for an assumed metallicity of [Fe/H] = −1.5 and log g values of 3.0 and 4.0.

5.4 Temperature Distribution of BHB stars

We have determined the temperature of the detected BHB stars using two different methods and compared them with the spectroscopic estimates of Moehler et al. (2014) which are described below:

5.4.1 Temperature from colour - T_{eff} relation

We estimated the temperature of the BHB stars by comparing the dereddened UV colours with the theoretical colours of various temperatures. In order to do so, we convolved Kurucz stellar atmospheric models (Castelli et al. 1997) with the UVIT filter effective area curves, and estimated the theoretical colours for different temperatures for a metallicity [Fe/H]= −1.5 closest to the cluster metallicity (Carretta et al. 2009) and for a primordial helium abundance of Y = 0.248. We selected model spectra within 3.0 ≤ log g ≤ 4.0 and 4,000 K ≤ T_{eff} ≤ 24,000 K

to derive the theoretical UV colours as the temperature of the BHB stars are expected to be within this range. The colour - T_{eff} relation for a log g of 3.0 and 4.0 and for two UVIT filter combinations (F148W−V and N279N−V) are shown in Figure 5.10 in left and right panels respectively. It is clear from this figure that the F148W−V colour is more sensitive to T_{eff} variations as compared to N279N−V. In both the colours, the effect of surface gravity is visible below $\sim$ 8000 K. This is in accord with the study of the HB temperature distribution of M15 by Lagioia et al. (2015), where they found that the HB tracks of different masses show dependency of surface gravity below $\sim$ 8000 K for the NUV−V colour. We also found that the metallicity variations do not significantly affect the colour - T_{eff} relation which is in agreement with Lagioia et al. (2015). Typical photometric errors of the BHB stars in the colour F148W−V and N279N−V are $\sigma \sim 0.02$ and 0.04 which leads to a small error of $\Delta T_{eff} \sim 100$ K and 170 K respectively.

We used the dereddened colours for deriving the T_{eff} of the BHBs by doing a cubic interpolation along the theoretical colour - T_{eff} relation. The BHBs with $T_{eff} <$ 8000 K obtained using the colour - T_{eff} relation were not considered due to the effect of surface gravity as mentioned earlier. The temperature distribution of 109 BHBs obtained from F148W−V - T_{eff} relation (cyan filled histogram) and 103 BHBs obtained from N279N−V - T_{eff} relation (red hatched histogram) are shown in Figure 5.11. We identified peaks in the BHB distribution using dual Gaussian fits. The temperature distribution of the BHBs show a main peak located at $T_{eff} \sim$ 10,300 K and another peak at $\sim$ 14,000 K which extends up to $\sim$ 18,000 K. The cumulative temperature distributions of the BHBs obtained from the two different UVIT colours are shown in Figure 5.13. According to the K-S test, the difference between the distributions of effective temperatures obtained from both the UVIT colours is not significant with a p-value of ~ 0.45.

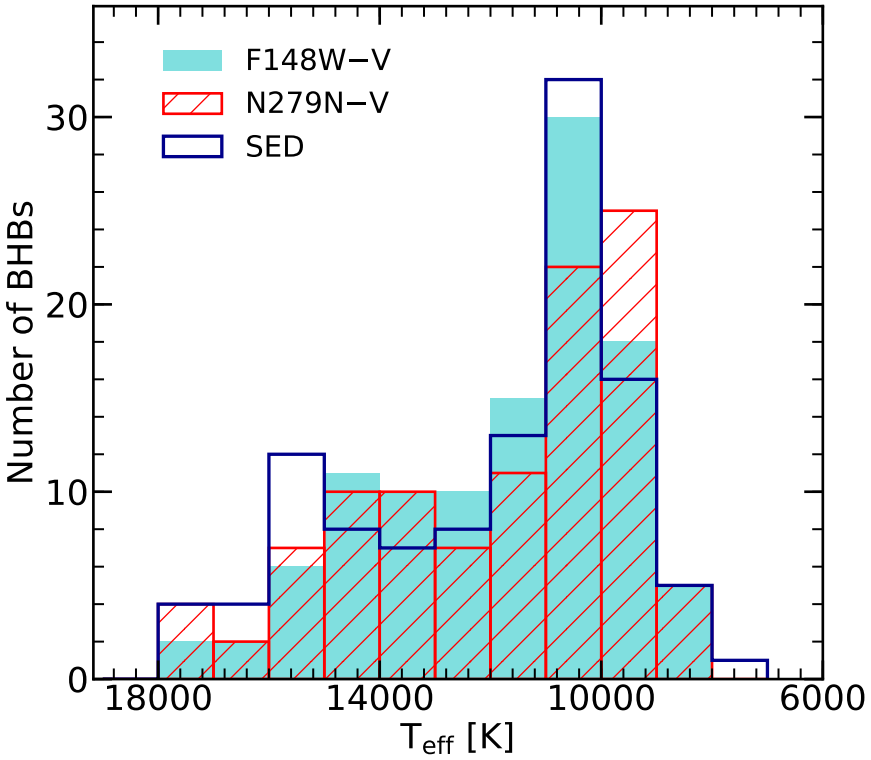

FIGURE 5.11: Temperature distribution of 109, 103 and 110 BHB stars estimated from F148W−V - T_{eff} relation (cyan filled), N279N−V - T_{eff} relation (red hatched) and SED fitting (dark blue step) respectively.

5.4.2 Temperature from SED fitting

We obtained the temperature of 110 BHB stars using the python SED fitter tool (Robitaille et al. 2007). For this, we used Kurucz stellar atmospheric models Castelli et al. (1997) to fit the SEDs of the BHBs stars. The model fluxes are scaled to the observed fluxes by considering a cluster distance of 8.8 Kpc (Paust et al. 2010).The SEDs of 2 BHB stars corresponding to UVIT-HST and UVIT-Ground detections are shown in Figure 5.12 in upper and lower panels respectively. We used the dereddened fluxes obtained from three filters of UVIT (F148W, F169M, N279N), three filters from Ground (B, V, I) to generate the SEDs of 74 BHB stars and three filters of UVIT (F148W, F169M, N279N), two filters of HST (V, I) for the SEDs of 36 BHB stars. The temperature distribution of 110 BHB stars is shown in

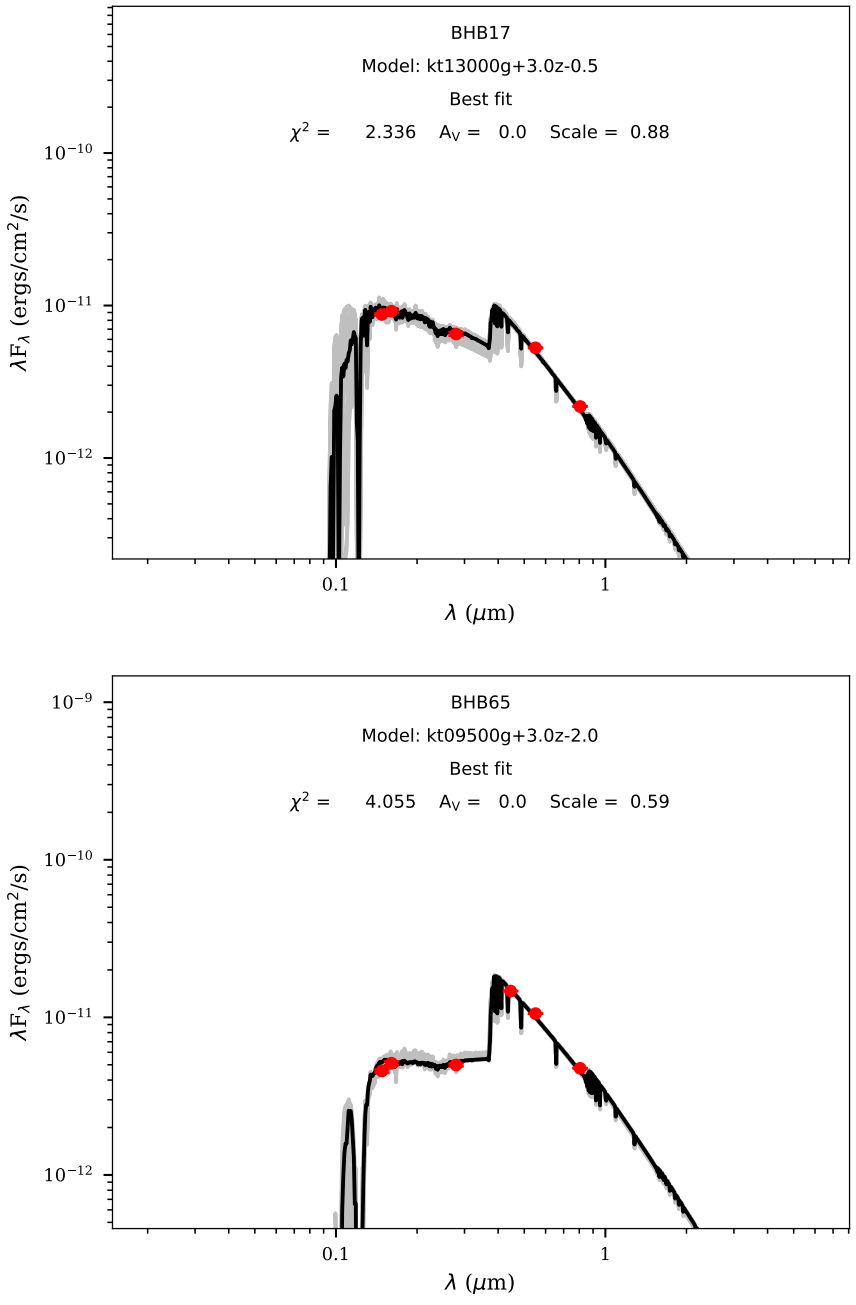

FIGURE 5.12: SEDs of UVIT cross-matched HST and ground detected BHB stars (star id- BHB17 and BHB65) as shown in top and bottom panels respectively.

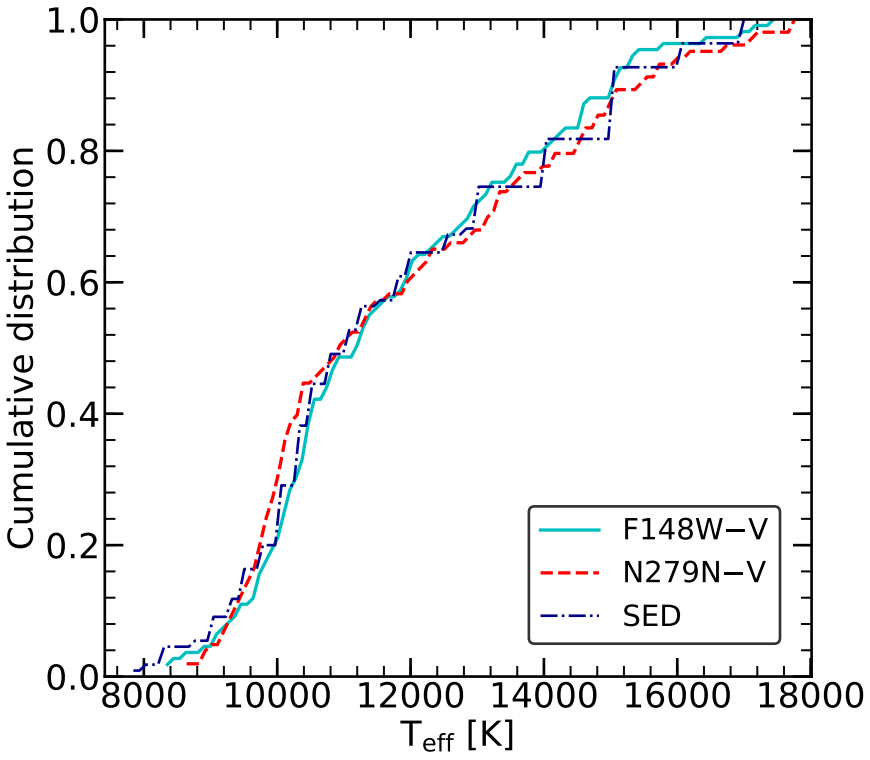

FIGURE 5.13: Cumulative temperature distribution of the BHB stars obtained from F148W−V - T_{eff} (cyan line), N279N−V - T_{eff} (red dashed line) and SED fitting (blue dash dotted line).

Figure 5.11 (blue histogram). We found a main peak located at $T_{eff} \sim$ 10,380 K and another peak at $T_{eff} \sim$ 14,600 K using dual Gaussian fits which are similar to those estimated using colour - T_{eff} relation. The temperature range of the BHBs are also similar in both the cases. According to the K-S test as shown in Figure 5.13, the difference between the distributions of effective temperatures obtained from SEDs and F148W−V and N279N−V colour - T_{eff} relation is not significant with a p-value of $\sim$ 0.65 and 0.55 respectively. This test also suggests that the temperatures of the BHBs estimated using SED fitting are in better agreement with those estimated using F148W−V as compared to N279N−V colour - T_{eff} relation.

TABLE 5.3: Temperature and log g estimates of 110 BHB stars using different methods. Columns 2, 6 and 3, 7 corresponds to the T_{eff} and log g estimates obtained using N279N-V and F148W-V color-T_{eff} relation respectively whereas Columns 4 and 8 corresponds to the estimates obtained from the SED fitting. The typical uncertainties in the T_{eff} measurements are $\sim$ 100 K, 170 K and 250 K for the three methods respectively. The uncertainty in the log g value is around 0.5 dex for all the methods. Columns 5 and 9 corresponds to the values obtained by Moehler et al. (2014) from Spectroscopy.

Star ID	$T_{eff}^{N279N-V}$ [K]	$T_{eff}^{F148W-V}$ [K]	T_{eff}^{SED} [K]	T_{eff}^{Spec} [K]	log $g^{N279N-V}$	log $g^{F148W-V}$	log g^{SED}	log g^{Spec}
BHB1	9894	10397	11250	9756	3.5	3.5	4.5	3.4
BHB2	15548	15246	15000	16869	3.5	3.0	3.0	4.3
BHB3	13161	10809	13000	-	3.5	4.0	5.0	-
BHB4	9980	10312	10250	-	4.0	4.0	3.0	-
BHB5	10648	11151	11000	10343	3.5	3.5	2.5	3.5
BHB6	8889	9216	9000	-	3.5	3.0	2.0	-
BHB7	10312	-	10500	-	4.0	-	4.0	-
BHB8	11970	12030	11750	-	4.0	3.0	5.0	-
BHB9	9814	10322	10000	-	4.0	3.0	3.5	-
BHB10	10724	-	10750	-	3.0	-	4.5	-
BHB11	13296	13131	13000	-	4.0	4.0	5.0	-
BHB12	12799	12658	12500	-	4.0	3.5	4.0	-
BHB13	10809	11126	10750	-	4.0	3.0	5.0	-
BHB14	15045	15146	15000	-	3.5	3.0	5.0	-
BHB15	10146	10523	10250	9811	3.5	3.0	2.5	3.4
BHB16	9719	10121	10000	-	3.0	3.0	2.5	-
BHB17	13286	12910	13000	-	3.5	3.5	3.0	-
BHB18	10322	10824	10500	9917	3.0	3.0	3.0	3.4
BHB19	10146	10523	10250	-	4.0	3.5	3.0	-
BHB20	10271	10643	10500	9761	3.5	4.0	3.0	3.4
BHB21	11025	11427	11000	-	3.5	3.0	4.0	-
BHB22	13638	13538	14000	13314	3.0	3.0	3.5	4.0
BHB23	15171	14643	15000	-	3.5	3.0	3.0	-
BHB24	11472	11628	11500	11587	4.0	3.0	3.0	3.8
BHB25	-	9015	9000	-	-	3.5	2.0	-
BHB26	15045	14955	15000	15416	3.0	4.0	3.0	4.1
BHB27	12030	11970	12000	-	3.0	4.0	3.0	-
BHB28	16116	15950	16000	-	4.0	3.0	2.5	-
BHB29	15286	14668	15000	15433	4.0	3.5	2.5	4.2
BHB30	14543	14241	14000	14433	3.0	3.0	3.0	4.1
BHB31	10824	11327	11000	10553	3.0	3.0	2.5	3.6
BHB32	11729	12231	11750	12287	3.0	3.0	5.0	3.9
BHB33	9151	9643	9500	9290	4.0	3.5	2.5	3.4
BHB34	14789	14543	14000	-	4.0	3.5	5.0	-
BHB35	11276	12633	11250	11436	3.5	4.0	4.0	3.7
BHB36	12965	13161	13000	13280	4.0	3.5	5.0	4.0
BHB37	-	-	10000	-	-	-	3.5	-
BHB38	12734	13035	13000	-	3.0	3.0	3.5	-

TABLE 5.4: Table 5.3 continued.

Star ID	$T_{eff}^{N279N-V}$ [K]	$T_{eff}^{F148W-V}$ [K]	T_{eff}^{SED} [K]	T_{eff}^{Spec} [K]	log $g^{N279N-V}$	log $g^{F148W-V}$	log g^{SED}	log g^{Spec}
BHB39	17759	17136	17000	-	4.0	4.0	3.0	-
BHB40	9894	-	10250	-	3.5	-	3.5	-
BHB41	13412	13437	14000	-	3.5	3.0	2.5	-
BHB42	13337	13236	14000	13072	3.0	3.0	2.5	4.0
BHB43	10899	11276	11250	10390	3.5	3.5	3.5	3.5
BHB44	16352	15422	16000	-	3.0	3.5	2.5	-
BHB45	10422	10899	10750	-	3.0	3.5	3.5	-
BHB46	9216	9317	9250	-	3.0	3.0	3.0	-
BHB47	14342	14643	15000	-	3.0	3.0	3.0	-
BHB48	15707	15294	16000	-	3.5	3.5	3.0	-
BHB49	-	10397	10250	9756	-	3.5	3.5	3.4
BHB50	-	10312	10250	-	-	4.0	3.5	-
BHB51	12281	12332	12500	12402	3.5	3.0	3.0	3.9
BHB52	10020	10523	10250	-	3.0	3.0	3.5	-
BHB53	9643	10146	10000	-	3.5	4.0	3.5	-
BHB54	13161	12658	13000	12904	3.5	3.5	3.0	3.9
BHB55	-	11779	12000	-	-	3.5	3.5	-
BHB56	-	10422	10250	9663	-	3.0	3.5	3.4
BHB57	13940	14166	15000	-	3.0	3.5	3.0	-
BHB58	-	14291	15000	-	-	4.0	2.5	-
BHB59	-	-	10000	9434	-	-	3.0	3.4
BHB60	9151	9769	9500	-	4.0	3.5	3.0	-
BHB61	9141	9392	9250	-	3.5	3.5	3.0	-
BHB62	12156	12156	12500	-	3.5	3.5	3.5	-
BHB63	15045	-	15000	-	3.5	-	3.0	-
BHB64	10312	10774	10750	9797	4.0	3.5	3.5	3.4
BHB65	9292	9677	9500	-	4.0	3.0	3.0	-
BHB66	9819	-	10000	9442	3.0	-	3.0	3.4
BHB67	9392	9719	9750	9226	3.5	3.0	3.0	3.3
BHB68	-	8412	8250	-	-	3.0	3.0	-
BHB69	15548	15447	16000	15124	3.5	3.0	3.0	4.2
BHB70	17683	17432	17000	-	3.5	3.5	3.0	-
BHB71	8985	9417	9250	-	4.0	3.0	3.0	-
BHB72	13663	13940	14000	13780	3.5	3.0	3.0	4.1
BHB73	-	9015	9000	-	-	3.5	3.5	-
BHB74	11402	11528	11750	11440	3.5	3.0	3.0	3.7
BHB75	10322	10724	10500	10048	3.0	3.0	3.0	3.5
BHB76	12407	12633	12750	12356	3.5	3.0	3.0	3.9
BHB77	-	-	9750	9128	-	-	3.5	3.3
BHB78	-	10146	10000	-	-	3.5	3.0	-
BHB79	9618	9920	9750	9214	3.0	3.0	3.5	3.3
BHB80	9417	-	9500	9347	3.0	-	3.5	3.4

TABLE 5.5: Table 5.3 continued.

Star ID	$T_{eff}^{N279N-V}$ [K]	$T_{eff}^{F148W-V}$ [K]	T_{eff}^{SED} [K]	T_{eff}^{Spec} [K]	log $g^{N279N-V}$	log $g^{F148W-V}$	log g^{SED}	log g^{Spec}
BHB81	-	10020	10000	9470	-	3.5	3.0	3.4
BHB82	10146	10623	10500	9805	4.0	3.0	3.5	3.4
BHB83	-	-	8250	-	-	-	1.0	-
BHB84	-	-	7750	-	-	-	3.0	-
BHB85	14442	14141	15000	14333	3.0	3.0	3.0	4.0
BHB86	11276	11905	11750	-	3.5	3.5	3.0	-
BHB87	10523	10925	11000	11421	3.0	3.0	3.0	3.8
BHB88	11528	11930	12000	12259	3.0	3.0	3.0	3.9
BHB89	-	8211	8250	-	-	3.0	1.0	-
BHB90	14166	13739	14000	13831	3.5	3.0	3.0	4.0
BHB91	-	8889	8750	-	-	3.5	3.0	-
BHB92	9482	9814	9750	9277	4.0	4.0	3.5	3.3
BHB93	11141	11427	11250	11612	4.0	3.0	3.5	3.8
BHB94	9648	9980	10000	9341	4.0	4.0	3.5	3.3
BHB95	16116	14789	15000	15190	4.0	4.0	3.0	4.1
BHB96	17181	16955	17000	16417	3.5	3.0	3.0	4.4
BHB97	13035	12784	13000	12922	3.0	3.5	3.5	3.9
BHB98	-	8136	8000	-	-	3.5	3.5	-
BHB99	9980	-	10500	9577	4.0	-	3.0	3.3
BHB100	9015	9141	9000	-	3.0	3.5	3.0	-
BHB101	11930	12131	12000	-	3.0	3.0	3.5	-
BHB102	-	9618	9500	-	-	3.0	3.0	-
BHB103	10146	10523	10500	9850	3.5	3.5	3.0	3.3
BHB104	10020	10322	10250	9741	3.5	3.0	3.5	3.4
BHB105	13789	13462	14000	-	3.5	4.0	3.0	-
BHB106	-	10121	10000	-	-	3.0	3.0	-
BHB107	14241	14126	15000	-	3.0	4.0	3.0	-
BHB108	17276	16427	17000	-	4.0	3.5	3.5	-
BHB109	9769	-	10250	-	3.5	-	3.5	-
BHB110	10121	-	10750	-	3.0	-	3.5	-

5.4.3 Comparison with Spectroscopic data

As described earlier in Section 5.3, Moehler et al. (2014) catalogue consists of T_{eff} (> 9000 K) and log g for 51 BHB stars based on spectroscopy. We used the spectroscopic temperature estimates of BHBs to validate with our temperature estimations using the colour - T_{eff} relation and SED fitting. Our comparisons of temperatures of 51 BHB stars obtained using F148W−V - T_{eff}, N279N−V - T_{eff} relation and SED fitting with the spectroscopic data are shown as cyan squares, red triangles and blue circles respectively in Figure 5.14. The top panel of Figure 5.14 shows the difference between the temperatures estimated from spectra and colour - T_{eff} relation/SED fitting whereas the bottom panel shows the fractional difference. The median difference of temperatures are $\sim$ 214 K, 95 K and 30 K for $T_{eff} >$ 11,000 K and ~ -666 K, -334 K and -566 K for $T_{eff} <$ 11,000 K for F148W−V, N279N−V colour - T_{eff} relation and SED fitting respectively. In the bottom panel of the Figure 5.14, all the BHB stars scatter around $|\Delta T/T_{Spec}| =$ 0.018, 0.026 and 0.03 for $T_{eff} >$ 11,000 K and around $|\Delta T/T_{Spec}| =$ 0.068, 0.034, 0.06 for $T_{eff} <$ 11,000 K for F148W−V, N279N−V colour - T_{eff} relation and SED fitting respectively.

Overall, the temperatures of BHB stars with $T_{eff} >$ 11,000 K obtained from both the methods have better consistency with the spectroscopic estimates. Further, the comparisons of the two methods with Moehler et al. (2014) suggest that SED fitting or F148W−V - T_{eff} should be preferred for estimating the temperatures of BHBs with $T_{eff} >$ 11,000 K whereas N279N−V - T_{eff} relation for BHBs with temperatures between 8000 K $< T_{eff} <$ 11,000 K.

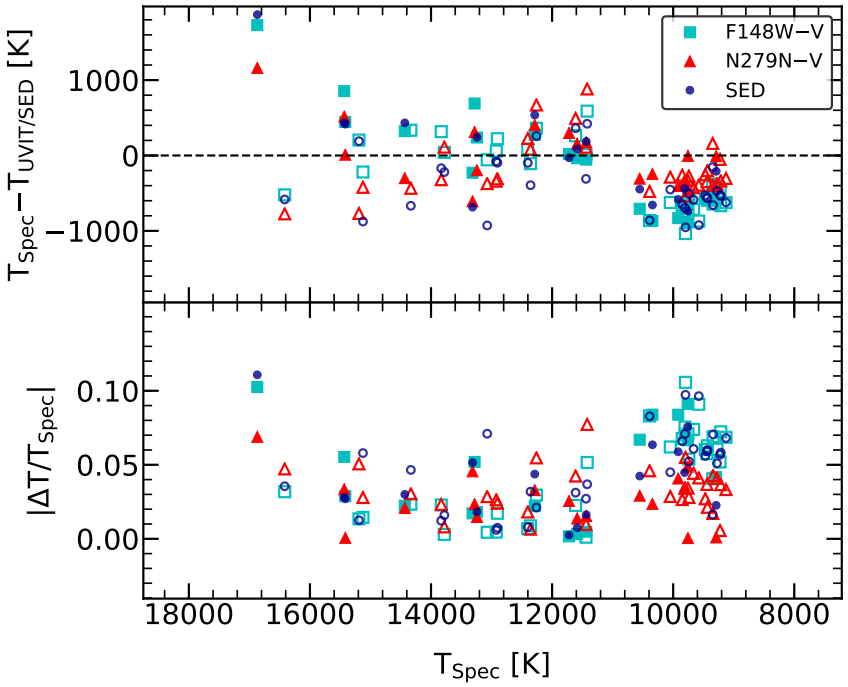

FIGURE 5.14: Top panel: The difference between the temperatures estimated from spectroscopy ($T_{Spectro}$) ((Moehler et al. 2014) and photometry/SED (T_{UVIT}) obtained from F148W−V - T_{eff} (cyan squares), N279N−V - T_{eff} (red triangles) relation and SED fitting (blue circles) respectively.
Bottom panel: The absolute value of the fractional differences between the temperatures estimated from spectroscopy and colour - T_{eff}/SED fitting as mentioned earlier. The filled circles are the UVIT cross-matched HST detections and the open circles are UVIT cross-matched ground detections in both the panels.

5.4.4 Identification of Gaps

Using the temperature estimations of the BHBs obtained from Section 5.4.1, we attempt to identify possible gaps in the BHB distribution and their corresponding temperatures. In Figure 5.15, we show F148W−V vs F148W and N279N−V vs N279N CMDs with only the BHB stars. We have marked the locations of the temperatures estimated from the respective colour - T_{eff} relation. The gaps known in the literature are shown in black arrows in F148W−V vs F148W CMD (upper panel). In N279N−V vs N279N CMD of Figure 5.15 (lower panel), we notice that the distribution of BHB stars hotter than $T_{eff} \sim$ 10,500 K show a larger scatter

in N279N magnitude. The bottom panels of figure 5.15 show the KDE plot of the BHB distribution. The KDE plots were generated using seaborn package and considering Scott's rule for bin width. The KDE plots in both the FUV and NUV CMDs show two groups of BHB stars separated around the location of the G-jump. The separation between the two BHB groups around the Grundahl-jump (G-jump) (Grundahl et al. 1999) are seen clearly in the FUV CMD as compared to the NUV CMD. The BHB stars hotter than G-jump show a flat distribution in FUV vs V CMD whereas it shows a curved distribution in NUV vs V CMD. The three red stars marked in both the panels in Figure 5.15 are B22, B186 and B302 which are spectroscopically confirmed to show a vertical stratification of iron in their atmospheres (Khalack et al. 2010). These stars are located in the FUV plateau near the G3 gap in F148W−V vs F148W CMD. The pentagons marked in the Figures are the 10 over-luminous BHB stars as classified by Moehler et al. (2014). We note that the over-luminous HB stars show a jump in magnitude from that of BHBs which is more prominent in the T_{eff} ranging from $\sim$ 10,200 K to $\sim$ 12,000 K in both the CMDs.

The (F148W−V) colour distribution of BHB stars are shown in Figure 5.16. We find gaps at $T_{eff} \sim$ 10,200 K, 11,000 K and 12,300 K in F148W−V vs F148W CMD which corresponds to the G0, G1 and G2 gaps respectively identified by Ferraro et al. (1998) in the HST FUV CMD of cluster M80. The gaps with F148W−V colour and the corresponding temperatures are given in Table 5.6. In F148W−V vs F148W CMD, we identify the G-jump gap (G2) at $T_{eff} \sim$ 11,700 K which is close to the value identified by Grundahl et al. (1999) for this cluster.

5.4.5 Discussion

The BaSTI isochrone used for the comparison is able to reproduce the BHB distribution in UV CMDs upto $T_{eff} \sim$ 11,500 K. Spectroscopic observations of the

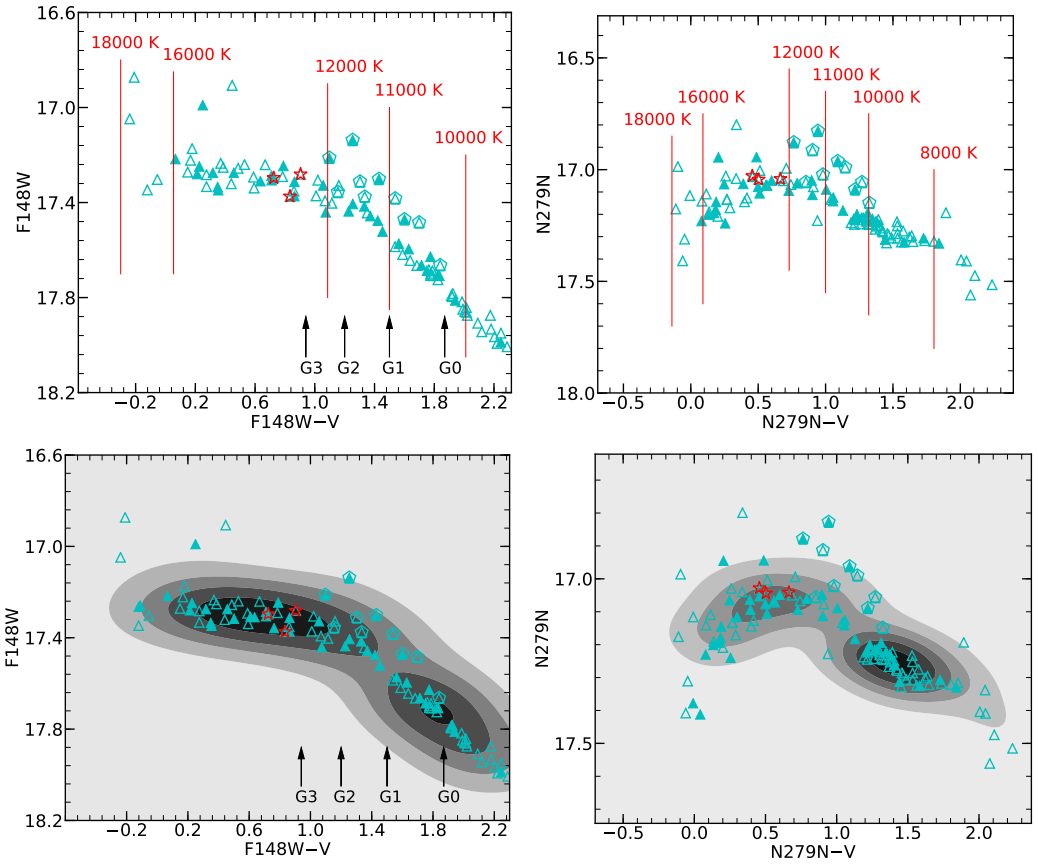

FIGURE 5.15: Top panels : A zoomed in view of the (F148W−V) vs F148W (left) and (N279N−V) vs N279N CMDs (right) showing only the BHB stars where the temperature locations for a log $g = 3.5$ and [Fe/H] $= -1.5$ are marked in red. The BHB gaps are marked with black arrows in the figure in the left panels.
Bottom panels : The corresponding Kernel Density Estimation (KDE) plots are shown for the BHB stars. The cyan pentagons are the over luminous BHB stars as classified by (Moehler et al. 2014) in both the panels. The three red stars marked in the figures are B22, B186 and B302 (Khalack et al. 2010).

TABLE 5.6: Temperature and reddening corrected colour of the BHB Gaps

Gap	F148W−V	T_{eff} [K]
G0	1.87	10,200
G1	1.48	11,000
G2	1.18	11,700
G3	0.97	12,300

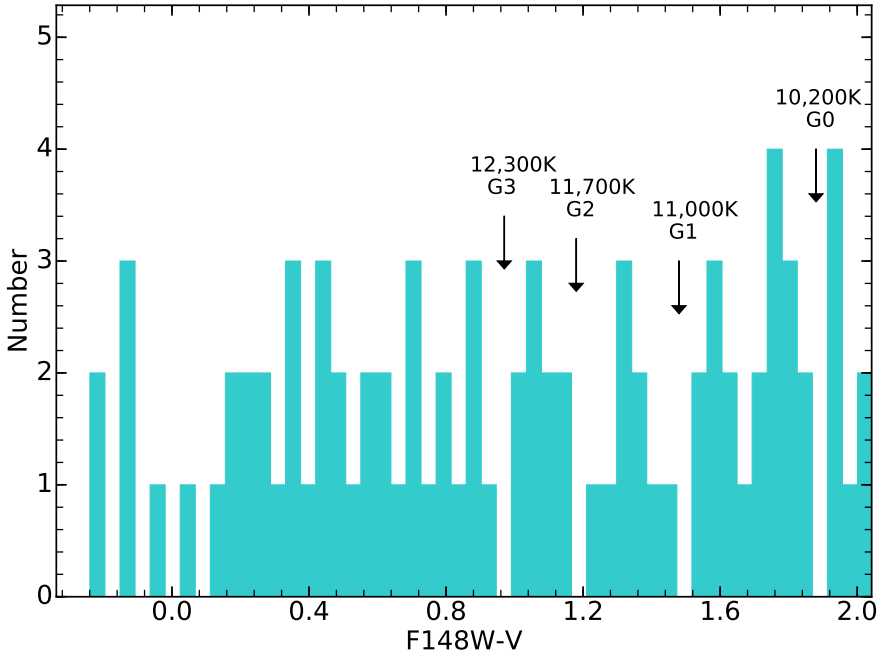

FIGURE 5.16: Distribution of (F148W−V) colour for BHB stars where the identified gaps in the BHB are shown with black arrows along with the corresponding temperatures.

BHB stars by Moehler et al. (2014) revealed that the BHB stars hotter than $T_{eff} \sim$ 11,500 K suffer from the effects of atomic diffusion as a result of which they show an overabundance of metals. They found that the hotter BHB stars have lower He I abundances whereas Si II and Fe II abundances are higher as compared to the BHB stars with $T_{eff} <$ 11,500 K. As the effects of diffusion in BHB stars are not addressed in the BaSTI isochrones generated from the FSPS model, we see a significant deviation in the FUV luminosity between the model and the observed BHB distribution (Figures 5.4-5.8) for stars with $T_{eff} >$ 11,500 K.

The plateau in the FUV magnitudes found in the FUV−V vs FUV CMDs (Figures 5.4 and 5.7), start at about 11,500 K, indicating that the luminosity plateau could be a result of diffusion. The reduction in the FUV luminosity can be caused by the increased absorption in the FUV due to enhanced atmospheric metallicity from atomic diffusion. This study thus demonstrates that the FUV−V vs FUV CMDs

could be used as an ideal proxy to detect the presence of diffusion among the BHB stars.

We notice two groups in the temperature distribution (Figure 5.11) that are mainly due to the BHB stars with and without the effect of diffusion. In the study of HB population in NGC 2808, Dalessandro et al. (2011) found that the observed distribution of T_{eff} has four groups which can be well reproduced by synthetic models by assuming different initial He abundances with Y_{ini} varying from 0.248 to 0.30. They concluded that the separate groups in the HB temperature distribution are due to the MSPs present in the cluster. Piotto et al. (2013) studied the multiple stellar phenomena in NGC 288 and found that the initial He difference in the two populations of MS and RGB is very small ($\Delta Y_{ini} \sim 0.013$). The Y_{ini} abundance in the Kurucz and BaSTI models that is used for HB analysis in our study is $\sim$ 0.248. Thus, the two peaks seen in the temperature distribution of BHBs may not be arising due to the small variations in the initial He abundances. It is possible that these are actually caused due to the presence of gaps in the BHB distribution. The effects of atomic diffusion combined with variations in the initial He abundances, if any, need to be properly incorporated in the models in order to explain the UV properties of the BHB stars.

The NUV−V distribution of the BHB shows a curved profile, with bluer and the redder BHB stars showing fainter NUV magnitudes. A comparison of bottom panel of Figure 5.15 with the Figure 8 of Moehler et al. (2014) indicates that the NUV magnitude profile directly correlates with the Mg II strength. The cooler ($T_{eff} <$ 11,000 K) and the hotter stars ($T_{eff} >$ 14,000 K) have relatively large Mg II strength, resulting in fainter N279N magnitude. Therefore, the NUV magnitudes presented here closely match with the estimated Mg II abundances.

According to the study by Momany et al. (2004), the HB of NGC 288 terminates at 16,000 K whereas our analysis suggests that the HB population extends till

18,000 K (Figure 5.11). This is primarily due to the contribution of stars located outside the HST FOV, which in turn shows the advantage of combining UVIT with the ground and Gaia data owing to their larger FOV.

5.5 SEDs of bright gap object and EHB stars

We derived the parameters (Luminosity, temperature and radius) of the two candidate EHB stars and the bright gap object using virtual observatory tool, VOSA (VO SED Analyser, Bayo et al. (2008)). We used Kurucz models (Castelli et al. 1997) for fitting the SEDs by adopting a distance of 8.8 Kpc, fixing the metallicity close to that of the cluster i.e. [Fe/H] $= -1.5$, and taking $\log g = 5.0$ by assuming them to be sub-dwarfs. The radius of the objects were calculated from the scaling factor which is equal to $\big(R/D\big)^2$, where R is the radius and D is the distance to the object.

We generated the SEDs of two candidate EHB stars designated as EHB1 and EHB2 by combining the flux measurements of UVIT (F148W, F169M, N279N) with GALEX (FUV, NUV), Gaia (G) (Gaia Collaboration et al. 2016, 2018a) and Ground (B, V, I). For the bright gap object, we generated the SED by combining the flux measurements of UVIT (F148W, F169M, N279N) with GALEX (FUV, NUV), Gaia (G) (Gaia Collaboration et al. 2016, 2018a) and HST (V, I) pass bands. The SEDs of the 3 stars are shown in Figure 5.17 and 5.18.

The best fit SED parameters of the gap object and EHB stars are given in Table 5.7. We find that the UVIT FUV flux measurements are consistent with GALEX FUV measurements whereas the GALEX NUV flux measurements show deviations from the model expected fluxes. These stars are located in the crowded regions close to the cluster centre where the GALEX NUV band suffers from poor

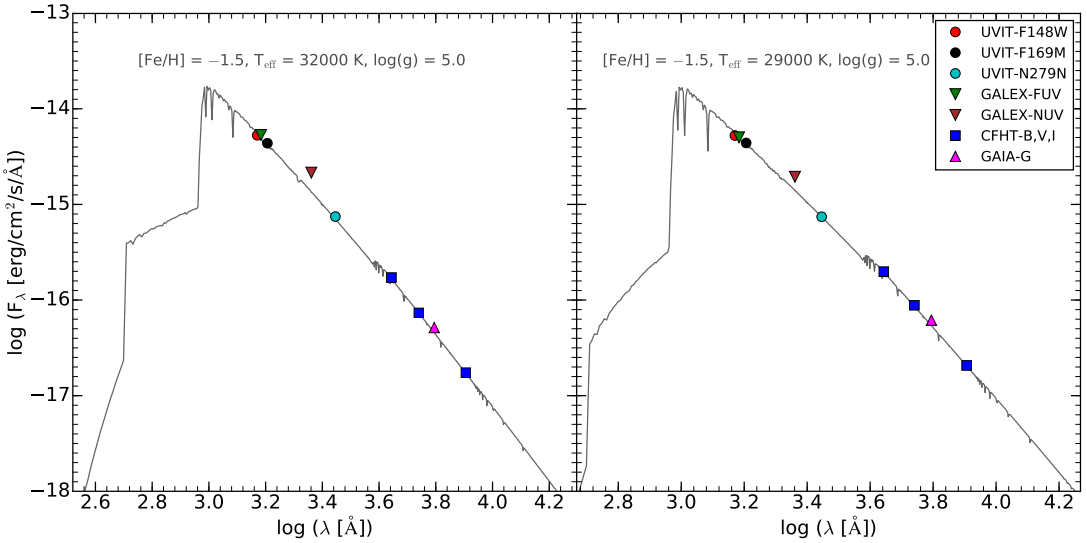

FIGURE 5.17: SED of EHB stars after correcting for extinction. The best fit parameters are mentioned in the figure.

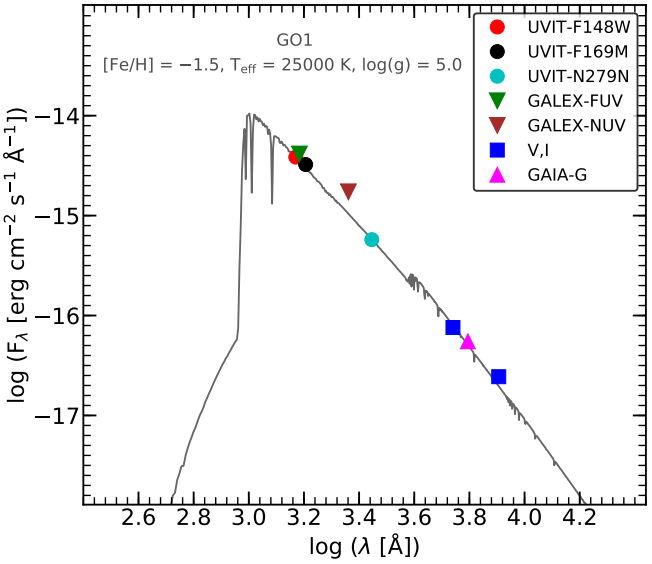

FIGURE 5.18: SED of the bright gap object after correcting for extinction. The best fit parameters are mentioned in the figure.

resolution. This could lead to an overestimation of the NUV flux due to the contamination from nearby stars. The reduced χ^2 ($\chi^2_{reduced}$) value mentioned in the Table 5.7 are obtained after excluding the GALEX NUV data point.

TABLE 5.7: SED fit parameters of bright gap object and EHB candidates

Star ID	[Fe/H]	T_{eff} [K]	log g	$L/L_\odot$	$R/R_\odot$	$\chi^2_{reduced}$
GO1	-1.5	25000±500	5.0±0.25	16.60±0.04	0.22±0.01	46.38
EHB1	-1.5	32000±500	5.0±0.25	21.93±0.05	0.15±0.01	14.66
EHB2	-1.5	29000±500	5.0±0.25	22.39±0.05	0.19±0.01	10.56

From Table 5.7, we notice that the EHB stars have similar luminosity whereas the bright gap object is $\sim$ 1.3 times less luminous than the EHB stars. All of them have similar radii (R $\sim$ 0.2 $R_\odot$). The temperatures of the EHB1 and EHB2 ($T_{eff} \sim$ 32,000 and 29,000 K respectively) clearly suggest that they belong to the class of EHBs/subdwarfs (Heber 1986). The temperature and radius of the bright gap object along with its location in the UV CMDs suggest that it is likely to be a subdwarf. The large $\chi^2_{reduced}$ value (46.38) for the SED fit (even after excluding the GALEX NUV data point), as compared to the two EHB stars, is due to the excess observed flux in the I band, excluding which reduces the value to 5.92. This might suggest the presence of a cooler companion which can be verified if we include the observations from the longer wavelengths in the SED. The locations of the EHB stars and the bright gap object in the cluster are shown as blue circles and green square respectively in Figure 5.19. The EHB stars are located at around the half-light radius of the cluster ($r_h \sim 2.23'$) shown as red circle whereas the bright gap object is located near the core radius of the cluster ($r_c \sim 1.35'$) which is shown as yellow circle in the figure.

5.5.1 Discussion

Generally, we see a large number of EHB population with a well defined sequence in the CMDs of massive GCs such as NGC 2808, ωCen, M 54, NGC 6752 (Momany et al. 2004; Dalessandro et al. 2011) whereas in low mass GCs they are less in

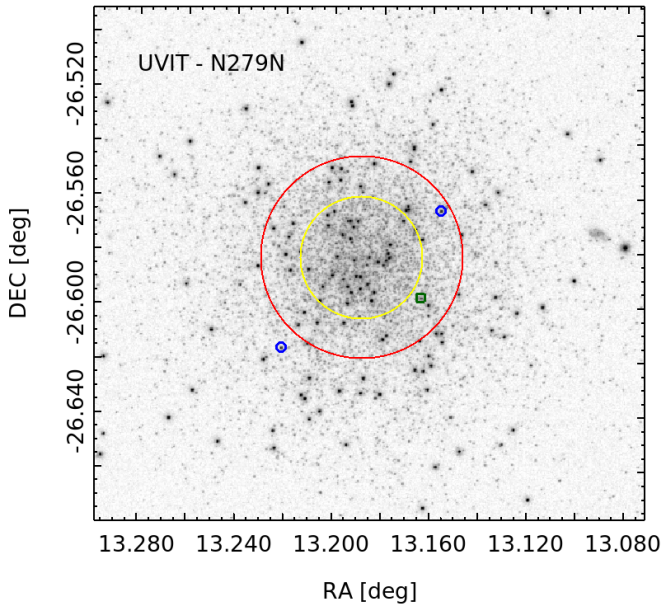

FIGURE 5.19: Locations of the EHB stars and bright gap object shown in blue circles and green square respectively plotted over a zoomed in image of the N279N filter of UVIT. The yellow circle and red circle are the core radius ($r_c \sim 1.35'$) and half-light radius ($r_h \sim 2.23'$) of the cluster respectively.

number and are hard to detect at the faint HB end of the optical CMDs. In these cases, UV CMDs are very useful where the EHB stars are very bright and form a separate sequence as compared to the optical CMDs. Momany et al. (2004) reported a discontinuity/gap at $T_{eff} \sim$ 23,000 K present in the massive GCs with EHB stars and suggested that these are early Helium flashers. Two such EHBs/subdwarfs detected in the cluster NGC 288 have temperatures $>$ 23,000 K consistent with the previous studies (Momany et al. 2004). The SED analysis of bright gap object suggests that this could be a subdwarf-binary candidate with a cooler companion. This is also supported by the fact that most of the binary systems are present within $1r_h$ of the cluster where the binary fraction $8\% < f_b < 38\%$ is very high as compared to the cluster outskirts (Bellazzini et al. 2002). This coincides with the positions of EHB stars within $1r_h$ of the cluster suggesting that the binary scenario could be the dominant formation channel for the three subdwarfs in the cluster (Podsiadlowski et al. 2008).

5.6 Summary

We summarise the results obtained from our UVIT imaging study of HB morphology of cluster NGC 288:

1. The UV bright stars in this cluster consist of 115 BHBs, 2 RRLs, 68 BSSs (6 SX Phes), 2 EHBs and 1 bright object gap object which are possible cluster members according to the PMs from Gaia DR2.

2. The comparison of FUV and NUV CMDs of the cluster with BaSTI isochrones shows that the isochrones are unable to reproduce the observed HB distribution in the UV CMDs for stars with $T_{eff} > 11{,}500$ K which are known to suffer from the diffusion effects such as radiative levitation. We detect a luminosity plateau in the FUV at this temperature, suggesting the FUV CMDs to be a good proxy to detect the onset of diffusion in the BHB distribution.

3. The BHB temperature distribution derived from two approaches, UVIT colour - T_{eff} relation and SED fitting using Kurucz models are consistent with the spectroscopic observations. The T_{eff} distribution consists of two groups with the peaks located at $\sim$ 10,300 K and 14,000 K which terminates at $\sim$ 18,000 K. The BHB stars in the hotter peak are affected by atomic diffusion. The dip between the peaks could be caused by the presence of four gaps located mainly around the G-jump.

4. The temperatures and radii of the two EHB candidates and bright gap object derived from the SED fitting lie in the range 25,000 - 32,000 K and 0.15 - 0.2 $R_{\odot}$ respectively. The presence of these EHB candidates in this low density and binary rich GC could suggest binary pathways for their formation.

Chapter 6

UVIT-HST-Gaia View of NGC 288: Blue Straggler Stars †

6.1 Introduction

Bellazzini & Messineo (2000) discovered a binary sequence in the optical CMD of NGC 288 from the HST-WFPC2 observations of the cluster. Later, Bellazzini et al. (2002) studied the binary systems and BSSs in the cluster with HST-WFPC2 survey data and estimated the binary fraction (f_b) to range from 8% to 38%. They found that most of the binary systems are located within the half-light radius of the cluster. They also found a high specific frequency of BSSs where they used ($m_{F255W} - m_{F336W}$) vs m_{F255W} CMD to select the BSS population of the cluster. They concluded that the mass transfer between the primordial binary systems might have led to the formation of BSSs.

This chapter mainly focuses on the BSS study of the cluster which include: (a) to

†Results of this chapter are published in Sahu et al. (2019a)

derive the parameters of BSSs from photometry and SEDs, (b) to study the radial distribution of BSSs in the cluster, (c) to derive the specific frequency of BSSs.

6.2 Properties of BSSs

6.2.1 Parameters of BSSs from Photometry

In order to estimate the parameters of 68 BSS members selected from the N297N−V vs N279N CMD and Gaia DR2 data, we used BaSTI isochrones of ages ranging from 1.5 Gyr to 10 Gyr with [Fe/H] = −1.28 and Y = 0.248 in such a way that it covers the location of BSS region in the CMD. These isochrones, over-plotted in the observed CMD are shown in the top panel of the Figure 6.1. We divided the BSS sample into two groups based on the N279N magnitude where the BSSs with N279N < 19.95 are the Bright BSSs (BBSSs) whereas those with N279N > 19.95 are the Faint BSSs (FBSSs). The KDE plot of the BSSs shown in the bottom panel of the Figure 6.1 clearly shows two population of BSSs separated by the plotted dotted line (at N279N = 19.95) which is in the middle of the two distributions. The BBSSs are less in number and span a larger range in magnitude as compared to the FBSSs which have a broader colour distribution.

We derived the parameters of the BSSs by cross-matching the N279N−V colour and N279N magnitude with those of the model colour and magnitude of BaSTI isochrones of different ages. The histogram of mass and age of 54 BSSs (22 BBSSs, 32 FBSSs) are shown in Figure 6.2. From the left panel of the figure, we notice that the mass of the BSSs range from 0.86 $M_\odot$ to 1.25 $M_\odot$ with a peak at $\sim$ 1.03 $M_\odot$. The mass of the FBSSs range from 0.86 - 1.1 $M_\odot$ with an average mass $\sim$ 0.97 $M_\odot$ whereas those of the BBSSs range from 0.98 - 1.25 $M_\odot$ with an average mass $\sim$ 1.1 $M_\odot$, which are less than $2M_{TO}$ ($\sim$ 1.56 $M_\odot$) of the cluster.

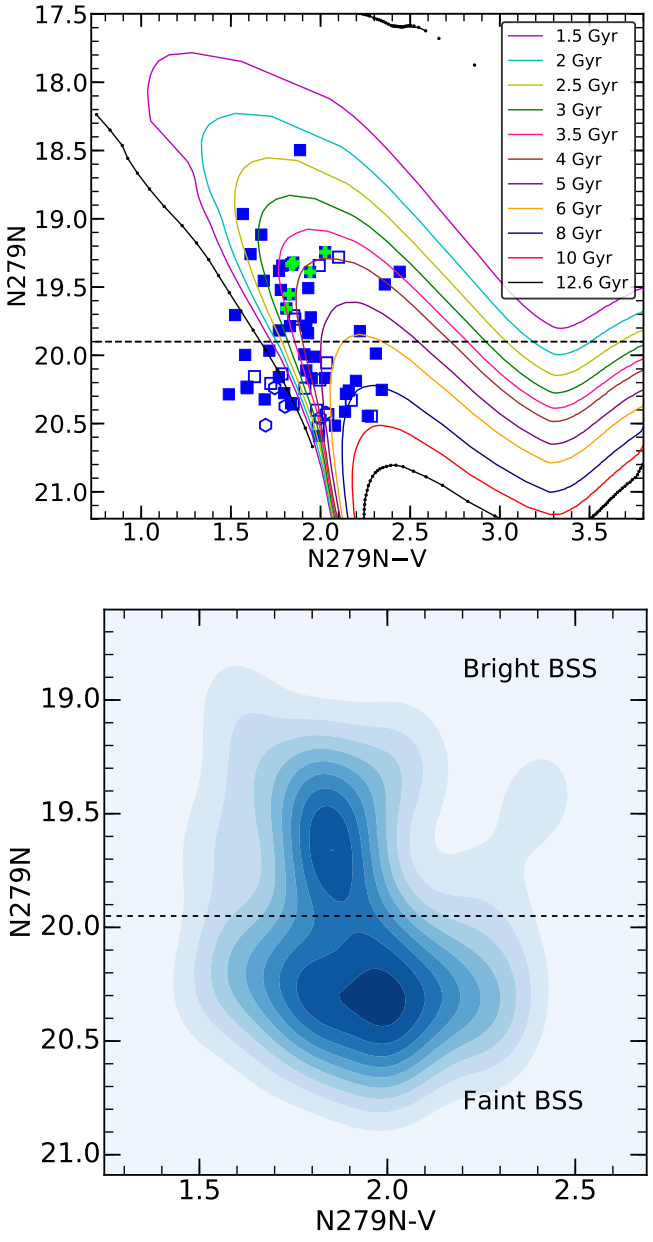

FIGURE 6.1: Top panel: A zoomed in view of Figure 5.8 where only identified BSSs are shown in the N279N−V vs N279N CMD. BaSTI isochrones of [Fe/H] = −1.28, Y = 0.248 and different ages marked in the legend are over plotted on the CMD.
Bottom panel: KDE plot of the BSSs distribution. The black dashed line divides the BSSs sample into bright and faint BSSs in both the plots.

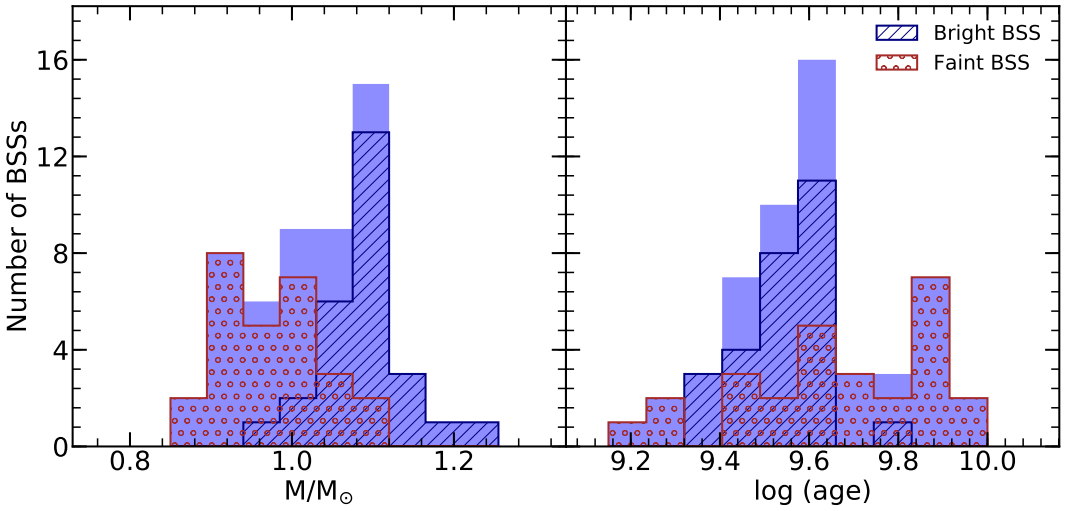

FIGURE 6.2: Mass (left panel) and age (right panel) distribution of 54 BSSs (light blue shaded), 22 BBSSs (blue hatched) and 32 FBSSs (brown circles) estimated from the BaSTI model isochrones of [Fe/H] = −1.28. The mass and age of the BSSs peaks at ∼ 1.03 $M_\odot$ and ∼ 4 Gyr respectively.

The ages of the BSSs range from 2.0 - 10 Gyr with a peak at ∼ 4 Gyr as shown in the right panel of the Figure 6.2 which are in agreement with Bellazzini et al. (2002). The BBSSs are younger having an average age of ∼ 3.5 Gyr whereas the FBSSs have a large range in age, with an average age of ∼ 4.5 Gyr. The brightest BSS is of age ∼ 2.5 Gyr and mass ∼ 1.25 $M_\odot$. This BSS is located at a radius of ∼ 0.66′ from the cluster centre. There are ∼ 2 BSSs in N279N−V vs N279N CMD shown in Figure 6.1 which are redder than the other BSSs in the CMD. These BSSs could have evolved from the MS and are currently in the Sub-giant phase and potential candidates for the YSSs. The masses of the SX Phe variables are ∼ 1.07 $M_\odot$ which are in agreement with the masses of SX Phe variables estimated by Fiorentino et al. (2015) for different clusters.

6.2.2 SEDs of FUV detected BSSs

We generated the SEDs of the BSSs detected in FUV using VOSA. We constructed the SEDs of the BSSs by combining the UVIT fluxes (3 filters) with the optical fluxes (V, I), thus, covering the spectral range from optical to UV wavelengths. We considered the same cluster parameters for the SED fitting as mentioned earlier in Section 5.5 of Chapter 5. The SED fit parameters (T_{eff}, luminosity and radius) of the BSSs along with the errors are given in Table 6.1 where the ages and masses are derived from the BaSTI isochrones. The errors are small as these are arising only from the SED fits. All the FUV detected BSSs fall under BBSSs category except three of them which lie in the FBSSs category. Out of 15 BSSs, we found 11 BSSs (9 BBSSs and 2 FBSSs) with $\chi^2_{reduced} > 20$. The deviations of the observed fluxes from the model are due to FUV excess which are significant beyond the 3σ predictions of the model. This points to the possibility of the presence of a hot companion such as WD associated with the BSSs. These stars will be studied in detail in future.

For a better understanding of the present evolutionary phases of the FUV detected BSSs, we have plotted them in the H-R diagram as shown in Figure 6.3. The colour bar shows the radii of the BSSs estimated from the SED fitting. The BaSTI isochrones plotted are similar to the Figure 6.1. Here, we notice that the age of the BSSs peaks at $\sim$ 4 Gyr which is in agreement with the photometric estimates. The brightest BSS in the H-R diagram is of age 2.5 Gyr with a larger radius of R $\sim$ 1.9 $R_\odot$ as compared to other BSSs.

We also constructed the SED of the Evolved BSS candidate (Section 5.3) by combining UVIT flux (N279N) with the HST (V, I) and Gaia (G) fluxes. The temperature (T_{eff} $\sim$ 5500 K) and luminosity of the object (L$\sim$ 66.59$\pm$1.5 $L_\odot$) derived from the SED fit are in close agreement with Ferraro et al. (2016). These estimations along with the PM membership from the Gaia DR2 clearly suggests that it

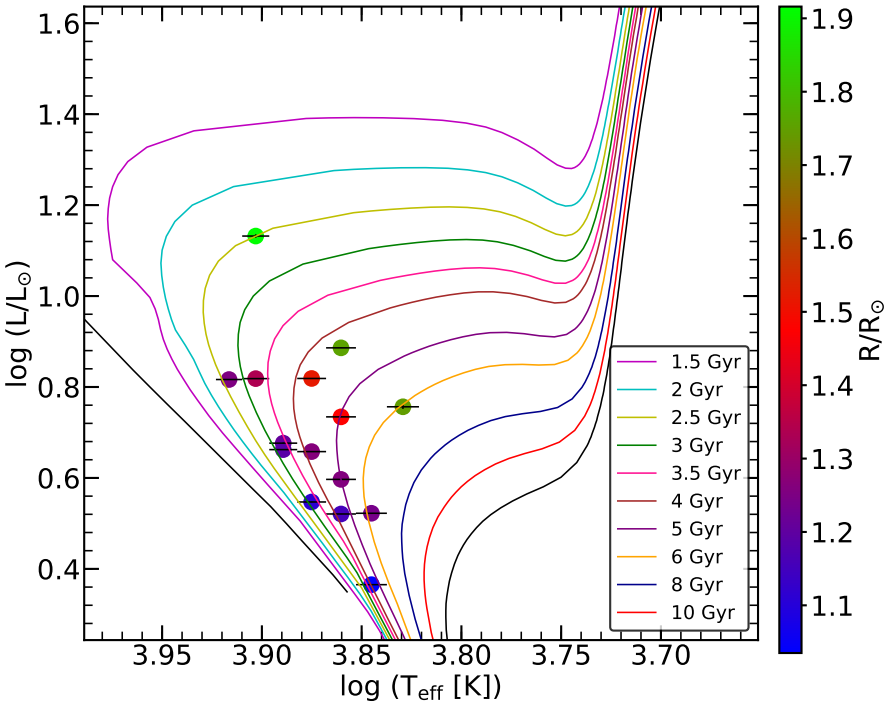

FIGURE 6.3: FUV detected BSSs plotted in the log L vs log T_{eff} H-R diagram based on the parameters derived from SED fitting where the colour bar represents the estimated radii. The parameters of the BaSTI isochrones plotted are similar to Figure 6.1.

can be very likely a EBSS candidate. This serves as a good spectroscopic target for future study of the evolution of BSSs.

6.2.3 Radial Distribution

BSSs being more massive than the HB and RGB stars, are expected to segregate towards the cluster centre due to dynamical friction, on the timescale of the order of half-mass relaxation time ($t_{r,h}$), which is $\sim$ 2 Gyr for this cluster (Harris 1996, 2010). Since $t_{r,h}$ timescale is much shorter than the age of the cluster, the mass segregation should have taken place long ago with the BSSs being more centrally concentrated than the HB and RGB stars. In order to check this, we derived the radial distribution of the BSSs and HBs. For transforming the RA and Dec

TABLE 6.1: SED fit parameters of FUV detected BSSs. Columns 2, 3 and 4 present the temperatures, luminosities and radii of BSSs derived from the SED fitting whereas columns 5 and 6 present the masses and ages of BSSs derived from the BaSTI isochrones.

Star ID	T_{eff} [K]	$L/L_{\odot}$	$R/R_{\odot}$	$M/M_{\odot}$	Age [Gyr]
BSS1	8000 ± 125	13.55 ± 0.12	1.92 ± 0.06	1.25	2.51
BSS2	7750 ± 125	4.75 ± 0.02	1.21 ± 0.04	1.07	3.47
BSS3	7250 ± 125	5.42 ± 0.01	1.48 ± 0.05	1.01	5.01
BSS4	6750 ± 125	5.71 ± 0.06	1.75 ± 0.07	0.98	6.03
BSS5	7500 ± 125	4.55 ± 0.01	1.26 ± 0.04	1.02	4.47
BSS6	7250 ± 125	3.95 ± 0.01	1.26 ± 0.04	0.99	5.01
BSS7	7500 ± 125	3.53 ± 0.01	1.11 ± 0.04	1.01	3.98
BSS8	7000 ± 125	3.33 ± 0.01	1.24 ± 0.04	0.94	6.03
BSS9	8250 ± 125	6.55 ± 0.01	1.25 ± 0.04	1.17	2.51
BSS10	8000 ± 125	6.58 ± 0.01	1.34 ± 0.04	1.14	3.02
BSS11	7000 ± 125	2.32 ± 0.01	1.04 ± 0.04	0.96	3.98
BSS12	7250 ± 125	3.32 ± 0.01	1.15 ± 0.04	1.00	3.98
BSS13	7750 ± 125	4.60 ± 0.01	1.19 ± 0.04	1.09	3.02
BSS14	7500 ± 125	6.59 ± 0.01	1.52 ± 0.05	1.08	3.98
BSS15	7250 ± 125	4.60 ± 0.01	1.76 ± 0.06	1.06	4.46

coordinates of these stars to XY system, we have used the cluster centre given in Table 5.1 of Chapter 5 and estimated their radial distance from it. For constructing the radial distribution, we have sampled the stellar populations up to a radius of $7'$ from the cluster centre. The final sample used for the radial distribution consists of 68 BSSs (28 BBSSs, 40 FBSSs) and 115 BHB stars.

The cumulative radial distribution of the BBSSs, FBSSs, BSSs and BHB populations are shown in top panel of the Figure 6.4. We have considered the BHB population as the reference population and performed K-S test to check the statistical significance of the differences among the radial distribution of the above stellar populations. According to the K-S test, the distribution of BSS population

is significantly different from the BHB population with a p-value of $\sim 3{\times}10^{-4}$. This shows that the BSS population is centrally concentrated than the BHB population. The K-S test also suggests that the BBSSs are more centrally concentrated than the FBSSs with p-values of $\sim 8{\times}\ 10^{-4}$ and ~ 0.12 respectively with respect to the reference BHB population. The probability that the BBSS and FBSS distributions are drawn from the same population is only 5.6%. The central concentration of BBSSs is likely due to their relatively large mass as compared to the FBSSs. The locations of the BBSSs, FBSSs and BHB stars plotted over the N279N UVIT image of the cluster are shown in the bottom panel of the Figure 6.4 marked with blue, brown and cyan colours respectively. It is clear that the BSSs are more centrally concentrated than the HBs with most of them lying inside the half-light radius of the cluster shown as a red circle in the figure. The difference in the radial distribution of BBSSs is comparatively large within $1r_c$ (yellow circle) of the cluster with respect to the FBSSs. We also find a few BBSSs to be located outside the $1r_h$ of the cluster. The central concentration of BBSSs is likely due to their relatively large mass compared to the FBSSs.

6.2.4 Specific frequency

We derived the specific frequency of BSSs (S_{BSS}) by dividing the observed cluster region into several concentric annuli (each of $1'$) and then counting the number of BSSs and HB stars in each annulus. The S_{BSS} as a function of the radial distance from the cluster centre (lower axis) and r/r_c (upper axis) is shown in Figure 6.5. Our estimation of the $S_{BSS} = 1.38 \pm 0.45$ in a region $r < 1r_c$ is consistent with that estimated by Bellazzini et al. (2002). Here, the error in the S_{BSS} is calculated by adopting the relation given by Sabbi et al. (2004). The number of BSSs within a radius $\sim 1'$ of the cluster is ~ 22 which is close to the number (~ 24) determined by Ferraro et al. (2003) for the cluster.

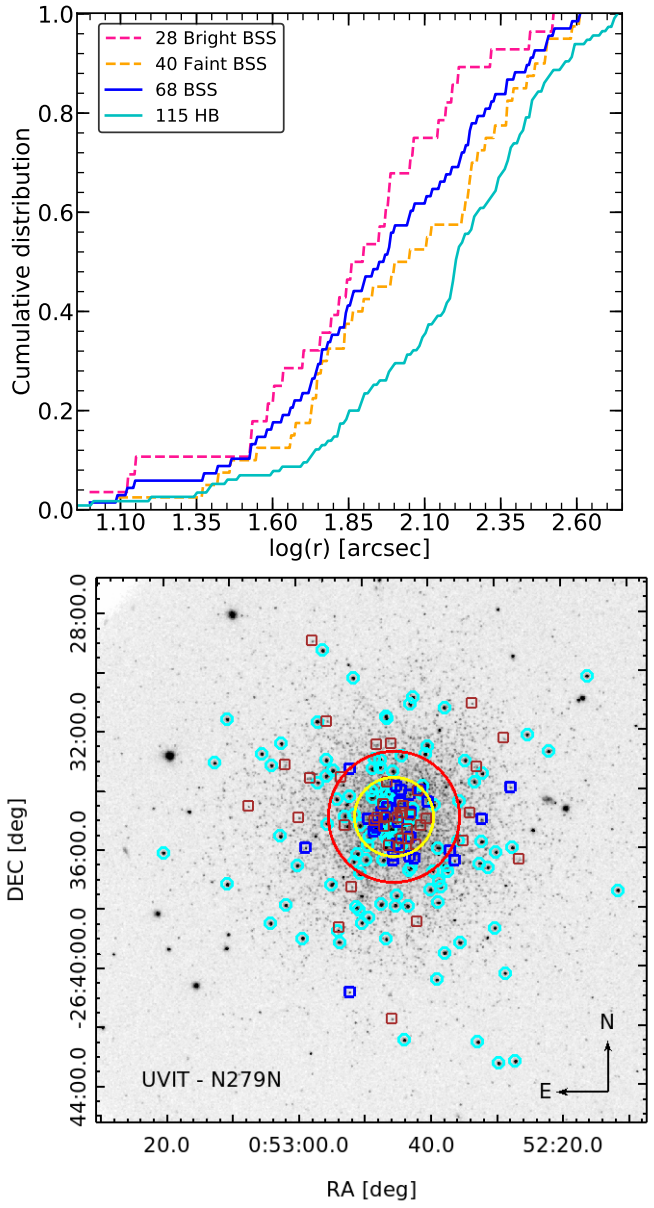

FIGURE 6.4: Top panel: Cumulative radial distribution of BBSS, FBSS and BSS population with respect to the HB population.
Bottom panel: Location of BBSSs (blue squares), FBSSs (brown squares) and HB stars (cyan circles) plotted over the N279N filter image of the cluster. The yellow circle and red circle are the core radius ($r_c \sim 1.35'$) and half-light radius ($r_h \sim 2.23'$) of the cluster.

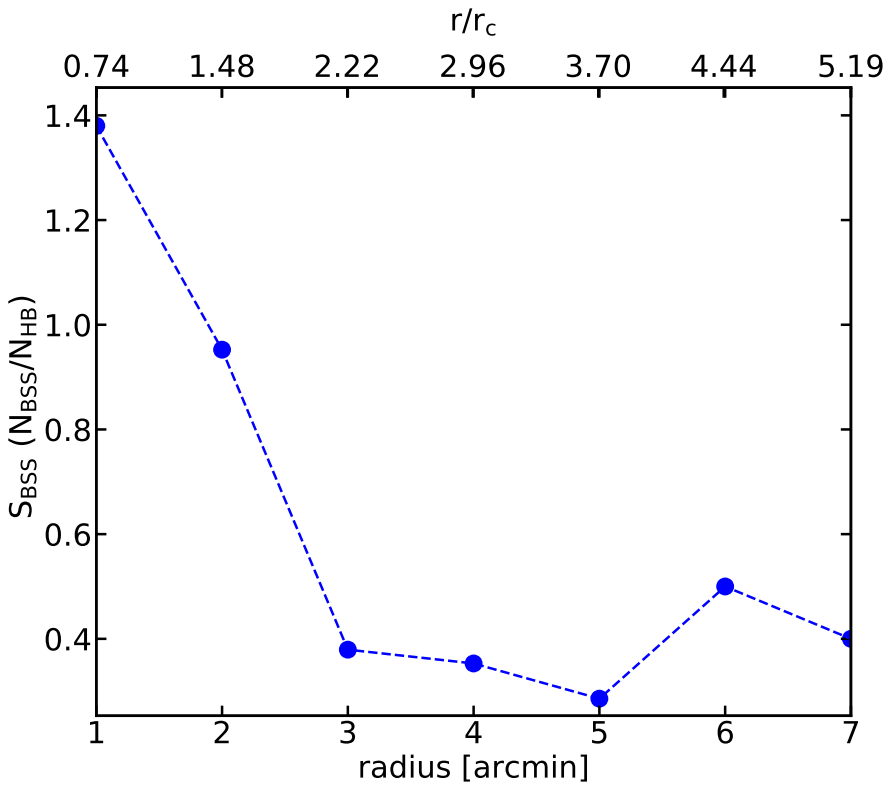

FIGURE 6.5: Specific frequency of BSSs with respect to HB stars plotted as a function of radial distance and r/r$_c$ from the cluster centre.

We notice that most of the BSSs are concentrated in the region $r < 2r_c$. In addition to the central peak, we also find a second peak S_{BSS} at $r \approx 4.5r_c$ with a sudden drop at $r \sim 3r_c$. This region with a sudden drop in S_{BSS} is defined as the zone of avoidance (Mapelli et al. 2004) which is at $r_{min} = 4'$ for the cluster in accordance with Lanzoni et al. (2016). This shows that the cluster has a bimodal BSS distribution. The second peak (r$\sim$ 6$'$) in the S_{BSS} is genuine as the BSSs in the cluster outskirts are PM members according to Gaia DR2 (Gaia Collaboration et al. 2018c).

6.2.5 Discussion

The observed BSS distribution in the NUV-V vs V CMD (Figure 6.1) closely matches with the distribution shown in Figure 8 by Ferraro et al. (2012) for NGC 288. The age distribution of the BSSs peaks at $\sim$ 4 Gyr (ranging from 2-10 Gyr) with most of them having ages older than the half-mass relaxation time of the cluster (t_{rh} $\sim$ 2 Gyr Harris (1996, 2010)). This is in agreement with the prediction of constant formation of BSS in the last 7 Gyr by (Ferraro et al. 2003). The brighter BSSs are found to be more massive and younger than the fainter ones. According to the two BSS evolutionary scenarios proposed by (Bellazzini et al. 2002), the evolutionary mass transfer scenario puts a lower mass limit of 0.92 $M_{\odot}$ for the BSS in the cluster which is more or less in agreement with our findings.

From the cumulative radial distribution, we found the BBSSs to be centrally concentrated as compared to the FBSSs unlike the previous studies on massive GCs such as M80, M15 (Dieball et al. 2010; Haurberg et al. 2010) where it was the other way around. The authors anticipated that the interactions of the bright BSSs with the cluster members in the high density environments such as central regions would have kicked them out of the cluster. Being a low density cluster, the dynamical interactions in NGC 288 are expected to be less active in the BSS formation as compared to the high density clusters ($\rho_c \sim 10^5$ $L_{\odot}/pc^3$ McLaughlin & van der Marel (2005b)). (Bellazzini et al. 2002) suggested that the large population of BSSs found in this cluster may be a result of their formation via mass transfer/coalescence of primordial binary systems. They found a high binary fraction within the $1r_h$ of the cluster where 65 % of our BSS sample resides in the cluster.

The two peaks found in the BSS specific frequency of the cluster suggests that the cluster is of intermediate dynamical age and falls in the Family II category

as per the definition given by Ferraro et al. (2012). This in turn, indicates that the dynamical friction has affected the BSS population only in the central regions of the cluster till the $r_{min} \sim 5'$ resulting in the mass segregation of the massive BSSs. The presence of a few BSSs in the cluster outskirts beyond $5'$ also conveys that the dynamical friction has not yet affected the BSS population in the outer regions.

6.3 Summary

We summarise the results obtained from our UV study of BSSs in the cluster NGC 288:

1. The BSS parameters were derived for 54 BSSs from photometry and SEDs. The distributions show a peak in age at ~ 4 Gyr and in mass at ~ 1 $M_{\odot}$.

2. This study separated the BSS population into bright and faint BSS, based on their location in the UV-optical CMD. The cumulative radial distribution clearly shows that the 22 bright BSSs are more centrally concentrated than the 32 faint BSSs and BHB stars.

3. The specific frequency of BSS shows a bimodal distribution suggesting that the cluster is of intermediate dynamical age.

Chapter 7

UV study of BSSs in NGC 5466 †

7.1 Introduction

NGC 5466 is an old, metal poor ($[Fe/H] = -2.0$, (Carretta et al. 2009) GGC located in the constellation Boötes. It is a low density GC ($\log_{10}\ \rho_c \sim 0.84\ L_\odot/pc^3$, McLaughlin & van der Marel (2005a)) as compared to other GGCs of similar luminosity. Belokurov et al. (2006) discovered huge tidal tails surrounding the cluster extending $\sim 4^\circ$ in the sky. This was supported by Grillmair & Johnson (2006) where they detected a 45° tidal stream associated with the cluster by examining a much larger region using SDSS data.

Nemec & Harris (1987) first studied and analyzed the BSS population covering a radius $\sim 9.1'$ from the cluster center using CFHT. They identified 48 BSSs from optical CMD. Later, Fekadu et al. (2007) provided a catalog of 94 BSS candidates and studied the radial distribution of the BSS population till r $\sim 13'$ from the cluster center. Recently, Beccari et al. (2013) (B13 hereafter) combined the data

†Results of this chapter are published in Sahu et al. (2019b)

from ACS, LBC, and CFHT data to study the BSS population up to the tidal radius of the cluster (r $\sim$ 26.3′). They found that the cluster contains a large fraction of binaries ($\sim$ 6%) and BSSs. They also concluded that the cluster has a bimodal radial distribution.

Mateo et al. (1990) discovered 2 contact binaries and 1 eclipsing binary suggesting that the evolution of primordial binaries in isolation in such a low density environment would have led to the BSS formation. So, the identification of such BSS binaries are crucial for understanding the BSS formation.

Previous studies on radial distribution of BSSs were mainly based on the BSS selection from the optical CMDs. The cluster field is contaminated by a large number of background sources which can cause a problem in the selection of BSSs using optical CMDs. In this study, we have addressed these issues by selecting the BSSs using UV CMDs i.e. by switching to UV wavelengths instead of optical and determining the PM membership of the BSSs which is extremely important in the outer regions of the cluster where the chance of false detection is very high.

In this Chapter, we aim 1) to identify and separate out the BSS members using UV images, 2) to identify the BSS binaries having a hot companion by constructing and fitting the models to the SEDs, 3) to derive the parameters of BSS from spectra and SEDs, 4) to study the radial distribution of BSS members covering large radial distances from the cluster center. In order to achieve the above aims, we have combined UVIT with HST and ground data to construct the UV-optical CMDs. We have used Gaia DR2 data to select the PM members. We have also obtained the spectra of FUV bright BSSs using the GMOS-N spectrograph, mounted in the Gemini Telescope.

7.2 Data and Analysis

We obtained the observations of the cluster in four filters (2 FUV and 2 NUV) of UVIT. The observation details of the cluster are given in Chapter 2. We used CCDLAB to generate the images of the cluster in the different filters. The UVIT image of the cluster is shown in Figure 7.1 where blue and yellow corresponds to detections in F169M and N245M filters of UVIT respectively. We can notice that the cluster centre is completely resolved in both NUV and FUV.

We extracted the magnitudes of the sources detected in different UVIT filters by performing PSF photometry on the images as described in Chapter 3.

We also performed the PSF photometry on the GALEX FUV and NUV intensity maps of the cluster to obtain the magnitudes of the sources. The GALEX image of the cluster is shown in the left panel of Figure 7.2.

7.3 UV and Optical Color-Magnitude Diagrams

We cross-matched UVIT data with HST-ACS survey data of the GC NGC 5466 (Sarajedini et al. 2007) for the central regions and ground based data provided by Peter Stetson for the region beyond the filed of view of HST. The HST-ACS image of the cluster is shown in right panel of Figure 7.2. We separated them into various stellar populations such as HB and BSS based on their locations in both the optical and UV CMDs. The parameters of the cluster adopted in this study are given in Table 7.1.

To check the membership of the detected stars, we used the Gaia DR2 PM catalog of the cluster NGC 5466 given by Gaia Collaboration et al. (2018b). Their catalog

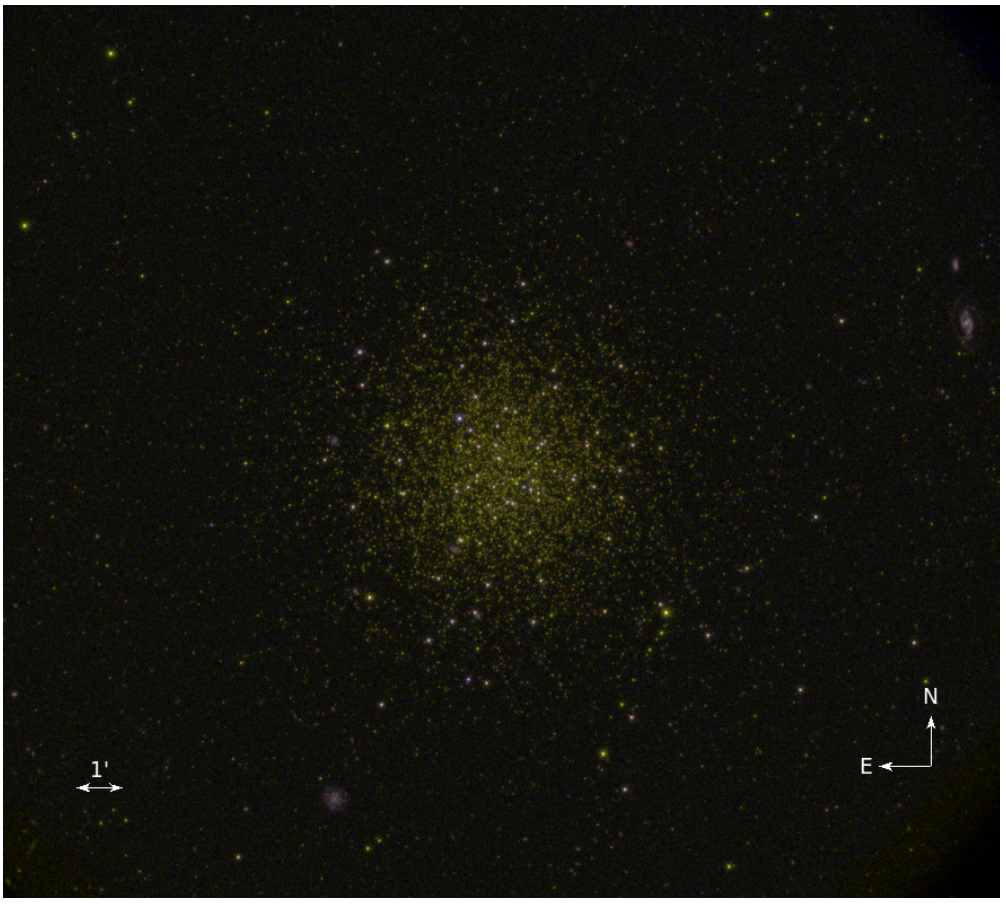

FIGURE 7.1: UVIT image of the GC NGC 5466 where blue corresponds to the FUV detections and yellow corresponds to the NUV detections acquired with F148W and N245M filters of UVIT respectively.

TABLE 7.1: Parameters of NGC 5466 used in this paper.

Parameter	Value	Reference
R.A. (J2000)	14 05 27.29	Goldsbury et al. (2010)
Dec (J2000)	+28 32 04.0	Goldsbury et al. (2010)
$[Fe/H]$	−2.0 dex	Carretta et al. (2009); Arellano Ferro et al. (2008)
Distance (Kpc)	16.0 ± 0.6	Arellano Ferro et al. (2008)
Core radius, r_c	1.43′	McLaughlin & van der Marel (2005a)
Half-light radius, r_h	2.3′	McLaughlin & van der Marel (2005a)
μ_{RA}(mas yr^{-1})	-5.404 ± 0.004	Gaia Collaboration et al. (2018b)
μ_{Dec} (mas yr^{-1})	-0.791 ± 0.004	Gaia Collaboration et al. (2018b)

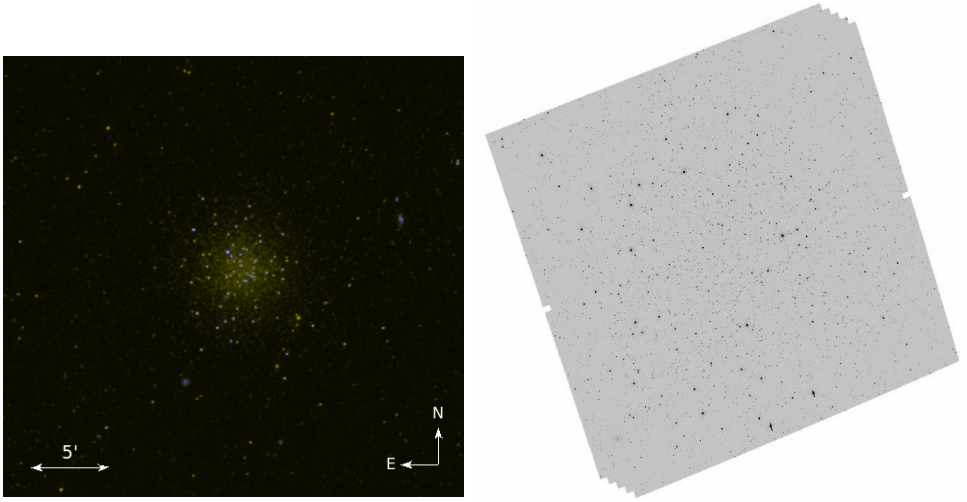

FIGURE 7.2: *Left:* GALEX image of NGC 5466 where blue and yellow corresponds to the detections in FUV and NUV filters of GALEX respectively. *Right*: HST image of NGC 5466 obtained with F606W filter of ACS/WFC camera under HST/ACS GC Treasury Program (Sarajedini et al. 2007).

consists of the list of PM member stars of the cluster where the procedure for the member selection is described in detail in Appendix A.1 of their paper. The vector-point diagram of BSSs (blue squares) relative to other cluster members (grey dots) in the PM catalog is shown in Figure 7.3 where we clearly notice that the FUV detected BSSs are grouped around the mean PM derived by Gaia Collaboration et al. (2018b) (Table 7.1) except BSS NH 48. According to the HST PM study by Simunovic & Puzia (2016), this BSS is a PM member. In total, we found 14 BSSs detected in all the UVIT filters to be PM members. In addition, 63 HB stars are also found to be PM members. The typical uncertainties in the PMs are ~ 0.12 and 0.42 mas yr^{-1} for the HB and BSSs respectively. These 14 BSSs are marked in the FUV (F169M) and NUV (N245M) images as shown in Figure 7.4, where we can clearly see that the BSS are spatially resolved and PSF photometry can be successfully performed.

The PM cleaned F169M vs (F169M−N245M) CMD (right panel) along with the optical CMD (left panel) are shown in Figure 7.5 where the detected BSSs are shown as blue squares. The UV CMD is over plotted with a Padova model (Marigo

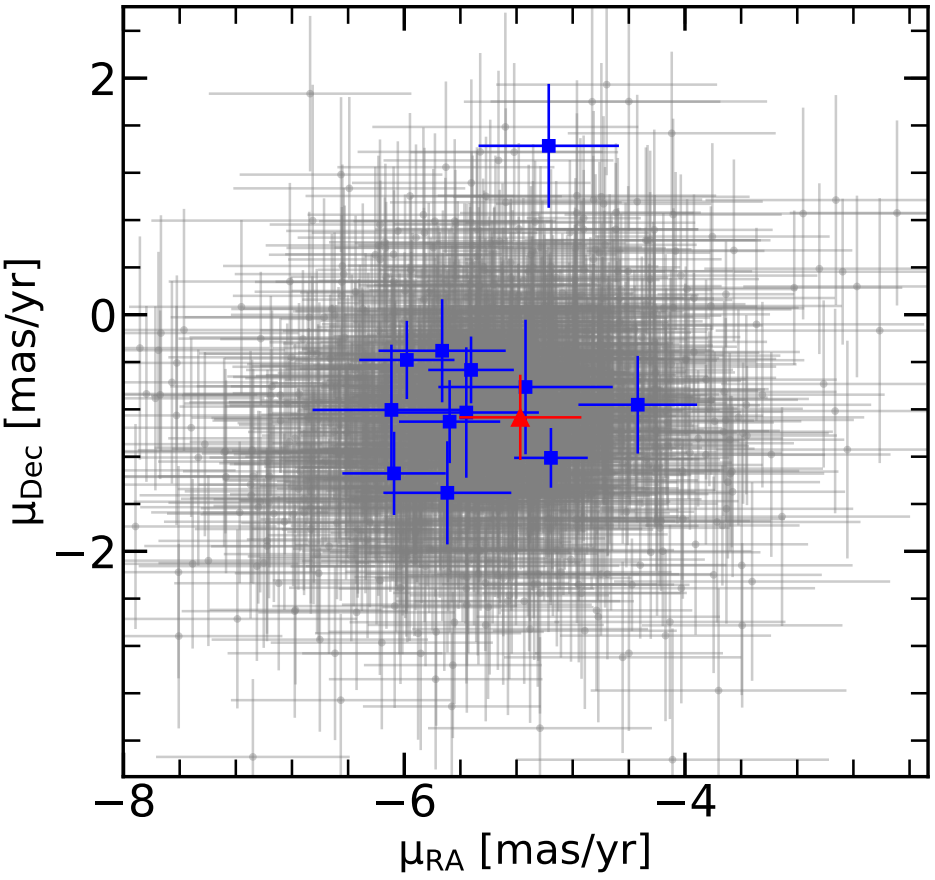

FIGURE 7.3: Vector-point diagram of the 14 BSSs (blue squares) detected by UVIT relative to other cluster members (grey) in the catalog given by Gaia Collaboration et al. (2018b). The red triangle in the figure is BSS NH 84.

& Girardi 2007; Marigo et al. 2008) isochrone (black line and dots) of age 12.6 Gyr, metallicity [Fe/H]= −1.98 (Carretta et al. 2009) for a distance modulus of 16.0 (Arellano Ferro et al. 2008), generated using the FSPS code. Reddening is not corrected here as it is close to zero, E(B−V) = 0.00 (Zinn 1985). The cross symbol in the figures is a known anomalous Cepheid (Zinn & Dahn 1976). The bright star in the UV CMD at F169M, F169M−N245M ∼ 17.5, -0.4, lying close to the PAGB evolutionary model track is classified as a AGB-manqué star by Schiavon et al. (2012). The same stars plotted in the F169M vs F169M−V CMD are shown in Figure 7.6 where the HB stars stretch more than 4 in F169M magnitude and color. The same stars detected in the UV CMD are plotted on F169M vs F169M−V CMD in Figure 7.6. Here, we clearly notice that the BSSs

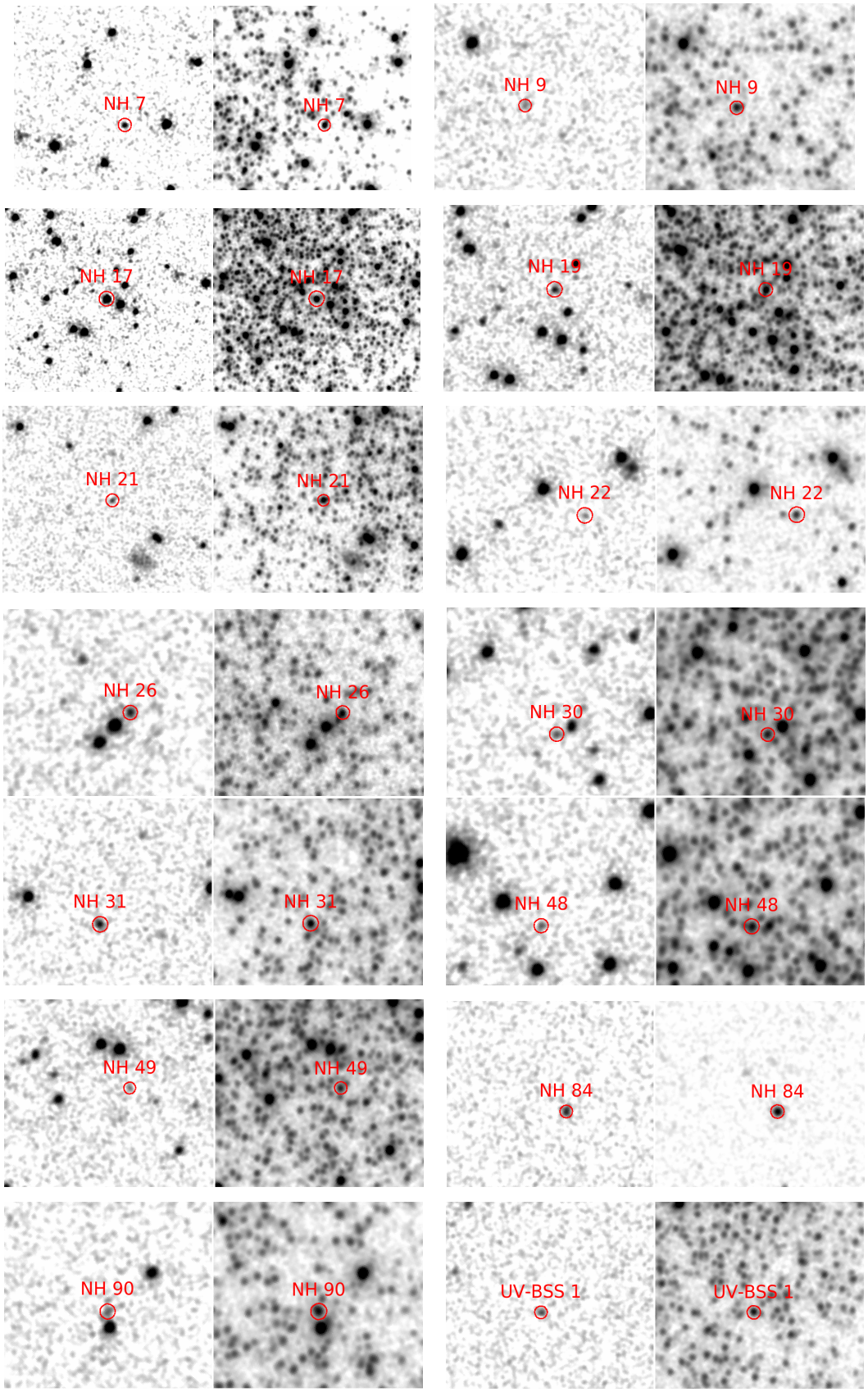

FIGURE 7.4: Location of BSSs on FUV-F169M (Left) and NUV-N245M (Right) images of UVIT.

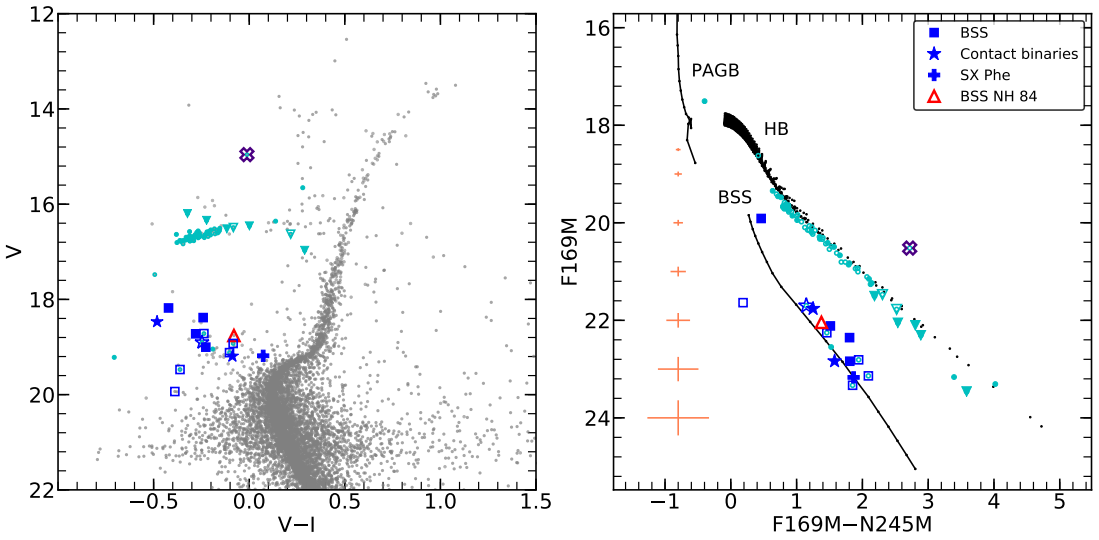

FIGURE 7.5: F169M, (F169M−N245M) UV CMD (right panel) and its corresponding V, (V−I) optical CMD (left panel) with BSSs detected in all the UVIT filters. Open symbols are UVIT cross-matched ground (CFHT) detections and closed symbols are the UVIT cross-matched HST detections. Cyan dots are the objects detected down to F169M = 24 mag. The cross symbol is an anomalous Cepheid whereas the lower triangles are RR lyrae variables. The UV CMD is over plotted with a Padova model isochrone (black line and dots) of age 12.6 Gyr and metallicity [Fe/H]= −1.98 (Carretta et al. 2009).

and HB stars span around 4 mag in color and magnitude.

Fekadu et al. (2007) presented BVI photometry of RGB and BSSs based on their observations with the KPNO 0.9m telescope. They identified 94 BSS candidates based on their locations in optical CMDs. Of the 14 BSSs detected by UVIT which are listed in Table 7.2, 13 BSSs were found to be in common with their catalog (Fekadu et al. 2007) suggesting that we have an additional BSS named as UV-BSS1 (Table 7.2). The GALEX magnitudes of the BSSs given in the table are obtained by performing PSF photometry on the GALEX FUV and NUV intensity maps (OBJECT ID- GI1_056017_NGC5466). We used the BSS nomenclature from Nemec & Harris (1987) for our study.

Among the UV detected BSSs, NH 17 is the brightest BSS as shown in the left panel of the Figure 7.5. NH 19, NH 30 are known W-UMa type contact binaries

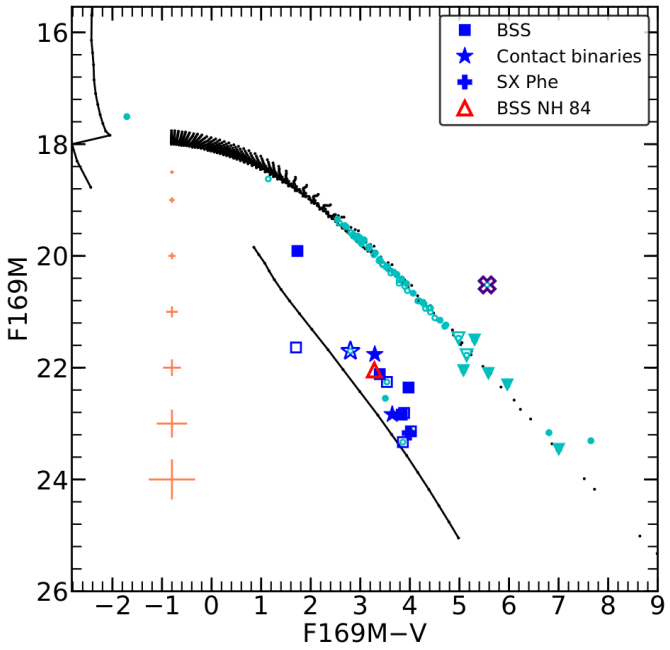

FIGURE 7.6: F169M vs (F169M−V) CMD. See Figure 7.5 for details.

and NH 31 is an eclipsing binary (Mateo et al. 1990). BSS NH 49 is a known SX Phe variable (Jeon et al. 2004). One of the BSS from the Fekadu et al. (2007) catalog, NH 87, is found to be bluer than the BSS model track in the UV CMD (empty blue box in right panel of Figure 7.5) whereas other BSSs are distributed around the track. This BSS does not have the PM information from Gaia DR2. We obtained the GMOS-N spectra of this object (see Section 7.4).

The location of the FUV detected BSSs from Table 7.2 are shown as blue circles in Figure 7.7 overlaid on UVIT's N245M filter image of the cluster. The red square in the figure is BSS NH 84. We found that most of the BSSs (12 out of 14) are located inside the half-light radius of the cluster.

The PM cleaned N245M vs N245M−V CMD is shown in right panel of Figure 7.8 along with its corresponding optical CMD in the left panel. We detected 23 HB PM members in only NUV filters, in addition to the 63 HB members in all UVIT filters which leads to a total of 86 HB members in the cluster. We also detected the 24 known variables among which 7 are SX Phes and 3 are binaries

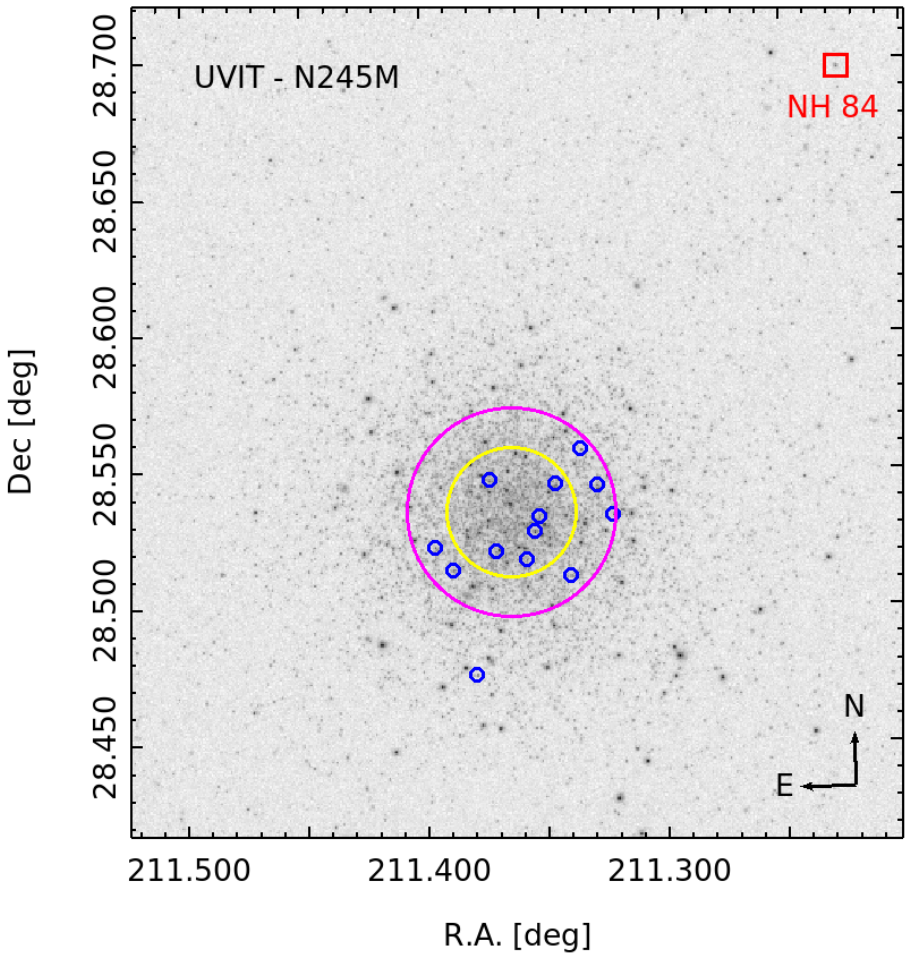

FIGURE 7.7: 14 BSSs detected by UVIT are overlaid on top of an N245M filter image of UVIT. The red square symbol in the figure is the BSS target in our study. The yellow and magenta circles are the core radius ($\sim 1.43'$) and half-light radius ($\sim 2.3'$) of the cluster from the center (McLaughlin & van der Marel 2005a).

falling in the expected BSS location and 14 are RR Lyrae variables falling in the HB location in the CMD.

We checked the PM membership of all the BSSs available in the catalog given by Fekadu et al. (2007) using Gaia DR2 and found 8 of them to be non-members. Of the 8 non-members, 3 of them (NH 64, 83, 86) are classified as quasars by Ahn et al. (2012); Flesch (2015). 3 BSSs (NH 85, 87, 89) which do not have PM information from Gaia DR2 are classified as galaxies by SDSS survey (Alam et al. 2015). These 6 sources (galaxies and quasars) are mainly located outside $2r_h$ of the cluster.

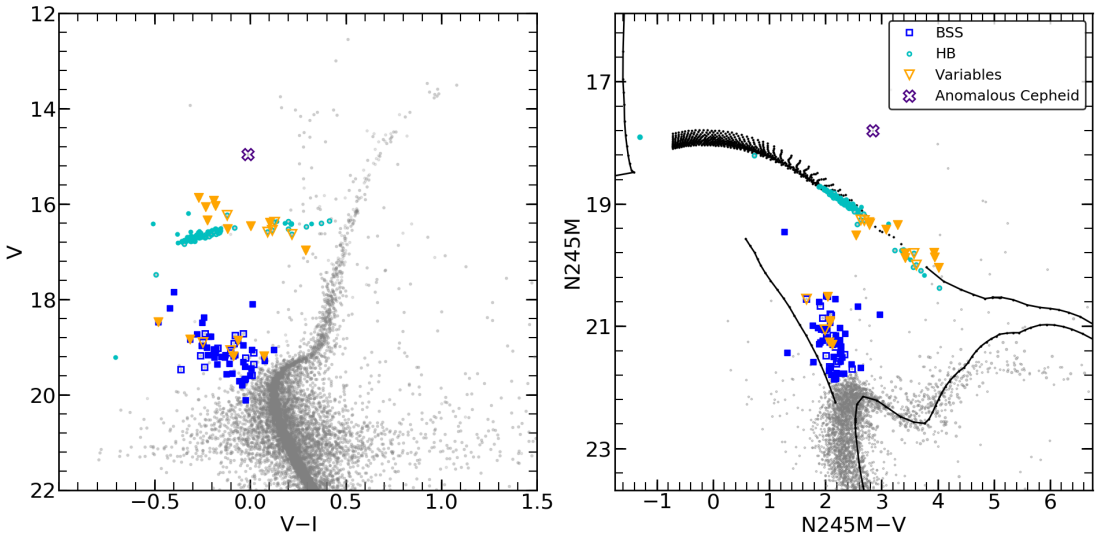

FIGURE 7.8: *Left:* V vs V−I optical CMD *Right:* N245M vs N245M−V CMD over-plotted with Padova isochrone (black line and dots, refer Figure 7.5 for details) where the closed symbols are UVIT cross-matched HST detections and open symbols are UVIT cross-matched ground detections. The different symbols marked in the legend are: BSSs (blue squares), HB (cyan circles) and the known Variables including RR Lyrae and SX Phes (orange triangles).

Considering those BSSs in the catalog which are PM members and excluding 11 background sources, we cross-matched the revised BSS catalog with the N245M filter data of UVIT to find the NUV magnitude of the BSSs. We plotted them in the NUV vs NUV−V CMD (Figure 7.8) to check their locations and rejected 15 of the BSS candidates from our sample as they do not qualify our criteria of falling in the expected BSS location in NUV vs NUV−V CMD. They were either located in the SGB region or they had redder NUV colors (N245M−V¿3.0). Finally, we are left with a sample of 66 BSS members which were used to study the radial distribution of BSSs in the cluster as described in Section 7.6.

TABLE 7.2: UV magnitudes of the FUV detected BSS candidates in all the UVIT and GALEX filters that are PM members (Gaia Collaboration et al. 2018b). The UV-BSS1 does not have a counterpart in the BSS catalog of Fekadu et al. (2007).

				UVIT				GALEX		Proper motion	
BSS ID	RA (J2000)	DEC (J2000)	r	F148W	F169M	N245M	N263M	FUV	NUV	μ_{RA}	μ_{Dec}
	[deg]	[deg]	[′]	[mag]	[mag]	[mag]	[mag]	[mag]	[mag]	[mas yr^{-1}]	[mas yr^{-1}]
UV-BSS 1	211.3393	28.51122	1.83	23.08 ± 0.30	22.55 ± 0.19	21.02 ± 0.06	21.09 ± 0.09	23.24 ± 0.20	21.13 ± 0.07	-5.63 ± 0.58	-0.69 ± 0.49
NH 7	211.32196	28.53361	2.22	22.88 ± 0.30	22.26 ± 0.18	20.80 ± 0.05	20.63 ± 0.08	22.63 ± 0.15	20.81 ± 0.04	-5.98 ± 0.34	-0.38 ± 0.33
NH 9	211.33525	28.55766	2.06	23.15 ± 0.31	23.14 ± 0.28	21.05 ± 0.07	21.65 ± 0.18	-	21.10 ± 0.04	-6.09 ± 0.56	-0.80 ± 0.55
NH 17	211.35456	28.52768	0.64	20.05 ± 0.08	19.91 ± 0.06	19.45 ± 0.03	19.43 ± 0.04	19.96 ± 0.08	19.56 ± 0.04	-4.95 ± 0.26	-1.21 ± 0.25
NH 19[a]	211.35267	28.53305	0.6	21.66 ± 0.16	21.76 ± 0.12	20.51 ± 0.05	19.97 ± 0.10	21.68 ± 0.11	20.30 ± 0.06	-6.07 ± 0.37	-1.34 ± 0.35
NH 21	211.38859	28.51381	1.79	22.39 ± 0.20	22.36 ± 0.16	20.55 ± 0.05	20.37 ± 0.09	22.60 ± 0.18	20.33 ± 0.04	-5.52 ± 0.31	-0.47 ± 0.28
NH 22	211.37913	28.4753	3.64	23.59 ± 0.35	23.33 ± 0.26	21.48 ± 0.09	21.47 ± 0.13	-	21.59 ± 0.08	-5.14 ± 0.62	-0.61 ± 0.57
NH 26	211.34568	28.54491	1.15	22.23 ± 0.18	22.12 ± 0.17	20.60 ± 0.07	20.39 ± 0.08	-	20.61 ± 0.09	-5.69 ± 0.46	-1.51 ± 0.44
NH 30[a]	211.37085	28.52038	0.92	23.32 ± 0.36	22.84 ± 0.20	21.26 ± 0.09	21.66 ± 0.14	-	-	-5.73 ± 0.45	-0.30 ± 0.44
NH 31[a]	211.39603	28.52215	1.84	22.15 ± 0.22	21.70 ± 0.13	20.55 ± 0.06	20.48 ± 0.06	21.82 ± 0.12	20.42 ± 0.07	-5.68 ± 0.36	-0.90 ± 0.35
NH 48	211.37318	28.54648	0.87	23.17 ± 0.33	22.84 ± 0.25	21.03 ± 0.07	20.97 ± 0.13	-	21.06 ± 0.07	-4.97 ± 0.50	1.43 ± 0.52
NH 49[b]	211.35802	28.51746	1.07	23.68 ± 0.39	23.17 ± 0.25	21.30 ± 0.07	21.31 ± 0.10	23.53 ± 0.34	-	-5.56 ± 0.52	-0.83 ± 0.55
NH 90	211.3281	28.54438	1.92	22.84 ± 0.28	22.81 ± 0.25	20.87 ± 0.09	20.56 ± 0.10	-	-	-5.10 ± 0.38	-1.32 ± 0.35
NH 84	211.22649	28.69703	12.15	22.47 ± 0.25	22.04 ± 0.14	20.67 ± 0.06	20.39 ± 0.09	22.28 ± 0.13	20.68 ± 0.03	-5.17 ± 0.44	-0.87 ± 0.36

[a]Eclipsing and contact binaries (Mateo et al. 1990)

[b]SX Phe variable (Jeon et al. 2004; Arellano Ferro et al. 2008)

7.4 GMOS-N spectroscopic data

We obtained spectroscopic data using the GMOS-N spectrograph mounted on the 8.1-meter Gemini-North telescope for two sources detected in FUV filters, namely NH 87 and NH 84 (see Table 7.2). The observations were part of the Gemini program GN-2018A-FT-113 (PI: M. Simunovic) and were taken during June, 2018. We used the R400_G5305 grating and a 0.75″ long slit which yielded a dispersion of 0.074 nm/pix and a spectral resolution R ≈ 1300 for the ∼ 460-900 nm spectral range. We took 4×330 sec exposures in each central wavelength (700 and 705 nm) in order to cover the GMOS-N detector chip gaps. The data were reduced using standard IRAF routines available in the Gemini/GMOS package which resulted in flux-calibrated spectra at a signal-to-noise of ∼60, shown in Figure 7.13 for NH 84.

The spectrum of NH 87 showed a flat continuum and strong emission lines consistent with an HII region, suggesting it to be a star-forming galaxy at a redshift of z ∼ 0.09. This also supports the previous classification by SDSS of this object as a galaxy. Hence we discard this object as a contaminant and focus on the spectroscopic analysis of NH 84, which is confirmed as a stellar source.

Radial velocity and spectral fitting of NH 84

The stellar parameters $T_{\rm eff}$ and log g were obtained by fitting the shape of the H_α line present in the spectrum of NH84, which is commonly used as a $T_{\rm eff}$ and log g indicator and independent of rotational broadening. The spectral fitting method was a χ^2 minimization using the pPXF python package (Cappellari 2017) with a grid of synthetic spectra from the Coelho library (Coelho 2014), fixed at [Fe/H] = −2.0 dex. The grid was limited to $T_{\rm eff}$ values between 7000−12000 K

in 250 K steps, whereas log g were taken between 2.0−5.0 in steps of 0.5. The synthetic spectra were then degraded to the spectral resolution of the GMOS-N data and the pPXF spectral fitting was performed allowing only a radial velocity shift and no kinematic broadening. The observed spectrum of NH 84 and best-fit model are shown in Figure 7.9. We obtained $T_{\rm eff}$ = 8000 K and log g = 4.0 as the best-fit parameters of NH 84. As it can be seen in the lower panel of Figure 7.9, the estimated χ^2 for a range of parameters is not uniformly distributed around the minimum, and hence asymmetric uncertainties are present. To obtain robust uncertainties, we take the best-fit synthetic model and add random Gaussian noise such that its signal-to-noise=60, as in the observed data, and run pPXF to obtain the best-fit model of this artificial data sample. We run 1000 iterations and obtain probability distributions for the best-fit parameters. This way, we adopt $T_{\rm eff} = 8000^{+1000}_{-250}$ K and log $g = 4.0^{+0.5}_{-0.5}$ as the uncertainties, obtained from the parameter distribution interval that contains 95% of the probability, as found with our Monte Carlo approach.

We used the Fourier cross-correlation method to derive the radial velocity of NH 84. The data were cross-correlated against the best-fit synthetic spectra using the FXCOR routine in IRAF. The measured heliocentric radial velocity for NH 84 is $v_{helio} = 128 \pm 30$ km s^{-1}, which is consistent with previous measurements of the systemic radial velocity of NGC 5466 found in the literature. Harris (1996) reported 110.7 km s^{-1}, while Shetrone et al. (2010) measured a weighted average value of 118.0 ± 0.4 km s^{-1} for 67 stars, and Lamb et al. (2015) obtained an average value of 121.05 km s^{-1} for 3 stars in NGC 5466. Hence our results are consistent with NH 84 being a kinematic cluster member.

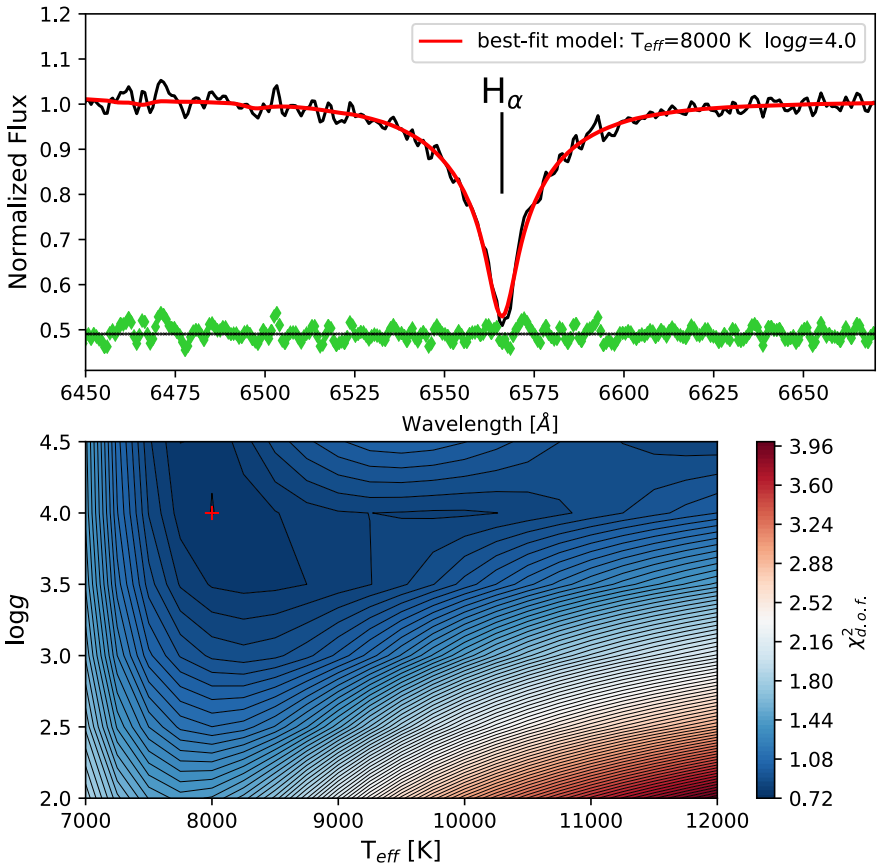

FIGURE 7.9: Top: GMOS-N spectrum of NH 84 around the H_α line. The best-fit model is shown in the red solid line and the residual values in green points. Bottom: Color map and contour plot of the reduced χ^2 as a function of T_{eff} and log g. The best-fit value is marked as a red cross in the upper left corner.

7.5 SED of BSSs

In order to understand the multi-wavelength energy budget of the FUV detected BSSs, we generated their SEDs and estimated the temperature, luminosity and radius. We used the virtual observatory tool, VOSA as explained in Chapter 3 for SED analysis. We used Kurucz stellar atmospheric models (Castelli et al. 1997; Castelli & Kurucz 2003) for the BSSs which cover the UV to IR wavelength range. We fixed the metallicity as [Fe/H] = −2.0, which is closer to the cluster metallicity value and varied the other two parameters (T_{eff} and log g) in the Kurucz models to fit the SED of the BSSs.

The SED of the BSS NH 84 was constructed by combining the flux measurements of UVIT (4 passbands) with GALEX (FUV and NUV), Gaia DR2 (3 passbands) (Gaia Collaboration et al. 2016, 2018a), KPNO (3 passbands), SDSS (4 passbands) (Ahn et al. 2012), and Pan-STARRS (2 passbands) (Chambers & Pan-STARRS Team 2018) surveys (upper panel, Figure 7.10) obtained from VO photometry. The number of photometric points used for constructing the SED of NH 84 is 16. The UV flux measurements of NH 84 along with the exposure times are given in Table 7.3. We found that fitting the full SED with a single Kurucz model spectrum of $T_{eff} = 8000 \pm 125$ K and $\log g = 4.0 \pm 0.5$ resulted in a large $\chi^2_{red} \sim 5.75$ for the given degrees of freedom (14). This is clear from the residual plot shown in the lower panel of Figure 7.10, which shows the difference between the observed flux and the synthetic flux normalised with respect to the observed flux, corresponding to the flux measurements in each passband. We find that the residual plot shows a rise in flux in the UV wavelengths for a single spectrum fit (shown as light-red empty triangles in the figure). Similarly, we checked the SEDs and the residual plot of other 13 BSSs as shown in Figures 7.11 and 7.12. If we find the residual to be more than 50% in the FUV wavelengths, we classify the BSS as having UV excess. We found that out of 14 BSSs, there are 6 BSSs which show UV excess. Our focus is on BSS NH 84 in this study as we have the radial velocity membership confirmation from our spectroscopic study (Section 7.4).

In order to address the UV-excess found in BSS NH 84, we generated a composite spectrum by combining the fluxes of Kurucz models for BSS (Castelli et al. 1997; Castelli & Kurucz 2003) and Koester WD models (Tremblay & Bergeron 2009) for the hot component. We independently obtained the SED fit parameters of the BSS using Kurucz models for a fixed metallicity ([Fe/H] $= -2.0$) considering wavelengths longer than 2000 $\mathring{A}$ and found that it is in agreement with the parameters obtained from spectra (Section 7.4). The SED fit parameters for the BSS are given in Table 7.4. The Gemini spectrum is consistent with the photometric flux measurements and the best fit composite model (grey line), as shown

TABLE 7.3: UV Flux measurements of BSS NH 84

Filter	Exposure time	Flux	Flux Error
	sec	erg cm^{-2} s^{-1} Å^{-1}	erg cm^{-2} s^{-1} Å^{-1}
		UVIT	
F148W	2609	5.12E-17	1.06E-17
F169M	6036	6.41E-17	7.96E-18
N245M	6091	9.87E-17	5.65E-18
N263M	4258	1.10E-16	8.29E-18
		GALEX	
FUV	1838	5.80E-17	6.45E-18
NUV	3529	1.19E-16	3.79E-18

in Figure 7.13. Note that the observed absorption features redward of the H_α line are telluric bands. Note also that the shown model (grey line) comes from very low resolution spectral models, which explains why the Balmer line shapes are not well matched, as compared to Figure 7.9. We found T_{eff} = 8000 K as the best fit value for the cool component from both the SED and the spectrum. Keeping the BSS parameters fixed, we varied the parameters of the Koester WD models assuming a log g = 7.5, to get the best fit combination for the full SED as given in Table 7.4.

The UV excess part of the SED fitted with a single Kurucz spectrum and composite spectrum are shown in a zoomed in plot of the SED (upper panel of Figure 7.10) where the light-red empty triangles indicate the single-component Kurucz synthetic flux and grey empty squares indicate the combined synthetic flux (Kurucz + Koester) in the respective FUV filters. When inspecting the zoomed in panel in Figure 7.10, the reader should focus their attention on the synthetic flux points (light-red empty triangles and grey empty squares) when comparing to the observed data points, instead of comparing to the solid-line model spectra, which

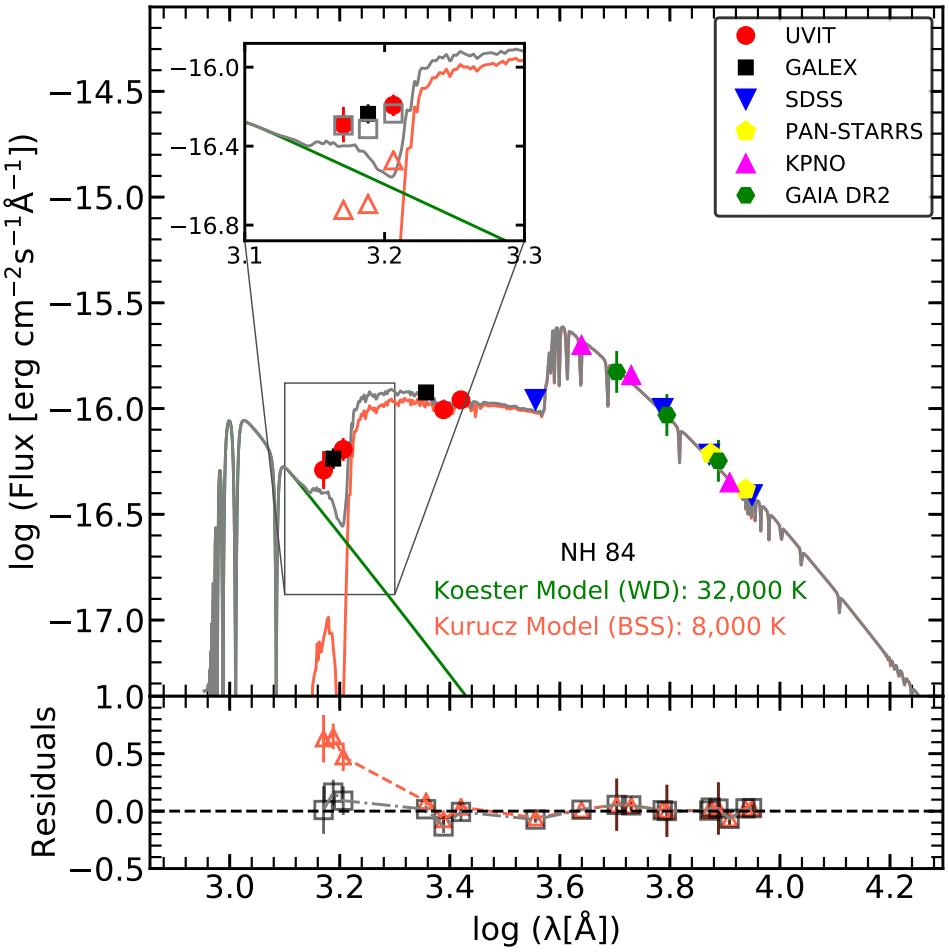

FIGURE 7.10: SED of NH 84 with a composite spectra (gray color) consisting of Kurucz model (light-red color) and Koester WD model (green color). The zoomed in plot shows the FUV part of the SED fitted with a single and composite spectrum where the light-red empty triangles indicate the Kurucz synthetic flux and grey empty squares indicate the combined synthetic flux. The residuals obtained with a single and composite spectrum fit are shown as light-red empty triangles and grey empty squares in the lower panel. See Section 7.5 for details.

give the misleading impression of a bad fit. Large residuals found for single spectrum fit reduce to almost zero with the composite spectrum fit, in particular for the residuals in the UV filters (shown as grey empty squares in the lower panel of Figure 7.10). Thus, NH 84 is found to have a hotter WD companion of temperature 32,000 ± 2000 K. The χ^2_{red} value for the composite spectrum of NH 84 is ∼ 1.62 corresponding to a 95% confidence level. We note that the largest non-zero residuals are still at the far blue end, where the WD fit is supposed to compensate.

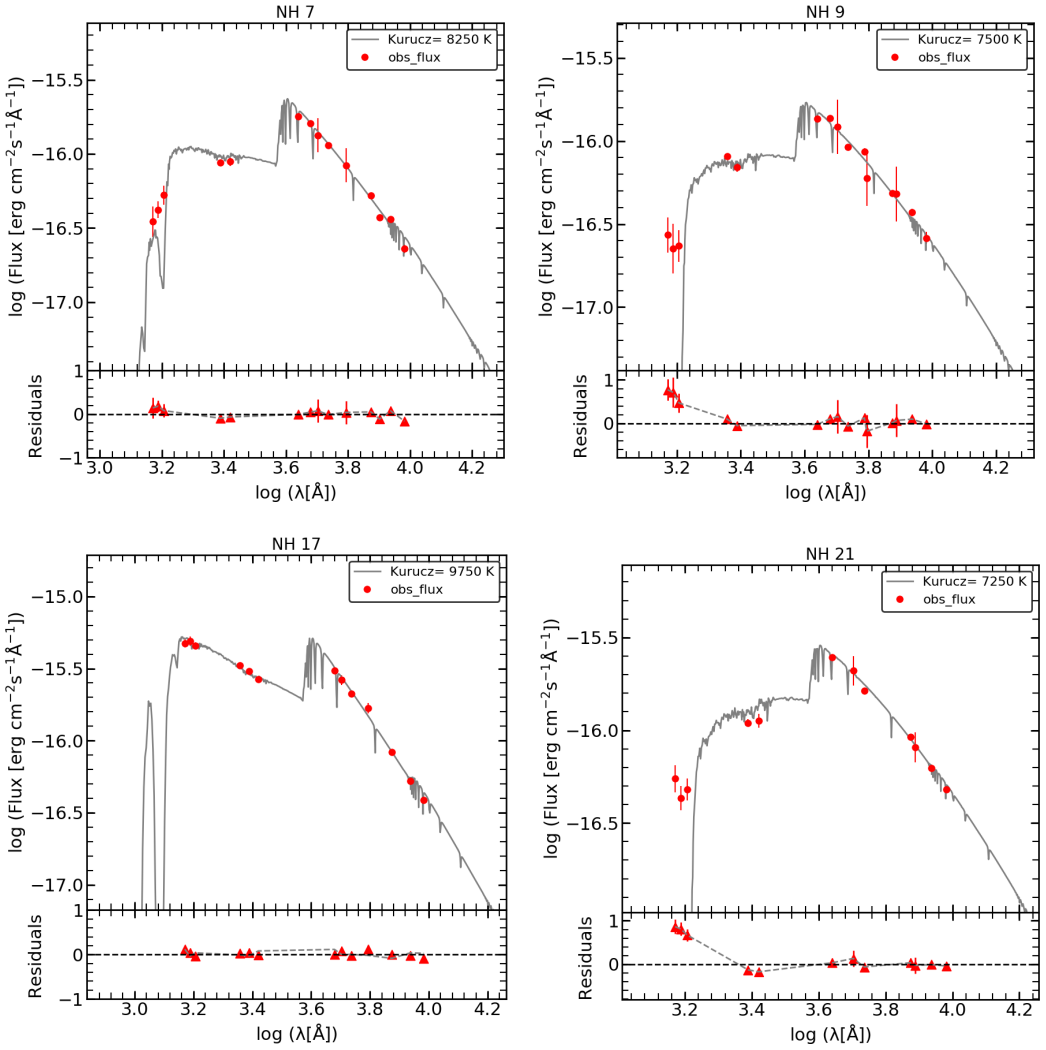

FIGURE 7.11: SEDs of FUV detected BSSs NH7, NH9, NH17 and NH 21 shown in top and bottom panels.

We estimated the basic parameters (luminosities and radii) of the components of BSS NH 84 using the values (T_{eff}, M_d) obtained from the SED fitting. For estimating the radii of the components, we used the relation of M_d as mentioned in Chapter 3 by adopting a distance of 16 ± 0.6 kpc (Arellano Ferro et al. 2008). The radius of the cool component of BSS NH 84 is ∼ 1.44 ± 0.05 $R_\odot$ whereas that of the hot component is ∼ 0.021 ± 0.001 $R_\odot$ which is close to the typical radii of WDs (Tremblay et al. 2017). The uncertainties in the radii are estimated using the equation $\Delta R = \frac{R\Delta D}{D}$ where, ΔD = 0.6 kpc taken from Arellano Ferro et al. (2008). We calculated the luminosities of the components of the BSS using

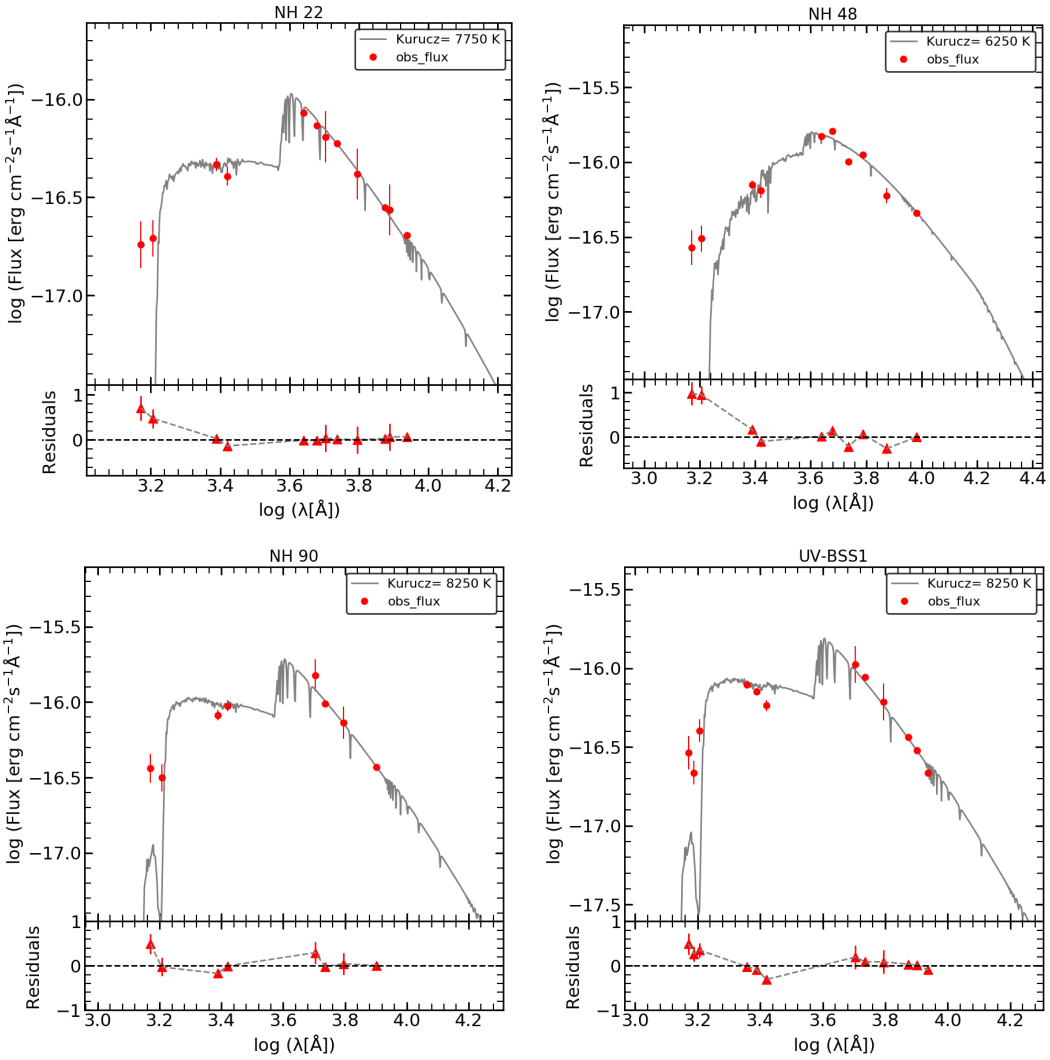

FIGURE 7.12: SEDs of FUV detected BSSs NH22, NH48, NH90 and UV-BSS1 shown in top and bottom panels.

Equation 3.14 in Chapter 3 by considering the parameters given in Table 7.4. The hot component has a luminosity of $\sim 0.42 \pm 0.11$ $L_{\odot}$ whereas the cool component has $\sim 7.58 \pm 1.10$ $L_{\odot}$.

Uncertainties in the WD parameters:

In order to evaluate the upper limit of uncertainty found in T_{eff} estimate of the BSS from spectroscopy (Section 7.4), we checked the SED fits for the BSS temperatures ranging from 8000 - 9000 K using Kurucz models. We found that

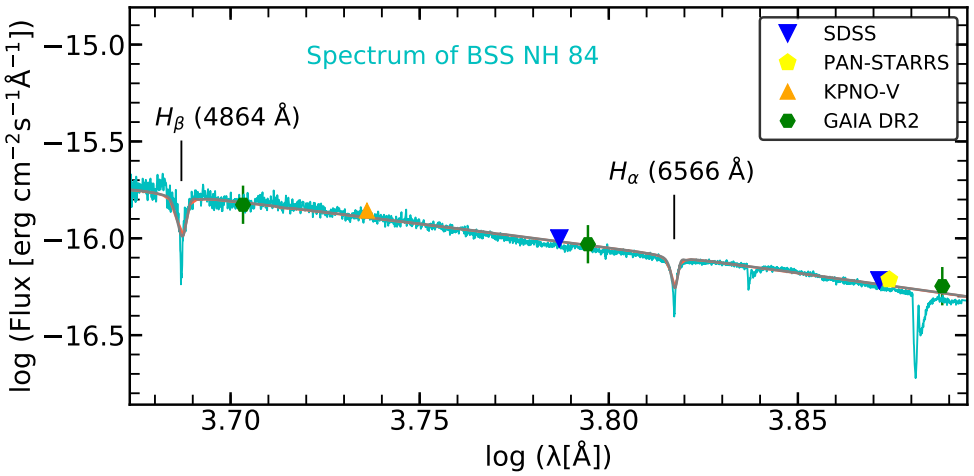

FIGURE 7.13: Gemini spectrum of NH 84 (cyan color) overplotted on the SED of NH 84. The wavelengths corresponding to H_α and H_β absorption lines of the BSS are marked in the figure. Note that the absorption features redward of the H_α line are telluric bands.

fitting the SED of the BSS with T_{eff} = 8250 K has less χ^2_{red} than that of 8000 K. Though, it brings down the residuals in the UV wavelengths to 30% from 50%, the individual χ^2 for the passband near the Balmer jump (KPNO B) increases with increasing T_{eff}. As the Balmer jump is very sensitive to T_{eff} of the cooler component, 8000 K is more appropriate for the T_{eff} of the BSS from the SED fits. We also note that, if we consider a T_{eff} of 8250 K for the BSS, then the best fitting parameters using Koester models (T_{eff} and R) are 30,000 K and 0.014 $R_\odot$ which are also consistent with the hot component being a WD. The total χ^2_{red} value increases for temperatures larger than 8250 K for the BSS.

The typical log g values for the WDs reported in the GCs (NGC 6397, NGC 6752, 47 Tuc), based on the spectra from earlier studies (Moehler et al. 2000, 2004; Knigge et al. 2008) lie in the range 7.5 - 7.8. The log g values available in the Koester models that fall in this range are 7.5 and 7.75. We found that, for a fixed temperature and scaling factor, the SED fit is insensitive to the above two log g values. This shows that the log g value is not well constrained by the SED fit. We calculated the mass of the WD for two different log values (7.5 and 7.75) using the relation:

TABLE 7.4: SED fit parameters of NH 84

Parameters	BSS	WD
T_{eff}	8000 ± 250 K	32000 ± 2000 K
log g	4.0 ± 0.5	7.5 - 7.75
M_d	4.1E-24	8.8E-28

$$\frac{M}{M_\odot} = \left(\frac{g}{g_\odot}\right)\left(\frac{R}{R_\odot}\right)^2 \tag{7.1}$$

For a fixed T_{eff} and R of the WD given in Table 7.4, we found that the mass of the WD varies from 0.5 - 0.9 $M_\odot$ for log g values of 7.5 and 7.75. We assumed log $g = 7.5$ in the SED fit as it corresponds to a WD mass $\sim 0.51\ M_\odot$ for the given radius, which is close to the average mass of WDs ($0.53 \pm 0.02\ M_\odot$) suggested in GCs (Renzini & Fusi Pecci 1988; Renzini et al. 1996).

7.6 Radial distribution of BSSs

We selected 86 HB stars that are PM members as a reference population for studying the radial distribution. The cumulative radial distribution of 66 BSSs and 86 HB stars are shown in the left panel of Figure 7.14. We can notice that the BSSs are more centrally concentrated than HB stars. According to the K-S test, the probability that BSSs and HB stars are drawn from the same population is negligible with p-value $\sim 5.7 \times 10^{-6}$.

We derived the specific frequency of BSSs (S_{BSS}) which is defined as the ratio of number of BSSs (N_{BSS}) to the number of HB stars (N_{HB}). To do this, we divided the observed cluster region into several concentric annuli and counted the

number of BSSs and HB stars in each radial bin which is given in Table 7.5. The radial annuli selected for this study are similar to those given by Beccari et al. (2013) except in the outermost annulus where the outer radius (R_{out}) of the radial bin is 850″ instead of 1400″. Besides, they used red giant stars as reference population instead of HB stars. The comparison of the number of BSSs found in each radial bin using our sample with those reported by Beccari et al. (2013) is also given in Table 7.5. The specific frequency of BSSs as a function of radial distance is shown in the right panel of Figure 7.14. We find that the distribution shows a first dip or minimum at $r_{min} \sim 180''$ which is in agreement with Beccari et al. (2013). This minimum is close to $1.5r_h$ of the cluster suggesting that the dynamical friction has affected the BSSs located in the internal regions ($< 1.5r_h$) causing them to segregate towards the cluster center. According to the study by Beccari et al. (2013), there was a rising trend in the distribution at $r < 500''$ unlike, the decreasing trend that we found in our study. This is because the number of BSSs in their sample with radial interval $200'' < r < 500''$ was 11 whereas it reduces to 5 in our sample after rejecting non-members. We do not find any upturn in the distribution at radial interval $500 < r < 850''$ which is subjected to large error due to poor statistics. This large error in the estimation along with the incomplete coverage (till radius $\sim 14'$) prevents us from confirming whether the rise in the upturn as reported in the earlier study is significant or not. Further, the presence of background contaminants suggests that extreme care has to be taken while selecting the BSSs that are located in the outer regions of the cluster.

7.7 Discussion

From the SED analysis, we found that 6 out of 14 BSSs show significant excess in UV, among which one is a known contact binary (NH 19) and one is a SX Phe variable (NH 49). We studied the UV excess of BSS NH 84 in detail, as we have

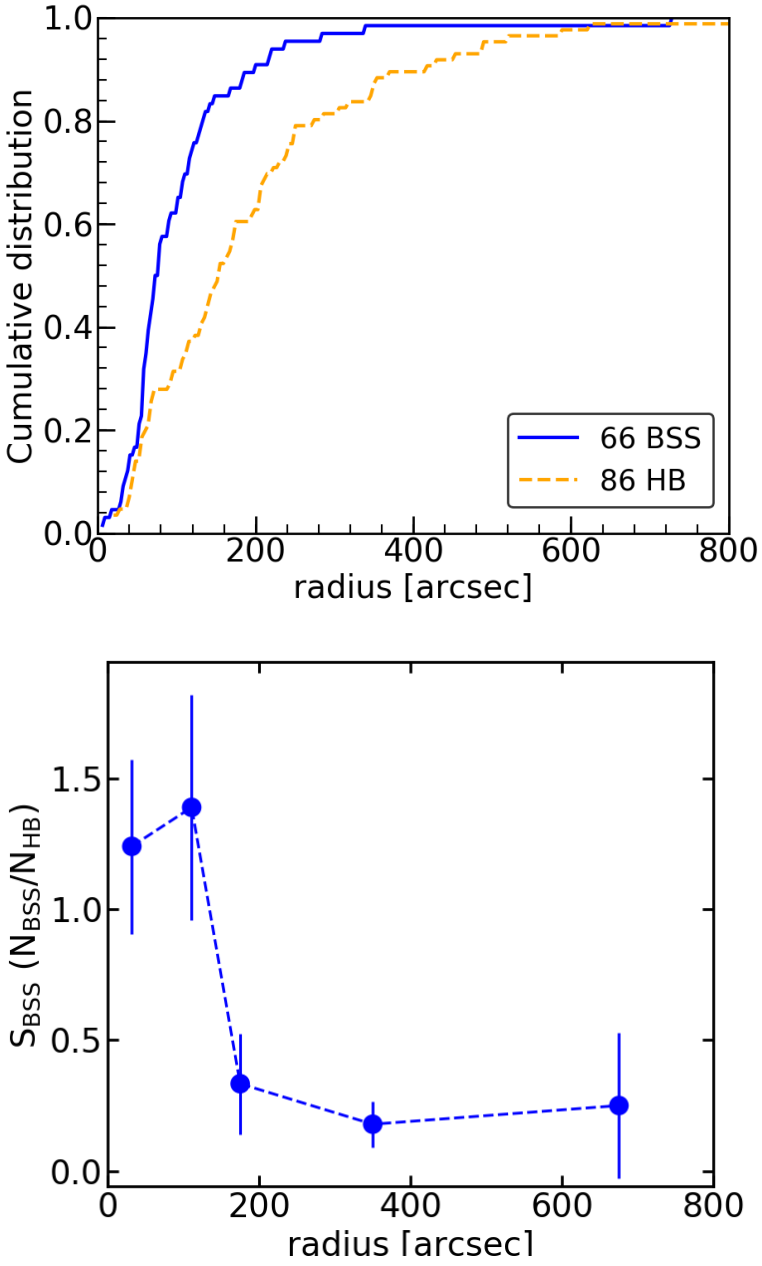

FIGURE 7.14: *Left:* Cumulative radial distribution of BSSs (blue line) and HB stars (orange dashed line) and *Right:* Specific frequency of BSSs i.e. S_{BSS} as a function of radial distance from cluster center.

TABLE 7.5: Number of BSSs and HB stars in the radial annuli that are considered to study the radial distribution of BSSs. R_{in} and R_{out} are the inner and outer radius of the radial bin selected for counting the BSSs and HB stars. Column 5 gives the number of BSSs detected by Beccari et al. (2013).

R''_{in}	R''_{out}	N_{BSS}	N_{HB}	$N_{BSS}^{Beccari}$
0	72	31	24	32
72	150	25	18	37
150	200	4	12	4
200	500	5	28	11
500	850	1	4	10*

*for $R''_{out} = 1400$ (Beccari et al. 2013)

the radial velocity measurements from Gemini spectra in addition to PM from Gaia DR2. The rest of the UV excess BSSs will be studied in detail in future.

The mass of the BSS NH 84 is ~ 1.1 $M_\odot$ when compared with the Padova isochrone (Figure 7.5). The mass of WD ranges from 0.5-0.9 $M_\odot$ as described in Section 7.5. This suggests that the hot component of the BSS NH 84 is more likely to be a C/O WD as inferred from the fit parameters and the associated uncertainties.

A comparison of the L and T_{eff} of the hot companion of BSS NH 84 with the Bergeron WD cooling models which are basically for C/O WDs (Tremblay et al. 2011) suggests that the mass of the WD varies from 0.45-0.62 $M_\odot$ with a cooling age $\sim$ 15 Myr. This indicates that the system might have recently undergone a MT. According to the initial-final mass relationship by (Althaus et al. 2015) for low metallicity systems (Z=0.0001), the progenitor mass corresponds to 0.8 $M_\odot$ for a final WD mass of ~ 0.51 $M_\odot$ ($\log g = 7.5$). This suggests that the progenitor mass is likely to be only slightly higher than the MSTO mass of the cluster. Thus, we speculate that the BSS could have formed as a result of a Case B or Case C MT (Paczyński 1971). The artistic illustration showing one possibility of how the BSS would have formed is shown in Figure 7.15.

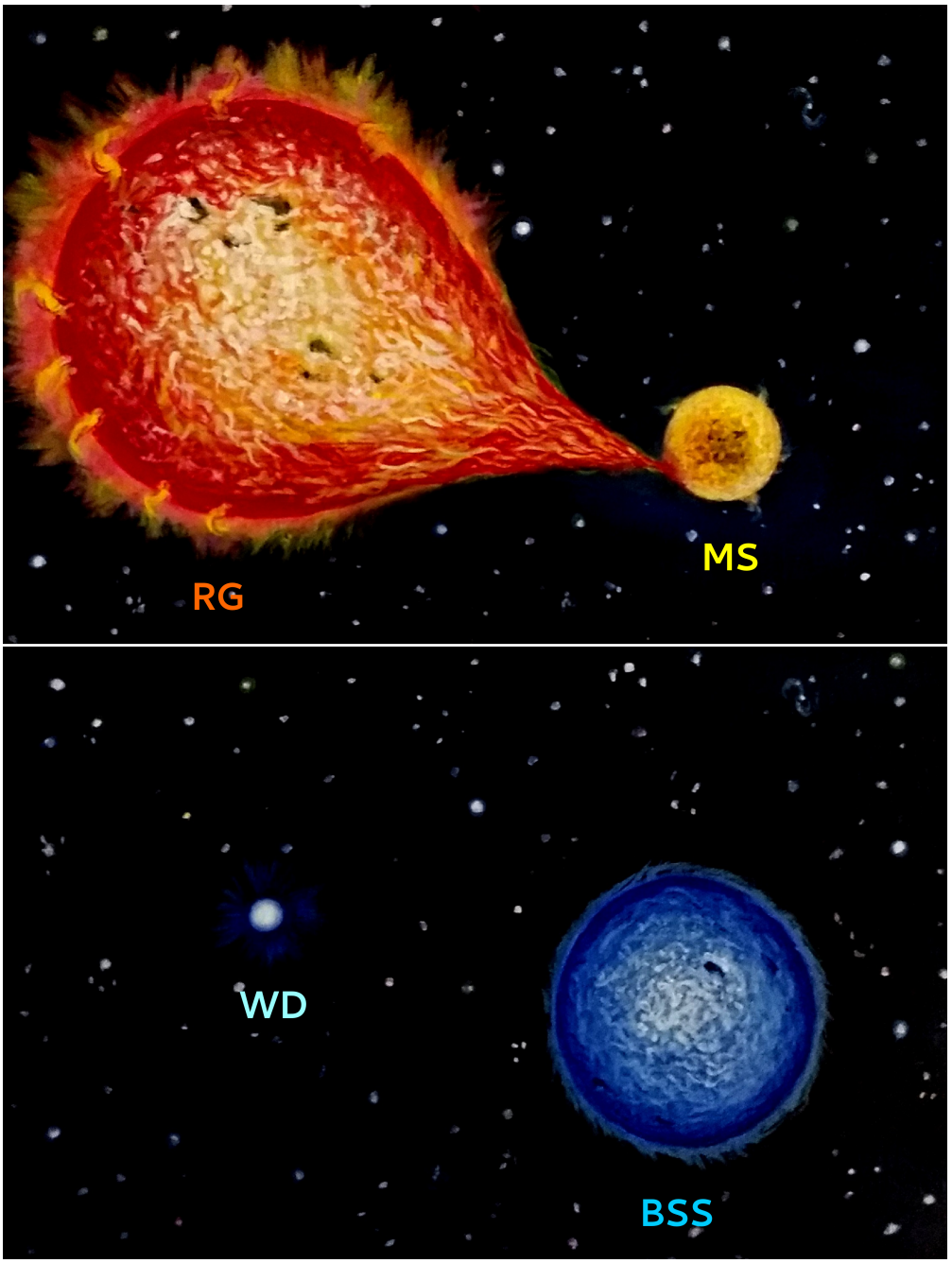

FIGURE 7.15: An art depicting the Case B MT where a MS star is sucking mass from its RGB companion that represents the past state of the NH 84 system (top) and its present state (bottom) where the MT has finished and the RGB and MS companion have evolved into a WD and a BSS respectively. Credit: Snehalata Sahu

The WD parameters obtained for BSS NH 84 are similar to the parameters derived by Knigge et al. (2008) for a BSS-WD system in 47 Tuc. This is the second BSS-WD system to be detected in a GC after the first detection of one such system in 47 Tuc (Knigge et al. 2008).

Of the 66 BSSs that are detected in NUV CMD and are found to be PM members, we find that $\sim 15\%$ of them reside outside $1r_h$ corresponding to 12 sources. From FUV CMDs, we have identified 14 BSSs where $\sim 14\%$ (2 BSSs) of the BSS population lie outside $1r_h$ of the cluster. This shows that the distribution of FUV detected BSSs is consistent with the distribution of NUV and optically identified BSSs in the cluster.

Beccari et al. (2013) found the radial distribution of BSSs in NGC 5466 to be bimodal with a centrally-concentrated and an outer BSS sub-population, with a minimum in the radial surface density distribution at about $r \approx 180''$. They estimated the binary fraction in the cluster outskirts ($400'' < r < 800''$) to be $\sim 5\%$. NH 84 is located at $r \approx 730''$ ($\sim 8.5r_c$, McLaughlin & van der Marel (2005a)) from the cluster center which is at half the distance of the tidal radius of the cluster ($r_t \sim 1580''$ (Miocchi et al. 2013)). They concluded that the unperturbed evolution of primordial binaries could be the dominant formation mechanism for the BSSs in the low density environments. According to Ferraro et al. (2012), NGC 5466 is in its dynamical infancy. The binaries present in the cluster outskirts has just recently begun to segregate towards the GC center. In light of the bimodal radial BSS density distribution, we speculate that NH 84 might be a MT binary system that has not yet experienced any significant dynamical interaction with the ambient stellar population and has evolved in relative isolation so far. The consistent picture of the location of NH 84 in NGC 5466 and its dynamical age together with the radially bimodal density distribution suggests that MT is one of the primary BSS formation mechanism in the low density environments (Knigge et al. 2009; Geller & Mathieu 2011; Leigh et al. 2013; Gosnell et al. 2014).

The $r_{min} \sim 180''$ in the radial distribution found in our study confirms the result of Beccari et al. (2013) that NGC 5466 is the second youngest in the category of dynamically intermediate-age clusters (Family II, as defined by Ferraro et al. (2012)). This implies that the innermost BSSs have already segregated towards the cluster center unlike, the outer ones which have not yet experienced the mass segregation and are evolving in isolation. In such cases, we should expect a bimodal radial distribution which is not found in our results. Fekadu et al. (2007) pointed out that the tidal stripping of the cluster could be responsible for causing the removal of BSSs from the cluster potential, that are located in the cluster outskirts. Therefore, we find a dearth of BSSs in the outer regions resulting in a unimodel radial distribution.

7.8 Summary and Conclusions

Our study demonstrates the significance of using UV photometry and membership information to study the BSS population. The important conclusion from our UV study on the BSSs in NGC 5466 are as follows:

1. We detected 14 BSSs in NGC 5466, all of which have measured fluxes in all four UVIT filters and are likely PM members according to Gaia DR2.

2. The parameters of the BSS NH 84 obtained from the GMOS-N spectrum are $T_{eff} = 8000^{+1000}_{-250}$K and log $g = 4.0 \pm 0.5$. It is a radial velocity ($\sim 128 \pm 30$ km/s) member.

3. The SED decomposition analysis found the presence of a hot component in the SED of BSS NH 84. The hot component is found to have a temperature of $T_{eff} = 32000 \pm 2000$ K and a radius ~ 0.02 $R_{\odot}$ suggesting it to be a WD.

4. NH 84 is the first BSS-WD candidate found in the outskirts of a low density GC. This is the second BSS-WD system reported in a GC. As NGC 5466 is a dynamically young cluster, this result suggests a MT pathway for BSS formation in low density environments.

5. We find that the BSSs are more centrally concentrated than HB stars from NUV CMDs. We also derived the specific frequency and found a unimodal radial distribution of the BSSs.

Chapter 8

Conclusions and Future Work

In this thesis, we identified and characterised the HB stars and BSSs, which are among the hot stellar populations found in GCs. This study generated UV as well as UV-optical CMDs for the entire GC by combining the UV data with other archival data mainly form the HST/ACS and the ground observations. The comparison of these CMDs with theoretical isochrones, helped in the identification of various evolutionary stages including the identification of EHB and BHk stars. In addition, the proper motion data from Gaia DR2 helped in confirming the membership of the UV detected stars in the cluster. Below we highlight the important results of the thesis that we have obtained from our study on three GCs.

8.1 HB morphology of GCs

- NGC 1851: We detected the bluest part of the HB in FUV whereas in NUV we detected the full extent of the HB, including the BHB, RHB and RR Lyrae stars. The RHBs show very tight distribution in the NUV whereas

the BHBs show a moderate scatter. We also detected UV variability of 18 RR Lyrae stars and found three new RR Lyrae candidates in the central regions of the cluster. We found certain BHB stars which form a hook-like structure in the FUV CMDs similar to the BHk stars.

- NGC 288: We identified several gaps in the BHB distribution from the FUV-optical CMDs. Based on the temperatures estimated from the UV-optical colors, we found two peaks in the temperature distribution of 110 BHB stars with a main peak at 10,300 K, with the distribution extending upto 18,000 K. We detected a plateau in the FUV magnitude for stars hotter than the G-jump (11,500 K) which could be caused by the atomic diffusion. In addition, we detected two EHB candidates based on their location in UV CMDs. In order to check whether they satisfy the criteria of being EHBs, we constructed SEDs and derived their physical parameters. Their T_{eff} were found to range from 29-32 kK and radii 0.2 $R_{\odot}$ confirming that they are EHB/subdwarfs.

Overall, our study on the HB morphology suggests that the observations in FUV filters are very useful for identifying the peculiarities in the GCs hosting bluer HB stars. Since, the slopes of the spectra of BHB stars are extremely sensitive in UV wavelengths, UV-optical colors (such as F148W−V) are recommended for estimating their temperatures from the models. UV observations should also be preferred for detecting the EHB, PAGB candidates that remain hidden in the optical CMDs. Identification and characterisation of these stars help in understanding the formation mechanism of these rare type of stars, found mainly in the crowded central regions of GCs. These stars also play an important role in the UV energy budget of old stellar population which include GCs as well as elliptical galaxies.

8.2 MSPs in GCs

We studied massive GC NGC 1851 as a test case for understanding the effect of MSPs among the HB stars. The comparison of isochrone of a single age, metallicity and He showed deviations from the observed bluer HB distribution in both the FUV and NUV CMDs which is discussed in Chapter 4. We varied parameters such as age, metallicity and Y_{ini} to check the cause for deviations using BaSTI and synthetic HB (Y^2) models. Our analysis suggested that the HB hosts two stellar populations with an age difference of either around 2 Gyr (BHBs being older than the RHBs) or an initial He difference of $\Delta Y_{ini} \sim 0.05$ (BHBs are more He rich than RHBs) for a metallicity of -1.2 to -1.3. The non-uniformity in the azimuthal distribution of the BHB and RHB stars supports the hypothesis of the cluster being a merger remnant.

In case of the low-density cluster NGC 288 which is known to have multiple RGBs, the BHB distribution in the FUV-optical CMDs matches well with the isochrone models till the G-jump after which the deviations arise, that are attributed to the onset of diffusion. In FUV$-$NUV and NUV$-$optical CMDs, deviations also exist for stars cooler than G-jump suggesting that these stars have relatively higher Mg abundances than the BHB stars hotter than G-jump. On the other hand, the isochrone of a single metallicity, age and Y_{ini} matches perfectly with the BHB distribution of another low-density cluster NGC 5466 in UV CMDs (that does not contain stars hotter than G-jump). Thus, we do not find any evidence of MSPs in the HB population of this cluster.

To conclude, our study on MSPs brings out the importance of UV CMDs for identifying the discrepancies between the model and observed HB distributions. This can in turn help to incorporate variations in the stellar evolutionary models for reproducing the observed HB and study the second parameter effect in GCs. It is important to fit the sub-giant branch and the MS, along with the HB stars,

to confirm the MSP and their parameters. We were able to detect the MS and sub-giant branch stars in the cluster NGC 288, in the NUV band. One of the draw backs which we found in this study is the inability of UVIT to detect the RHB, sub-giants and MS population in the FUV. More sensitive UV telescopes are needed to detect fainter population in the FUV.

8.3 BSSs in GCs

We studied the properties of BSSs in two low-density GCs, NGC 288 and NGC 5466 with similar r_c, r_h and relatively high binary fraction $> 6\%$ (Sollima et al. 2007) compared to other GCs. These clusters are fully resolved in FUV and NUV filters of UVIT. An estimation of the parameters of FUV detected BSSs from SEDs suggest that they mostly lie in a temperature range from 6250 to 8500 K. We found that Kurucz models of single T_{eff} cannot fit the entire SEDs of many BSSs, as they show excess UV flux. In order to explore the reason for excess UV flux, we studied an FUV bright BSS (NH 84) of NGC 5466 and analysed its SED in detail. We derived its physical parameters by obtaining optical spectra. Using these parameters, we did a multi-component SED fit and found that the BSS shows the presence of a hot companion of $T_{eff} \sim 32000K$ and $R \sim 0.02R_{\odot}$, suggesting it to be a WD (Chapter 7).

The NUV-optical CMD was chosen for selecting the BSS population to study its radial distribution. The cumulative radial distribution of the BSSs with respect to the HB stars in both the clusters show that the BSSs are more centrally concentrated than the HB stars. The specific frequency of the BSSs as a function of radius convey that the dynamical friction has affected the clusters till radii of $r_{min} \sim 180''$ and $240''$ for NGC 5466 and NGC 288 respectively that are nearly

1.5-1.7 r_h in both the cases. This also suggests that the clusters are of intermediate dynamical age. The overall specific frequency of BSSs is 0.56 and 0.77 for NGC 288 and NGC 5466 respectively. The large number of BSSs detected in these binary rich clusters which are known to have eclipsing and contact binaries suggest that the MT in primordial binaries could be the dominant formation channel of BSSs in these clusters.

Thus, our study on BSSs highlights the advantage of observing them in multiple filters of UVIT and identifying the presence of a hot companion to a BSS, which in turn can throw light on their formation mechanism. Our study shows that UVIT with Gaia and optical observations are suitable for the sample selection of member BSSs that are important for studying the radial distribution and hence the dynamical age of the clusters.

8.4 Future perspectives

This thesis demonstrates that UVIT photometry, in combination with the optical data (HST/ground) and Gaia, can be a powerful tool for studying hot stars in GGCs. To study the CMDs of more such GCs using UVIT, we have carried out a UVIT Legacy survey of GCs (GlobULeS). The main aim of this survey is i) to present a complete FUV-optical CMDs of GCs by combining with HST, Gaia and other ground observations, ii) to test the stellar evolutionary models in the UV, iii) to study the HB morphology and the peculiarities in the HB distribution, and iv) to identify the UV counterparts of the exotic stars such as BSSs.

The list of GCs in the survey with program ID A04_011, A05_072, A06_005 along with their observational details are provided in Table 8.1. The list of other clusters (NGC 362, NGC 1904, NGC 5272, NGC 104) which are not part of survey but

TABLE 8.1: List of GCs observed with UVIT under GlobULeS survey and other programs. The work that are part of the thesis are marked in bold.

Clusters	R.A. (h m s)*	Dec (d m s)*	[Fe/H]*	HB type	Proposal ID	UVIT Channel
NGC 1851	**05 14 06.76**	**-40 02 47.6**	**−1.18**	**BHB, RHB**	**T01_071**	**FUV, NUV**
NGC 288	**00 52 45.24**	**-26 34 57.4**	**-1.32**	**BHB**	**G05_009**	**FUV, NUV**
NGC 5466	**14 05 27.29**	**+28 32 04.0**	**-1.98**	**BHB**	**G05_009**	**FUV, NUV**
NGC362	01 03 14.26	-70 50 55.6	-1.26	RHB, few BHB	G06_130	FUV, NUV
NGC 1904	05 24 11.09	-24 31 29.0	-1.6	BHB,EHB	A02_152	FUV, NUV
NGC 5272	13 42 11.62	+28 22 38.2	-1.5	BHB,RHB	A05_083	FUV
NGC 104	00 24 05.67	-72 04 52.6	-0.72	RHB	A05_078	FUV
NGC 5897	15 17 24.50	-21 00 37.0	-1.9	BHB	A04_011	FUV
NGC 6341	17 17 07.39	+43 08 09.4	-2.31	BHB	A04_011	FUV
NGC 6809	19 39 59.71	-30 57 53.1	-1.94	BHB	A05_072	FUV
NGC 5024	13 12 55.25	+18 10 05.4	-2.1	BHB	A05_072	FUV
NGC 3201	10 17 36.82	-46 24 44.9	-1.59	RHB, few BHB	A06_005	FUV
NGC 5286	13 46 26.81	-51 22 27.3	-1.69	BHB, EHB	A06_005	FUV
NGC 5986	15 46 03.00	-37 47 11.1	-1.59	BHB, EHB	A06_005	FUV
NGC 6723	18 59 33.15	-36 37 56.1	-1.1	BHB,RHB	A06_005	FUV

*Harris (1996, 2010)

are observed under a separate program are also given. The observations of all the clusters under the survey are just completed as of September 2019 and the data of some of the clusters have been already released. The clusters under GlobULeS survey have only FUV observations, as the NUV channel is not available. Most of the clusters in the list are metal-poor ([Fe/H] < -1.5) and contain BHB and other hot HB stars such as EHB and BHk stars.

The data reduction of the clusters NGC 362, NGC 5272, NGC 1904 are complete. We are currently analysing the data of NGC 362 which is a second parameter pair to the cluster NGC 288 which is presented in this thesis. These clusters have similar metallicity and age but very different HB morphology, the cause of which is not yet understood. We plan to generate synthetic HB models in UV filters to check the effect of other parameters such as variation in He content, mass loss in the HB distribution etc.,. with the aim of shining light on the second parameter

problem in GCs.

In order to verify the evolutionary status of the two EHB stars and one bright gap object detected in NGC 288 (Chapter 5), we have proposed for their spectroscopic observations with FORS2 spectrograph in VLT, ESO. NGC 288 is at the very low-mass/low helium end of GCs where BHk stars have been found so far. Finding BHk stars in such an environment would raise new questions about the evolutionary status of these stars and also about the history and status of the cluster itself. Spectroscopy will allow us to determine their physical parameters and compare them to those observed in the massive GCs ω Cen and NGC 2808.

Bibliography

Ahn, C. P., Alexandroff, R., Allende Prieto, C., et al. 2012, *Astrophysical Journal Supplement*, 203, 21

Alam, S., Albareti, F. D., Allende Prieto, C., et al. 2015, The Astrophysical Journal Supplement Series, 219, 12

Althaus, L. G., Camisassa, M. E., Miller Bertolami, M. M., Córsico, A. H., & García-Berro, E. 2015, *Astronomy and Astrophysics*, 576, A9

Arellano Ferro, A., Bramich, D. M., Giridhar, S., et al. 2013, Acta Astronomica, 63, 429

Arellano Ferro, A., Rojas López, V., Giridhar, S., & Bramich, D. M. 2008, *Monthly Notices of the Royal Astronomical Society*, 384, 1444

Assmann, P., Fellhauer, M., Kroupa, P., Brüns, R. C., & Smith, R. 2011, *Monthly Notices of the Royal Astronomical Society*, 415, 1280

Bastian, N., & Lardo, C. 2018, *Annual Reviews of Astronomy and Astrophysics*, 56, 83

Bayo, A., Rodrigo, C., Barrado Y Navascués, D., et al. 2008, *Astronomy and Astrophysics*, 492, 277

Beccari, G., Dalessandro, E., Lanzoni, B., et al. 2013, *Astrophysical Journal*, 776, 60

Bedin, L. R., Piotto, G., Anderson, J., et al. 2004, Memorie della Societa Astronomica Italiana Supplementi, 5, 105

Behr, B. B. 2003, *Astrophysical Journal Supplement*, 149, 67

Bellazzini, M., Fusi Pecci, F., Messineo, M., Monaco, L., & Rood, R. T. 2002, *Astronomical Journal*, 123, 1509

Bellazzini, M., & Messineo, M. 2000, in Astrophysics and Space Science Library, Vol. 255, Astrophysics and Space Science Library, ed. F. Matteucci & F. Giovannelli, 213

Bellazzini, M., Pecci, F. F., Ferraro, F. R., et al. 2001, *Astronomical Journal*, 122, 2569

Bellini, A., Bedin, L. R., Piotto, G., et al. 2010, *Astronomical Journal*, 140, 631

Belokurov, V., Evans, N. W., Irwin, M. J., Hewett, P. C., & Wilkinson, M. I. 2006, *Astrophysical Journal Letters*, 637, L29

Bertola, F., Capaccioli, M., & Oke, J. B. 1982, *Astrophysical Journal*, 254, 494

Brodie, J. P., & Strader, J. 2006, *Annual Reviews of Astronomy and Astrophysics*, 44, 193

Brown, T. M., Ferguson, H. C., Davidsen, A. F., & Dorman, B. 1997, *Astrophysical Journal*, 482, 685

Brown, T. M., Sweigart, A. V., Lanz, T., Land sman, W. B., & Hubeny, I. 2001, *Astrophysical Journal*, 562, 368

Brown, T. M., Ferguson, H. C., Smith, E., et al. 2005, The Astronomical Journal, 130, 1693

Brown, T. M., Cassisi, S., D'Antona, F., et al. 2016, *Astrophysical Journal*, 822, 44

Buonanno, R., Corsi, C. E., Pecci, F. F., Liller, W., & Alcaino, G. 1984, *Astrophysical Journal*, 277, 220

Burbidge, E. M., & Sandage, A. 1958, *Astrophysical Journal*, 128, 174

Cannon, R. D. 1974, *Monthly Notices of the Royal Astronomical Society*, 167, 551

Cappellari, M. 2017, *Monthly Notices of the Royal Astronomical Society*, 466, 798

Carretta, E., Bragaglia, A., Gratton, R., & Lucatello, S. 2009, *Astronomy and Astrophysics*, 505, 139

Carretta, E., Lucatello, S., Gratton, R. G., Bragaglia, A., & D'Orazi, V. 2011, *Astronomy and Astrophysics*, 533, A69

Cassisi, S., Salaris, M., Pietrinferni, A., et al. 2008, *Astrophysical Journal Letters*, 672, L115

Castelli, F., Gratton, R. G., & Kurucz, R. L. 1997, *Astronomy and Astrophysics*, 318, 841

Castelli, F., & Kurucz, R. L. 2003, in IAU Symposium, Vol. 210, Modelling of Stellar Atmospheres, ed. N. Piskunov, W. W. Weiss, & D. F. Gray, A20

Catelan, M., Bellazzini, M., Landsman, W. B., et al. 2001, *Astronomical Journal*, 122, 3171

Chambers, K., & Pan-STARRS Team. 2018, in American Astronomical Society Meeting Abstracts, Vol. 231, American Astronomical Society Meeting Abstracts #231, 102.01

Chandrasekhar, S. 1943, *Astrophysical Journal*, 97, 255

Chen, X., & Han, Z. 2008, *Monthly Notices of the Royal Astronomical Society*, 387, 1416

Chung, C., Yoon, S.-J., & Lee, Y.-W. 2017, *Astrophysical Journal*, 842, 91

Code, A. D., & Welch, G. A. 1979, *Astrophysical Journal*, 228, 95

Coelho, P. R. T. 2014, *Monthly Notices of the Royal Astronomical Society*, 440, 1027

Cohen, R. E., & Sarajedini, A. 2011, Monthly Notices of the Royal Astronomical Society, 419, 342. https://doi.org/10.1111/j.1365-2966.2011.19697.x

Conroy, C., & Gunn, J. E. 2010, *Astrophysical Journal*, 712, 833

Conroy, C., Gunn, J. E., & White, M. 2009, *Astrophysical Journal*, 699, 486

Dalessandro, E., Salaris, M., Ferraro, F. R., et al. 2011, *Monthly Notices of the Royal Astronomical Society*, 410, 694

Decressin, T., Meynet, G., Charbonnel, C., Prantzos, N., & Ekström, S. 2007, *Astronomy and Astrophysics*, 464, 1029

D'Ercole, A., Vesperini, E., D'Antona, F., McMillan, S. L. W., & Recchi, S. 2008, *Monthly Notices of the Royal Astronomical Society*, 391, 825

Dieball, A., Long, K. S., Knigge, C., Thomson, G. S., & Zurek, D. R. 2010, *Astrophysical Journal*, 710, 332

Dinescu, D. I., Girard, T. M., van Altena, W. F., Mendez, R. A., & Lopez, C. E. 1997, *Astronomical Journal*, 114, 1014

Dotter, A., Sarajedini, A., Anderson, J., et al. 2010, *Astrophysical Journal*, 708, 698

Downes, R. A., Margon, B., Homer, L., & Anderson, S. F. 2004, *Astronomical Journal*, 128, 2288

Eggleton, P. P., & Kisseleva-Eggleton, L. 2006, Astrophysics and Space Science, 304, 75

Fabrycky, D., & Tremaine, S. 2007, *Astrophysical Journal*, 669, 1298

Fekadu, N., Sandquist, E. L., & Bolte, M. 2007, *Astrophysical Journal*, 663, 277

Ferraro, F. R., Lapenna, E., Mucciarelli, A., et al. 2016, *Astrophysical Journal*, 816, 70

Ferraro, F. R., Paltrinieri, B., Fusi Pecci, F., Rood, R. T., & Dorman, B. 1998, *Astrophysical Journal*, 500, 311

Ferraro, F. R., Pecci, F. F., Cacciari, C., et al. 1993, *Astronomical Journal*, 106, 2324

Ferraro, F. R., Sills, A., Rood, R. T., Paltrinieri, B., & Buonanno, R. 2003, *Astrophysical Journal*, 588, 464

Ferraro, F. R., Lanzoni, B., Dalessandro, E., et al. 2012, *Nature*, 492, 393

Fiorentino, G., Marconi, M., Bono, G., et al. 2015, *Astrophysical Journal*, 810, 15

Flesch, E. W. 2015, Publications of the Astronomical Society of Australia, 32, e010

Flewelling, H. A., Magnier, E. A., Chambers, K. C., et al. 2016, arXiv e-prints, arXiv:1612.05243

Fusi Pecci, F., Ferraro, F. R., Corsi, C. E., Cacciari, C., & Buonanno, R. 1992, *Astronomical Journal*, 104, 1831

Gaia Collaboration, Brown, A. G. A., Vallenari, A., et al. 2018a, ArXiv e-prints, arXiv:1804.09365

Gaia Collaboration, Prusti, T., de Bruijne, J. H. J., et al. 2016, *Astronomy and Astrophysics*, 595, A1

Gaia Collaboration, Helmi, A., van Leeuwen, F., et al. 2018b, *Astronomy and Astrophysics*, 616, A12

—. 2018c, *Astronomy and Astrophysics*, 616, A12

Geller, A. M., & Mathieu, R. D. 2011, *Nature*, 478, 356

Goldsbury, R., Richer, H. B., Anderson, J., et al. 2010, *Astronomical Journal*, 140, 1830

Gosnell, N. M., Mathieu, R. D., Geller, A. M., et al. 2014, *Astrophysical Journal Letters*, 783, L8

Gratton, R. G., Lucatello, S., Carretta, E., et al. 2012, *Astronomy and Astrophysics*, 539, A19

Grillmair, C. J., & Johnson, R. 2006, *Astrophysical Journal Letters*, 639, L17

Grundahl, F., Catelan, M., Landsman, W. B., Stetson, P. B., & Andersen, M. I. 1999, *Astrophysical Journal*, 524, 242

Han, S.-I., Lee, Y.-W., Joo, S.-J., et al. 2009, *Astrophysical Journal Letters*, 707, L190

Harris, W. E. 1996, *Astronomical Journal*, 112, 1487

—. 2010, ArXiv e-prints, arXiv:1012.3224

Haurberg, N. C., Lubell, G. M. G., Cohn, H. N., et al. 2010, *Astrophysical Journal*, 722, 158

Heber, U. 1986, *Astronomy and Astrophysics*, 155, 33

Hills, J. G., & Day, C. A. 1976, *Astrophysical Journal Letters*, 17, 87

Hutchings, J. B., Postma, J., Asquin, D., & Leahy, D. 2007, *Publications of the Astronomical Society of the Pacific*, 119, 1152

Jeon, Y.-B., Lee, M. G., Kim, S.-L., & Lee, H. 2004, *Astronomical Journal*, 128, 287

Joo, S.-J., & Lee, Y.-W. 2013, *Astrophysical Journal*, 762, 36

Kaluzny, J. 1996, *Astronomy and Astrophysics Supplement*, 120, 83

Kaluzny, J., Krzeminski, W., & Nalezyty, M. 1997, *Astronomy and Astrophysics Supplement*, 125, 337

Khalack, V., LeBlanc, F., & Behr, B. B. 2010, *Monthly Notices of the Royal Astronomical Society*, 407, 1767

Kippenhahn, R., & Weigert, A. 1967, Z. Astrophys., 65, 251

Knigge, C., Dieball, A., Maíz Apellániz, J., et al. 2008, *Astrophysical Journal*, 683, 1006

Knigge, C., Leigh, N., & Sills, A. 2009, *Nature*, 457, 288

Koester, D. 2010, Mem. Societa Astronomica Italiana, 81, 921

Kong, A. K. H., Bassa, C., Pooley, D., et al. 2006, *Astrophysical Journal*, 647, 1065

Kozai, Y. 1962, *Astronomical Journal*, 67, 591

Krauss, L. M., & Chaboyer, B. 2003, Science, 299, 65

Kumar, A., Ghosh, S. K., Hutchings, J., et al. 2012, in Society of Photo-Optical Instrumentation Engineers (SPIE) Conference Series, Vol. 8443, *Proceedings of SPIE*, 84431N

Kunder, A., Salaris, M., Cassisi, S., et al. 2013, *Astronomical Journal*, 145, 25

Kurucz, R. 1993, ATLAS9 Stellar Atmosphere Programs and 2 km/s grid. Kurucz CD-ROM No. 13. Cambridge, Mass.: Smithsonian Astrophysical Observatory, 1993., 13

Lagioia, E. P., Dalessandro, E., Ferraro, F. R., et al. 2015, *Astrophysical Journal*, 800, 52

Lamb, M. P., Venn, K. A., Shetrone, M. D., Sakari, C. M., & Pritzl, B. J. 2015, *Monthly Notices of the Royal Astronomical Society*, 448, 42

Lanzoni, B., Ferraro, F. R., Alessandrini, E., et al. 2016, *Astrophysical Journal Letters*, 833, L29

Lee, Y.-W., Joo, S.-J., Han, S.-I., et al. 2015, Highlights of Astronomy, 16, 247

Leigh, N., Knigge, C., Sills, A., et al. 2013, *Monthly Notices of the Royal Astronomical Society*, 428, 897

Leon, S., Meylan, G., & Combes, F. 2000, *Astronomy and Astrophysics*, 359, 907

Lidov, M. L. 1962, Planetary and Space Science, 9, 719

Mapelli, M., Sigurdsson, S., Colpi, M., et al. 2004, *Astrophysical Journal Letters*, 605, L29

Marigo, P., & Girardi, L. 2007, *Astronomy and Astrophysics*, 469, 239

Marigo, P., Girardi, L., Bressan, A., et al. 2008, *Astronomy and Astrophysics*, 482, 883

Marino, A. F., Villanova, S., Piotto, G., et al. 2008, *Astronomy and Astrophysics*, 490, 625

Marino, A. F., Milone, A. P., Przybilla, N., et al. 2013, Monthly Notices of the Royal Astronomical Society, 437, 1609. `https://doi.org/10.1093/mnras/stt1993`

Martinazzi, E., Kepler, S. O., Costa, J. E. S., et al. 2015, *Monthly Notices of the Royal Astronomical Society*, 447, 2235

Mateo, M., Harris, H. C., Nemec, J., & Olszewski, E. W. 1990, *Astronomical Journal*, 100, 469

McCrea, W. H. 1964, *Monthly Notices of the Royal Astronomical Society*, 128, 147

McLaughlin, D. E., & van der Marel, R. P. 2005a, *Astrophysical Journal Supplement*, 161, 304

—. 2005b, *Astrophysical Journal Supplement*, 161, 304

Milone, A. P., Bedin, L. R., Piotto, G., et al. 2008, *Astrophysical Journal*, 673, 241

Milone, A. P., Marino, A. F., Piotto, G., et al. 2015, *Astrophysical Journal*, 808, 51

Miocchi, P., Lanzoni, B., Ferraro, F. R., et al. 2013, *Astrophysical Journal*, 774, 151

Moehler, S., Dreizler, S., LeBlanc, F., et al. 2014, *Astronomy and Astrophysics*, 565, A100

Moehler, S., Koester, D., Zoccali, M., et al. 2004, *Astronomy and Astrophysics*, 420, 515

Moehler, S., Sweigart, A. V., Landsman, W. B., & Heber, U. 2000, *Astronomy and Astrophysics*, 360, 120

Moehler, S., Sweigart, A. V., Landsman, W. B., Heber, U., & Catelan, M. 1999, *Astronomy and Astrophysics*, 346, L1

Momany, Y., Bedin, L. R., Cassisi, S., et al. 2004, *Astronomy and Astrophysics*, 420, 605

Momany, Y., Piotto, G., Recio-Blanco, A., et al. 2002, *Astrophysical Journal Letters*, 576, L65

Morrissey, P., Conrow, T., Barlow, T. A., et al. 2007, *Astrophysical Journal Supplement*, 173, 682

Nemec, J., & Mateo, M. 1990, in Astronomical Society of the Pacific Conference Series, Vol. 11, Confrontation Between Stellar Pulsation and Evolution, ed. C. Cacciari & G. Clementini, 64–84

Nemec, J. M., & Harris, H. C. 1987, *Astrophysical Journal*, 316, 172

Olszewski, E. W., Saha, A., Knezek, P., et al. 2009, *Astronomical Journal*, 138, 1570

Pace, G., Recio-Blanco, A., Piotto, G., & Momany, Y. 2006, *Astronomy and Astrophysics*, 452, 493

Paczyński, B. 1971, *Annual Reviews of Astronomy and Astrophysics*, 9, 183

Paust, N. E. Q., Reid, I. N., Piotto, G., et al. 2010, *Astronomical Journal*, 139, 476

Perets, H. B., & Fabrycky, D. C. 2009, *Astrophysical Journal*, 697, 1048

Pietrinferni, A., Cassisi, S., Salaris, M., & Castelli, F. 2004, *Astrophysical Journal*, 612, 168

Piotto, G., Milone, A. P., Marino, A. F., et al. 2013, *Astrophysical Journal*, 775, 15

Piotto, G., Zoccali, M., King, I. R., et al. 1999, *Astronomical Journal*, 118, 1727

Piotto, G., De Angeli, F., King, I. R., et al. 2004, *Astrophysical Journal Letters*, 604, L109

Piotto, G., Bedin, L. R., Anderson, J., et al. 2007, *Astrophysical Journal Letters*, 661, L53

Piotto, G., Milone, A. P., Anderson, J., et al. 2012, *Astrophysical Journal*, 760, 39

Piotto, G., Milone, A. P., Bedin, L. R., et al. 2015, *Astronomical Journal*, 149, 91

Podsiadlowski, P., Han, Z., Lynas-Gray, A. E., & Brown, D. 2008, in Astronomical Society of the Pacific Conference Series, Vol. 392, Hot Subdwarf Stars and Related Objects, ed. U. Heber, C. S. Jeffery, & R. Napiwotzki, 15

Postma, J., Hutchings, J. B., & Leahy, D. 2011, *Publications of the Astronomical Society of the Pacific*, 123, 833

Postma, J. E., & Leahy, D. 2017, *Publications of the Astronomical Society of the Pacific*, 129, 115002

Prantzos, N., & Charbonnel, C. 2006, *Astronomy and Astrophysics*, 458, 135

Raso, S., Ferraro, F. R., Dalessandro, E., et al. 2017, *Astrophysical Journal*, 839, 64

Reimers, D. 1977, *Astronomy and Astrophysics*, 57, 395

Renzini, A., & Fusi Pecci, F. 1988, *Annual Reviews of Astronomy and Astrophysics*, 26, 199

Renzini, A., Bragaglia, A., Ferraro, F. R., et al. 1996, *Astrophysical Journal Letters*, 465, L23

Robitaille, T. P., Whitney, B. A., Indebetouw, R., & Wood, K. 2007, *Astrophysical Journal Supplement*, 169, 328

Sabbi, E., Ferraro, F. R., Sills, A., & Rood, R. T. 2004, *Astrophysical Journal*, 617, 1296

Sahu, S., Subramaniam, A., Côté, P., Rao, N. K., & Stetson, P. B. 2019a, *Monthly Notices of the Royal Astronomical Society*, 482, 1080

Sahu, S., Subramaniam, A., Simunovic, M., et al. 2019b, *Astrophysical Journal*, 876, 34

Salaris, M., Cassisi, S., & Pietrinferni, A. 2008, *Astrophysical Journal Letters*, 678, L25

Sandage, A., & Wallerstein, G. 1960, *Astrophysical Journal*, 131, 598

Sandage, A., & Wildey, R. 1967, *Astrophysical Journal*, 150, 469

Sandage, A. R. 1953, *Astronomical Journal*, 58, 61

Sarajedini, A., Bedin, L. R., Chaboyer, B., et al. 2007, *Astronomical Journal*, 133, 1658

Schiavon, R. P., Dalessandro, E., Sohn, S. T., et al. 2012, *Astronomical Journal*, 143, 121

Shetrone, M., Martell, S. L., Wilkerson, R., et al. 2010, *Astronomical Journal*, 140, 1119

Simunovic, M., & Puzia, T. H. 2016, *Monthly Notices of the Royal Astronomical Society*, 462, 3401

Sirianni, M., Jee, M. J., Benítez, N., et al. 2005, *Publications of the Astronomical Society of the Pacific*, 117, 1049

Sollima, A., Beccari, G., Ferraro, F. R., Fusi Pecci, F., & Sarajedini, A. 2007, Monthly Notices of the Royal Astronomical Society, 380, 781. `https://doi.org/10.1111/j.1365-2966.2007.12116.x`

Sollima, A., Ferraro, F. R., Pancino, E., & Bellazzini, M. 2005, *Monthly Notices of the Royal Astronomical Society*, 357, 265

Stetson, P. B. 1987, *Publications of the Astronomical Society of the Pacific*, 99, 191

—. 1990, *Publications of the Astronomical Society of the Pacific*, 102, 932

Subramaniam, A., Tandon, S. N., Hutchings, J., et al. 2016, in *Proceedings of SPIE*, Vol. 9905, Space Telescopes and Instrumentation 2016: Ultraviolet to Gamma Ray, 99051F

Subramaniam, A., Sahu, S., Postma, J. E., et al. 2017, *Astronomical Journal*, 154, 233

Sweigart, A. V. 1987, *Astrophysical Journal Supplement*, 65, 95

—. 2002, Highlights of Astronomy, 12, 292

Tandon, S. N., Hutchings, J. B., Ghosh, S. K., et al. 2017a, Journal of Astrophysics and Astronomy, 38, 28

Tandon, S. N., Subramaniam, A., Girish, V., et al. 2017b, *Astronomical Journal*, 154, 128

Taylor, M. 2011, TOPCAT: Tool for OPerations on Catalogues And Tables, Astrophysics Source Code Library, , , ascl:1101.010

Tonry, J. L., Stubbs, C. W., Lykke, K. R., et al. 2012, *Astrophysical Journal*, 750, 99

Tremblay, P.-E., & Bergeron, P. 2009, *Astrophysical Journal*, 696, 1755

Tremblay, P.-E., Bergeron, P., & Gianninas, A. 2011, *Astrophysical Journal*, 730, 128

Tremblay, P.-E., Gentile-Fusillo, N., Raddi, R., et al. 2017, *Monthly Notices of the Royal Astronomical Society*, 465, 2849

van den Bergh, S. 1993, *Astronomical Journal*, 105, 971

van Leeuwen, F., de Bruijne, J. H. J., Arenou, F., et al. 2018, Gaia DR2 documentation, Tech. rep.

Ventura, P., Carini, R., & D'Antona, F. 2011, *Monthly Notices of the Royal Astronomical Society*, 415, 3865

Villanova, S., Piotto, G., Marino, A. F., et al. 2010, in IAU Symposium, Vol. 266, Star Clusters: Basic Galactic Building Blocks Throughout Time and Space, ed. R. de Grijs & J. R. D. Lépine, 326–332

Wagner-Kaiser, R., Sarajedini, A., von Hippel, T., et al. 2017, *Monthly Notices of the Royal Astronomical Society*, 468, 1038

Walker, A. R. 1992, *Publications of the Astronomical Society of the Pacific*, 104, 1063

—. 1998, *Astronomical Journal*, 116, 220

Watkins, L. L., van der Marel, R. P., Bellini, A., & Anderson, J. 2015, *Astrophysical Journal*, 803, 29

Weidner, C., & Kroupa, P. 2005, *Astrophysical Journal*, 625, 754

Yi, S. K., Lee, J., Sheen, Y.-K., et al. 2011, *Astrophysical Journal Supplement*, 195, 22

Yong, D., & Grundahl, F. 2008, *Astrophysical Journal Letters*, 672, L29

York, D. G., Adelman, J., Anderson, John E., J., et al. 2000, *Astronomical Journal*, 120, 1579

Zinn, R. 1985, *Astrophysical Journal*, 293, 424

Zinn, R., & Dahn, C. C. 1976, *Astronomical Journal*, 81, 527